

**MICROSTRUCTURE AND STRAIN RATE EFFECTS ON
THE MECHANICAL BEHAVIOR OF PARTICLE
REINFORCED EPOXY-BASED REACTIVE MATERIALS**

A Thesis
Presented to
The Academic Faculty

by

Bradley William White

In Partial Fulfillment
of the Requirements for the Degree
Doctor of Philosophy in the
School of Materials Science and Engineering

Georgia Institute of Technology
December 2011

MICROSTRUCTURE AND STRAIN RATE EFFECTS ON THE MECHANICAL BEHAVIOR OF PARTICLE REINFORCED EPOXY-BASED REACTIVE MATERIALS

Approved by:

Professor Naresh N. Thadhani,
Advisor
School of Materials Science and
Engineering
Georgia Institute of Technology

Professor Arun M. Gokhale
School of Materials Science and
Engineering
Georgia Institute of Technology

Professor Vladimir Tsukruk
School of Materials Science and
Engineering
Georgia Institute of Technology

Dr. Jennifer L. Jordan
Air Force Research Laboratory
Eglin Air Force Base

Dr. Jonathan E. Spowart
Air Force Research Laboratory
Wright-Patterson Air Force Base

Date Approved: September, 20 2011

*To all my friends and family,
who have been wondering what I have been up to all these years,
and what a dissertation is.
Well here it is. I hope you like it and that
it doesn't put you to sleep.*

ACKNOWLEDGEMENTS

Many individuals have made it possible for me to carry out this research through their support and aid, and I would like to take this time to thank them.

Firstly, I would like to thank my advisor, Dr. Thadhani, who has given me much freedom in the direction of my work and offering invaluable advice and guidance when needed. Your dedication to your students and work is unfounded and has been a key part to the success of my research while at Georgia Tech as well as others in the HSR Lab.

My time at Georgia Tech was supplemented by internships at Eglin AFB, Wright-Patterson AFB, and Lawrence Livermore National Laboratory where I was given the opportunity to work in some great facilities and learn a great deal from my mentors Dr. Jennifer Jordan, Dr. Jonathan Spowart and Dr. Keo Springer at these locations. To them a special thanks is extended for their guidance and the great learning experiences I had at those labs.

I would also like to thank Dan Eakins, Morgana Martin, Lou Ferranti, and those that have come before them for the foundations they have laid in the HSR lab that continue to be passed down from graduate student to graduate student in the fields of shock physics, experimental procedures with our equipment, and modeling. In addition I would like thank other group members, Anthony Fredenburg, Kit Neel, Chris Wehrenberg, Paul Specht, Brady Aydelotte, and Adam Jakus for their discussions, advice, and friendship inside and outside of the lab throughout my stay at Georgia Tech. To the other group members Sean Kelly, Mike Tucker, Tyler Jackson, and Jennifer Breidenich thanks for the occasional breaks from graduate work and conversations. A much needed thank you goes out to the undergraduate students,

Jim Painter, Jared Burdine, Ian Lehn, Sean Dixon, Nathan Causey, Anna Alexander, Alex Stewart and Blake Wilckens that have assisted me in the lab at one time or another.

The author would also like to acknowledge the funding sources for this research for which without them this research would not have been possible. This includes the Air Force Office of Scientific Research (AFOSR) through contract No. F-08630-03-C-0001, and Lawrence Livermore National Laboratory under contract No. DE-AC52-07NA27344.

Lastly, I would like to thank my family and friends, whose unwavering support and encouragement have helped me out greatly throughout my undergraduate and graduate careers. They include but are not limited to Garritt Tucker, Ashley Tucker, Paul Steinman, Morgan Millar, Walter Voit, Jackie Milhans, Jack Flicker, Greg Ellison, Hayes Stripling, Sandy Alexander, my brothers Jeff and Tony, and finally my parents Scott and Diana White.

TABLE OF CONTENTS

DEDICATION	iii
ACKNOWLEDGEMENTS	iv
LIST OF TABLES	x
LIST OF FIGURES	xii
SUMMARY	xxii
I INTRODUCTION AND MOTIVATION	1
1.1 Objectives and Overall Approach	3
II BACKGROUND	5
2.1 Structural Energetic Materials	6
2.2 Epoxy as a Composite Matrix	7
2.2.1 Relaxation Mechanisms of Epoxy	8
2.3 Particle Reinforced Polymer Composites	13
2.3.1 Characteristics and Development of an Interphase in Polymer-Based Composites	15
2.3.2 Changes in the Thermomechanical Behavior	25
2.4 Mechanical Behavior of Polymers and Polymer Composites	35
2.4.1 Mechanical Behavior of Polymers	35
2.4.2 Mechanical Behavior of Polymer-Based Composites	39
2.4.3 Field Distributions Around Particles in a Matrix	51
2.4.4 Increase in Temperature due to Plastic Deformation	55
III EXPERIMENTAL PROCEDURE AND CHARACTERIZATION	60
3.1 Materials Characterization	60
3.1.1 Starting Powder Characterization	60
3.1.2 Epoxy Resin and Hardener System	61
3.2 Casting of Epoxy-Based Composites	64
3.3 Mechanical Property Characterization	67

3.3.1	Ultrasonic Sound Speed Measurement Techniques	67
3.3.2	Quasi-Static Compression Experiments	69
3.3.3	Split-Hopkinson Pressure Bar Experiments	75
3.3.4	Taylor Rod-On-Anvil Impact Experiments	80
3.4	Thermomechanical Property Characterization	85
3.4.1	Dynamic Mechanical Analysis	86
3.4.2	Differential Scanning Calorimetry	87
3.4.3	Thermogravimetric Analysis	89
IV	EXPERIMENTAL RESULTS AND DISCUSSIONS	91
4.1	Microstructure Features and Quantitative Characterization	91
4.1.1	Multi-Scalar Analysis of Area Fractions (MSAAF)	92
4.1.2	Nearest Neighbor Distributions	100
4.1.3	Summary of Homogeneous Length Scales and Nearest Neighbor Distances	106
4.2	Ultrasonic Sound Speed and Elastic Properties	108
4.2.1	Voigt-Reuss Upper and Lower Bounds for Effective Elastic Properties	111
4.2.2	Hashin-Shtrikman Upper and Lower Bounds for Effective Elastic Properties	113
4.2.3	Summary of Ultrasound and Hashin-Shtrikman Bounds	118
4.3	Uniaxial Stress Quasi-Static Compression Test Results	118
4.3.1	Young's Modulus at Quasi-Static Rates of Strain	120
4.3.2	Peak Stress and Peak Strain at Quasi-Static Rates of Strain .	126
4.3.3	Recovery Strain	128
4.3.4	Damage Accumulation at Quasi-Static Rates of Strain	129
4.3.5	Summary of Quasi-Static Compression Results	137
4.4	Split-Hopkinson Pressure Bar Results	140
4.4.1	Young's Modulus at Dynamic Strain Rates	147
4.4.2	Peak Stress and Strain at Dynamic Strain Rates	148
4.4.3	Summary of Dynamic Uniaxial Stress Compression Results .	152

4.5	Taylor Rod-On-Anvil Impact Test Results	153
4.5.1	Summary of Taylor Impact Test Results	157
4.6	Particle Strain Analysis	158
4.6.1	Measuring Particle Strain	159
4.6.2	Summary of Particle Strain Analysis from Microstructures	175
4.7	Thermomechanical Behavior of Epoxy-Based Polymer Composites	176
4.7.1	Effect of Particle Reinforcement on T_g and $\tan \delta$	176
4.7.2	Effects of Particle Reinforcement on Crosslink Density	183
4.7.3	Estimate of Interphase Thickness	187
4.7.4	Decomposition Temperature of Epoxy-Based Composites	190
4.7.5	Summary of Thermomechanical Behavior and Influence of Particles on Epoxy	193
V	MESO-SCALE SIMULATIONS OF EPOXY-BASED COMPOS- ITES USING ALE3D	197
5.1	Microstructure Generation	198
5.2	Mesoscale Simulation Boundary Conditions	202
5.3	Simulation Material Models	202
5.4	Mesh Resolution Effects	205
5.5	Composite Material Behavior from Simulations	208
5.6	Decomposing the Strain into Composite Constituents and Examina- tion of Strain Rate Behavior	212
5.7	Comparison of Simulation Microstructures with Experiments	218
5.8	Characterization of Strain Localization Effects	219
5.9	Epoxy Material Model Sensitivity	222
5.10	Summary of Mesoscale Modeling	228
VI	MECHANICAL BEHAVIOR DEPENDENCE ON MICROSTRUC- TURE AND EPOXY-MATRIX COMPOSITES	231
6.1	Mechanical Behavior Across a Wide Range of Strain Rates	232
6.1.1	Peak Stress and Transition Strain Rates for Epoxy-Based Com- posites	233

6.1.2	Strain-Rate Effects on Apparent Elastic Modulus	238
6.2	Effects of Homogeneous Length Scales on Composite Mechanical Properties	243
6.2.1	Dependence of Elastic Modulus on L_H	243
6.2.2	σ_y Dependence on L_H	247
6.3	Implications of Mesoscale Effects on Mechanical Behavior of Polymer Matrix Composites	247
VII CONCLUSIONS AND FUTURE WORK		252
7.1	Key Conclusions	252
7.2	Future Work	254
7.2.1	Dynamic Response of Composites Under Additional Loading Conditions	254
7.2.2	Effects of Epoxy Structure on Particle Strain	255
7.2.3	Alternative Matrix Materials for Enhanced Structural Properties	257
7.2.4	Alternative Matrix Materials for Increased Energetics	260
APPENDIX A — EPOXY RESIN AND CURING AGENT SYS- TEM		264
APPENDIX B — SPLIT-HOPKINSON PRESSURE BAR EQUATIONS		274
APPENDIX C — THERMOMECHANICAL LOSS MODULUS AND TAN-δ CURVES		278
APPENDIX D — PARTICLE STRAIN PLOTS FOR MNML-1, -3, -5, AND 7		282
REFERENCES		283

LIST OF TABLES

2.1	Experimentally measured mechanical properties of pure epoxy and Ni+Al powder-reinforced composites.	44
3.1	Material configurations determined from a two-factorial design of experiments	66
3.2	Relationships between elastic constants.	68
4.1	Calculated and measured densities for each composite material. . . .	94
4.2	Homogeneous length scales for Ni, Al, and Ni+Al calculated for CV=0.01 and the 1 st , 3 rd , 5 th , and 10 th nearest-neighbor distance values between Ni-Ni, and Al-Al particles for each composite.	102
4.3	Summary of ultrasonic sound speed measurements for each epoxy-based composites.	109
4.4	Summary of isotropic elastic properties calculated from ultrasonic sound speed measurements for each epoxy-based composites.	110
4.5	Elastic properties determined from the Voigt-Reuss bounds	114
4.6	Effective elastic properties for the epoxy-based composites, calculated using the Hashin-Shtrikman bounds [1].	116
4.7	Mechanical properties determined from linear and quadratic fits to virtual strain gage data.	119
4.8	Mechanical properties determined from linear and quadratic fits to virtual strain gage data.	119
4.9	Mechanical properties determined from split Hopkinson pressure bar experiments at a strain rate of $\dot{\epsilon} = 1 \times 10^3 s^{-1}$	141
4.10	Mechanical properties determined from split Hopkinson pressure bar experiments at a strain rate of $\dot{\epsilon} = 5 \times 10^3 s^{-1}$	142
4.11	Glass transition temperatures determined from DSC measurements . .	177
4.12	Loss modulus and $\tan \delta$ peak temperatures.	180
4.13	Crosslink densities for epoxy-based composites	184
4.14	Parameter values used in calculation of the interphase thickness and volume	189
4.15	Interphase thickness and volume calculated from changes in heat capacity	189
4.16	Decomposition temperature of epoxy-based composites	193

5.1	Tabular hardening parameters for Epoxy (Epon826/DEA). Reference curve for data at a strain rate of $3.9 \times 10^3 \text{ s}^{-1}$ was used to find the parameters in the dynamic strain rate regime.	205
5.2	Modified tabular hardening parameters for Epoxy (Epon826/DEA). . .	225
7.1	Material configurations determined from a two-factorial design of experiments with suggested initial configurations to expand the design space.	256
7.2	Mechanical properties of the thermal-cured fluorinated (BEF) and DGEBA epoxy resins with different curing agents.	261

LIST OF FIGURES

2.1	Example plot of polymer relaxation transitions	9
2.2	Dynamic mechanical analysis of epoxy (EPON 826/DEA) at 1, 10, and 100 Hz.	10
2.3	Structure for the Jeffamine D-Series curing agents	11
2.4	The glass transition temperature vs. cross-link density.	12
2.5	Tan δ -Temperature plot showing different beta transitions for epoxies cured with different amines.	14
2.6	Loss modulus-Temperature plot showing height differences for different epoxy beta transitions.	14
2.7	Schematic representation of the polymer surface, showing the effects of metal type on polymer binding for the same quantity of Cu, Ni, and Al deposited.	17
2.8	Binding energy of DEA with metals as a function of temperature. Plot showing bonding between the DEA and metal is either ionic or covalent, in contrast to the assumed hydrogen bonding.	19
2.9	Average values of the free volume obtained from free volume distribution using PALS at different filler-volume fractions.n	20
2.10	Free volume effects in an epoxy matrix due to the presence of particles.	22
2.11	TEM images of two neighboring silica nanoparticles in the epoxy matrix showing a 2-3 nm altered interphase region.	22
2.12	Interphase thickness and volumetric fraction as a function of the filler volume fraction calculated using method developed by Lipatov	24
2.13	Effects of particles on T_g and the tan δ peak.	27
2.14	Effects of particle volume fraction on the broadening and height of the tan δ peak.	28
2.15	Glass-transition temperature behavior of alumina/PMMA nanocomposites and the effects of particle weight percentage.	30
2.16	Effects of wt.% particles on T_g normalized to surface area.	31
2.17	Change in E' with increased particle loading fractions	33
2.18	Dependence of E' with temperature and particle loading fractions	33
2.19	Dependence of E' with particle size	34

2.20	Uniaxial Compression curves for PC	36
2.21	Uniaxial Compression curves for PTFE	37
2.22	PC and PVDF peak stress-strain rate plots	39
2.23	Drop in flow stress with strain rate	40
2.24	Drop in flow stress with strain rate	41
2.25	The effect of filler content of wollastonite and glass beads on tensile strength for nylon-6 based composites	42
2.26	Stress-strain curves for pure nylon-6 compressed at quasi-static and dynamic rates of strain.	43
2.27	Stress-strain curves for pure nylon-6 reinforced with 5 wt.% of clay compressed at quasi-static and dynamic rates of strain.	44
2.28	Summary of stress-strain relations of Al + Fe_2O_3 + Epoxy with different amounts of epoxy by weight acting as a binder for a mass loading of (Al + Fe_2O_3) consisting of 25.26% Al and 74.74% Fe_2O_3 by weight.	45
2.29	Comparison of stress strain relationships for metals and structural energetic materials.	46
2.30	Taylor impact deformation profiles for polycarbonate.	48
2.31	Taylor impact deformation profiles for poly(ether ether ketone).	48
2.32	Relative tensile strength of varying particulate filled composites.	50
2.33	Average tensile yield stress of particle filled composites.	52
2.34	Schematic of interacting stress fields between particles embedded in a matrix.	53
2.35	Schematic of stress volume around particles in a matrix.	54
2.36	Stress contour plot of hard spheres in a softer matrix material at 5% strain.	55
2.37	Beta heat conversion factor	58
2.38	Temperature rise due to work	58
3.1	Particle morphologies of aluminum and nickel powders.	62
3.2	Particle size distribution for aluminum and nickel particles.	63
3.3	Chemical structures for epoxy resin and DEA curing agent.	64
3.4	Examples of the cast particle reinforced epoxy composites.	66

3.5	Example of shear in specimen during quasi-static compression test prior to MTS frame alignment.	70
3.6	Placement of virtual strain gages on quasi-static compression samples	72
3.7	Representative stress strain curve for epoxy matrix composites at a strain-rate of 10^{-4} s^{-1}	72
3.8	Quasi-static compression sample at the (a) initial, and (b) final strain state.	73
3.9	Analysis of the composite stress strain curve to obtain Young's modulus.	74
3.10	Analysis of the composite stress strain curve to obtain the peak stress.	75
3.11	Comparison of true and engineering stress-strain curves.	76
3.12	77
3.13	One and two-wave split-Hopkinson pressure bar stress analysis	79
3.14	Taylor rod-on-anvil impact experimental apparatus and schematic of chamber and diagnostics.	81
3.15	Impact specimens for MNML-6	82
3.16	High resolution image of a recovered Taylor impact specimen	83
3.17	Geometry of a cylindrical projectile before and after impact with a rigid anvil.	83
3.18	Determination of the critical velocity for Hutching's analysis	84
3.19	Representative DMA curve for the MNML-1.	87
3.20	Representative DMA curve for the MNML-1 showing E' and $\tan-\delta$ curves.	88
3.21	Representative DSC curve for the MNML-7.	89
3.22	Representative TGA curve for the MNML-6.	90
4.1	Representative SEM microstructure images for each prepared epoxy-based composite. The white arrows in shown in images for MNML-3, 6, 7, and 8 denote examples of where particle pullout has occurred. The red arrow shown in the image for MNML-6 denotes pores/voids within the microstructure.	93
4.2	Typical MSAAF PLOT	95
4.3	Homogeneous length scale for each epoxy-based composite determined by MSAAF.	96
4.4	Homogeneous length scale predictions for different particle diameters.	98

4.5	Homogeneous length scale of aluminum for each epoxy-based composite determined by MSAAF.	99
4.6	Homogeneous length scale of nickel for each epoxy-based composite determined by MSAAF.	100
4.7	Nearest neighbor distances between nickel particles for composites MNML-1 through -4.	103
4.8	Nearest neighbor distances between nickel particles for composites MNML-3 and -4.	104
4.9	Microstructures for MNML-1 through -4 threshold for Ni particles, highlighting the spatial distribution of particles. In figures (a) and (b) there are regions of increased clustering of particles whereas for (c) and (d) the Ni is distributed more uniformly.	105
4.10	Nickel particle MSAAF-plots with indicated slopes for composite MNML-1 (a) and MNML-3 (b). The slopes characterized as being less negative than -1.0 indicates a clustering of the nickel particles.	106
4.11	Nearest neighbor distances between aluminum particles for each composite.	107
4.12	Ni and Al epoxy rule of mixtures	112
4.13	Ni/epoxy, Al/epoxy, and Ni/Al/epoxy rule of mixtures	113
4.14	Hashin-Shtrikman upper and lower bounds for the MNML-series epoxy-based composites.	117
4.15	Comparison of the elastic modulus from ultrasound test to the Hashin-Shtrikman upper and lower bounds for the MNML-series epoxy-based composites.	117
4.16	Representative quasi-static compression curves for MNML-1 through MNML-8 at a strain rate of 10^{-4} s^{-1}	120
4.17	Rescaled quasi-static compression curves for MNML-1 through MNML-8 at a strain rate of 10^{-4} s^{-1}	121
4.18	Representative quasi-static compression curves for MNML-1 through MNML-8 at a strain rate of 10^{-3} s^{-1}	121
4.19	Rescaled quasi-static compression curves for MNML-1 through MNML-8 at a strain rate of 10^{-3} s^{-1}	122
4.20	Quasi-static compression σ - ε curves for each composite. (CONTINUED IN NEXT FIGURE)	123
4.21	Quasi-static compression σ - ε curves for each composite.	124

4.22	Young's modulus as a function of volume fraction for quasi-static compression experiments.	125
4.23	Peak stress as a function of volume fraction for quasi-static compression experiments.	127
4.24	Peak strain as a function of volume fraction for quasi-static compression experiments.	128
4.25	Amount of strain recovered in samples following quasi-static compression tests.	130
4.26	Comparison of recovery strains for MNML-2 through -8.	131
4.27	Comparison of recovery strains between composites with a change in Al particle size.	132
4.28	Damage-plastic strain plot for MNML-1 and -2	134
4.29	Damage-plastic strain plot for MNML-3 and -4	135
4.30	Damage-plastic strain plot for MNML-5 and -6	135
4.31	Damage-plastic strain plot for MNML-7 and -8	136
4.32	Damage-plastic strain plot for MNML-5, -6, -7, and -8	137
4.33	Damage-plastic strain plot for MNML-1, -2, -5, and -6	138
4.34	Damage-plastic strain plot for MNML-3, -4, -7, and -8	138
4.35	Damage-plastic strain plot for MNML-1, -2, -3, and -4	139
4.36	$\sigma - \varepsilon$ curves for the composites tested at a strain rate of $1 \times 10^3 s^{-1}$. . .	143
4.37	$\sigma - \varepsilon$ curves for the composites tested at a strain rate of $5 \times 10^3 s^{-1}$. . .	144
4.38	Representative split-Hopkinson pressure bar $\sigma - \varepsilon$ curves for the two nominal rates of strain tested. (CONTINUED IN THE FOLLOWING FIGURE)	145
4.39	Representative split-Hopkinson pressure bar $\sigma - \varepsilon$ curves for the two nominal rates of strain tested.	146
4.40	Young's modulus as a function of particle volume fraction for dynamic strain rates	148
4.41	Peak stress as a function of particle volume fraction for dynamic strain rates	150
4.42	Peak strain as a function of particle volume fraction for dynamic strain rates	151
4.43	Determination of the critical velocity for Hutching's analysis	154

4.44	Dynamic $\sigma - \varepsilon$ curves from Taylor rod-on-anvil impact experiments. .	155
4.45	Critical velocity vs. particle concentration for each composite determined using Hutching's analysis	155
4.46	Yield stress vs. particle concentration for each composite determined using Hutching's analysis	156
4.47	Yield strain vs. particle concentration for each composite determined using Hutching's analysis	157
4.48	Schematic of the particle geometry before and after uniaxial compression experiments.	159
4.49	Microstructure of MNML-3 following quasi-static compression.	161
4.50	Microstructure of MNML-3 following dynamic uniaxial compression. .	162
4.51	Plot of aluminum particle plastic strain against bulk plastic strain. . .	163
4.52	Plot of aluminum particle plastic strain against bulk plastic strain for quasi-static and dynamic rates of strain.	165
4.53	Particle strain measured in Ni compared with Al particle strains . . .	166
4.54	Microstructure of MNML-1 following dynamic uniaxial compression. .	167
4.55	Particle strain in aluminum for MNML-2, -4, -6, and -8 at a strain rate of $1 \times 10^{-4} \text{ s}^{-1}$ and bulk strain of approximately 21.5%.	169
4.56	Particle strain distribution for aluminum in composites MNML-2, -3, -4 and -6, at a strain rate of $1 \times 10^{-4} \text{ s}^{-1}$ and bulk strain of approximately 21.5%.	170
4.57	Plot of particle size effects on the degree of particle plastic strain found in epoxy based composites.	171
4.58	Particle strain distribution for aluminum in composites MNML-1, and -2, at a strain rate of $5 \times 10^3 \text{ s}^{-1}$ and bulk strain of approximately 36.0%. 172	
4.59	Particle strain mapping for MNML-2 (40% $5 \mu\text{m}$ Al + 10% Ni) with a bulk plastic strain of 28.7%	174
4.60	Particle strain mapping for MNML-2 (40% $5 \mu\text{m}$ Al + 10% Ni) with a bulk plastic strain of 21.7%, Showing Ni constraining effects.	174
4.61	Particle strain mapping for MNML-1 (40% $50 \mu\text{m}$ Al + 10% Ni) with a bulk plastic strain of 36.0%	175
4.62	Glass transition temperature determined at two different heating rates using a DSC.	178
4.63	Glass transition temperature determined from $\tan \delta$ peaks.	179

4.64	Comparison of $\tan \delta$ curves for epoxy-based composites containing 5 μm sized aluminum particles.	182
4.65	Plot of the decrease in $\tan \delta$ peak height as the volume fraction of particle reinforcement increases.	182
4.66	Effect of particle loading fraction on the storage modulus for the materials containing 50 μm sized aluminum particles.	185
4.67	Effect of particle loading fraction on the storage modulus for the materials containing 5 μm sized aluminum particles.	186
4.68	Effect of particle loading fraction on the crosslink density and spacing in epoxy-based composites.	187
4.69	Comparison of the effect of particle loading fraction and size on the crosslink density and spacing in epoxy-based composites from multiple studies.	188
4.70	Plot of interphase thickness with volume fraction of particles	191
4.71	Plot of interphase volume fraction with volume fraction of particles	191
4.72	Plot of interphase in 2D microstructure for MNML-1	192
4.73	Thermogravimetric analysis of epoxy-based composites.	194
4.74	Thermogravimetric analysis of epoxy-based composites rescaled to show region at which decomposition begins.	194
4.75	Decomposition temperature of epoxy-based composites.	195
5.1	Two instances of microstructures generated using Particle Pack 2.4.	199
5.2	Composite microstructure domains. Aluminum is shown in red, nickel in blue, and epoxy gray.	201
5.3	Boundary conditions implemented in the three dimensional ALE3D simulations of composite microstructures uniaxially compressed at a strain rate of 4620 s^{-1}	203
5.4	Results of tabular hardening model parameter determination for epoxy at strain rates from 134 to 1.4x10 ⁴ s^{-1}	206
5.5	Mesh resolution optimization for particle reinforced epoxy composites.	207
5.6	Snapshot of MNML-3 at a time step of 21.6 μs for different element sizes.	208
5.7	Composite mechanical behavior comparison of experimental results with simulations.	211

5.8	Examination of effects on simulation results with a change in particle size. MNML-7 (20 vol.% 50 μ m Al) simulation results are compared with MNML-8 (20 vol.% 5 μ m Al) results.	212
5.9	Bulk, aluminum, epoxy, and nickel plastic strains as a function of time for 3D simulations conducted on (a) MNML-5 and (b) MNML-1. . . .	213
5.10	Examination of effects on simulation results with a change in particle size and volume fraction Ni. In (a) MNML-3 (20 vol.% 50 μ m Al + 10% Ni) simulation results are compared with a region of MNML-4 containing a high concentration of Ni (20 vol.% 5 μ m Al + 20% Ni) results. In (b) the strain-time decomposition for MNML-4 is depicted. Note the change in scale of from previous strain-time plots. This was done to be able to observe the higher strains due to the much higher strain rates produced in the Al and epoxy phased from increased amounts of Ni. .	215
5.11	Aluminum (a) and epoxy (b) plastic strains as a function of bulk plastic strains up to 40% for 3D simulations conducted on MNML-1, 3, 5, and 7. Plotted along with the composites is a 1:1 correspondance curve of the individual phase strain with bulk strain.	217
5.12	Comparison of Al particle strains in simulations with resultant real microstructure following dynamic compression to 36% for MNML-1 (40 vol.% 50 μ m Al + 10% Ni).	218
5.13	Plastic strain histogram data for a composite MNML-5 (left) and MNML-1 (right).	221
5.14	The effect of changing the tabular hardening parameters on the epoxy stress-strain behavior. The stress strain curves shown are the experimental results plotted along side the calculated curves using the tabular hardening model. Experimental data taken from [2].	224
5.15	Comparison of different modification to the epoxy model on the behavior of MNML-3 (20 vol.% 50 μ m Al + 10% Ni).	226
5.16	Using the epoxy model parameters: $a=0.085$, $m=704.7$, $b=0.14$, determined from optimization of the mechanical response for MNML-3 to examine the effects on other composite systems.	227
6.1	Peak stress for epoxy (Epon 826/DEA) across a wide range of strain rates from 10^{-3} to 10^4 s^{-1}	233
6.2	Compressive stress-strain curves for epoxy (Epon 826/DEA) across a wide range of strain rates from 10^{-3} to 10^4 s^{-1}	234
6.3	Representative σ - ε curves for each composite tested under a wide range of compressive strain-rates. (CONTINUED IN THE NEXT FIGURE)	235

6.4	Representative σ - ε curves for each composite tested under a wide range of compressive strain-rates.	236
6.5	Peak stress dependence on strain rate for quasi-static compression, dynamic compression, and Taylor impact loading conditions. (CONTINUED IN THE NEXT FIGURE)	239
6.6	Peak stress dependence on strain rate for quasi-static compression, dynamic compression, and Taylor impact loading conditions.	240
6.7	Summary of Young's modulus values across a wide range of strain rates.	242
6.8	Dependence of E on L_H^{Ni+Al} for composites containing 5 μ m diameter aluminum particles.	244
6.9	Dependence of E on L_H^{Ni+Al} for composites containing 50 μ m diameter aluminum particles.	245
6.10	Dependence of E on L_H^{Al} for composites containing 50 μ m diameter aluminum particles.	246
6.11	Dependence of σ_y on L_H^{Ni+Al} for composites containing 5 μ m diameter aluminum particles at dynamic strain rates.	248
6.12	Dependence of σ_y on L_H^{Ni+Al} for composites containing 5 μ m diameter aluminum particles at quasi-static strain rates.	248
7.1	Peak stress for PEEK and Epon826/DEA across a wide range of strain rates.	259
7.2	Comparison of tensile properties for various engineering thermoplastics.	260
7.3	Chemical structures of and self reinforcing polyphenylene.	260
7.4	Chemical structures of fluorinated and non-fluorinated epoxy resins and curing agents.	262
7.5	Structure of functionalized poly(p-phenylene).	263
A.1	BPA and Epichlorohydrin Reaction	265
A.2	DGEBA reaction with diethylamine	266
A.3	Amine-based curing agents	266
A.4	Curing times for DGEBA cured with common amines	267
A.5	Stability plot of 70% (w/w) DGEBA/diethylamine.	269
A.6	Tg vs. curing times for DGEBA cured with DEA	270
A.7	Etherification of an epoxy	271
A.8	Effect of water on glass transition of DER-SAA system.	273

A.9	Effect of water on activation energy of the gamma relaxation of DER-SAA system.	273
C.1	Loss modulus temperature plots for composites MNML-1 through 4. .	278
C.2	Representative loss modulus curves for each composite MNML-5 through 8 plotted along side the storage modulus. (Continuation of previous figures.)	279
C.3	Representative $\tan \delta$ curves for each composite MNML-1 through 4 plotted along side the storage modulus.	280
C.4	Representative $\tan \delta$ curves for each composite MNML-5 through 8 plotted along side the storage modulus. (Continuation of previous figures.)	281
D.1	The average amount of plastic strain in the aluminum particles for composites MNML-1, -3, -5, and -7 plotted against the bulk plastic strain.	282

SUMMARY

The effects of reactive metal particles on the microstructure and mechanical properties of epoxy-based composites is investigated in this work. Particle reinforced polymer composites show promise as structural energetic materials that can provide structural strength while simultaneously being capable of releasing large amounts of chemical energy through highly exothermic reactions occurring between the particles and with the matrix. This advanced class of materials is advantageous due to the decreased amount of high density inert casings needed for typical energetic materials and for their ability to increase payload expectancy and decrease collateral damage.

Structural energetic materials can be comprised of reactive particles that undergo thermite or intermetallic reactions. In this work nickel (Ni) and aluminum (Al) particles were chosen as reinforcing constituents due to their well characterized mechanical and energetic properties. Although, the reactivity of nickel and aluminum is well characterized, the effects of their particle size, volume fractions, and spatial distribution on the mechanical behavior of the epoxy matrix and composite, across a large range of strain rates, are not well understood. To examine these effects castings of epoxy reinforced with 20-40 vol.% Al and 0-10 vol.% Ni were prepared, while varying the aluminum nominal particle size from 5 to 50 μm and holding the nickel nominal particle size constant at 50 μm . Through these variations eight composite materials were produced, possessing unique microstructures exhibiting different particle spatial distributions and constituent makeup. In order to correlate the microstructure to the constitutive response of the composites, techniques such as nearest-neighbor distances, and multiscale analysis of area fractions (MSAAF) were used to quantitatively

characterize the microstructures. The composites were investigated under quasi-static and dynamic compressive loading conditions to characterize the effects of microstructure on their mechanical behavior at strain-rates from 10^{-4} to 10^4 s^{-1} . The dynamic response to compressive loads was obtained using the split Hopkinson pressure bar and Taylor rod-on-anvil impact experimental configurations. Microstructures from each composite and at each strain rate were analyzed to determine the amount of particle strain as a function of bulk strain and strain rate.

Also of key interest to this study are the epoxy matrix-metallic particle and particle-particle interactions at the mesoscale under dynamic compressive loading conditions. The composite microstructure is highly heterogeneous at the mesoscale and the high contrasting properties of the individual constituents drive localized deformations that are often more pronounced than those in the bulk material. To examine the mesoscale response to dynamic loading conditions, computational simulations of representative microstructures of select composites were conducted. The stress and strain localization effects were characterized at the mesoscale and the bulk mechanical behavior was decomposed into the individual contributions of the constituent phases. The analysis provided a greater understanding of the mechanisms associated with particle deformation and stress transfer between phases, and their influence on the overall mechanical response of polymer matrix composites reinforced with metallic particles. The influence of strain rate behavior of epoxy is shown to cause a strain rate dependent deformation response of reinforcement particle phases that are typically strain rate independent.

CHAPTER I

INTRODUCTION AND MOTIVATION

Particle reinforced polymer matrix composites are increasingly being studied for use as structural materials in applications at high rates of strain. These types of composites are very complex due to their heterogeneous microstructures, and because their mechanical response can be significantly influenced by the physical and chemical interactions of the constituents at the mesoscale. Depending on the composite, such as a soft polymer matrix reinforced with relatively hard (ductile or brittle) or soft (polymeric) particles, drastic differences in their strength and toughness characteristics relative to the properties of the polymer or reinforcement by itself, can be observed. Additionally, these effects can be exacerbated by the relative amounts of each constituent. In this research, polymer matrix composites reinforced with harder metallic particles are studied to obtain an increased understanding of their mechanical behavior over a range of strain rates. The understanding generated is expected to benefit in informing the design of such composite materials for high strain rate applications. One such type of a composite system is a relatively new class of materials known as structural energetic materials.

Typical energetic materials used in defense applications, such as high explosives, are often too weak to survive high rate accelerations and are therefore encased in a high density rigid inert material. While the casing provides increased kinetic energy to the overall system, it does not contribute to the chemical energy. Moreover, a large portion of the explosive energy is lost in the deformation and fracturing of the encasement material [3] during the rapid expansion of gases produced by reactions in the explosive. Thus, new generation energetic materials, "known as structural

energetic materials,” that also have mechanical strength combined with high reaction efficiency and controlled sensitivity are being considered.

Polymer matrix composites filled with either a single component reactive system or with different types of components that react under appropriate conditions (high temperatures, pressures) represent an example of such structural energetic materials. In these materials the polymeric matrix (binder), provides strength to reactive components, which also serve as reinforcement, so that the material can withstand dynamic loading conditions during high velocity impact prior to reaction. By tailoring the amount or type of binder used, the overall physical and mechanical properties can be tuned. The reactivity can also be increased if the matrix (such as fluorine from PTFE) aids in the energetic reactions through its decomposition and interaction with the reinforcement.

There is however, relatively little known about the effects of the polymer binder on the reactive components, as well as the converse effects of the reactive components on the polymer matrix and their overall mechanical behavior. This understanding is particularly important at high strain rates for which only few studies have been carried out for polymers and polymer-based composites alike. For example, it is important to understand how the load transfer from the matrix to the reactive filler constituents results in their deformation essential for reaction, and likewise, how does the mechanical behavior of the polymer matrix itself is altered by the filler constituents. For example, epoxy is known to have a bilinear dependence of yield strength on strain rate [2], with the yield strength being more rate dependent at dynamic rates of strain. However, it remains to be seen if these types of composites have similar strain rate dependencies on their bulk mechanical properties. More importantly, the mesoscale response at the level of the particles in the polymer composites has not been characterized as a function of strain rate. Since large variations of constituent ratios, particle sizes, and distribution can be employed, there can be large differences in

the meso- and bulk-scale mechanical behavior that can magnify difficulties in characterizing effects of matrix-particle interactions on the overall composite behavior. Therefore, an approach is needed that utilizes a systematic design to investigate the effects of particle size, type, and loading fractions on the composites behavior at the mesoscale and bulk levels under low and high strain rate conditions.

1.1 Objectives and Overall Approach

The purpose of this research is to investigate the mechanical behavior of an epoxy-cast composite reinforced with aluminum and nickel metallic particles. It builds on the previously studied epoxy system, by Jordan et al. [2] under compressive loading conditions. In these composites nickel-aluminum mixtures comprise an intermetallic forming material system. The composites vary in loading fractions of aluminum from 20 to 40 vol.% and nickel from 0 to 10 vol.%, allowing for the influence of volume fraction and interaction effects of Al with epoxy alone and the effects of a second phase (Ni particles) on the mechanical behavior of the composite to be systematically investigated. Additionally, the nominal particle size of aluminum varies from 5 to 50 μm in order to determine the effects of particle size on the epoxy and composite behavior at the bulk and mesoscale levels.

Changes in the composite were characterized by measuring the homogeneous length scales and nearest neighbor distances of the Ni and Al particles for each composite. The composites were tested at quasi-static (1×10^{-4} and $1 \times 10^{-3} \text{ s}^{-1}$) and dynamic (1×10^3 and $5 \times 10^3 \text{ s}^{-1}$) rates of strain under compressive loading conditions. This allowed for the variation of particle volume fraction, type, and size, along with homogeneous length scales and nearest neighbor distances to be related to the composite bulk mechanical behavior. Microstructures of the various composites, following static and dynamic loading were examined to determine the particle plastic strain as a function of bulk plastic strain and strain rate. Comparisons are made between the

different composites to obtain a better understanding of the effects of microstructure on the particle deformation behavior at the mesoscale. The epoxy matrix in these composites is also characterized using thermomechanical analyses to determine the effects of the filler particles on the chemical and physical behavior.

The mesoscale response of the composites and influence of the particles on the matrix deformation behavior, and conversely the effect of the matrix on particle deformation behavior, is investigated using computational simulations to understand the relationship between the mesoscale and bulk responses. The mesoscale response is further explored by examining the evolution of constituent strain at the mesoscale. Sensitivity studies are also conducted on the material models used in the simulations to better understand the effects of reinforcing metallic particles on the epoxy matrix.

In this thesis, the background and review of relevant literature is described first in Chapter 2, which includes some of the basics behind thermosets and different relaxation mechanisms in polymers that appear at different temperatures based on their chemistry. An introduction into the mechanical behavior of polymers and effects of introducing particle reinforcement on the composite mechanical behavior are also discussed. In Chapter 3, the techniques to quantitatively characterize the composite microstructures and experimental methods to determine the mechanical behavior and thermomechanical properties of the epoxy-based materials are discussed. Chapter 4 introduces the experimental results and discussion concerning the quasi-static and dynamic response of the epoxy-based composites under compressive loading conditions. The thermomechanical behavior of the composites using common polymeric characterization techniques is then investigated to determine the effects of metallic particles on the epoxy matrix chemistry. In Chapter 5, simulations on the representative microstructures are introduced and compared with the experimental results with a focus on the response of the individual constituents and their interactions. Finally, in Chapter 6 conclusions are given along with recommendations for future work.

CHAPTER II

BACKGROUND

Polymers offer many advantages over other conventional structural materials including reduced weight, resistance to corrosion, and ease of processing. These properties make polymers attractive materials for use as binders in composite materials. Typically, when polymers are combined with fibers or particles, it is most often with the intent to achieve enhanced material properties over that of the pure polymer. Polymer composites are used in many different applications ranging from composites for the construction industry to the high technology composites of the aerospace and defense industries. What makes these composites so versatile and applicable are the wide variety of properties that are possible due to the presence of particle or fiber reinforcement. Particle reinforced polymers are also often infiltrated with either conductive (carbon black or carbon nanotubes) or thermally insulating (clay) fillers to make materials with controlled conductive and fire retardant properties. Other polymer composites contain filler materials in order to make them more cost effective, as in the case of composites for the automotive industry. Broadly speaking particle reinforced polymer matrix composites can be broken into three categories; a) those reinforced with hard, ductile (metallic) or brittle (ceramic) particles to act as reinforcement, b) those reinforced with softer polymeric particles (such as rubber) in attempts to increase composite toughness and ductility, and c) combinations of both soft and hard particles. While many composite formulations exist with their own benefits and drawbacks, there has been a renewed interest in developing novel polymer-based composites, especially with the advent of complex material systems

needed for applications such as in aircraft (Boeing 787 Dreamliner components), panels for blast wave mitigation, as well as structural energetic materials, all of which require a good understanding of their high strain rate mechanical behavior.

2.1 Structural Energetic Materials

Efforts in the energetic materials community have been focused on investigating composite materials for use as next generation multifunctional structural energetic materials. Structural energetic materials are one such evolving class of composites that combine mechanical strength with reactive property characteristics (high energy density and rapid energy release) from multiple materials into a single systems design. While many of the applications for structural energetic materials are defense related (military and civilian), other applications include uses as solid-propellants [4, 5] or laminated reactive foils for micro-welding [6]. Structural energetic materials are typically designed to be inert under static loads and react and release energy under dynamic impact loading conditions [7, 8]. Some advantages to this type of system are: 1) the elimination of mass typically used to encase and provide structural stability to traditional energetic materials, 2) increased efficiency by replacing inert material with reactive structural materials, 3) increased energy release by using materials properly selected that encase as well as enhance the reactive characteristics of the energetic material, and 4) increased safety due to the insensitive nature of these materials under quasi-static and static loading conditions.

In this research, studies were conducted on epoxy-based structural energetic materials. However, many other types of structural energetic material exist which include but are not limited to, consolidated metal/metal-oxide mixtures [6, 9], intermetallic forming mixtures [10, 11, 12], metal/fluoropolymer mixtures [8, 13], metal/polymer (unfluorinated) mixtures [14, 15], and linear cellular alloy/reactive material mixtures [16]. While all of these energetic materials are non-explosive, and non-detonable, they

can rapidly release large amounts of energy from the heat of reaction.

2.2 Epoxy as a Composite Matrix

Due to the densely cross-linked networks possible, epoxy-based polymers exhibit ideal properties. They are thermally stable, have high glass transition temperatures, high elastic modulus in relation to other polymers, fairly high strength, low shrinkage at elevated temperatures, are resistant to chemicals, are fairly easy to process with curing agents, and have good adhesion to other materials. Epoxies are widely used in many composites ranging from structural to electrically insulating to flame and heat resistance applications which take advantage of the unique properties of epoxy. The chemical structure of the epoxy matrix and the processing conditions influence the degree of cross-linking and networks in these systems which influence their mechanical properties. In epoxy based materials with a low cross-link density, the movement of the chain segments is easier than in higher cross-linked networks. In low cross-linked networks, there is additional free volume in the matrix that can provide the necessary space for molecules to move around, thereby affecting different epoxy relaxation mechanisms.

Epoxy systems are usually comprised of a resin and a curing agent, that when mixed together, form a physically, and more importantly, chemically cross-linked molecular network of polymer chains that is irreversible and cannot be re-shaped from the original geometry of the mold without machining. The most common resin used in epoxies is diglycidylether of bisphenol-A (DGEBA) which is synthesized from the reaction between epichlorohydrin and bisphenol-A (BPA) through a step- growth polymerization, in which the epoxide ($\text{CH}_2\text{-CH-O}$) three member ring groups act as the primary reaction sites for cross-linking when curing agents, such as diethanolamine are introduced. Many researchers have investigated the effects of curing temperature [17, 18, 19, 20] on the curing times of amine-cured DGEBA epoxy. For DGEBA cured

with diethanolamine (DEA) in a 100:11.65 ratio (DGEBA:DEA by wt.), Lundberg et. al [20] found that the epoxy is sufficiently cured within 8 days at a curing temperature of 24 °C, 3 days at 40 °C and 18 hours at 75 °C. For more information regarding different curing mechanisms and the effects of epoxy resin and curing agent molecular structure, the reader is referred to Appendix A.

2.2.1 Relaxation Mechanisms of Epoxy

The relaxation transitions in polymers depend on the loading conditions such as temperature, rate, and force. These relaxations act as mechanisms to accommodate the loads by rearranging the underlying structure (conformation) of the polymer. A polymer typically has many different relaxations that occur at different temperatures and are strain-rate dependent. The relaxations are also structure dependent and often are associated with the motion of different side groups or main chain groups of a polymer chain, and can also be affected by the degree of cross-linking. For example, as will be discussed later, there is an increase in the glass transition temperature that is associated with the decrease of the epoxy main chain length in DGEBA/Jeffamine epoxies. In this section, some of the relaxation mechanisms of epoxy systems will be summarized.

While the glass transition is the most commonly measured transition in polymers, other relaxation transitions exist. Each relaxation transition is labeled in terms of the order they appear with decreasing temperature starting from the glass transition (α -relaxation), then β -relaxation, and so on. The temperature at which each relaxation occurs, is dependent on the polymer. One method to obtain the transition temperatures is to use a dynamic mechanical analyzer and examine a $\tan \delta$ -temperature plot¹,

¹For polymers the elastic modulus is considered a complex value, since the stress and strain no longer occur in phase under oscillatory loads, and is expressed as $E^* = E' + iE''$. Here $E' = (\sigma/\varepsilon)\cos\delta$ and $E'' = (\sigma/\varepsilon)\sin\delta$ for the storage and loss modulus respectively where δ is the phase lag between the stress and strain. The phase angle, $\tan \delta$, is defined as the ratio of the storage and loss modulus, as $\tan\delta = E''/E'$.

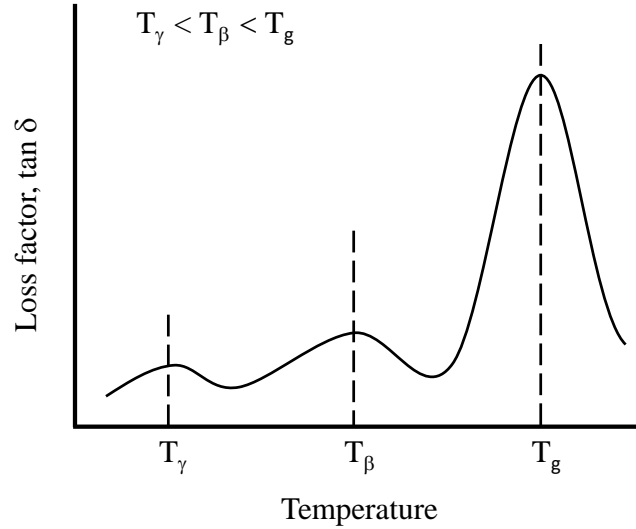


Figure 2.1: A possible $\tan \delta$ -temperature plot for a polymer showing the primary (glass) and two secondary transitions.

as shown in Fig. 2.1.

For observing the glass transition temperature, other methods such as examining storage modulus² (E')- or loss modulus (E'')-temperature plots are often useful. The glass transition is marked by a large change in the storage modulus, often over a few orders of magnitude. This effect can be seen for Epon 826/DEA epoxy in Figure 2.2 for which the glass transition is observed to occur around 350 K. Also in the figure we can see the effect that strain-rate has on the relaxations. By examining the loss modulus curve we see the β -relaxation, occurring between 200 and 250 K, shift to higher temperatures as the strain-rate is increased (oscillatory rates from 1 to 100 Hz). This is common in polymers and the amount of shifting observed due to a change in strain-rate is different for the different relaxation transitions.

While the glass transition in polymers is associated with large scale movements in the polymer, secondary transitions are often associated with one or more combinations

²The storage modulus, in viscoelastic materials, represents the elastic portion of the the dynamic modulus while the loss modulus represents the viscous contribution to the dynamic modulus.

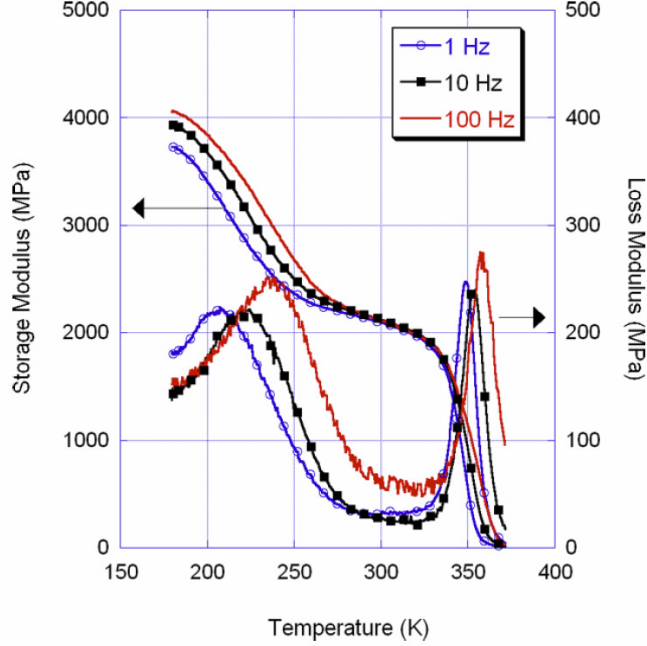


Figure 2.2: Dynamic mechanical analysis of epoxy (EPON 826/DEA) at 1, 10, and 100 Hz. Figure taken from [2].

of molecular rotations, oscillations and motions of the polymer main chain segments or side chain groups. In PMMA for example, the β -relaxation is associated with side chain motions of ester groups while the γ -relaxation is associated with the methyl groups attached to the main chain, and the δ -relaxation is associated with the methyl groups attached to the side chains [21].

Although the glass transition is fairly easy to measure, the phenomenological process behind the transition is not well understood and most of the relationships are empirical in nature. While discussion of glass transition theories in polymers is beyond the scope of this work, the free volume and cooperativity theories will briefly be described. The free volume theory assumes that when the polymer is in the glassy state ($T < T_g$) there is a certain amount of free volume locked into the structure that limits the large scale mobility of the polymer chain segments. Then, as the temperature in the polymer is increased approaching T_g , the free volume increases until a

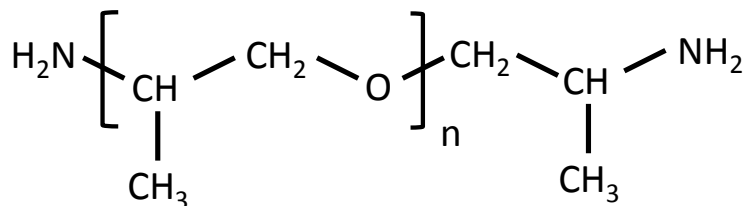


Figure 2.3: Structure for the Jeffamine D-Series curing agents, [23, 24].

critical free volume (at T_g) is reached that allows for large scale molecular motion to occur. According to the cooperativity theory [22], for a given temperature there are different degrees of cooperative rearrangements of the surrounding neighbor regions for a segment to be able to move into a new conformation. At high temperatures or low densities, there are smaller amounts of neighbor segments needed to move (in an uncoordinated manner) in order for a segment to assume a new conformation. This is due to the greater local vibrations and motions associated with the higher temperatures. However, as the temperature is decreased or density is increased more neighbor regions are needed to cooperatively move in order to make room for the new segment conformation. This is due to the smaller molecular vibrations of the local neighboring regions. At lower and lower temperatures the size of the neighboring domains needed to cooperatively move in order for a segment to assume a new conformation increases and eventually becomes infinite.

The glass transition temperature is affected by the length of the curing agent used. In DGEBA systems cured with different lengths of polyoxypropylendiamine/polyetheramines (Jeffamine, Huntsman Corporation) the glass transition temperature decreases with an increase in length of the backbone of the polyoxypropylendiamine molecule. For stoichiometric ratios of DGEBA mixed with Jeffamine D400 ($n = 6.1$ [23]), as opposed to DGEBA mixed with Jeffamine D230 ($n = 2.5$ [24]), the maximum attainable glass transition temperatures were found to be 40°C and 80°C respectively [19]. The structure of the Jeffamine D-Series curing agents is shown in Fig. 2.3.

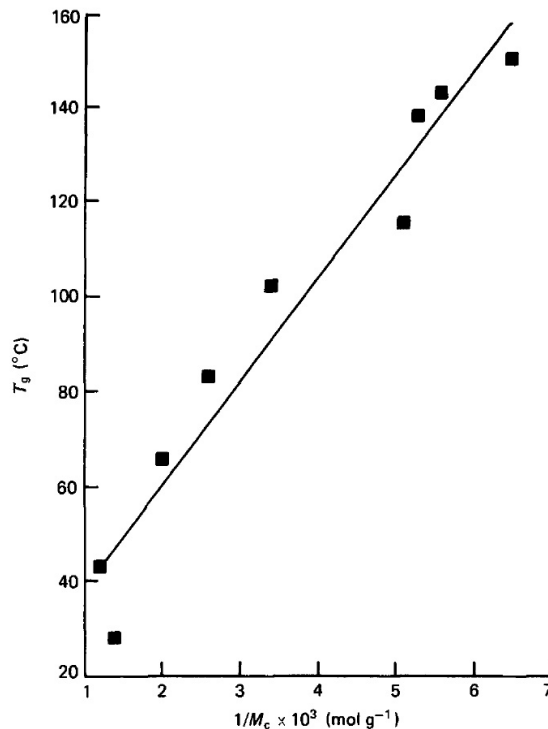


Figure 2.4: The glass transition temperature vs. cross-link density. Figure taken from [26].

Studies by Cukierman et al. [25] have shown that the glass transition temperature in amine-cured epoxies is related to the cross-link density and chain flexibility. By changing the type of diamine used to cure the epoxy they found the glass transition temperature decreased as the chain rigidity decreased. They also suggest that the bulkier the mono-amine used to cure DGEBA with some amount of diamine, and as the amount of diamine is decreased (or increase in amine percentage), the more the free volume is increased which allows for a greater decrease in T_g . As the cross-link density decreases the chain mobility becomes easier “as a consequence of a decrease of steric hindrance and chain interactions.” For aromatic- and aliphatic-cured epoxies, the glass-transition temperature increases linearly with cross-link density [26], as shown in Fig. 2.4.

Secondary transitions, while not as important to the selection of the materials for

use in most applications due to the smaller changes in storage modulus, have been more easily identified with specific motions of polymer chain groups. Ochi et al. [27], were able to use dynamic mechanical analysis with an inverted free oscillation pendulum in order to relate the β -transition to the motion of the hydroxyether group in the main epoxy chain in amine cured-DGEBA epoxies. They were able to determine this by monitoring the curing of epoxy with amines, and comparing the results to epoxies cured with ether. When the DGEBA was cured with ether, the β -transition did not change in temperature or peak height, while for the amine cured epoxies, the β -transition increased in temperature and altered the peak height as the epoxy cured due to the formation of hydroxyether groups, which are absent in ether cured epoxies. For this system, the β -transition was found to occur around -40°C . The researchers went further and acetylated the hydroxyether groups causing the β -transition to separate into two peaks (β' and β''), with the relaxation of the β' due to the acetylated hydroxether groups and β'' other polymer segments. Fig. 2.5 shows the different β -transitions for these epoxies. In each case, the β -transition was found to be directly linked to the motion of the newly added chain segment to the main epoxy chain from the cross-linker, with similar results found in other studies [28, 29].

Cukierman et al. [25] found the height and width of the β -transition peak to be related to the degree of cross-link density (altered by using different combinations of mono-and diamines) in an amine-cured epoxy. For networks with a higher cross-link density (more diamines) the peak height and width of the β -transition in a loss modulus curve increases (see Fig. 2.6 in which HDMA refers to the epoxy with greatest degree of cross-linking and HA the least).

2.3 Particle Reinforced Polymer Composites

In the previous sections, we have seen how T_g increases with the amount of energy required to keep epoxy segments moving and how secondary relaxation transitions in

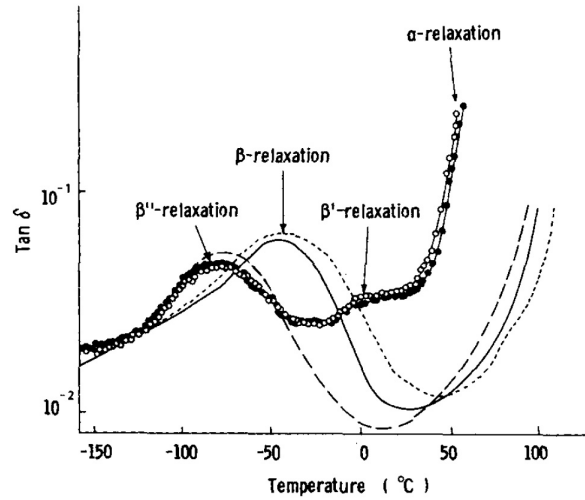


Figure 2.5: Dynamic mechanical properties of cured epoxide resins acetylated with acetyl chloride. Amine linkages (acetylated) (open circles), amine-and-ether linkages (acetylated) (filled circles), amine linkages (short dashes), amine and ether linkages (solid line), ether linkages (long dashes). Figure taken from [27].

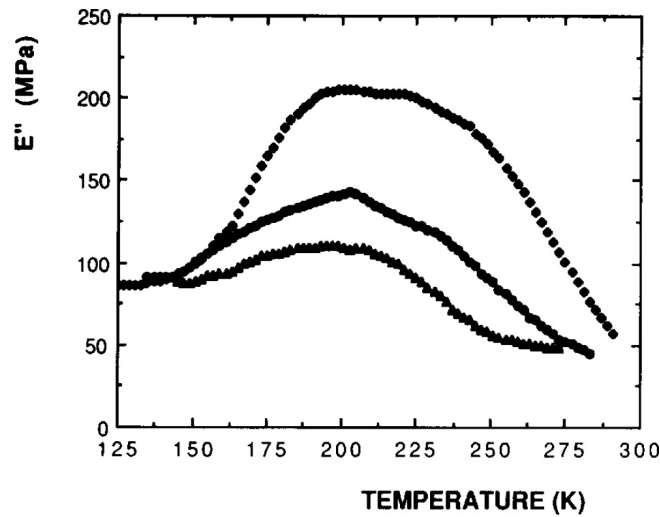


Figure 2.6: Loss modulus, E'' , versus temperature in the glassy state at the frequency 1 Hz. HDMA (diamonds/top curve), HMDA/HA (circles/middle curve), HA (triangles/ bottom curve). Figure taken from [25].

epoxy are dependent on the structural characteristics of the polymer such as cross-link density and steric effects. These steric effects are due to atoms within the polymer chains occupying space. When the atoms in the polymer molecules are brought close to each other, the overlapping electron clouds affect the polymer's conformation. Thus, it is important to understand how the presence of metal particles or any other type of introduced phase in an epoxy matrix can alter either the polymer structure itself or introduce any physical hindrance to the polymer chain motions thereby changing the relaxations mechanisms.

It is well known that the mechanical behavior of composites depend on the constituent's properties, composition, phase morphology, and the bonding or adhesion between the matrix phase and the other constituents. However, the mechanical behavior is a result of the interaction of the individual constituents with one another to produce the overall bulk response of the composite. In this section, the effects that reinforcing particles have on the thermomechanical behavior of the polymer matrix and the interaction effects between the polymer matrix and particles, producing an interphase, will be described. To quantify these interaction effects, methods such as differential scanning calorimetry, NMR, and dynamic mechanical analysis are often used.

2.3.1 Characteristics and Development of an Interphase in Polymer-Based Composites

The mechanisms behind the changes in the thermomechanical properties are largely controlled by characteristics of the filler-polymer interfacial region. At the interfacial region adsorption of the polymers, resins, and curing agents can occur creating additional junction points for cross-linking (chemically and physically) of the polymer matrix. Diffusion of atoms from metals into the polymer matrix has been found to occur [30] creating a more gradual interface transition. Changes in the conformation of the polymer also occur in the interfacial region leading to changes in the free volume,

thereby altering the short and long-range segmental mobility. All of these methods contribute to the development of an interphase in the interfacial region between the polymer and filler material.

2.3.1.1 Binding Between Metal Particles and Polymers

Part of the development of an interphase stems from the binding of metal particles with the matrix phase of the composite. Often the metal reinforcement phases have an oxide layer which can change the chemistry at the interface between the particles and the matrix, influencing their binding. In the work of Bebin and Prud'homme [31], nitrogen (PAN, PS) and oxygen (PVME, PVMK, PMMA) containing polymers were coated with different metals (Ni, Al, and Cu) by evaporation in a vacuum to investigate the interfacial properties between metals on polymer substrates using X-ray photoelectron spectroscopy (XPS). In their work, they focused on two main groups of metals: those that are strongly reactive (tightly fixed to the polymer) such as Cr, Ni, and Al, and those that are weakly reactive (lightly attached to polymer) such as Cu, Ag, and Au. The researchers first looked at Ni and found it to be strongly reactive with the polymers inducing changes at the interphase region. In both types of polymers (N and O containing) Ni-oxide and Ni-nitride formed. They also found amorphous carbon to be present as a result of degradation of the polymer surface. They then varied which metal they were using (Cu, Ni, and Al) in order to change the reactivity of the metal with polymer surface. In each case they found results to be similar with the formations of metal-oxide and metal-nitride as well as the formation of amorphous carbon. However, they found that Cu diffuses more easily into polymers while Ni forms a slight diffuse interface layer, and Al remains at the surface (a schematic of the phenomenon is shown in Fig. 2.7). Cu with a weaker reactivity with polymers over other metals is allowed to diffuse more readily when the polymers are in their rubbery state due to their natural molecular motion. The

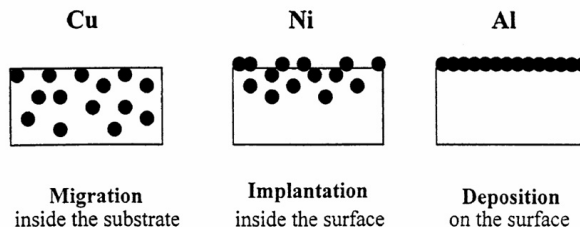


Figure 2.7: Schematic representation of the polymer surface for the same quantity of Cu, Ni, and Al deposited. Figure taken from [31].

stronger reactivity of Cu with metals also caused clusters to form. In the case of Ni and Al, the nature of the diffuse layer of nickel was related to its higher energy of condensation ($|\Delta H| = 370$ kJ/mol for Ni vs. 300 kJ/mol for Al) allowing for nickel to penetrate deeper, while for aluminum a uniform layer is formed due to its high reactivity thereby locking in the mobility of the polymer at the surface. They also noticed that nitrogen tended to diffuse towards the metal layer which is opposite of the mobility observed for oxygen. In other polymers the nitrogen in amine groups has been shown to interact with the metal surfaces [32].

In another study by Gettings et al. [30], iron was found to diffuse up to 115 nm into the epoxy region near the interfacial region of abraded steel-epoxy based materials creating an interphase. After studying the failure of these materials, the researchers found crack propagation to occur within the interphase region and not exactly at the epoxy-iron oxide interface itself indicating that a modification of the fracture mechanism had occurred. Using XPS, binding energies of iron core electrons as high as 709.7 - 713.4 eV were detected at fracture surfaces between the iron and epoxy. Thus, the changes in affinity of atoms in polymers for different metals and alterations in the bonding characteristics between metals and a polymer matrix, indicates the importance of understanding the larger role of interactions between constituents in polymer-based composites.

With the introduction of metal particles into polymer surfaces, the curing process

may also be affected. Work done by Kelber and Brow [32] found diethanolamine (a common curing agent) to interact with the oxide surfaces of metals in amine-cured epoxies. They used XPS to monitor desorption of diethanolamine from aluminum and copper oxide surfaces as they increased the temperature to above 700 K. In the case of desorption of diethanolamine from oxidized aluminum they found the binding of the nitrogen in diethanolamine to persist with the oxide to temperatures above 500 K without a significant loss of nitrogen. Their results are shown in Fig. 2.8. They noted that any molecules between DEA and the oxide bound by hydrogen would desorb below 350 K ruling out the possibility of hydrogen bonding between the two and suggesting that the molecules are bound covalently or ionically which would desorb at higher temperatures. They also found that the binding interactions for copper oxide and DEA were lower than aluminum oxide and DEA.

Since many epoxy composites are processed using DEA as a curing agent, the DEA may interact with the metal particles as well as the epoxy resin altering the stoichiometric balance between the resin and curing agent in the bulk matrix affecting the curing mechanisms. Any preferential adsorption of the DEA with the metal surfaces would create additional cross-linking in an epoxy at the particle-matrix interface and may also leave unreacted epoxide in the matrix making cross-linking by etherification (discussed in Section A.2) more likely. Rosso and Ye [33], found an increase in the composite’s degree of cure to occur with an increase in silica particles. This was marked with an increase in cross-link density as well as the creation of an interphase around the particles.

2.3.1.2 Changes in Free Volume within a Polymer Matrix

When a filler material is introduced into a polymer matrix the manner in which the molecules of the polymer are arranged changes. The changes in the conformation of the polymer molecules can change the free volume in the material. Marzocca et

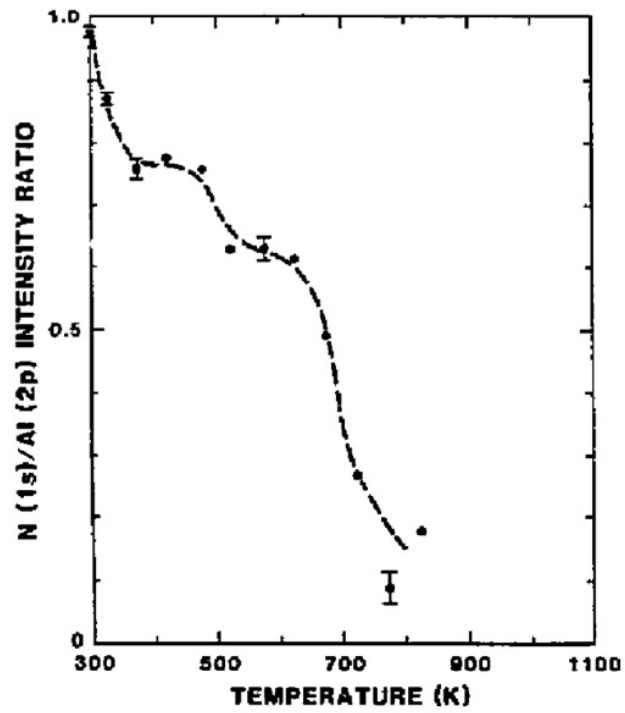


Figure 2.8: N 1s/Al 2p peak area ratio versus substrate temperature for DEA/air-oxidized Al heated in vacuum. The error bars are derived from estimated uncertainties in measuring peak areas. The dotted line is a guide for the eye. Figure taken from [32].

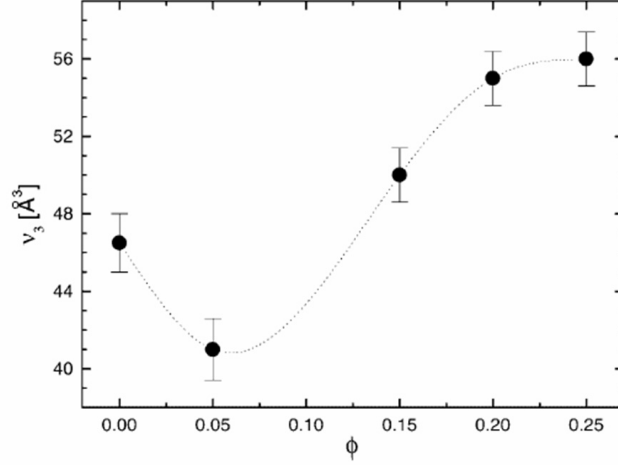


Figure 2.9: Average values of the free volume obtained from free volume distribution using PALS at different filler-volume fractions. Figure taken from [34].

al. [34] characterized the free volume of epoxy reinforced with quartz particles using positron annihilation lifetime spectroscopy (PALS). They found that the free volume of the matrix was dependent on the volume fraction of the particles within the matrix and followed a nonlinear trend. At dilute filler concentrations of quartz particles (5 vol.%) in epoxy, there was a decrease in the free volume. At higher concentrations (> 15 vol.%) the free volume increased with filler concentration. The dependency of free volume with concentration of quartz particles in epoxy can be seen in Fig. 2.9.

Due to a negative mismatch in coefficient of thermal expansion between the filler and polymer matrix, thermal stresses develop in both the matrix and filler as a result of the when the composite cools following curing at an elevated temperature. When the coefficient of thermal expansion is less for the filler than the matrix, tensile stresses are created in the matrix side and compressive stresses in the inclusion side of the interface [35, 36]. As a result of these stresses, the free volume decreases in the matrix near the filler, and at far enough distances away from the inclusions the free volume in the polymer is the same as the unfilled polymer due to negligible thermally induced stresses in this region. However, this is only true for dilute filler

concentrations. At higher concentrations of filler, the inclusions have smaller mean free distances and the thermally induced stress in the regions between the inclusions begin to overlap and become more important in comparison to thermally induced stresses at the interfacial region. This results in an increase in the overall free volume of the composite. Similar results in the free volume were also obtained by Tognana and colleagues [37]. However, at larger volume fractions of aluminum particles in an epoxy matrix they measured a decrease in the free volume (see Fig. 2.10(a)). They attributed this decrease in free volume to an increasing amount in production of an interphase around the particles. To corroborate their findings they showed two distinct peaks in the free volume distribution from PALS experiments (see Fig. 2.10(b)). Since both studies used epoxy matrices reinforced with particles with sizes in the range 106 to 125 μm , the difference in the free volumes at higher loading fractions may be due to the use of different particle types (aluminum vs. quartz), which may cause different effects on production of thermally induced stresses or chemically based interaction between the epoxy and the particles. In cases where the filler has a higher coefficient of thermal expansion than the matrix, the stresses will be tensile in the filler and compressive in the matrix.

2.3.1.3 Thickness of the Interphase at the Particle-Matrix Interface

Many studies have been carried out to characterize the interphase thickness in polymer-based composites. Using TEM images, researchers were able to estimate the interphase thickness to be around 2 to 3 nm in a silica nanoparticle reinforced epoxy composite [33]. As shown in the TEM image in Fig. 2.11, they observed a region in the matrix surrounding the particles that appears different than the bulk. Other methods rely on calculating the interphase thickness through other means.

One common method to calculating the thickness of the interphase was developed by Lipatov [38] and used by others [37, 39, 40]. Lipatov investigated filled polymer

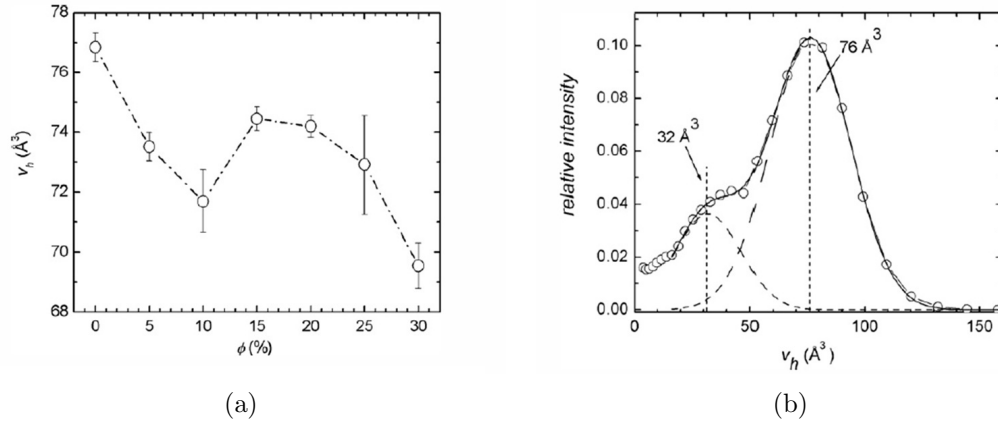


Figure 2.10: Free volume effects in an epoxy matrix due to the presence of particles. (a) Average free volume versus filler volume fraction obtained from PALS measurements. Lines are only eye guides. (b) Free volume distribution for the composite containing 15% of filler volume fraction. Images are taken from[37].

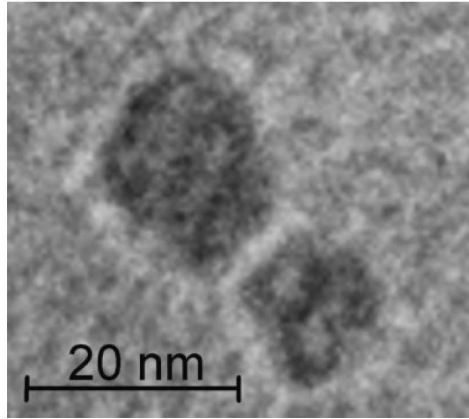


Figure 2.11: TEM images of two neighboring silica nanoparticles in the epoxy matrix showing a 2-3 nm altered interphase region. Image is taken from [33].

systems and noticed by plotting the dependence of temperature on heat capacity, that there was a shift in the glass transition temperature as well as a change in heat capacity across this transition from that of the neat polymer. The data also showed that change in heat capacity decreased regularly with an increase in filler concentration. This was cited as clear evidence for the polymer near the particle interface decreasing in mobility keeping that region from participating in the cooperative long range motion that occurs during the glass transition. Using this assumption, Lipatov [38] was able to calculate an interphase thickness (Δr_i) by relating the heat capacity of the composite and volume fraction of particle reinforcement (ϕ) through the following equations:

$$\Delta r_i = r_f \left(\frac{\lambda_i \phi}{1 - \phi} + 1 \right)^{1/3} - r_f \quad (1)$$

where,

$$\lambda_i = 1 - \frac{\Delta C_p^{fill}}{\Delta C_p^{Unfill}} \quad (2)$$

Here, ΔC_p^{fill} and ΔC_p^{Unfill} are the changes in the heat capacities for the filled and unfilled polymers respectively, determined from values above and below the glass transition temperature ($\Delta C_p = C_p(T > T_g) - C_p(T < T_g)$), and r_f is the filler radius. From the interphase thickness the volume fraction of the interphase (ν_i) can be calculated using:

$$\nu_i = \left(\left(\frac{\Delta r_i}{r_f} + 1 \right)^3 - 1 \right) \phi \quad (3)$$

The interphase thickness has been found to be approximately 2 to 85 nm for nano-sized particle reinforced composites [33, 41, 42], and 0.06 to 6.25 μm for micron-sized particles [37, 43, 44]. While the interphase thickness is dependent on particle size, the volume fraction of particles [37, 41], particle type and coupling agents [41, 44]

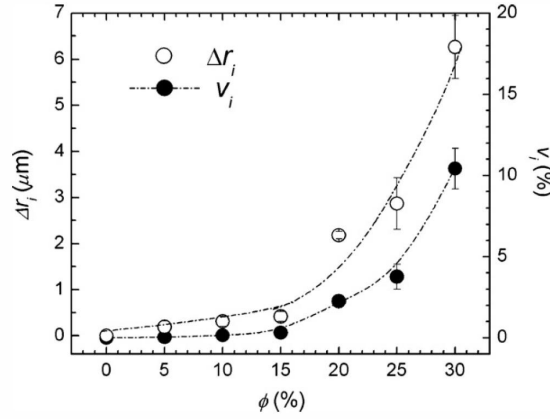


Figure 2.12: Interphase thickness and volumetric fraction of interphase as a function of the filler volume fraction. Lines are only eye guides. Image is taken from [37].

play a role as well. Using the method developed by Lipatov, Tognana et al. [37] showed that the thickness and volume fraction of the interphase increased for epoxy reinforced with varying volume fractions of aluminum particles (approximate size of $100 \mu\text{m}$) from 0% to 30 vol.% (see Fig. 2.12). Vassileva and Friedrich on the other hand reinforced epoxy with 40 nm sized alumina and found the interphase to decrease with increased loading fractions of nanoparticles. This may indicate that there are different mechanisms for developing an interphase at the nano-scale then micron-scale. They also observed that depending on the type of coating they used they were able to increase the thickness or decrease the interphase thickness for composites containing 3 vol.% particles. However, trends in the interphase thickness dependence with volume fraction of coated particles remains to be observed since no additional composites were prepared with varying loading fractions of surface coated nanoparticles.

Other methods for calculating an effective interphase thickness have been used by Hergeth et al. [42], Vassileva and Friedrich [41], and Iisaka and Shibayama [43, 44]. Vassileva and Friedrich found that the effective interphase thickness was larger when calculated for temperatures in the rubbery regime than those for the glassy regime. In addition to these studies computational efforts to understand the effects of filler

size on the properties of nanocomposites have been carried out by Brown et al. [45]. In their study they found the interphase thickness to be independent of nanoparticle sizes used in this study which are on the order of a magnitude smaller (14 to 59 Å) than those used in experimental studies in a similar nano-scale regime (26 [42] to 40 nm [41]).

2.3.2 Changes in the Thermomechanical Behavior

When a portion of a polymeric material is replaced with different material phase or type, there are changes in the thermomechanical properties. These changes can be divided into two main categories: 1) those that stem from the interactions between the polymer and the replacement material phase and 2) those that only evolve from the replacement of a percentage of the polymer with a different phase or material type. In the first type, there are the changes in thermomechanical properties such as relaxation temperatures and mechanisms, $\tan \delta$ peak height or width for these relaxations, change in the dynamic moduli (for $T > T_g$), and activation energies for the relaxations. In the second type, there are the changes in the dynamic moduli (for $T < T_g$) which are dependent on the volume fractions of the material constituents, leading to greater ease of predicting their values using models such as the one based on Lewis and Nielsen equations [46] for predicting dynamic elastic moduli based on the volume fraction of inclusions.

2.3.2.1 *The Effect of Particles on T_g and Activation Energies*

The glass transition temperature is a measure of the polymer's ability to obtain large scale molecular motions. However, in polymer-matrix composites the glass transition temperature of the polymer matrix can be affected by the presence of inclusion (voids, metal particles, etc.) as a result of the creation of an interphase. These inclusions have been known to cause the glass transition temperatures to increase [33, 37, 41, 47, 48, 49, 50, 51, 52, 53, 54, 55], stay the same [42, 47], or decrease [56, 57, 58, 59,

60, 61, 62], and the extent to which they change are affected by the volume fraction [34, 37, 41, 52] and size of the inclusions [43, 44, 59, 63, 64]. The application of a coating or coupling agent on the surface of particles also affects the glass transition temperature [41, 47, 58, 60] by modifying the surface interaction between the particles and polymer matrix.

In one particular study, by Alberola and Mele [47], many of the effects of microstructure on the glass transition temperature were observed. Alberola and Mele [47] used polystyrene (PS) and styrene-co-methacrylic acid copolymer (SAMA) to investigate the effects of reinforcement with uncoated and silane coated glass beads on the glass transition relaxation and the change in specific heat (ΔC_p) from above and below the glass transition temperature. For neat PS and SAMA, there was a higher T_g for SAMA (129 vs. 100°C) which they related to a decrease in the mobility of macromolecular chains, i.e. requiring more energy to induce large scale motion. They then varied the volume fraction of filler and found that for the composites containing PS there is essentially no change in ΔC_p or the glass transition temperature from the neat PS. In SAMA however, the T_g shifted to higher temperatures to 130, 132, 134, and 138°C, for 15, 20, 30 and 40% by volume, respectively, of coated glass beads. This shift also coincided with a decrease in the magnitude of the $\tan \delta$ peak corresponding to the glass transition. This decrease in $\tan \delta$ peak height is commonly found in particle reinforced polymers and is usually accompanied by a broadening of the peak as well [34, 51, 50, 63, 65]. An example of this effect is shown in Fig. 2.13 for different coatings on glass beads and Fig. 2.14 for different volume fractions.

ΔC_p also decreased for the SAMA system with increasing volume fraction of filler, indicating that there is a decrease in the molecular mobility of the polymer chain segments due to either interactions between the silane coating on the glass beads with functional groups in SAMA or physical reinforcement effect with the increase vol.% of filler or both.

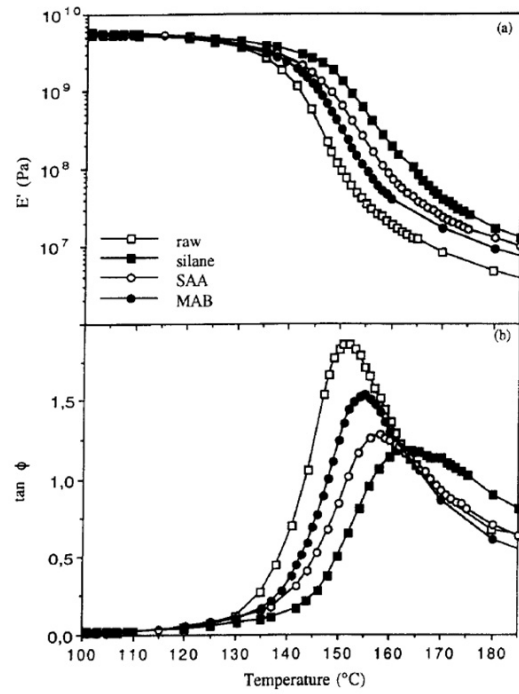


Figure 2.13: Plot of (a) $\log E'$ and (b) $\tan \phi$ versus temperature at 5 Hz for SMAA15 copolymer reinforced with 50 vol% or 20 μm (open squares) raw glass beads, (filled squares) silane-coated glass beads, (open circles) SAA-coated glass beads and (filled circles) MAB-coated glass beads. Image is taken from [63].

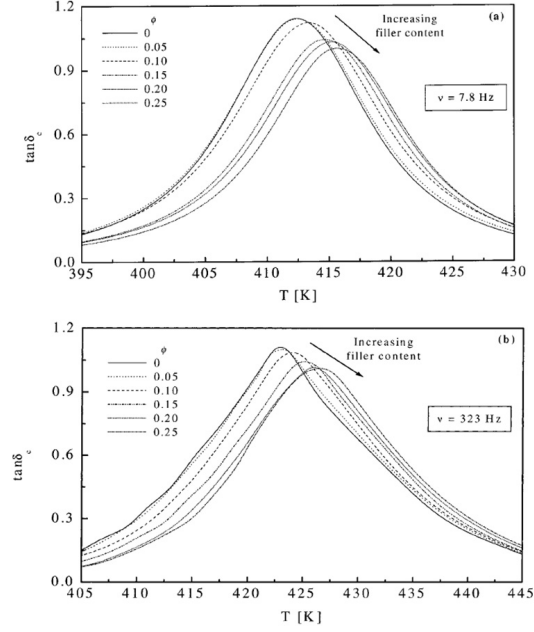


Figure 2.14: Effects of particle volume fraction on the broadening and height of the $\tan \delta$ peak. Here, $\tan \delta$ is plotted as a function of temperature for two frequency values: (a) 7.8 and (b) 323 Hz. Image is taken from [50].

Alberola and Mele [47] also proposed a self-consistent model for calculating the effective complex elastic properties for a range of volume fractions of spherical fillers taking into account the percolation thresholds and the maximum packing fraction of spherical particles. The percolation threshold is experimentally determined, and in their case they used 0.20 volume fraction of spherical glass beads in PS or SAMA matrix materials as the criteria since composites with volume fractions of 0.20 or more glass beads exhibited large decreases in the damping factor in DMA tests. For the maximum packing fraction they used:

$$\phi_{max} = 1 - 0.47 \left(\frac{d}{D} \right)^{1/5} \quad (4)$$

where d and D , are the lower and upper bounds of the particle size distribution, respectively. They then used the volume fractions of the particles and percolation matrix material to determine the radii of each phase in a three concentric sphere

model with the layers representing the non-percolated matrix, percolated matrix, and particle phases. The last layer is then surrounded by an equivalent homogeneous medium. This method is similar to the one used in the Hashin-Shtrikman Model [1]. The radii of the layers are then used to find the complex bulk (B^*) and shear (μ^*) moduli of the particulate reinforced composite. Knowing that the complex Young's modulus (E^*) can be found from B^* and μ^* they were able to compare their results with experimental data obtained from DMA tests. While their model matched data fairly well when there were no interactions between the glass beads and the matrix, as was the case for the glass beads/PS composite, the $\tan \delta$ of the glass beads/SAMA composite was predicted to have a peak for the glass transition that was larger in magnitude and shifted towards lower temperatures.

Ash et al. [59], took a more extensive look at results from previous studies [58, 57] and the effect of 17 nm and 38 nm sized alumina particles on the glass transition temperature of PMMA nanocomposites. They found that with just a small amount of filler (0.5 wt.%) there was a reduction in T_g up to 25 °C. Their research showed that the T_g in nanocomposites shows a surface area effect and not an interparticle dependence. By the introduction of aluminum particles a particle/polymer interaction zone (IZ)/interphase could be up to 50 nm or more thick following the ideas found in ultrathin film literature. They suggested the interaction zone could be hundreds of nanometers thick. In this interaction zone, if there is little interaction of the polymer with the surface of the particles, there is an increase in the mobility of the polymer due to the introduced surface area mimicking free surfaces. If there is a high interaction of the polymer with the particle surfaces, then the polymer has less mobility than the bulk matrix. With the creation of the interaction zones of higher mobility the percolation network of the bulk matrix (of lower mobility/ slower dynamic response regions) in the composite material has a far field affect, in dropping the overall glass transition temperature of the composite. In the case of high matrix-particle surface

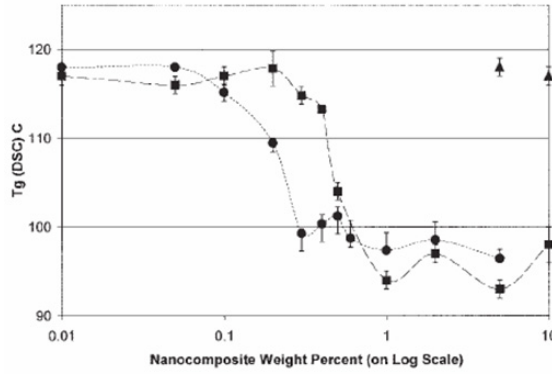


Figure 2.15: Glass-transition temperature behavior of alumina/PMMA nanocomposites (squares: 38/39 nm alumina, circles: 17 nm alumina). Image is taken from [59].

interactions zones of decreased polymer chain mobility can be present in large enough quantities to disrupt the percolation of the bulk matrix (of higher mobility) which will cause an increase in the glass transition temperature. They tested a case with particles coated with a surfactant that would interact with the matrix. In this case they saw no dramatic decrease in T_g . They also tested the composites with higher increased alumina particle content up to 10 wt.% and saw no additional drop in glass transition temperature indicating that the IZ does indeed extend up to quite large distances and that there is only a critical amount of particle introduction to cause these effects. For the small particles (17 nm) weight fractions $> 0.5\%$ show no further decrease while in composites with larger particles (38 nm) no further decrease is observed with weight fractions $> 1.0\%$. While this points towards a particle size dependence on the glass transition temperature, normalizing this dependence by surface area to volume ratio, results in the dependence of T_g on particle size collapsing onto a single curve (see Figs. 2.15 and 2.16)

The glass transition temperature increases due to a strong interaction between the particles with the polymer matrix. When this happens the mobility of the polymer surrounding the particles decreases and contributes very little to the overall long range

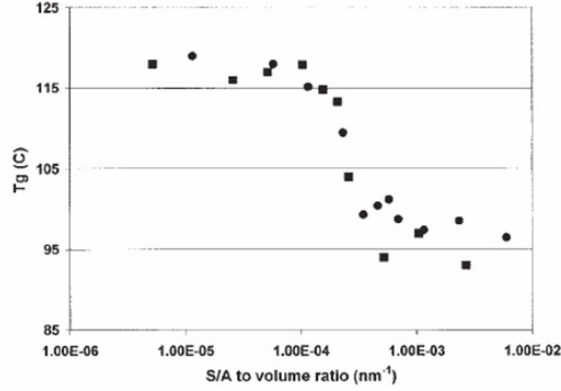


Figure 2.16: Glass-transition temperature behavior of alumina/PMMA nanocomposites (squares: 38/39 nm alumina, circles: 17 nm alumina). The data are now plotted with respect to surface-area-to-volume ratio. Image is taken from [59].

polymer segmental motion responsible for the glass relaxation due to the increased energy needed. The increase is also accompanied with a broadening and decrease in height of the corresponding $\tan \delta$ peak. Due to the decreased mobility the activation energy also increases, as has been shown by several researchers [34, 41, 51]. Vasileva [41] also found that the β -relaxation temperature and activation energy, both increased with volume fraction of particle reinforcement.

When the glass transition temperature decreases, it is a result of weak interactions between the particles and the matrix. The interface in this case is characteristic of a free surface allowing the polymer to have increased mobility decreasing the energy needed to sustain the long range segmental motion. This is due to the regions of higher mobility disrupting the percolating network of lower mobility regions in the bulk matrix. As the volume fraction of particles increases, the disruption to the bulk matrix behavior is more pronounced, T_g further decreases until a threshold in particle volume fraction is reached beyond which no further decrease in T_g is observed, as shown by Ash et al. [59]. The same argument could also be made for the increase in T_g for strong interactions at the polymer-particle interface.

2.3.2.2 *Change in the Storage Modulus and Cross-Link Density*

In the glassy regime ($T < T_g$) of particle reinforced composites there is an increase in the storage modulus. This is an artifact of having a stiffer material in place of a material with a lower stiffness. As the volume fraction of reinforcement increases the storage modulus increases in this regime. As discussed earlier the dependence of the storage modulus on the volume fractions of the material constituents lends well to predicting the composite storage modulus using models such as the one based on Lewis and Nielsen [46] equations.

In the rubbery regime ($T > T_g$) there is also an increase in the storage modulus, however, the percentage increase with volume fraction of reinforcement is often greater than the increase in the glassy regime, as was observed in PEEK reinforced with aluminum nitride [65] and epoxy filled with quartz [50, 51]. Results from [50] and [51] can be seen in Figs. 2.17 and 2.18 respectively. In this regime the polymer behaves as a rubber and the modulus is a measure of its ability to elastically recover and is dependent on the cross-link density.

In thermoplastics, the cross-links are due to physical entanglements and are marked with lower storage moduli in this regime. Upon further increases in temperature a critical temperature is reached (T_m), referred to as the melting temperature, which is marked with large amounts of chain slippage resulting in a further decrease of the storage modulus. In thermoset polymers the storage modulus in the rubbery regime is higher and increases with increased cross-link density with no melting transition. Therefore, the storage modulus is not only dependent on the addition of filler material but the influence of the fillers on the chemistry of the matrix. According to the theory of rubber elasticity, for a cross-linked network the average cross-link density (N) is related to the elastic modulus through the following relation [14, 21, 66]:

$$N = \frac{E'}{3kT} \quad (5)$$

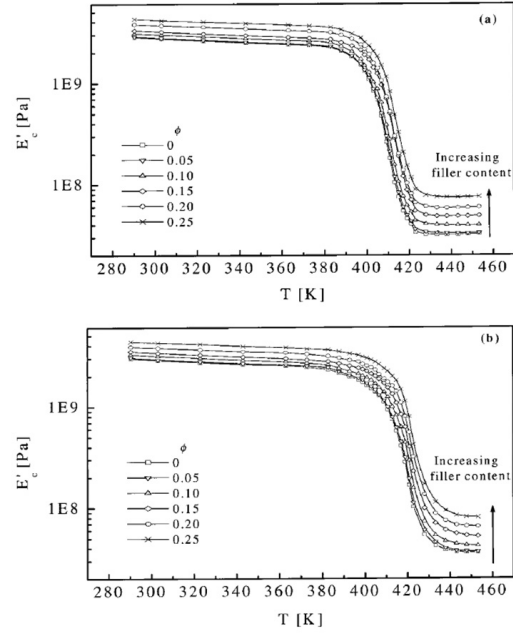


Figure 2.17: Dependence of E' with temperature for samples with different filler contents (a) 7.8 and (b) 323 Hz. Image is taken from [50].

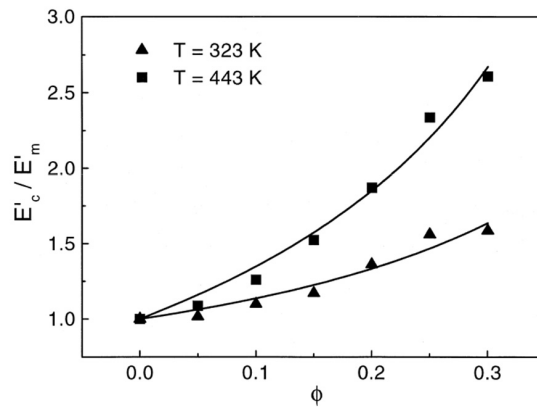


Figure 2.18: Dependence of relative modulus with ϕ at 323 K (glassy zone) and 443 K (rubbery zone). Image is taken from [51].

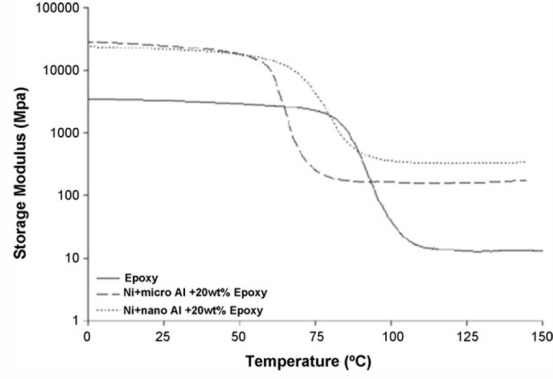


Figure 2.19: Dependence of storage modulus with particle size of nickel+aluminum epoxy-reinforced composites. Data curves obtained using DMA. Image is taken from [14].

where, E' is Young's storage moduli taken at an absolute temperature well above T_g in the rubbery plateau, and k is Boltzman's constant. In work carried out by Martin and Thadhani [14], an increase in cross-link density was observed for epoxy-based composites that had nano-sized aluminum reinforcement (see Fig. 2.19). These studies suggest that the surface to volume ratio of the filler, as well as their concentrations, plays an important role in the epoxy chemistry, and therefore, the composite's mechanical behavior.

2.3.2.3 Effect of Particles on the Decomposition Temperature

The effect of particle reinforcement on decomposition temperature is not as widely studied as the primary and secondary transitions, however work by Goyal and coworkers [65] found the decomposition temperature to be dependent on the volume fraction of reinforcement in poly(ether-ether-ketone) (PEEK) composites reinforced with 5 μm sized aluminum nitride particles. They found the decomposition temperature (determined by 10% weight loss) increased with particle loading fraction, and at 50 wt.% AlN there was an increase by 20 °C). Upon further increase in particle loading the decomposition temperature decreased. They suggested that at this concentration, aggregation of the particles increases due to the decrease in the inter-particle distance,

which reduces the thermal stability of the composite. When the particles begin to aggregate, the interphase regions overlap reducing the total amount of interphase that would be available for increased thermal stability if no aggregation of particles were to occur.

2.4 Mechanical Behavior of Polymers and Polymer Composites

2.4.1 Mechanical Behavior of Polymers

Compared with metallic materials, polymers typically have lower strengths and stiffness, and exhibit pronounced viscoelastic to viscoplastic behavior. They can be extremely ductile, recover large amounts of strain, and are very sensitive to temperature and strain rate. These changes vary in degree with polymer type and loading conditions making the characterization of polymers more difficult. These effects can be attributed to wide range of differences in their molecular structure. Also, many properties are rate dependent. For example, with an increase in strain rate or decrease in temperature the stress over the entire range of strain tends to increase.

There are two main characteristics of mechanical behavior observed for polymers, one that is typical of glassy polymers and the other for semicrystalline polymers³. For glassy polymers, the mechanical behavior exhibits a linear elastic response followed by a viscoelastic to viscoplastic transition up to yielding. Following yield, the glassy polymers undergo strain softening marked by a decrease in the flow stress with strain. At larger strains following the strain softening, the deformation behavior is often perfect-plastic with subsequent strain hardening at even larger strains. PMMA [67, 68], PC [68, 69, 70], PVDF [69, 70] and Epoxy [15] are a few materials that exhibit this behavior. For semicrystalline polymers, however, strain softening is typically suppressed, and instead there is subsequent strain hardening following yield. An

³Rubbers can be considered as exhibiting a third type of stress strain response, resembling the letter 's' with very shallow slopes, and large attainable and recoverable strains.

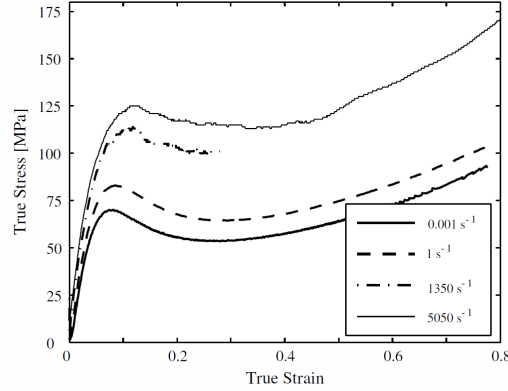


Figure 2.20: Representative curves of PC true stress-true strain behavior in uniaxial compression at four low, moderate, and high rates. The reported high strain rates were averaged over the duration of the test. Figure was taken from [68].

example of this type of behavior is observed for PTFE [71, 72], HDPE [73] and Nylon [74]. Representative figures showing the mechanical behavior for glassy (PC) and semicrystalline (PTFE) polymers can be seen in Figs. 2.20 and 2.21 respectively.

2.4.1.1 Strain-Rate Behavior of Polymers

While the mechanical properties of polymers are of great importance for applications at many different strain rates, for most engineering applications polymers are subjected to strain rates $< 10^0 s^{-1}$, and experiments are accordingly carried out primarily at low strain rates. However, as polymers have become increasingly useful for structural applications in impact loading conditions, knowledge of their high strain rate behavior has become increasingly important. Unfortunately, in comparison to low strain rate mechanical behavior of polymers, there is relatively little work published on their mechanical behavior at high strain rates.

Since studies as early as those carried out by Roetling [75] in 1965 on PEMA and Chou et al. [76], in 1973, on PMMA, cellulose acetate butyrate, polypropylene and nylon 66, in compression, the mechanical properties of polymers have been known to be strain rate and temperature dependent, and linked through the strain

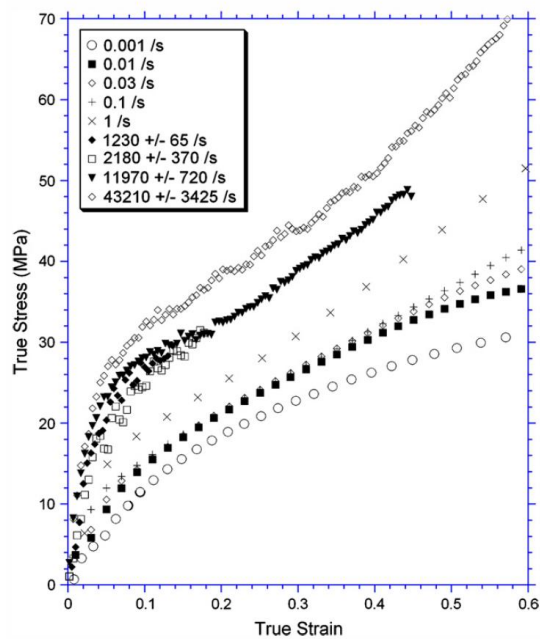


Figure 2.21: Representative mechanical behavior for a semicrystalline polymer. Shown are true stress-true strain uniaxial compression curves for polytetrafluoroethylene tested across a range of strain rates at room temperature. Figure was taken from [71].

rate/temperature superposition principle. In particular, it has been observed for some polymers that the dependence of yield stress on strain rate is greater at high strain rates or at decreased temperatures. In work carried out by Siviour et al. [69, 70], they have shown that for polycarbonate (PC) and polyvinylidene difluoride (PVDF) there is a bilinear relationship of the yield stress with $\log(\dot{\epsilon})$ as shown in Fig. 2.22. The bilinear relationship has also been observed for epoxy [15], PMMA [76], PP [76], and other polymers [68, 77, 78].

While it is often widely accepted that there is an increase in yield stress with strain rate, this is not always the case. In some instances there is a bilinear relationship for yield stress with strain rate, however, at much higher strain rates the yield stress begins to decrease with increasing strain rate. This behavior was observed in the case of PEEK and Nylatron by Al-Maliky et al. [79] and can be seen in Fig. 2.23 where at strain rates above $10^4 s^{-1}$, the flow stress begins to decrease for both materials. For PEEK, this behavior was also observed by Hamdan et al. [80]. Siviour et al. concluded that by mapping the peak stress to the temperature dependence, the effects could be explained in terms of molecular transitions of the two polymers: β -relaxation for PC and glass-transition for PVDF. These relaxations are strain rate dependent and shift towards higher temperatures as the rate of strain increases. The strain rate at which the change in yield strength occurs has been correlated to the strain rate in which certain transitions take place at room temperature. Many authors including Richeton et al. (for the polymers: PC, PMMA, PAI) [81], Bauwens-Crowet (for polymer: PMMA) [82], and Rietsch and Bouette (for the polymer: PMMA) [83] believe this to be due to molecular transitions as well, while others have attributed these effects to an increase in crystallinity [79, 80], or a decrease in the activation volume [84] with increased strain rates. This effect of a transition in the molecular relaxation process is marked by a decrease in the molecular mobility of the polymer chains which essentially makes the chains stiffer at increasing strain rates or low

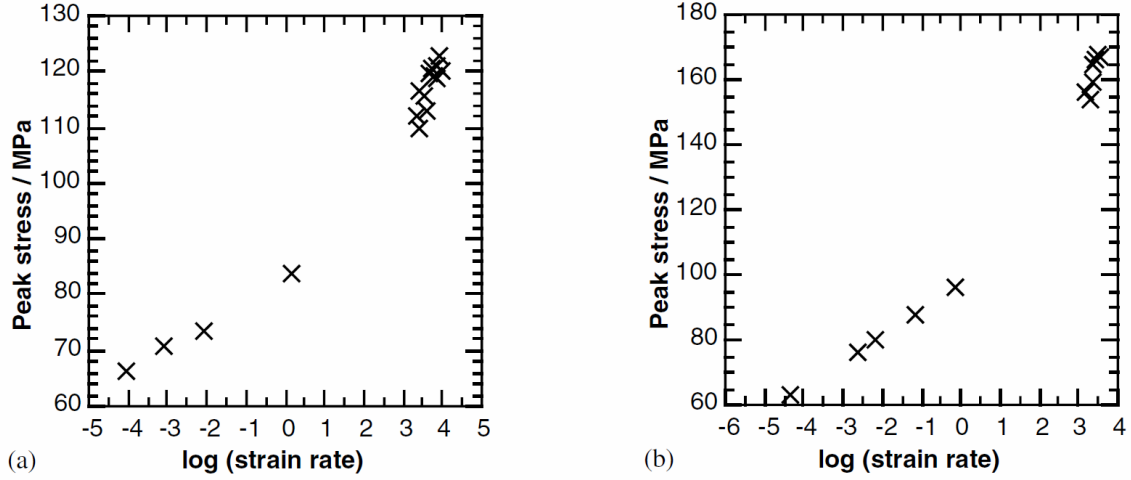


Figure 2.22: Strain rate dependence of the peak stress at yield for PC (a) and PVDF (b). Figure was taken from [70].

temperatures. With increased temperatures or low strain rates the opposite trend is observed.

The elastic moduli has also been observed to be strain rate dependent for some polymers [70, 85]. In the case of PC, PMMA, and PAI studied by Richeton et al. [85], the Young's modulus was observed to increase with increasing strain rates over a range of 0.001 s^{-1} to approximately 3000 s^{-1} as shown in Fig. 2.24. For PC and PVDF [70], there was an observed increase in the elastic modulus with a decrease in temperature as revealed by experiments carried out on a split-Hopkinson pressure bar at approximately 5500 s^{-1} for PC, and 2700 s^{-1} for PMMA at temperatures ranging from -61°C to 150°C .

2.4.2 Mechanical Behavior of Polymer-Based Composites

When polymers are combined with fibers or particles it is most often with the intent to achieve enhanced material properties over that of the pure polymer. Reinforced polymers typically show an increase in Young's modulus [74, 86, 87, 88], a mixed response for the tensile strength (decrease [89]/increase [86, 87]) and a decrease in

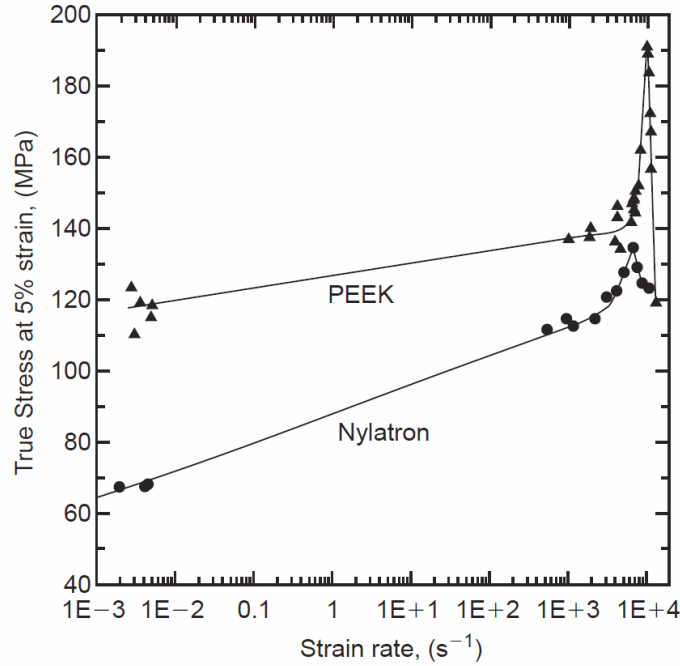


Figure 2.23: Flow stress at 5% strain PEEK and Nylatron at a wide range of strain rates. Figure was taken from [79].

the ductility of the material that exhibits a lower elongation at break [87] with reduced toughness and fracture strength. In order to produce a polymer composite, for use as a structural energetic material, the composite needs to possess high modulus and strength.

Polymers are widely used materials but their lower strengths and modulus compared to metals prevent them from being highly used as structural components. Therefore, studies have been conducted on increasing the strength of polymers by introducing reinforcing particles. When nylon-6 was infiltrated with glass beads or wollastonite, the material exhibited an increase in tensile strength (see Fig. 2.25) [87]. This increase in tensile strength was as much as 17% or 12% for the wollastonite and glass beads respectively, depending on the filler concentration. However, it can also be seen from the figure that the wollastonite-filled and glass bead-filled nylon exhibit different trends in the tensile strength as a function of the filler content. While both

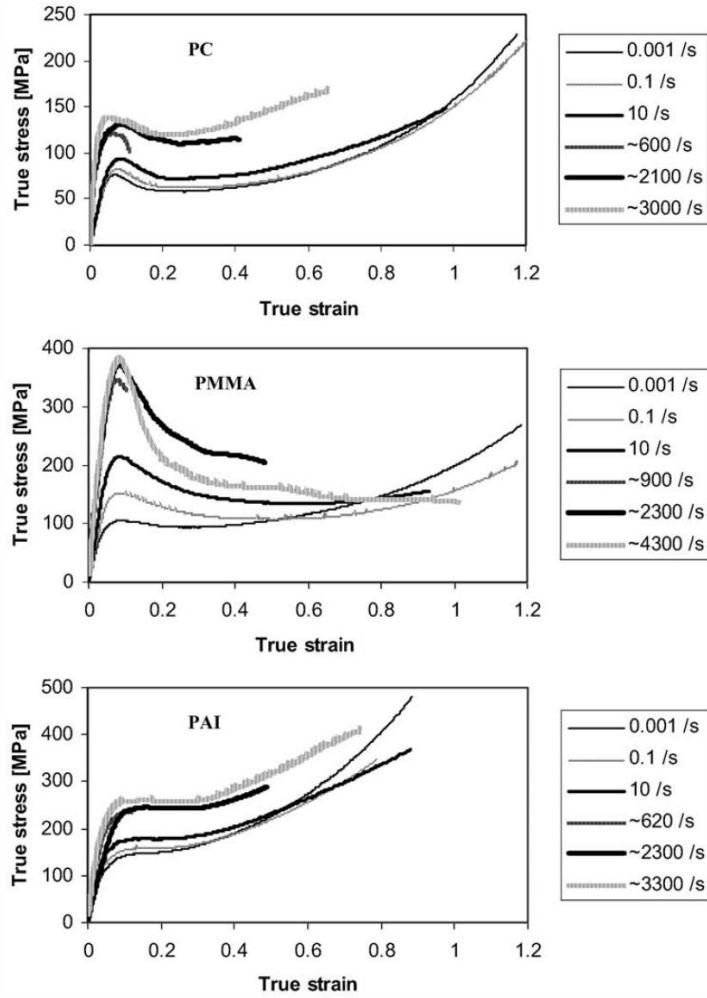


Figure 2.24: Experimental uniaxial compression true stress-true strain curves for PC, PMMA, and PAI at the temperature 25°C over a wide range of strain rates. Figure was taken from [85].

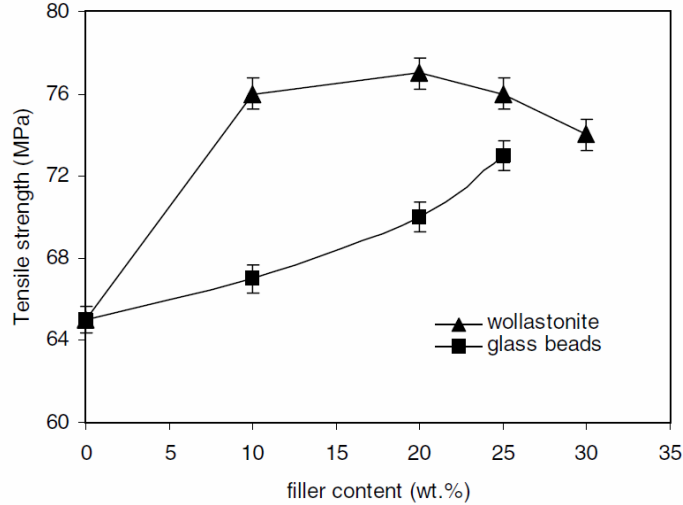


Figure 2.25: The effect of filler content of wollastonite and glass beads on tensile strength for nylon-6 based composites. Figure was taken from [87].

composites have higher tensile strengths than pure nylon, wollastonite-filled nylon shows an initial increase in the tensile strength followed by a gradual tapering off as the filler wt.% is increased, whereas the glass bead-filled nylon has a continuous increase in strength with a fill content of up to 25 wt.%. This suggests that loading fractions of the filler material cannot account for all the changes in material properties.

While the previous example was for tensile loading conditions, the infiltration of particles into a polymer matrix can also enhance the stress-strain response of polymers under compression loading conditions. When Tsai and Huang [74] subjected unreinforced nylon-6 and nylon-6 reinforced with 5 wt.% clay particles to quasi-static and dynamic compression tests the linear portion of the elastic regime in the stress-strain response of the materials were shown to increase with increasing strain rate for both materials (see Figs. 2.26 and 2.27). This increase in the elastic regime also corresponded to an increase in the peak or yield stress of the materials. In addition to these observations, the researchers found the Young's modulus to increase by up to as much as 32% to 4.1 GPa due to the reinforcement of 5 wt.% clay. It is worthwhile

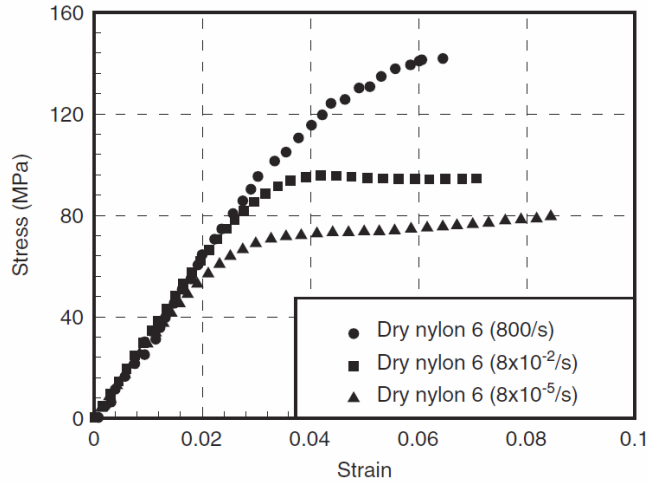


Figure 2.26: Stress-strain curves for pure nylon-6 compressed at quasi-static and dynamic rates of strain. Figure was taken from [74].

to note that Tsai and Hueng [74] also examined the effects of water absorption by the nylon-6 on the mechanical properties in this study. In all cases the hygroscopic nature of the nylon produced negative responses on the mechanical properties (marked by decrease in stiffness) due to the presence of $\approx 7\text{-}8\%$ moisture content which caused a plasticization effect.

While most polymer composites that are studied are fiber reinforced and use either carbon nanotubes or organic fiber fillers, research has also been conducted on polymers reinforced with metal and metal oxide particles, although to a very limited amount. In previous work by Martin [14] on epoxy, infiltrated with nickel and nano- and micro-sized aluminum, dynamic and static compression tests were used to determine the strengths of a composite containing 20 wt.% of epoxy mixed with an equivolumetric mixture of Ni and Al, and compared with that of pure epoxy. The findings showed that the yield strengths as well as the Young's modulus increased for the particle filled epoxy and that the use of nano-sized Al had a greater increase for both properties than when micron-sized Al was used. Results for static compression tests are shown in Table 2.1. These results suggest that the reinforcement particle size

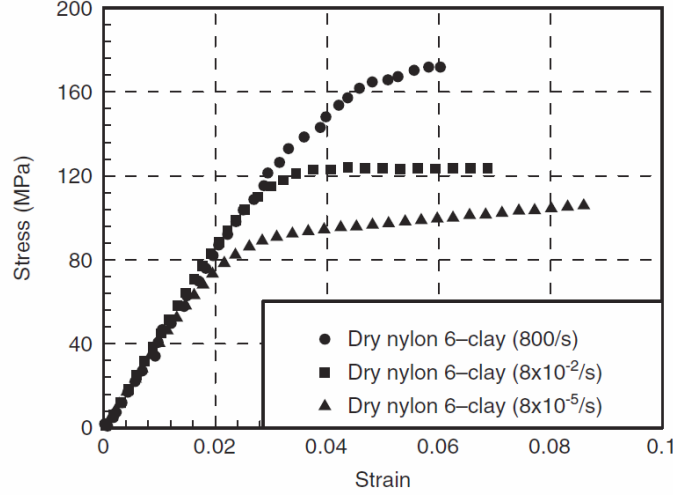


Figure 2.27: Stress-strain curves for pure nylon-6 reinforced with 5 wt.% of clay compressed at quasi-static and dynamic rates of strain. Note the difference in scale on the ordinate axis. Figure was taken from [74].

is a contributing factor to the changes in mechanical properties. However, it is unclear if the contribution is primarily due to the reinforcement effect or the influence of the nano-size filler on the chemical and physical response of the polymer with altered cross-linking density.

Table 2.1: Experimentally measured mechanical properties of pure epoxy and Ni+Al powder-reinforced composites. Table data is from [14]

Material	Density (g/cm^3)	Measured E (GPa)	Measured σ_y (MPa)
Epoxy	1.19 ± 0.00	3.0 ± 0.5	100.0 ± 4.1
Micro Ni + micro Al + Epoxy	3.50 ± 0.13	7.5 ± 0.8	103.8 ± 12.2
Micro Ni + nano Al + Epoxy	3.26 ± 0.01	11.4 ± 1.3	156.8 ± 4.4

Another study conducted by Patel [90] investigated the mechanical behavior of epoxy composites filled with Al and Fe_2O_3 powders, under dynamic loading conditions. Dynamic compression tests using a split Hopkinson pressure bar apparatus were conducted on composites of different weight percentages of epoxy binder with the remaining powder mixture consisting of 25.26% Al and 74.74% Fe_2O_3 by weight.

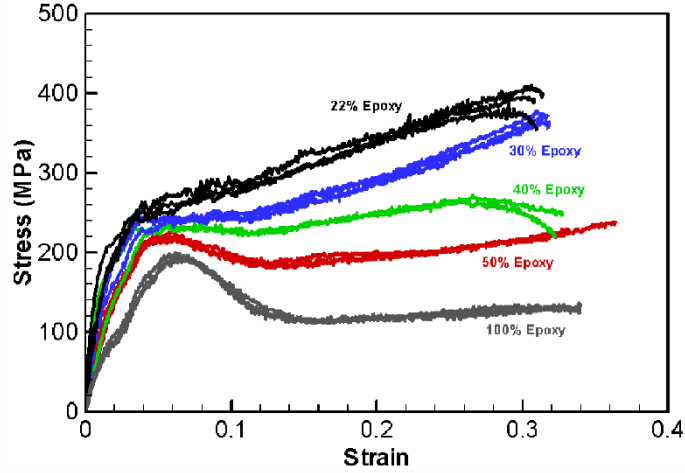


Figure 2.28: Summary of stress-strain relations of $\text{Al} + \text{Fe}_2\text{O}_3 + \text{Epoxy}$ with different amounts of epoxy by weight acting as a binder for a mass loading of $(\text{Al} + \text{Fe}_2\text{O}_3)$ consisting of 25.26% Al and 74.74% Fe_2O_3 by weight. Figure was taken from [90].

The tests revealed that both the elastic modulus and yield stress of the composites increased with decreasing amount of epoxy (see Fig. 2.28). Work hardening was also shown to increase with filler content. While these results are similar to those found in the study by Martin [14], the stress-strain curves also showed that as the amount of epoxy is decreased, the behavior deviates with an increasing degree away from the typical behavior of strain softening polymers, which have a linear elastic to viscoelastic transition followed by yielding, and then strain softening which is usually followed by a region of strain hardening or perfect plastic deformation. The stress-strain response of the material containing 22 wt.% epoxy was then compared with those of a Ni + Al powder compact mixture, Steel (1045) and Al (6061-T6) (see Fig. 2.29). Although the polymer composite did not reach the same maximum stress level as that of the metals or powder mixture, the shape of the curve for the composites more closely resembles that of the metals than that of the 100% epoxy indicating the metal particles are playing a more dominant role on the mechanical behavior. It is also possible that the presence of the particles modify the behavior of the epoxy.

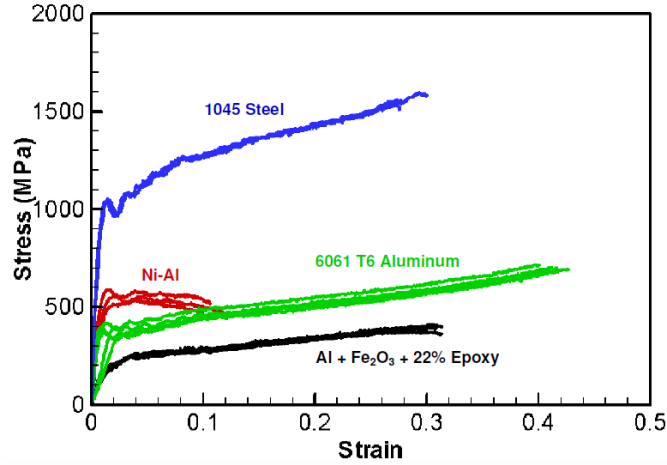


Figure 2.29: Comparison of stress strain relationships for metals and structural energetic materials. Figure was taken from [90].

Not all mechanical testing on polymers and polymer matrix particle reinforced composites are conducted under conditions in which the strain rate is constant. They are often subjected to ballistic type impacts in order to determine their dynamic strengths and deformation behavior. The most common test is the Taylor rod-on-anvil impact test developed by G.I. Taylor for metals [91], in which a cylindrical projectile impacts against a rigid elastic anvil at high velocities. This results in stresses and strain rates that are nonuniform and nonconstant. Many researchers have adopted this test since its inception for determining the dynamic mechanical behavior of metals. However, little focus has been placed on using this testing method on polymers and polymer matrix composites and what has been carried out has mostly been on PC [92, 93, 94, 95, 96], PTFE [97], and PTFE-matrix composites [98, 99]. Polycarbonate was found to have a yield strength of approximately 180 MPa at mean strain rate of $7.4 \times 10^3 \text{ s}^{-1}$ [92]. This was consistent with values reported by Lee et al. [93] and Min et al. [94]. The yield strength value is also approximately 30% higher than that which is typically found for PC (120 MPa [69]) at similar strain rates (approximately $2.2 \times 10^3 - 10.3 \times 10^3 \text{ s}^{-1}$) under uniaxial compression using a split

Hopkinson pressure bar (SHPB) apparatus. This is due to the nonuniform strain rates associated with Taylor impact tests. Initially the strain rates are much higher, hence PC has a higher compressive loading yield strength giving an overall dynamic yield strength higher than that found in a SHPB test. Most of the researchers conducted the impact tests at velocities between 150 and 300 m/s. Since PC is known to be ductile, at these velocities no fracturing of the specimens is observed. Instead extensive barreling and mushrooming of the samples near the impact end occurs. This type of deformation can be seen in Fig. 2.30, which shows profiles of the PC projectile during impact. Due to the ductile deformation of the PC, there is often an appreciable amount of strain recovery on the perimeter near the impact face that results in a cupped endcap. In Taylor rod-on-anvil impact tests carried out on poly(ether ether ketone) (PEEK) by Millet et al. [100] extensive mushrooming of the impact end was observed, and as with PC at lower velocities there was cupping. However, at impact velocities greater than 303 m/s, the projectile fractured in a ductile manner and discoloration of the material was observed (see Fig. 2.31). This suggests that high temperatures were reached in the impact region. However, there was no temperature data to support this finding. Additionally, ductile fracture was not observed for PC at velocities less than 300 m/s. This is most likely due to a higher velocity needed for fracturing to occur and may be possible that other modes of fracture exist. In fact in polymers a ductile-to-brittle transition behavior can also be found such as in the case of PTFE where a pressure induced solid-solid phase transformation occurs at approximately 0.5-0.65 GPa [97]. As the impact velocity increases, this results in transition of ductile behavior with plastic deformation and stress-whitening, to localized cracking of the specimen near the center axis at the impact end, to complete brittle fracture into two or more pieces.

In polymer matrix particle reinforced composites similar, types of deformation behavior are observed during the Taylor impact test. However, as was discussed by

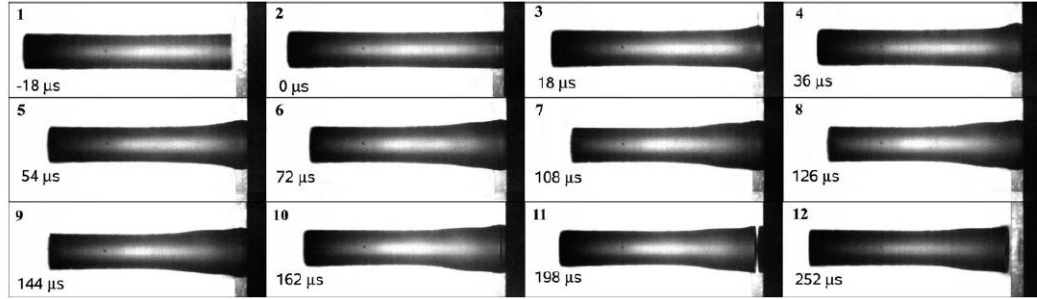


Figure 2.30: Image of transient deformation profiles for polycarbonate during a Taylor rod-on-anvil impact test at 187 m/s. Figure was taken from [96].

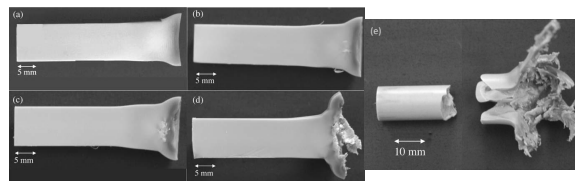


Figure 2.31: Image of transient deformation profiles for poly(ether ether ketone) during a Taylor rod-on-anvil impact test at (a) 247, (b) 276, (c) 303, (d) 349, and (e) 408 m/s. At this velocity extensive fracture by a ductile manner is observed. Figure was taken from [100].

Raftenberg et al. [98] on PTFE reinforced with aluminum, chemical reactions can take place which produces an additional fracturing mode by internal porosity growth. Additionally, with the addition of the metal particles in a polymer matrix a decrease in the necessary impact velocity for plastic deformation and/or fracturing of the specimens can occur, as was shown by Ferranti et al.[3] for epoxy reinforced with aluminum and hematite. Ferranti et al. [3] also showed that composites with greater than 1% porosity were more likely to have a "double frustrum" type deformation profile and fracture initiating near sharp changes in the profile slope, while the composites with less than 1% porosity had an extended mushrooming type profile. Interestingly, the composites with lower porosity levels had a different plastic deformation response from the pure epoxy matrix which has double frustrum plastic deformation profile. This can be indicative of the reinforcing particles playing a key role in the plastic deformation in polymer matrix composites under impact loading conditions. While research conducted by Ferranti et al. [3] shows that the presence of metal particles changes the deformation response of the epoxy matrix composite from that of the pure epoxy, there have been no systematic studies examining effects of particle size or particle type on the dynamic mechanical deformation behavior of polymer matrix composites under impact loading conditions. This lack in knowledge is exacerbated by relatively few studies being conducted on neat polymers.

These studies have shown that particle reinforced polymers have advantageous properties including increased strength and modulus that are needed in structural materials. However, particle reinforcement does not always lead to an increase in mechanical properties. Work carried out by Pukanszky and Voros [89], summarized the effects of glass reinforcement in epoxy, polystyrene (PS), and polypropylene (PP) on the tensile strength of the composites from previous studies (see Fig. 2.32). The researches found that the change in tensile strength, due to the glass reinforcement,

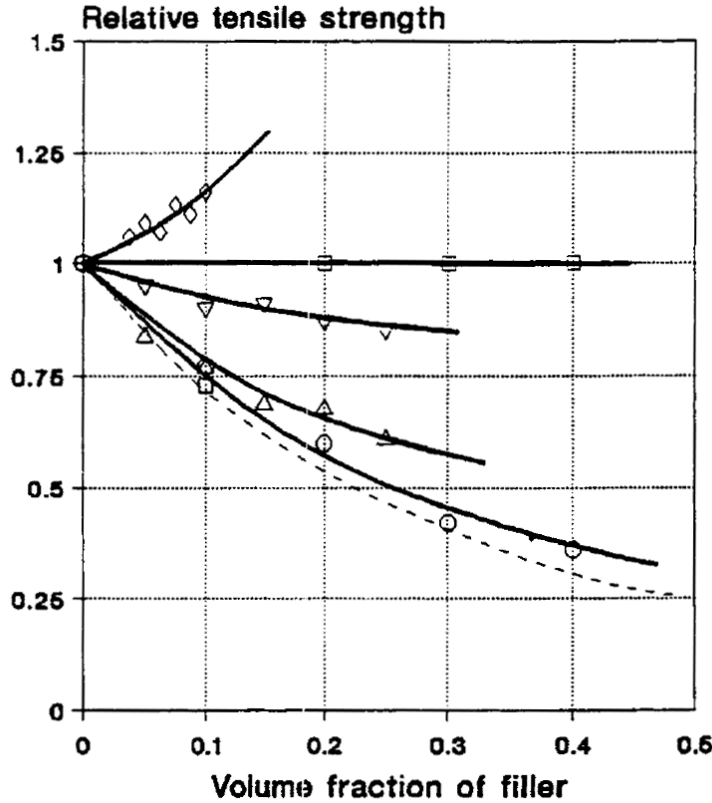


Figure 2.32: Volume fraction dependence of the relative tensile strength of varying particulate filled composites. Epoxy/glass: (open circles) no adhesion, (open squares) good adhesion. PS/glass: (open triangles) poor adhesion, (inverted triangles) good adhesion, PP/glass (diamonds). Dashed line is the theoretical minimum. Figure was taken from [89].

varied with the use of different polymer matrix materials as well as the adhesion between the matrix and particles. In Fig. 2.32 the introduction of the glass is shown to have a positive influence on PP while, the epoxy and PS based composites exhibit either a negligible effect (epoxy/glass with good adhesion) or a negative effect as the volume fraction of the material is increased. Thus, from this study we can determine that there is no clear guideline as to what we can expect the effect of particle reinforcement on the mechanical properties of a composite material ought to be for a polymer type (thermoplastic or thermoset).

2.4.3 Field Distributions Around Particles in a Matrix

Explanations as to the cause of changes in the mechanical behavior of polymers reinforced with particles have been proposed by Pukanszky and Voros [89], Vollenberg and Heikens [88], and He and Jiang [101]. Pukansky and Voros suggested stress distributions around particles are responsible for changes in the mechanical behavior. Thus, the researchers were particularly interested in determining the stress distributions around inclusions in the matrix and then using those results to analytically evaluate the tensile yield stress of polymer-particle composites. They first assumed the stress carried by the matrix and filler to be proportional to the particle volume fractions through the following relation based on volume fraction averaging:

$$\phi k \sigma^e + (1 - \phi) \langle \sigma^m \rangle = \sigma^e \quad (6)$$

here, ϕ is the volume fraction of the filler, k is a proportionality constant for stress transfer, σ^e is the external load, $\langle \sigma^m \rangle$ is the average stress in the matrix and the term $\phi k \sigma^e$, the stress carried by the filler (σ^i). From this equation, assuming yield occurs when the maximum stress reaches the yield stress (i.e. when $\langle \sigma^m \rangle = \sigma_{y0}$), two boundary conditions can be examined for the stress distributions that depend on the filler properties and particle interactions. The first case assumes that the rigid particles adhere perfectly to the matrix that then allow the stiffer particles (in relation to the matrix) to carry a significant portion of the load which contributes to an increase in the yield stress of the composite as the volume fraction of the particles is increased with $k > 0$ (see Fig. 2.33 (a) for a schematic). For the other case it is assumed that the particles are softer than the matrix material which then corresponds to the matrix carrying the external load thereby causing the yield stress to decrease as the volume fraction of the particles is increased with $0 \leq k \leq 1$ (see Fig. 2.33 (b) for a schematic). However, the researchers recognized that this method did not account for the location of the maximum stresses that cause the yielding

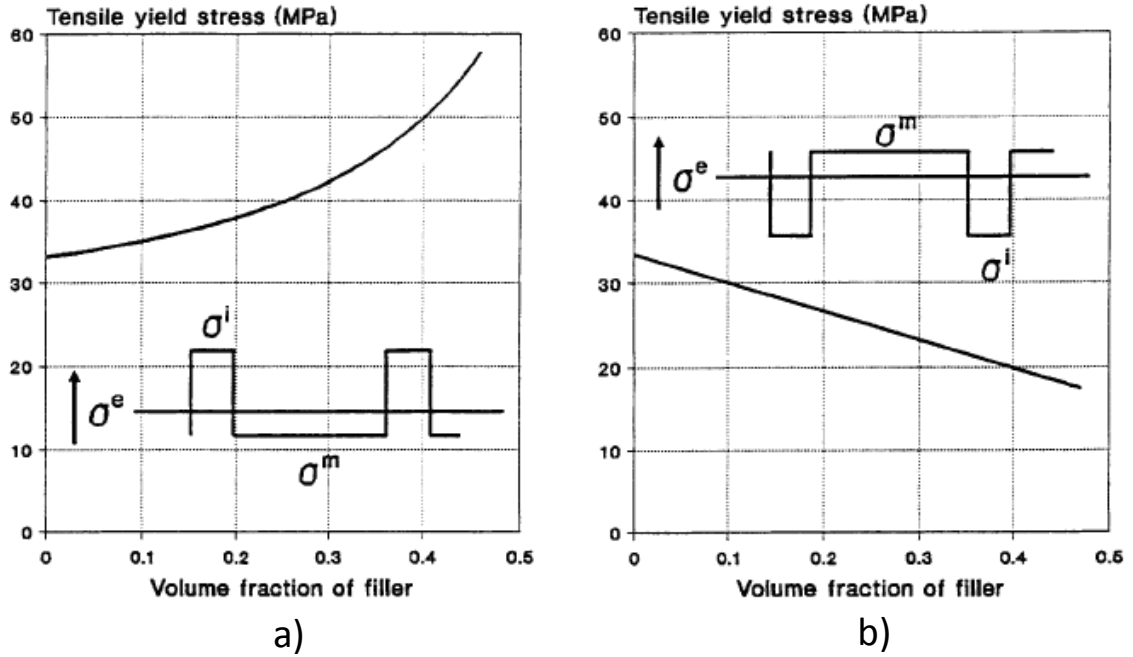


Figure 2.33: Average tensile yield stress of particle-filled composites (a), and composites containing voids or soft particles (b), in a polypropylene matrix. Figures are taken from [89].

behavior to occur. Therefore, they chose to incorporate the Goodier approach to calculating stress distributions around inclusions into the von Mises yield criterion in order to take into account interacting stress distributions around the particles as well as the dependence of local stresses. The negligible interacting stress fields and the significantly interacting stress fields are shown schematically in Fig. 2.34.

In a different study, Vollenberg and Heikens [88] investigated the relationship between particle size and Young's modulus for various loading fractions of glass beads, ranging in size from $.035\mu\text{m}$ to $100\mu\text{m}$, in the polymers polystyrene, polycarbonate, polypropylene and styrene-acrylonitrile. In each case they found the Young's modulus to increase with increasing loading fraction of the glass beads and the Young's modulus to increase with decreasing particle size. They proposed the increase in the modulus to be a result of a change in the morphology of the polymer matrix around

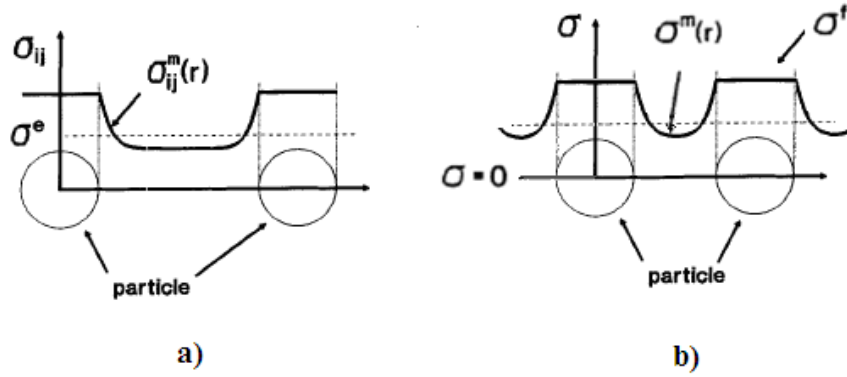


Figure 2.34: Schematic of interacting stress fields between particles embedded in a matrix where in (a), the particles are far apart and (b), the particles have a small interparticle spacing. Figures are taken from [89].

the particles. As the polymer melt begins to solidify the particles act as an initiation site for the solidification of the melt. This causes the melt to contract to a greater degree around the particle which then forms a region of higher density surrounded by a region of lower density bulk material. The regions of higher density then have a higher Young's modulus and the lower density regions have a lower Young's modulus. Considering a material with a constant volume fraction of filler material, if a smaller particle reinforcement is used than the solidification process will take place more homogeneously throughout the material due to the increase in initiation sites. This would then result in a material with a higher matrix modulus that then contributes to a higher composite Young's modulus.

In another study by He and Jiang [101] of clay filled polymer composites, they suggested that the increase in modulus to be due to stress zones around the clay particles that join together when the distance between them is small enough to form a percolation network in the polymer matrix that is then responsible for increasing the modulus. They first assume that under loading conditions a stress shell around each particle is formed. Also critical thickness for that shell can be defined as $T_C/2$ (see Fig. 2.35 (a)). The interparticle distance is also defined to be T (see Fig. 2.35

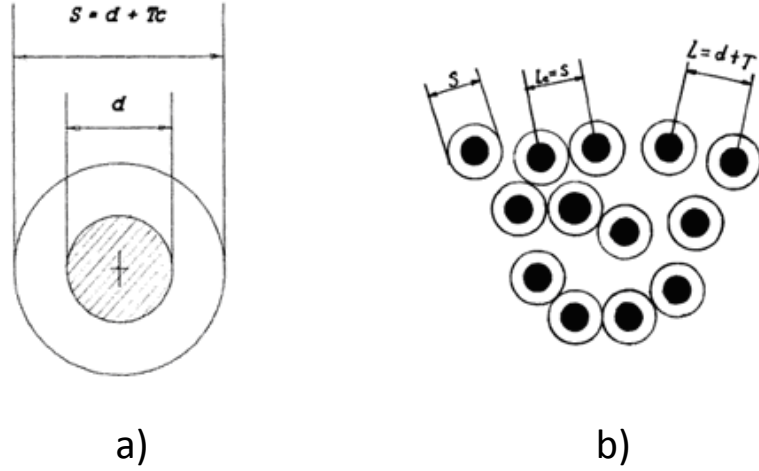


Figure 2.35: Schematic of stress volume around (a) a single particle and (b) multiple particles in a matrix. Figures are taken from [101].

(b)). If $T < T_C/2$, then the stress shells interact to produce a shear stress region between the nearest particles. These shear stress regions can then connect to form a percolation pathway within the matrix. If the volume fraction is high enough, than large clusters of percolation pathways can form networks within the material which results in an increase in modulus due to stress field interactions. Also, since the researchers defined T_C to be independent of particle size, with a constant volume fraction of particle reinforcement, the modulus will have a greater increase for smaller diameter particles due to an increase in the amount of stress field interactions.

Simulations have been conducted on the mechanical behavior of an elasto-plastic matrix reinforced with 15 vol.% of stiff spherical particles, by Seguardo and LLorca [102]. In their simulations the effect of the spatial distribution of spheres on the mechanical behavior was studied by changing the degree of particle clustering in the matrix. They found the particle distribution had a small effect on the resulting composite properties. However, they found that as the degree of particle clustering increased the stresses were much higher in the particles which increased the amount of damage by as much as three to six times than were found through simulations for

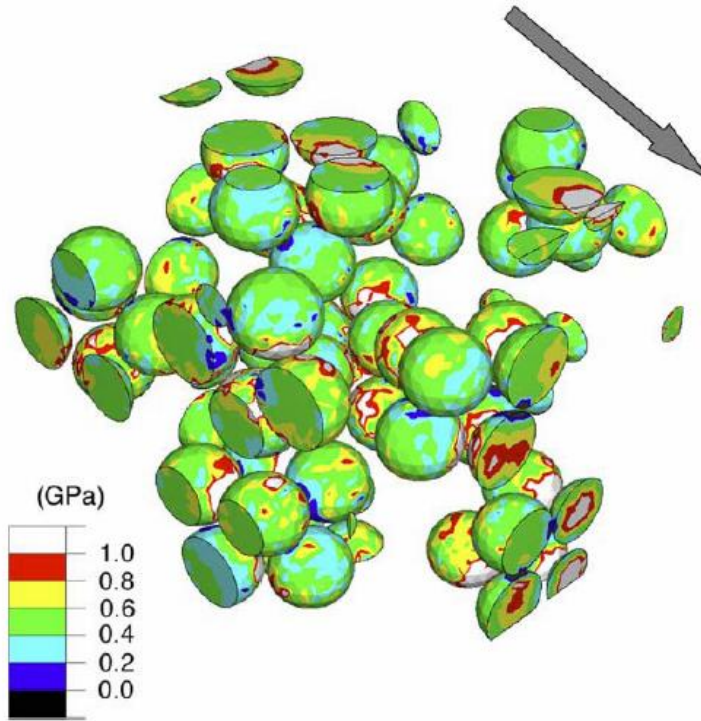


Figure 2.36: Stress contour plot of hard particles in a softer matrix material at 5% strain. The arrow indicates the direction of the applied force. Stress concentrations are in spheres that are near one another and oriented along the loading axis. Figure is taken from [102].

a homogenous arrangement of particles. This increase in damage, by particle fracture and decohesion of the matrix from the particle, led to negative effects in the stiffness and strain hardening of the composite. The location of the damage nucleation sites were found to be located near regions of higher particle clustering and oriented along the loading axis, as shown in Fig. 2.36.

2.4.4 Increase in Temperature due to Plastic Deformation

Due to the strain rate and temperature sensitivities in the mechanical behavior of polymers it is important to understand how any heating (isothermal or adiabatic) evolves throughout the loading process. With an increase in strain rate it is generally accepted that the temperature increase in the polymer increases as well. However, as

was discussed in a previous section, the relaxation mechanisms in a polymer generally shift towards higher temperatures with increases in strain rate. If the change in temperature due to heating is large enough, it may be possible for the polymer to undergo a transition from the glassy to rubbery regime, reducing its strength. This requires a greater understanding of both the increase in temperature of the polymer and shift in relaxation mechanism phenomenon if polymers are to be used as structural materials under dynamic loading conditions. Also, any localized straining in polymer composites may produce local hot spots that are more susceptible to experience temperature effects.

At slower rates of strain, heat generated due to deformation dissipates to the surrounding at a time scale on the order of the loading time, causing a smaller increase in temperature. In this case the heat generation is isothermal. Whereas, at faster rates of strain, the heat dissipation time scale is larger than the loading time and there is a subsequent increase in the bulk material temperature. This adiabatic heating can often be quite large in the sample and since polymers have lower thermal conductivities than metals, the strain rate effects on heat generation may be more pronounced. It has long been known that during plastic deformation only some of the plastic work is converted into heat [103, 91]. When a material begins to deform a portion of the plastic work goes into stored energy while the rest goes into heat generation. In the elastic regime much of the work is converted into stored energy with very little temperature rise within the material. When there is enough supplied energy into the material, yielding and different relaxations take place reducing the materials ability to store energy. When this occurs most of the work is converted into heat and β increases as well. At higher strains the decrease in the percent or fraction of mechanical work converted into heat (β), may be due to an increase in the materials ability to store energy once a new configuration of the microstructure takes place. For strain rates above 500 s^{-1} [104] the amount of plastic work converted into

heat generation can be calculated from the following equation [105, 104, 106, 107]:

$$\Delta T = \frac{\beta}{\rho C_p} \int_0^{\epsilon_f} \sigma(\epsilon) d\epsilon \quad (7)$$

where, ΔT is the associated rise in temperature, β the percentage of plastic work converted into heat, ρ the density, and C_p the heat capacity. For most metals, β is traditionally taken to be around 0.85 to 1.0 (with steels having a value of 0.85-0.865 [106, 103], copper 0.905 [103], aluminum 0.85-0.945 [103, 106]). While a constant value is often used in temperature increase calculations, β has been shown to be strain and strain rate dependent [76, 106, 107, 108]. Even though the conversion parameter β is not as simple as traditionally believed, and most of the research associated with measuring the temperature rise due to plastic work has primarily been conducted on metals, β values for polymers do exist. Adams and Farris [109] found 50 - 80% of the work was converted in to heat for polycarbonate drawn in a calorimeter at low strain rates of 0.18 min^{-1} to 1.80 min^{-1} (0.003 s^{-1} - 0.03 s^{-1}). In work carried out by Rittel [107], β values for polycarbonate undergoing compression experiments, at strain rates of 5000 - 8000 s^{-1} using a split Hopkinson pressure bar were determined to have a maximums of 0.4 to 1.0 depending on the strain rate. For the lower strain rates, β was lower and at each rate, β generally increased with strain with greater rate of increase occurring just following yield. The maximum value for β also occurred at strains following yield, and at higher strains it begins to decrease. The behavior in β can be seen in Fig. 2.37 for a strain rate of 6500 s^{-1} with the corresponding temperature rise in Fig. 2.38. For this system the maximum increase in temperature for polycarbonate was 14, 29, and 37°C for strain rates of 5000, 6500, and 8000 s^{-1} respectively.

Chou et al. [76] examined a variety of polymers and measured the rise in temperature during compression tests using embedded thermocouples. For two different polymers, PMMA and PC the temperature rise at around 20% strain was measured

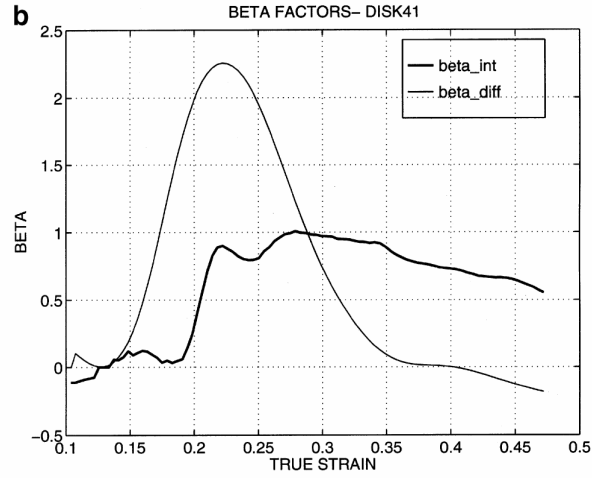


Figure 2.37: Evolution of β factors with the true strain for polycarbonate compressed at a nominal strain rate of 6500 s^{-1} . Figure was taken from [107].

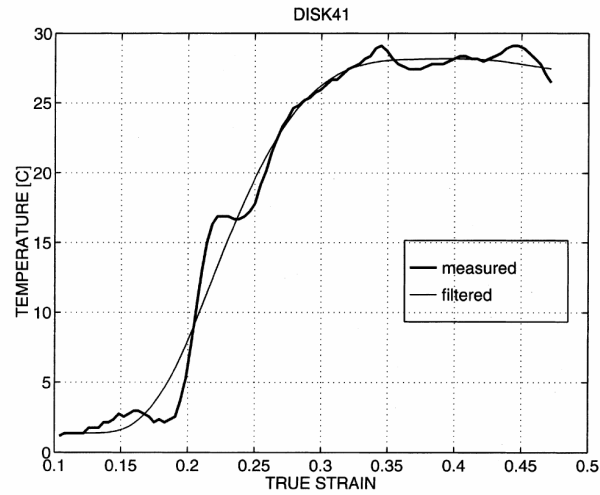


Figure 2.38: Temperature rise due to work plotted against the true strain for polycarbonate compressed at a nominal strain rate of 6500 s^{-1} . Figure was taken from [107].

to be approximately 19 °C and 26 °C at 3 s^{-1} and 45 s^{-1} respectively for PMMA and for PP to be approximately 8 °C and 13 °C at 4 s^{-1} and 50 s^{-1} respectively. As with other studies [107, 108] the researchers in this study found the temperature rise to increase at a higher rate for strains greater than yield strains. For an epoxy system studied by Trojanowski et al. [108], results were similar and the temperature was found to increase by as much as 40 °C. However, there was a much lower β value of 0.15 (calculated by Rittel [107]) than that reported for the polycarbonate and metal systems discussed earlier. For polymer composite systems, there are relatively few studies examining the temperature increase and heat conversion factors for high strain rate loading conditions. For an epoxy-based composite reinforced with hematite and aluminum particles the temperature rise was estimated using (Eqn. 7) to be as much as 84 °C during Taylor impact experiments [3]. While, this value is higher than those for the mentioned neat polymers, a significant amount of the composite (as much as 30 vol.%) is comprised of metal particles which are known to have higher β values. Also, the Taylor impact tests were carried out at strain rates on the order of $10^4 s^{-1}$ which would contribute to the larger temperatures.

CHAPTER III

EXPERIMENTAL PROCEDURE AND CHARACTERIZATION

In this section, casting procedures used to produce the composite materials, and experimental methodology used to characterize the elastic, viscoelastic, and thermomechanical properties will be discussed. The experimental procedures for determining the mechanical behavior of the epoxy-based composites include: ultrasound speed measurements, quasi-static uniaxial compression tests using an MTS test frame, dynamic uniaxial compression tests using the split Hopkinson pressure bar (SHPB) apparatus, and rod-on-anvil impact tests using the gas gun in a Taylor rod-on-anvil impact configuration. There will also be a section describing the thermomechanical property characterization techniques using dynamic mechanical analysis (DMA), differential scanning calorimetry (DSC), and thermogravimetric analysis (TGA).

3.1 Materials Characterization

As described earlier, the effects of size, volume fraction, and spatial distribution of the Ni and Al reinforcing particles on the constitutive response of the epoxy-cast composites are of key interest in this work. This requires well characterized constituent phases.

3.1.1 Starting Powder Characterization

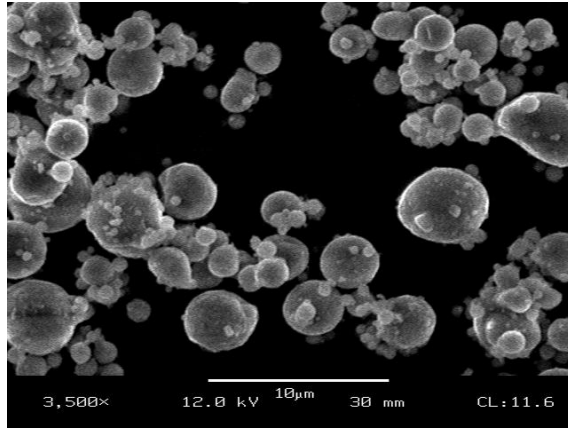
Figure 3.1 shows SEM micrographs illustrating the morphology of the two types of aluminum powders ((a) type H3 and (b) type H50) and the nickel powder ((c) Ni-120), used in the present work. The nominal particles size for the two types of aluminum powders were approximately 5 μm (H3 grade, Valimet, Inc.) and 50 μm

(H50 grade, Valimet, Inc.) in diameter. Using light scattering analysis techniques on a Saturn DigiSizer 5200 V1.09 (Micromeritics Instrument Corporation) the H3 aluminum powder was found to have a mean particle diameter of $5.5\ \mu\text{m}$ and monomodal size distribution with 99% of the particle diameters in the range of $0.5\ \mu\text{m}$ to $15.9\ \mu\text{m}$. Similarly the average particle diameter for the H50 aluminum powder was found to be $51.9\ \mu\text{m}$, which also exhibited a somewhat monomodal size distribution with 99% of the particle diameters in the range of $112.2\ \mu\text{m}$ to $4.7\ \mu\text{m}$. The particle size distributions for the H3 and H50 aluminum powders can be seen in Fig. 3.2. As illustrated in the SEM images, both types of Al powders are of spherical morphology with smooth surfaces.

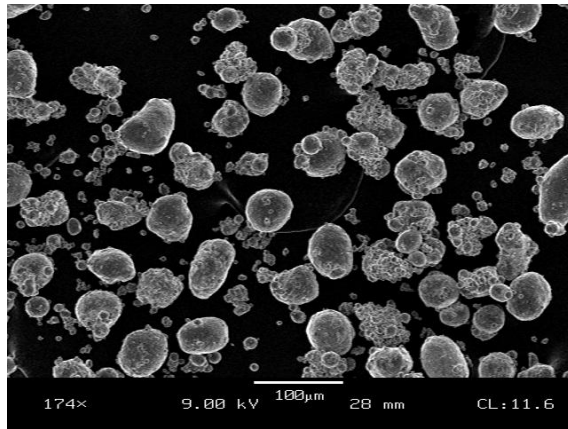
The nickel powder (NI-120 grade, Micron Metals, Inc.) was reported by the manufacturer to have a nominal particle size of -325 mesh ($<45\ \mu\text{m}$). As with the aluminum powders, the nickel particle size was verified using light scattering analysis techniques. As can be seen in Fig. 3.2 the particle diameters for the nickel powder are in the range of $12.6\ \mu\text{m}$ to $112.2\ \mu\text{m}$. The particle size distribution is bimodal with the largest peak having a mean particle size of $44.1\ \mu\text{m}$ and the smaller peak a mean particle size of $97.4\ \mu\text{m}$. Since the smaller peak contributes only 6.6% of the total distribution the mean particle size was considered to be $47.5\ \mu\text{m}$, and used for all models and calculations in this work. In contrast to the aluminum particle morphology, the nickel particles have a rougher surface texture and non-spherical globular shape, Fig. 3.1.

3.1.2 Epoxy Resin and Hardener System

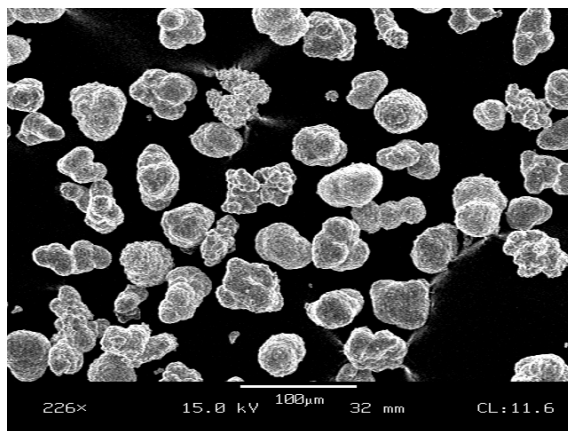
An epoxy system is usually comprised of two components, a resin and a hardener (curing agent). The hardener is often used to chemically cross-link the epoxy resin molecules to one another to form a rigid infinite network of polymer chains known as a thermoset. The advantage to using an epoxy is its ability to bond to most surfaces



(a) H3 aluminum powder morphology

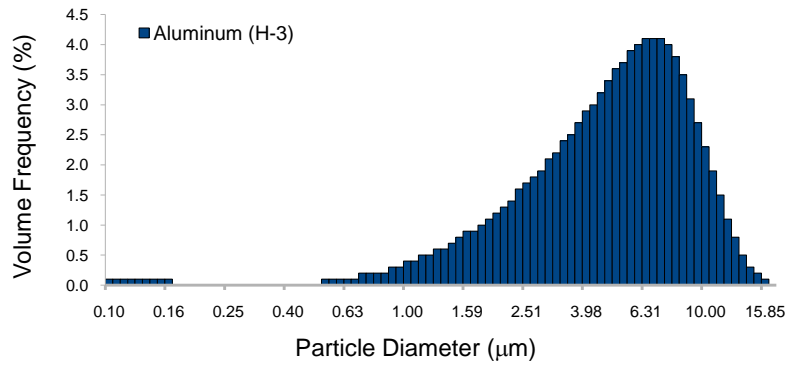


(b) H50 aluminum powder morphology

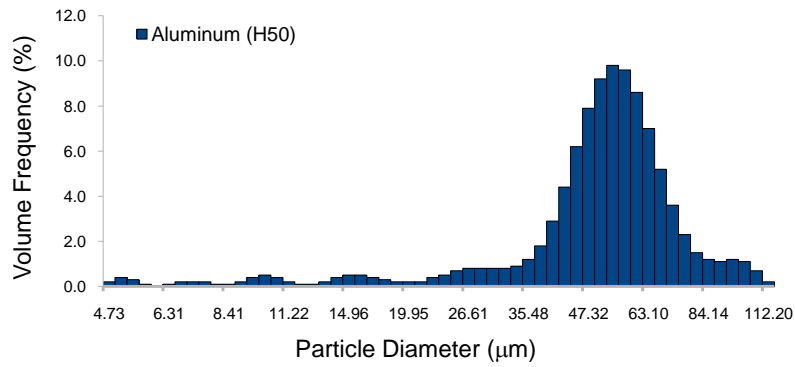


(c) NI-120 nickel powder morphology

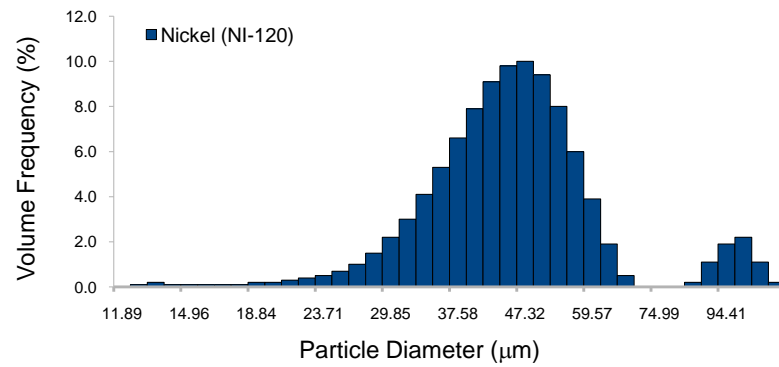
Figure 3.1: Particle morphology for a) H3 aluminum, b) H50 aluminum, and c) NI-120 nickel powders. Notice how the aluminum particles are smooth and spherical while the nickel particles have a tendency to be more rough and oblong or globular in shape.



(a) H3 aluminum powder particle size distribution

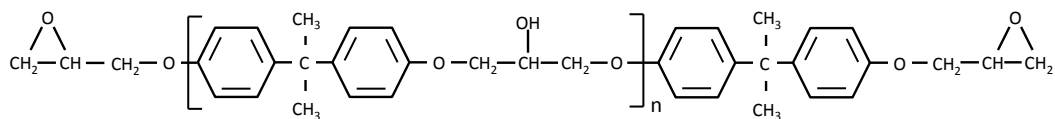


(b) H50 aluminum powder particle size distribution

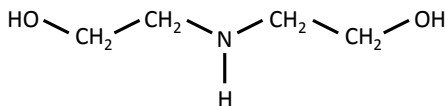


(c) NI-120 nickel powder particle size distribution

Figure 3.2: Particle size distributions for H3 (top) and H50 (middle) aluminum powders as well as the particle size distribution for the nickel powder (bottom). The Particle size distributions were determined using light scattering analysis techniques based on Mie theory of light scattering by particles.



(a) Epoxy Resin Structure



(b) Diethanolamine (DEA) Structure

Figure 3.3: Chemical Structures for a) the epoxy resin (Epon 826) and b) cross-linker diethanolamine. For Epon 826 $n = 0.085$ [110].

and to be easily processed. However, due to its cross-linked network, epoxy can not be reshaped or processed. EPON 826 (Hexion Specialty Chemicals) epoxy which is a diglycidyl ether of Bisphenol A (DGEBA) type resin was used in this project. EPON 826 is similar to the more commonly used resin EPON 828, however, it has a lower molecular weight that allows for easier composite processing. The cross-link agent used in the processing of the epoxy and epoxy-based composites is diethanolamine (Sigma-Aldrich, St. Louis, MO). The chemical structures for the epoxy resin and diethanolamine (DEA) are shown in Fig. 3.3

3.2 Casting of Epoxy-Based Composites

While most studies only change one factor at a time and examine the effect on the behavior of the material property, interaction effects between variables need to be taken into account. A 2^k factorial design of experiments is an efficient technique that can be used to determine appropriate material compositions for testing and analyzing the effects of multiple factors. For this type of design, each factor k has two possible

states, either a low or high state, giving a total number of 2^k material configurations for a particular design space. This approach is taken in this work to examine the interaction effects of particle size and loading fractions of two particle types on the mechanical behavior of epoxy cast particulate composites.

In order to determine the effects of aluminum particle size, and volume fractions of aluminum and nickel on the mechanical behavior of epoxy-matrix based composites, materials were prepared according to a 2^3 factorial design of experiments [111] to account for each one of these variables. The average nominal aluminum particle size was varied between 5 μm and 50 μm , the volume fraction of aluminum varied between 0.20 and 0.40, and the volume fraction of nickel varied from 0.00 to 0.10. The resultant material combinations (eight in total) from the factorial design are shown in Table 3.1 along with their material designations and theoretical densities using a rule of mixtures. Polymer-matrix composites of aluminum and nickel powders within an epoxy (EPON-826/DEA) binder were prepared by casting, and machined down to the sample geometries used in each type of experiment. The composite materials were prepared by mixing the aluminum and nickel powders separately into the Epon 826 resin. Diethanolamine was then added into the mixture with a 100:12 (Epon826/DEA) ratio by weight percentage. To increase the curing rate the mixtures were allowed to cure in a furnace for a 24 hour period at 80.0°C. Prior to any mixing the powders, epoxy resin, and DEA were placed in a furnace for 24 hours set to 80.0°C to drive off any moisture in the materials. Figure 3.4 shows what the composites look like after being machined from a larger block of cast material. The composites with the 50 μm sized aluminum are more speckled due to light reflecting off the larger particles, where as, the composites containing 5 μm have a more even coloration. Since epoxy is transparent and the aluminum and nickel powders are gray, the composites take on a grayish hue.

Table 3.1: Material configurations determined from a two-factorial design of experiments. Nominal density values were calculated using the rule of mixtures with density values of 2.70 [112], 8.90 [112], and 1.19 g/cm³ [14] for Al, Ni, and Epoxy, respectively.

Material	Nominal Al Particle Size (μm)	Al Volume Fraction (%)	Ni Volume Fraction (%)	Nominal Density (g/cm ³)
MNML-1	50	40	10	2.565
MNML-2	5	40	10	2.565
MNML-3	50	20	10	2.263
MNML-4	5	20	10	2.263
MNML-5	50	40	0	1.794
MNML-6	5	40	0	1.794
MNML-7	50	20	0	1.492
MNML-8	5	20	0	1.492

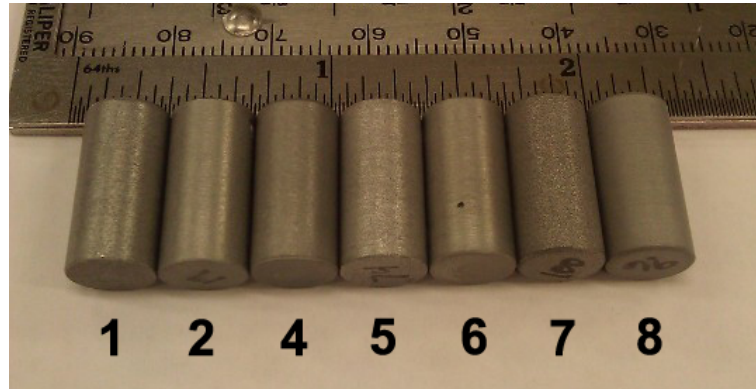


Figure 3.4: Examples the cast particle reinforced epoxy composites. All but composite MNML-3 is shown with the number below each cylindrical sample corresponding the MNML-designation number for that sample. Samples shown have the nominal dimensions of 8 mm (dia) x 16 mm (height).

3.3 Mechanical Property Characterization

This section gives an overview of ultrasonic sound speed measurement techniques and several compression test methods used to determine the mechanical properties of the epoxy-based composites over a large range of strain-rates from 10^{-4}s^{-1} to 10^4s^{-1} .

3.3.1 Ultrasonic Sound Speed Measurement Techniques

Ultrasound speed measurements were used to determine the elastic properties of the composite materials, as well as their longitudinal (C_l), shear or transverse (C_t), and bulk (C_0) sound speeds using a time of flight method. For each material cylindrical specimens were machined (from a larger block of as-cast material) with nominal dimensions of 6.35 mm x 25.4 mm (length x diameter) and 12.85 mm thick x 25.4 mm length x diameter). A GE Panametrics 25HP Plus ultrasonic thickness gauge (Olympus NDT) was used in conjunction with Panametrics M106 (2250 kHz) and V154 (100 kHz) transducers to measure the longitudinal and shear sound speeds respectively. Three specimens for each geometry were used to obtain average sound speed values, measured at room temperature. A minimum of five measurements of both the longitudinal and shear wave time of flights were taken, for each specimen, from which the sound speeds are calculated using the known thickness of the specimens. Couplants were used for making these of measurements, as such glycerin was used for the longitudinal sound speed measurements and honey for the shear sound speed measurements. Care was taken to only apply enough couplant to produce a reasonable reading on the gauge.

Using the shear and longitudinal sounds speeds along with the material density (ρ), the bulk mechanical elastic properties can be determined through the use of the following equations:

$$C_t^2 = \frac{\mu}{\rho} \tag{8}$$

$$C_l^2 = \frac{\lambda + 2\mu}{\rho} \quad (9)$$

$$C_0 = \left(C_l^2 - \frac{4}{3} C_t^2 \right)^{1/2} \quad (10)$$

$$E = \frac{\rho C_t^2 (3C_l^2 - 4C_t^2)}{C_l^2 - C_t^2} \quad (11)$$

$$K = \rho \left(C_l^2 - \frac{4}{3} C_t^2 \right) \quad (12)$$

$$\nu = \frac{1 - 2 \left(\frac{C_t}{C_l} \right)^2}{2 \left(1 - \left(\frac{C_t}{C_l} \right)^2 \right)} \quad (13)$$

While, Eqns. 8, 11, 12, and 13 allow for the shear modulus (μ), elastic modulus (E), bulk modulus (K), and Poisson's ratio (ν) to be calculated directly from the longitudinal and shear sound speeds, Eq. 9 can be used to first determine the value for the Lamé constant λ and use another set of relationships along with the calculated value for μ to obtain isotropic elastic constants (see Table 3.2) [113].

Table 3.2: Relationships used to determine isotropic elastic constants from λ and μ .

	E, ν	E, μ	λ, μ
λ	$\frac{E\nu}{(1+\nu)(1-2\nu)}$	$\frac{\mu(E-2\mu)}{3\mu-E}$	λ
μ	$\frac{E}{2(1+\nu)}$	μ	μ
E	E	E	$\frac{\mu(3\lambda+2\mu)}{\lambda+\mu}$
K	$\frac{E}{3(1-2\nu)}$	$\frac{\mu E}{3(3\mu-E)}$	$\lambda + \frac{2}{3}\mu$
ν	ν	$\frac{E-2\mu}{2\mu}$	$\frac{\lambda}{2(\lambda+\mu)}$

3.3.2 Quasi-Static Compression Experiments

Uniaxial quasi-static compression experiments were conducted using an MTS 810 compression frame at Wright-Patterson AFB. The compression frame has a 100 kN load cell and is controlled using MTS software. Experiments were carried out on 8mm x 16 mm (diameter x length) specimens at strain-rates of approximately 1×10^{-4} and $1 \times 10^{-3} \text{ s}^{-1}$ at room temperature using a constant cross-head displacement rate. Since these types of composites were found to be highly sensitive to alignment, the machine alignment was calibrated using an aluminum slug fitted with 12 strain gages evenly spaced on the outside of the slug. The strain in the slug for each strain gage was then tracked using the MTS alignment software. The machine was then adjusted until the strain difference between each gage was minimized. As the specimens were placed on the platens, calipers were then used to align the specimen's center axis with the machine loading axis. This system minimized any non-axial loadings which eliminated the "leaning tower of Pisa" results seen in earlier attempts (see Fig. 3.5). Prior to placing the specimens on the platens, lubricants were sprayed onto the platen surfaces using a two-layer approach. The first layer was a thin film of boron nitride (*BN*) with a second layer of molybdenum disilicide (*MoSi₂*) sprayed on top. This was used to reduce frictional effects common in compression experiments. To minimize errors, tests were conducted in a random order. For each strain rate the experimental order was determined by randomizing both the composite type (MNML-1 - MNML-8) and specimen number for each composite.

To track the strain and stress states throughout each experiment, MTS Tech Works 4.0 software was used to record test frame loads and displacements. The VIC Gauge 2.0 (Correlated Solutions Inc.) software was also used to track the strain within the specimen by interfacing with an ES 4.0 MegaPlus camera and tracking virtual strain gages. The strain gages were placed at high contrasting boundaries (fiducial marks) drawn on the specimens by hand using a permanent marker. This not only

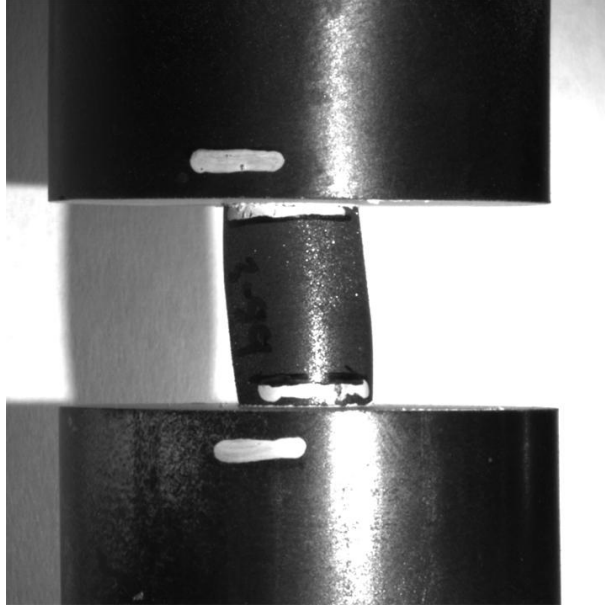


Figure 3.5: Example of shear in specimen during quasi-static compression test prior to MTS frame alignment.

has an advantage over using strains recorded by the MTS software by measuring the strains associated only with the specimen itself, but it also has an advantage over mechanical extensometers in that strains throughout the entire test (and not only up to certain strain value) can be recorded. There is also the advantage of being able to place multiple strain gages (virtual) on the specimens easily. For the tests performed in this work, at least four virtual strain gages were used in order to compare results between each gage, gather statistics, and ensure that data was collected for the entire experiment in the very rare event that gages would fail to track. An example of typical virtual strain gage placements is shown in Fig. 3.6. In this manner the strain was measured by tracking the endpoints of the virtual strain gages. The stress was computed from voltage outputs read by the MTS software by first converting these voltage outputs into force (F). The engineering stress (σ_{eng}) and strain (ε_{eng}) were then determined using the following equations:

$$\sigma_{eng} = \frac{F}{A_0} \quad (14)$$

$$\varepsilon_{eng} = \frac{l_0 - l_i}{l_0} \quad (15)$$

where A_0 is the initial area calculated from the specimen diameter prior to testing, l_0 the initial virtual gage length, and l_i the instantaneous length of the virtual strain gage. The load, F , was read as a voltage output, V , from the MTS compression frame and converted into a force value using the following equation:

$$F = \alpha V \quad (16)$$

where α is the conversion factor from voltage to force which in this case was 10000 lbs/10 V. Once the engineering stress and strains were calculated the true stress (σ_{true}) and strain (ε_{true}) are found using Eqns. 17 and 18 respectively.

$$\sigma_{true} = \sigma_{eng} (1 + \varepsilon_{eng}) \quad (17)$$

$$\varepsilon_{true} = \ln(1 + \varepsilon_{eng}) \quad (18)$$

Using the procedure outlined above, the stress-strain curves were determined. A representative true-stress true-strain curve is shown in Fig. 3.7. The results from multiple virtual strain gages show that the stress-strain response from each gage are consistent with one another despite their placements in different locations. Figure 3.8 shows what a typical specimen looks like prior and following compression up to its final strain value.

The stress-strain response can be broken up in to three distinct regions. At low strains ($\sim 0.00 - 0.015$) the behavior is dominated by a linear elastic response. At

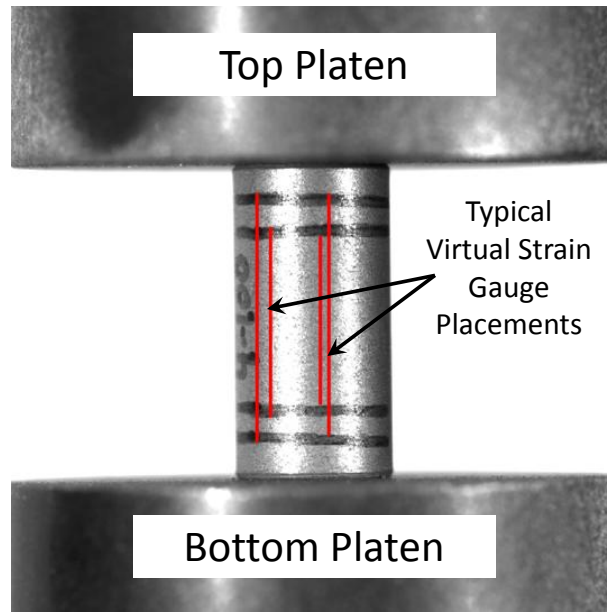


Figure 3.6: Example of virtual strain gage placements using high contrasting fiducial marks as boundaries at endpoints of gage lengths.

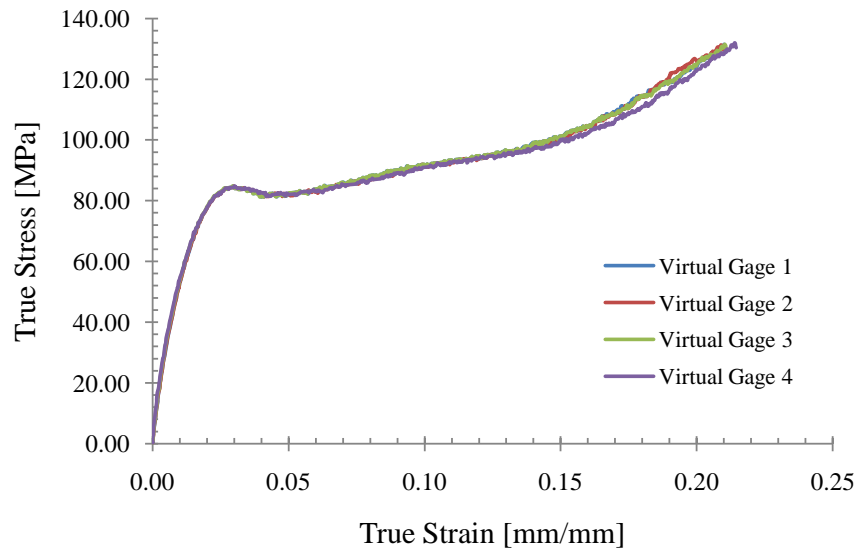


Figure 3.7: Representative true stress-true strain curve for MNML-3 at a strain-rate of 10^{-4} s^{-1} . The stress-strain behavior of each virtual strain gage show good agreement with one another.

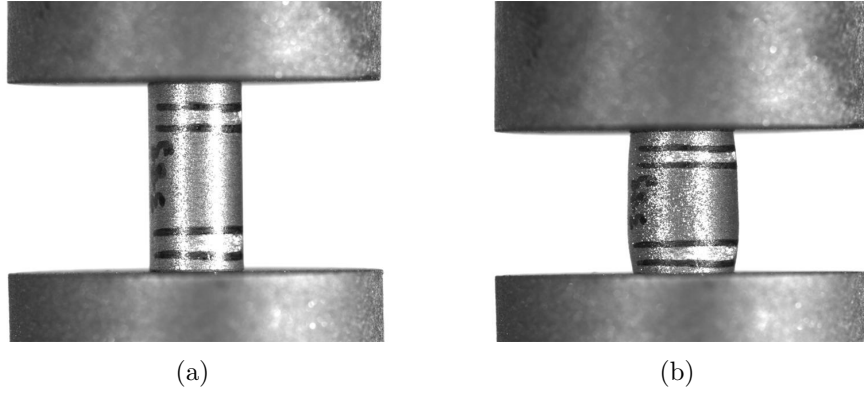


Figure 3.8: Quasi-static compression sample at the (a) initial, and (b) final strain state.

higher strains ($\sim 0.015 - 0.04$) the response shifts from a linear response to a viscoelastic to viscoplastic response. In this region the stress peaks and is followed by strain softening. At larger strains, strain softening proceeds and eventually transitions into strain hardening at large amounts of plastic deformation.

Using the data in the linear elastic region the Young's modulus (E) can be calculated from the slope of the curve within a specified strain or stress range. For these experiments the Young's modulus was calculated from the slope of a linear fit to the data for the stress-strain curve between strains of 0.0005 and 0.002. This is carried out on all strain gages so that an average Young's modulus can be obtained for each sample. An example of the analysis (for the stress-strain curve in Fig. 3.7) is shown in Fig. 3.9.

In the viscoelastic to viscoplastic region the peak stress of the material is found by taking a quadratic fit to the stress-strain curve in that region. From the equation of the quadratic fit the peak strain (ϵ_y) is first solved by taking the derivative of the curve and setting it equal to zero. The peak strain value is then used in the original quadratic equation to determine the peak stress (σ_y). This procedure was used on each virtual strain gage curve to determine the sample average. A representative peak stress analysis (for the stress-strain curve in Fig. 3.7) is shown in Fig. 3.10. In

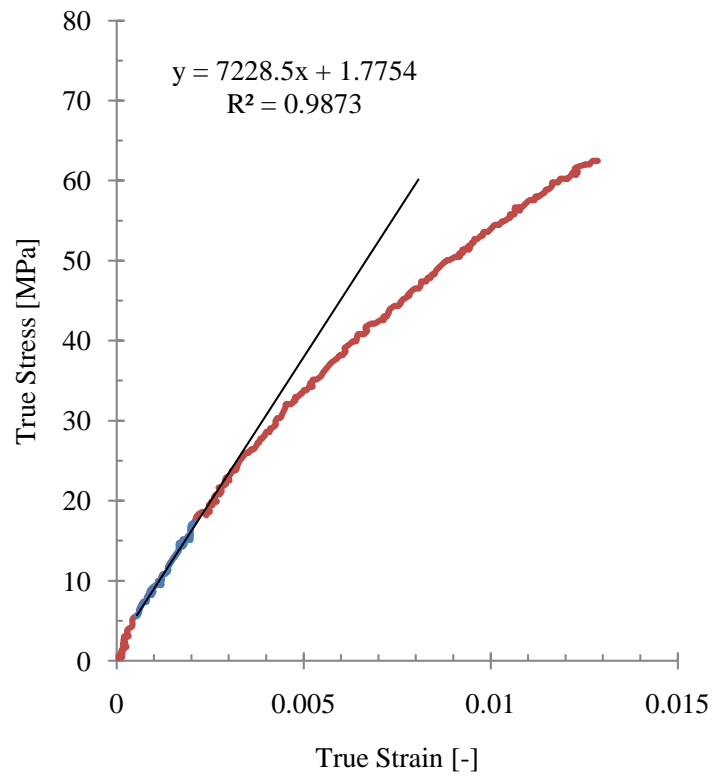


Figure 3.9: Representative Young's modulus analysis curve (blue) and linear fit equation for the stress-strain curve (red).

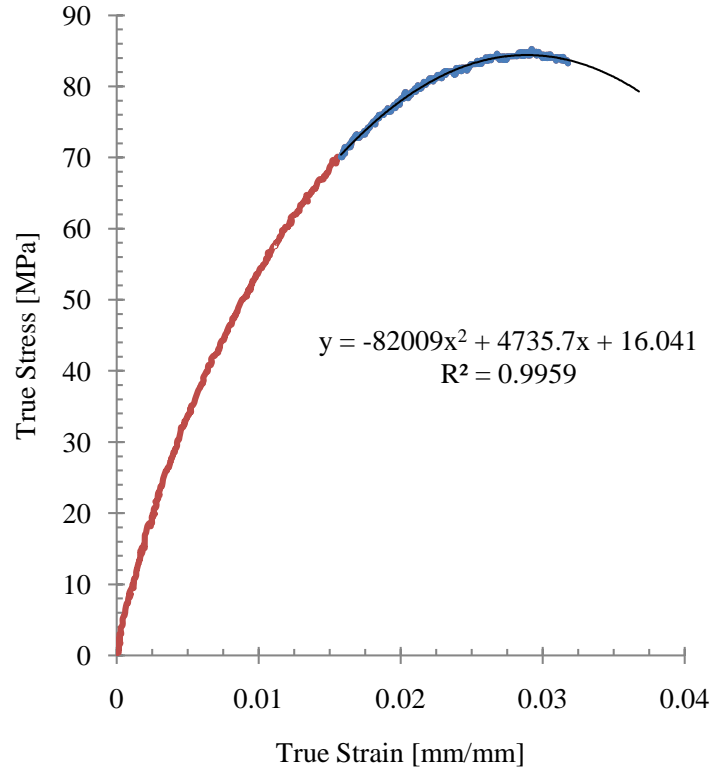


Figure 3.10: Representative peak stress analysis curve (blue) and quadratic fit equation for the stress-strain curve (red).

Fig. 3.11 the engineering and true stress strain curves are shown. Up to the point of strain softening the two curves are nearly identical with peak stresses deviating by $< 3\%$ (2.38 MPa). Beyond this the peak strain the true stress strain curve is shown to have a much higher degree of strain hardening.

3.3.3 Split-Hopkinson Pressure Bar Experiments

Uniaxial dynamic compression experiments were conducted on a split-Hopkinson pressure bar (SHPB) apparatus to achieve strain-rates of approximately 1×10^3 and $5 \times 10^3 \text{ s}^{-1}$. Traditionally, a SHPB consists of a striker bar and specimen placed in between an incident and transmission bar. The SHPB system at AFRL/RWME, Eglin AFB, FL was used for the present work. A schematic of the key components is shown in Fig. 3.12. The SHPB system uses a 6061-T6 aluminum striker bar 610 mm x 12.7 mm

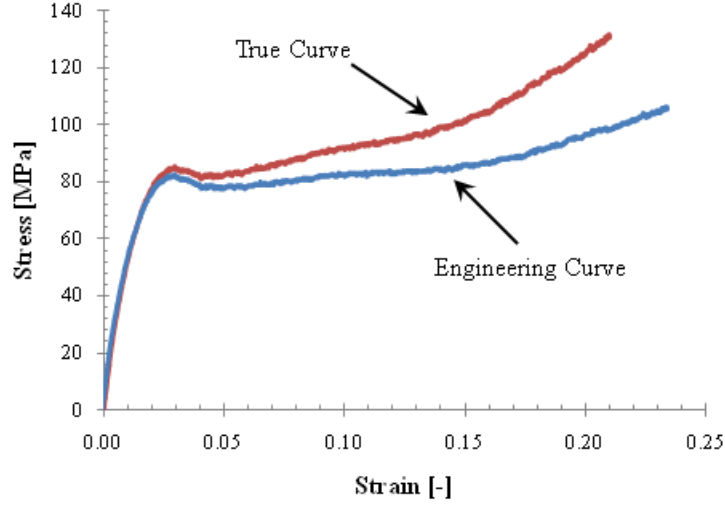
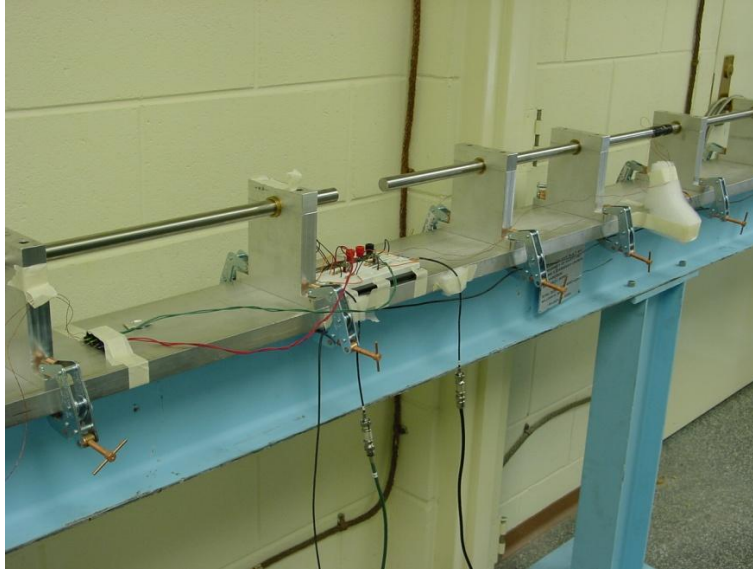


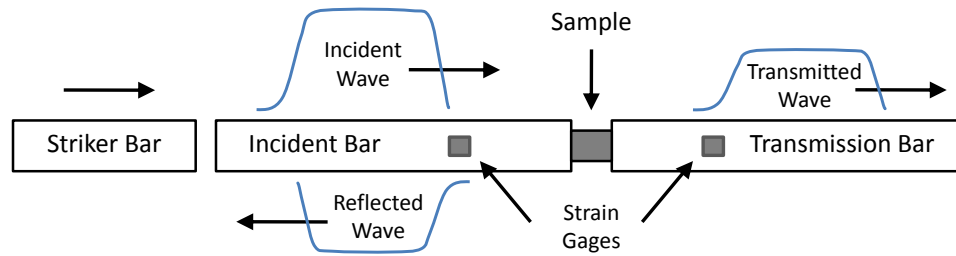
Figure 3.11: Comparison of true (red) and engineering (blue) stress-strain curves.

(length x diameter) and incident and transmitted bars 1524 mm x 12.7 mm (length x diameter) that were also made from 6061-T6 aluminum. Two different specimen nominal geometries were used, 3.5 mm x 8 mm (length x diameter) and 2.5 mm x 5mm (length x diameter) in order to obtain strain-rates of 1×10^3 and $5 \times 10^3 \text{ s}^{-1}$, respectively. To minimize friction during testing, lubrication was used on the ends of the input and transmission bars in contact with the sample. For each strain rate five tests were carried out to obtain an average dynamic mechanical response for each composite.

Compressed gas was used to propel the striker bar into the incident bar. When the striker bar impacts the incident bar an elastic compressive wave (incident wave) is created and propagates down the bar towards the sample. When the stress wave reaches the incident bar-specimen interface, part of the wave reflects back into the incident bar to create a tensile reflected wave while the rest of the wave is transmitted into the specimen towards the transmission bar. Upon reaching the specimen-transmission bar interface, again part of the transmitted pulse continues down the transmission



(a) Split-Hopkinson pressure bar apparatus located at Eglin AFB



(b) Schematic of split-Hopkinson pressure bar apparatus

Figure 3.12: Split-Hopkinson experimental apparatus and schematic of wave propagation within the bars.

bar while the rest of the stress pulse is reflected back into the specimen. This transmission and reflection of the stress wave within the specimen causes a ringing-up state in the specimen. In this state if the specimen is then assumed to be in force equilibrium and deforming uniformly (i.e. mechanical equilibrium) then stress-strain state in the specimen can be more readily determined using one-dimensional wave propagation analysis along with voltage outputs that are converted into forces from Kulite AFP-500-90 semiconductor strain gages located on the incident and transmission bars. For this approach one- and/or two-wave analysis can be carried out to determine the stress state of the specimen. However, it is not necessary to assume that the specimen is in mechanical equilibrium, and instead a 3-wave analysis is used to determine the strain-rate by using the forces recorded by the strain gages for the propagating incident, reflected, and transmitted waves. The following equations are used for dynamic stress-strain analysis in this work:

$$\dot{\varepsilon}(t) = \frac{C_b}{l_s} (-\varepsilon_i(t) + \varepsilon_r(t) + \varepsilon_t(t)) \quad (19)$$

$$\sigma(t) = \frac{E_b A_b \varepsilon_t(t)}{A_s} \quad (20)$$

where ε_i , ε_r , and ε_t are the incident, reflected, and transmitted strain pulses as a function of time, respectively, C_b the longitudinal wave speed in the pressure bars, l_s the instantaneous length of the specimen, E_b and A_b the elastic modulus and the cross-sectional area of the pressure bars, and A_s the cross-sectional area of the specimen. Upon integration of Eq. 19 with respect to time the total strain is determined (see Eq. 21). Equation 20 is used for calculating the stress for a one-wave analysis (i.e. only uses ε_t). For a two-wave stress analysis, ε_t is replaced with $(\varepsilon_i + \varepsilon_r)$. In Fig. 3.13 the results of the one- and two-wave analysis for one of the composites is shown with the two-wave analysis resulting in a profile that oscillates about the one-wave curve. This indicates that the sample attained a uniform stress state.

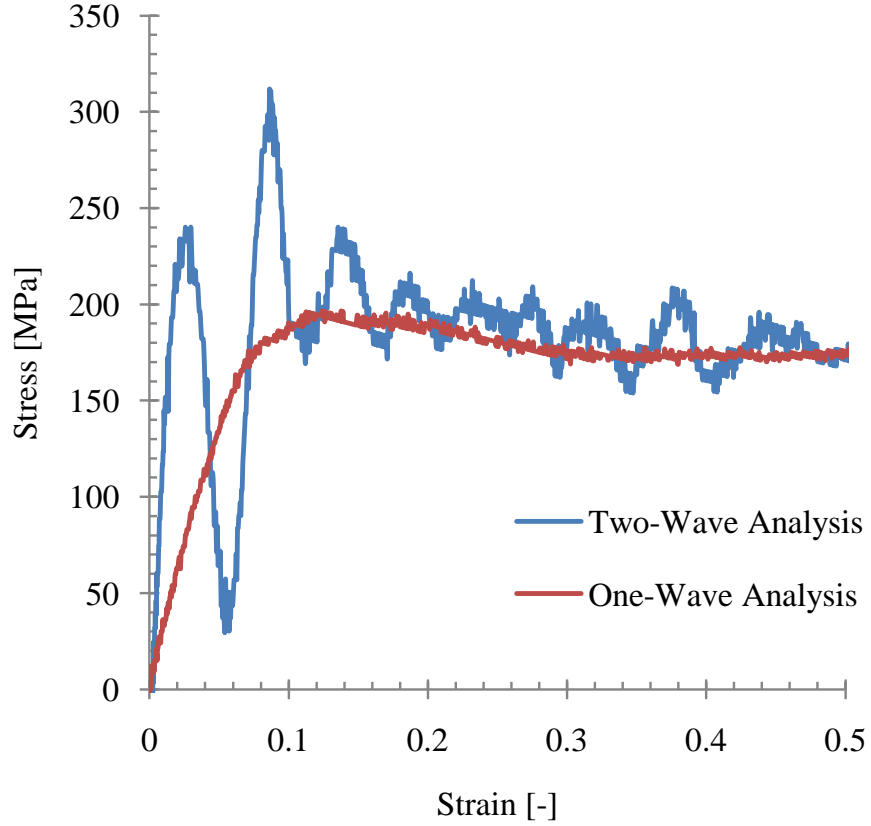


Figure 3.13: Representative stress-strain curve of a one- and two-wave stress analysis. The two-wave (blue) analysis curve oscillates about the one-way (red) curve. Stress-strain curve is of data for MNML-5 at a strain rate of $5 \times 10^3 \text{ s}^{-1}$.

$$\varepsilon(t) = \int_0^t \dot{\varepsilon}_t(t) dt \quad (21)$$

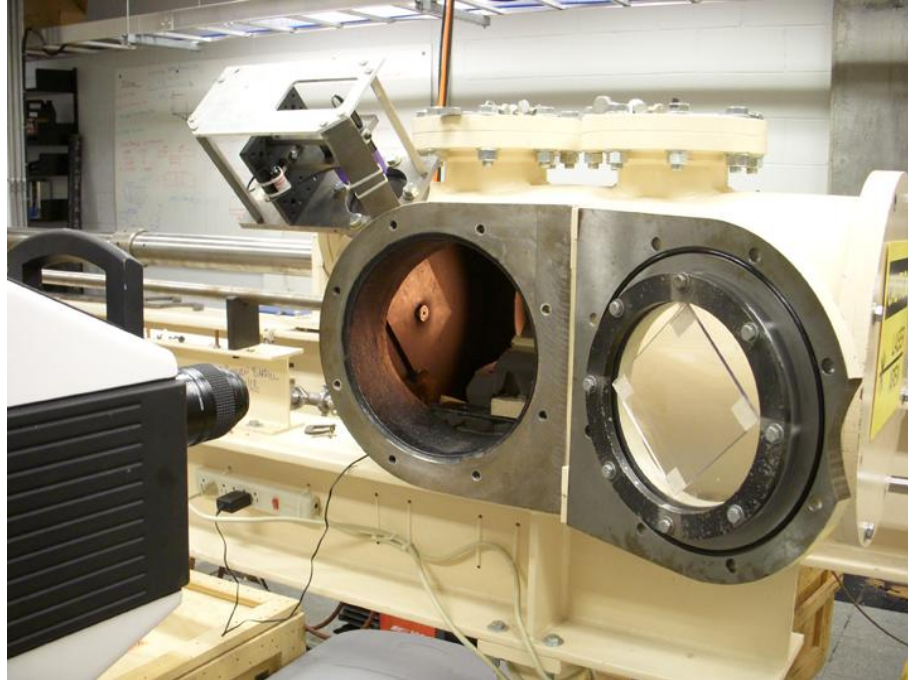
As with the uniaxial quasi-static compression experiments, the yield stress for the composites were determined by taking a quadratic fit to the viscoelastic-viscoplastic region of the stress-strain curve, and using the derivative to determine the strain value for where the slope is zero. This strain value was then used in the original quadratic equation to determine the stress at yield. The "apparent" Young's modulus was determined by taking the slope of a linear fit to the elastic region between 30 and 50 MPa. The term apparent Young's modulus is used to make a note that the specimen

is usually in a ringing-up state in the elastic regime and hence may not have reached stress equilibrium in the sample.

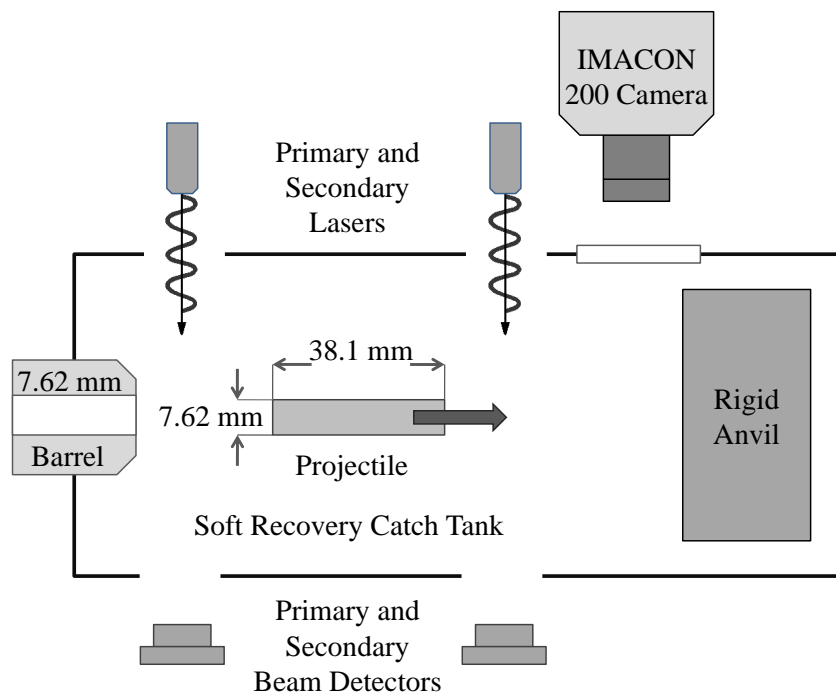
3.3.4 Taylor Rod-On-Anvil Impact Experiments

Taylor rod-on-anvil impact experiments were conducted on a 7.62 mm single-stage gas gun configured with a soft recovery catch tank and laser interrupted velocity measurement system, as shown in the schematic in Fig. 3.14 along with the gas gun at the High Strain Rate Laboratory, Georgia Institute of Technology. Specimens, 7.62 mm (dia.) x 38.1 mm (length), were propelled between 75 m/s and 200 m/s to produce maximum strain rates between 10^3 to 10^4 s⁻¹. Impacted specimens were then recovered from the soft catch tank and post impact geometry measurements were performed. An IMACON 200 high-speed camera (DRS Hadland Ltd.) was used to capture transient deformation states as the specimen impacts a rigid anvil. To ensure one dimensional wave analysis could be applied, perpendicularity of the impact event was verified from these transient images. Also, in the case where specimens were recovered in a fracture state the transient images were used to identify if fracturing occurred during impact with the rigid anvil or from secondary impacts with the catch tank. This aided in the determination of the lower velocity bound at which each material would fracture during impact with the rigid anvil so that intact specimens could be recovered and deformation profiles accurately measured. Taylor rod-on-anvil impact experiments were performed on each material type at varying velocities until a minimum of four intact specimens were recovered with a measurable amount of plastic deformation. Due to the difficulties associated with this type of experiment Taylor impact tests were not repeated for a given velocity and material. A series of specimens for MNML-6 at impact velocities ranging from 0 m/s to 177.32 m/s are shown in Fig. 3.15.

High resolution images were taken of the recovered impacted specimens (see



(a) 7.62mm gas gun located at Georgia Institute of Technology



(b) Schematic of Taylor impact apparatus

Figure 3.14: Taylor rod-on-anvil impact experimental apparatus and schematic of chamber and diagnostics.

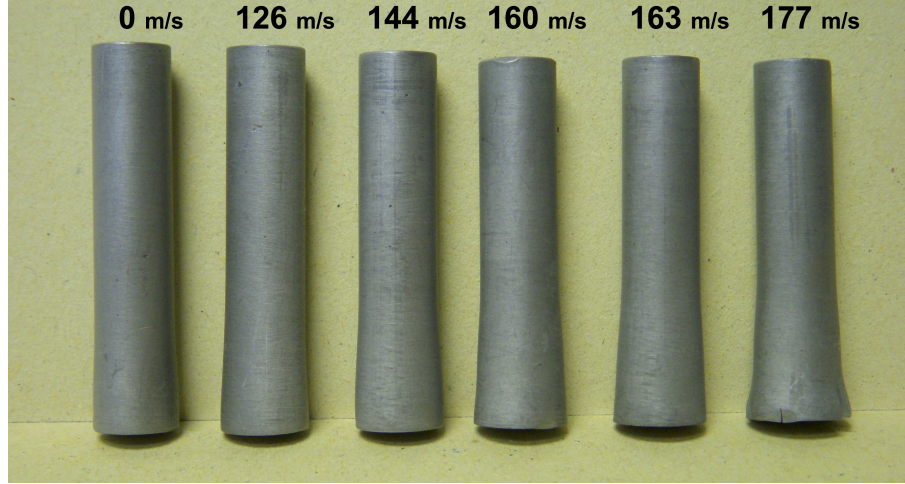


Figure 3.15: Taylor impact specimens from MNML-6. Impact velocities range from 0 m/s (left) to 177.32 m/s (right).

Fig. 3.16) and image processing software (Adobe Photoshop 7.0, Adobe Systems Inc.) was used for measuring the geometry of their deformed and undeformed regions. The undeformed length X and final length L were measured from the images, whereas the initial length L_0 (see Fig. 3.17) was measured using calipers prior to being loaded into the Taylor impact apparatus. Measurements of L were found to differ by less than 0.25 % (average difference of 0.137 %) when compared to measurements of L determined from calipers. This gave confidence in the values obtained for other measurements taken from the high resolution images.

The dynamic yield stress and strain of the epoxy composites can be determined using Hutching's analysis [92], which is an adaptation of the methods developed by Taylor [114] for determining the dynamic strength properties of polymers under Taylor rod-on-anvil impact loading conditions. Whereas Taylor's method was developed for primarily metals in mind and assumed a rigid-plastic behavior, Hutching's approach assumes an elastic-plastic behavior in order to take into account the large elastic strains often observed in polymeric materials.

Following Hutching's methods, the measured geometry and impact velocities are



Figure 3.16: High resolution image of a recovered specimen from material MNML-4 at an impact velocity of 168.97 m/s.

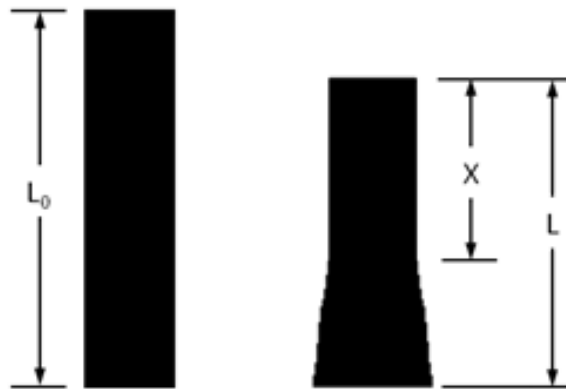


Figure 3.17: Geometry of a cylindrical projectile before and after impact with a rigid anvil.

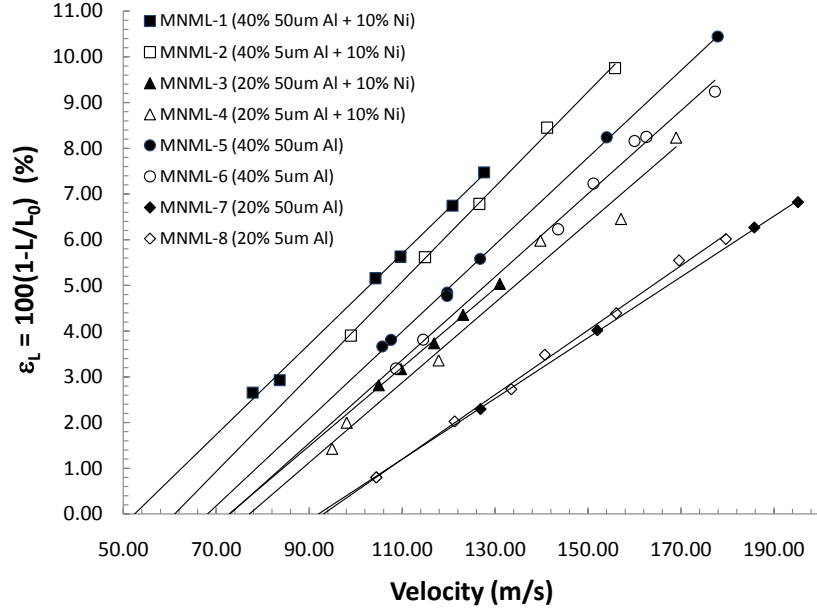


Figure 3.18: Axial plastic strain-impact velocity plot. Critical velocities are based on intercepts of linear-fits ($R^2=0.981-0.999$) with the velocity axis.

used to determine the dynamic yield stress and strain of the epoxy-based composites. This approach has been taken by other researchers investigating the dynamic strength properties of similar composites of epoxy reinforced with aluminum and hematite (Fe_2O_3) particles [115]. Plotting the axial plastic strain ($\varepsilon_L = 1 - L/L_0$) against the impact velocity, a relationship between impact velocity and plastic strain can be obtained and the critical velocity (V_c) determined. The critical velocity for deformation, defined as the minimum impact velocity necessary for producing plastic deformation in a Taylor impact test, is determined by conducting a linear fit of axial plastic strain-velocity data and extrapolating the velocity value for which the axial strain is zero, as shown in Fig. 3.18.

From these values, the dynamic yield stress (Y) and yield strain (ε_y) for each composite are solved iteratively using the following equations:

$$Y = \frac{\rho V_c^2 \bar{C}_p^2}{\varepsilon_y - \varepsilon_y^2} \left(\frac{1}{1 - \varepsilon} - \frac{1 - \bar{C}_p^2}{1 - \varepsilon_y} \right)^2 \quad (22)$$

$$Y = \frac{\rho V_c^2}{\varepsilon_y} (1 - \varepsilon_y) \quad (23)$$

where, ρ is the density, \bar{C}_p the ratio of elastic (C_0) and plastic wave (C_p) speeds given Eq. 24, and ε the strain given by Eq. 25.

$$\bar{C}_p = \frac{C_p}{C_0} = \left(\frac{\varepsilon_y}{1 - \varepsilon} \right)^{1/2} \quad (24)$$

$$\begin{aligned} \varepsilon = & \frac{1}{8\varepsilon_y} \left[(\varepsilon_L^2 - 8\varepsilon_y^2 - 4\varepsilon_L\varepsilon_y)^2 - 16\varepsilon_y (4\varepsilon_y^3 + 4\varepsilon_L\varepsilon_y^2 + \varepsilon_L^2\varepsilon_L - \varepsilon_L^2) \right]^{1/2} + \\ & \frac{1}{8\varepsilon_y} (8\varepsilon_y^2 + 4\varepsilon_L\varepsilon_y - \varepsilon_L^2) \end{aligned} \quad (25)$$

The strain rate of the impact loading event varies from an initially high strain rate that decreases throughout the experiment duration due to the nonconstant stress states. Therefore, the mean strain rate is calculated using the following equation developed by Taylor [114], and also adopted by Hutchings [92]:

$$\dot{\varepsilon} = \frac{V}{2(L_0 - X)} \quad (26)$$

Here, X and L_0 have the same meaning as used in the rest of Hutchings's analysis.

3.4 Thermomechanical Property Characterization

Previous experiments and modeling work investigating the mechanical behavior of epoxy-based composites reinforced with nickel and aluminum particles suggests that there is chemical effect of the particles on the epoxy matrix. To elucidate the particle-matrix interactions due to particle size and loading fractions, thermogravimetric analysis (TGA), dynamic mechanical analysis (DMA), and differential scanning calorimetry (DSC) tests were conducted on each composite (MNML-1 through -8).

3.4.1 Dynamic Mechanical Analysis

Dynamic mechanical analysis (DMA) was used to characterize the viscoelastic behavior of the epoxy-based composites. The analysis uses an oscillating force (stress) applied to the specimen while ramping the temperature through a set temperature range and rate. The advantage of using DMA is to determine change in the dynamic elastic mechanical properties under these oscillatory loads as a function of temperature and measure the strain. Some of the more common viscoelastic properties obtained from this analysis are the storage (E') and loss moduli (E''), and mechanical dampening ($\tan \delta$). The work was performed on a TA Q800 dynamic mechanical analyzer (TA Instruments, Inc.), located at Eglin AFB, at frequencies of 1, 10, and 100 Hz and over a temperature range of 148 K to 373 K. A single cantilever configuration was used with a rectangular prism sample geometry (60 mm x 12.5 mm x 3.2 mm).

Additional work using DMA to characterize the thermomechanical properties of the composites was carried out on a TA Q800 dynamical mechanical analyzer located at Georgia Institute of Technology. However, the behavior of the composites was examined at higher temperatures to determine the possible chemical and mechanical effects of the metal particles on the cross-link density of the epoxy matrix. Whereas the previous DMA experiments used a single cantilever configuration, these experiments were in a tensile configuration. In addition, the tests were conducted at a frequency of 1 Hz and samples were ramped from room temperature to 160 °C at a ramp rate of 5 °C/min. An upper bound temperature of 160 °C was used to ensure the composites were well within the rubbery regime so that the crosslink density could be calculated. The nominal geometry for the samples in this setup were rectangular prisms with a nominal geometry of 25.4 x 4.0 x 1.0 mm. Typical DMA curves for the composites resemble that of the one in Figs. 3.19 and 3.20 obtained using the system at Georgia Institute of Technology.

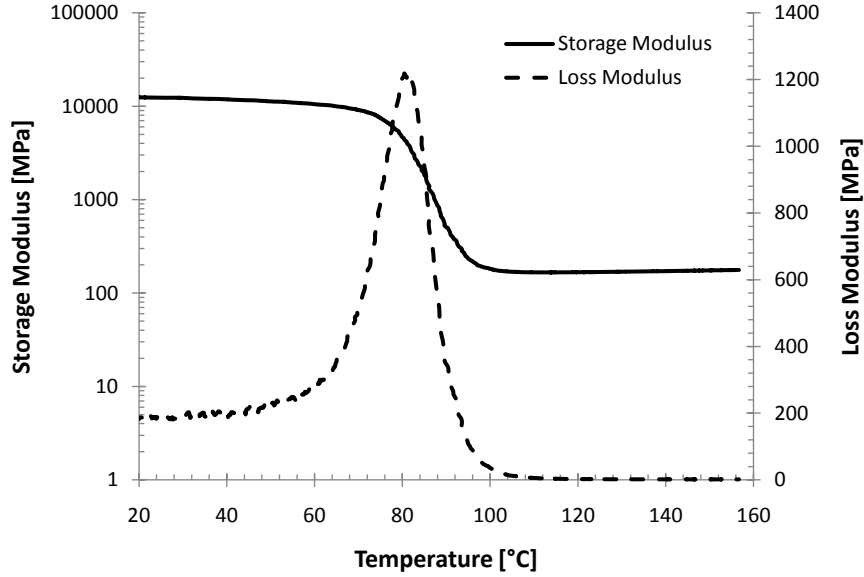


Figure 3.19: Representative DMA curve for the MNML-1 (40% 50 μ m Al + 10% Ni). In the figure the storage modulus and loss modulus are plotted against temperature.

In Fig. 3.19 the storage modulus and loss modulus is plotted against temperature. When the composite goes through a glass transition the storage modulus is observed to decrease by approximately two orders of magnitude. The temperature at which this occurs is known as the glass transition temperature (T_g), and is often found by one of three common methods; 1) by determining the temperature at which $\tan \delta$ is greatest, 2) determining the temperature at which E'' is greatest, or 3) by using a line intercept method to determine the onset and termination of the glass transition and finding the midpoint between these two values on the storage modulus curve. In this research, the glass transition temperature was determined using the first method which has been found to be the most common technique used for analyzing DMA data.

3.4.2 Differential Scanning Calorimetry

A Q100 (TA Instruments) differential scanning calorimeter was used to determine the effects of composite configuration on the glass transition temperature and change

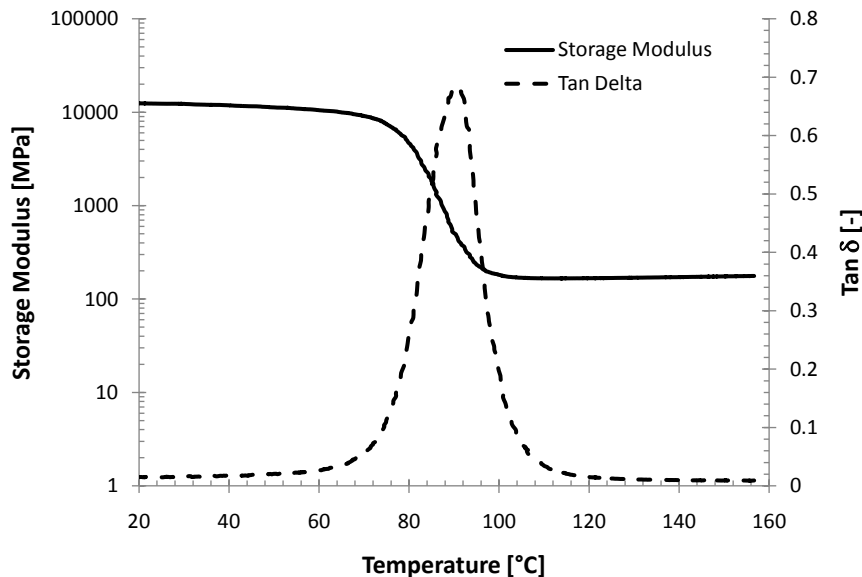


Figure 3.20: Representative DMA curve for the MNML-1 (40% 50 μ m Al + 10% Ni). In the figure the storage modulus and tan- δ are plotted against temperature. Notice how the tan- δ peak is more aligned with the mid-point of the glass transition.

in heat capacity across the glass transition regime. Samples weighing approximately 10 - 15mg were placed in aluminum pans and analyzed with a temperature ramp rate of 10 and 20 °C/min from 25 °C to 150 °C. Tests were conducted in a nitrogen environment with a flow rate of 10 mL/min and the amount of heat flow into the sample was recorded as the temperature increased. The glass transition temperature was then determined using the line intercept method described above for the DMA experimental procedure. TA Instruments analyzing software was used to find the glass transition temperature using this method. A representative DSC curve is shown in Fig. 3.21 with intersecting lines used in the calculations. The change in heat capacity (ΔC_p) across the glass transition was determined by first calculating the heat capacity at $T_g \pm 10^\circ\text{C}$, at $T_g \pm 20^\circ\text{C}$ and at $T = 50$ and 100°C . The values for ΔC_p were then used in interphase thickness calculations discussed later.

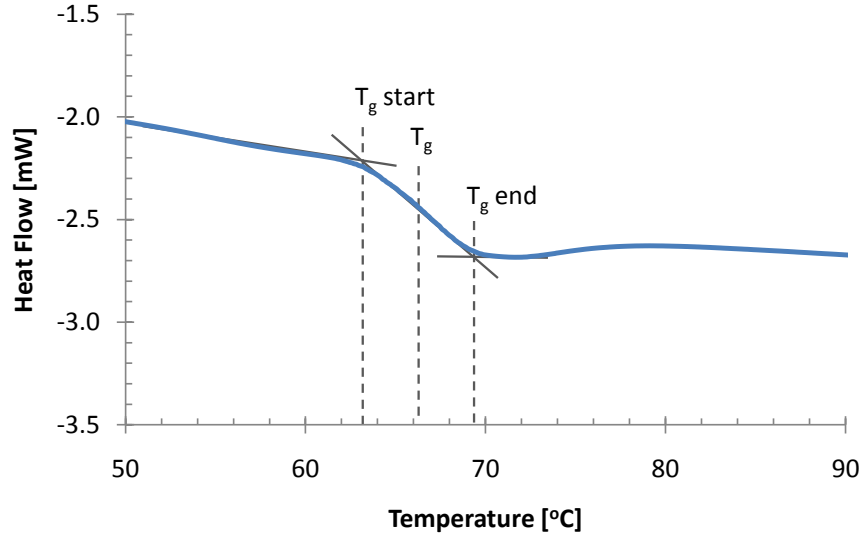


Figure 3.21: In the figure, a representative DSC curve for the MNML-7 is shown along with lines used in a line intercept method for calculating the glass transition temperature.

3.4.3 Thermogravimetric Analysis

The TGA was used to determine the effects of particle size and loading fraction on the decomposition temperature, (T_{decomp}) of the epoxy in the particle reinforced epoxy composites. Tests were carried out using a Q500 (TA Instruments) thermogravimetric analyzer on the composites with a temperature ramp rate of 5 °C/min from room temperature to 600 °C. Initial samples weighed in the range of 12 - 45 mg depending on the amount of particle reinforcement. The remaining weight percentage was recorded as the temperature was increased. The temperature at which 98% of the composite remained was taken as the decomposition temperature. A representative TGA curve for composite MNML-6 is shown in Fig. 3.22. In this curve the weight percent of the initial mass remains constant up to a certain temperature at which point the bonds in the epoxy chain as well as bonds between the particles with the epoxy matrix begin to break down. As the temperature continues to increase more and more of the bonds are broken and the sample begins to lose mass. Eventually

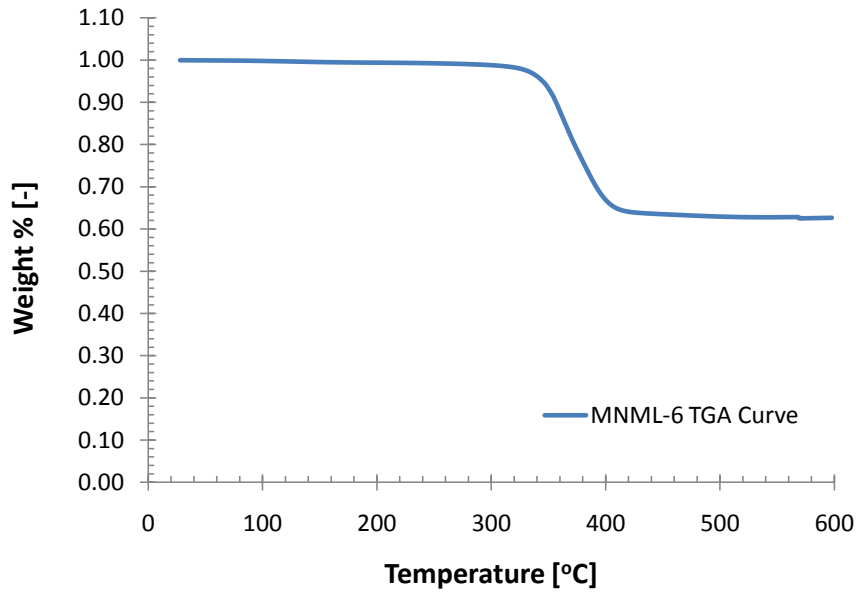


Figure 3.22: In the figure, a representative TGA curve for the MNML-6 is shown. At a temperature around 325 °C the weight % begins to decrease at a high rate of decomposition. At much larger temperature the decomposition slows down until only the aluminum remains along with some charred epoxy residue. The 62 wt.% of material left over is approximately equal to the 40 vol.% of Al used in the casting of this composite.

the rate at which the composite decomposes slows down until a minimal amount of polymer is left at this point, and the weight percent of the remaining composite levels off. This weight percent is representative of the particle material left over with some charred epoxy residue.

CHAPTER IV

EXPERIMENTAL RESULTS AND DISCUSSIONS

This project is focused on understanding the effects of microstructure on the bulk and mesoscale mechanical behavior of particle filled epoxy-cast composites (as an example of structural energetic materials) under compressive loading conditions across a range of strain-rates. Composites of epoxy reinforced with one of two particle sizes of aluminum (nominally 5 or 50 μm) and either 0% or 10% Nickel were produced. In the following sections the microstructures from each composite as well as their mechanical properties and overall mechanical behavior will be discussed.

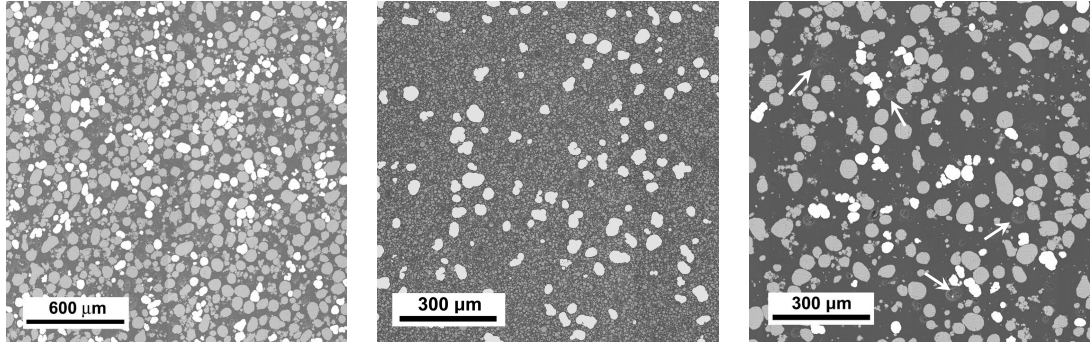
4.1 Microstructure Features and Quantitative Characterization

The composites were prepared according to a factorial design of experiments to modify the microstructure by the changing the volume fractions and size of the introduced nickel and aluminum powders. Due to these variations unique microstructures were produced, that are inherently controlled by each composite's constituent makeup, allowing for the effects of microstructure on the mechanical behavior of the composites to be investigated. Since two different sizes of aluminum were used in this research, there are two different length scales at which many of these composite microstructures have to be examined to properly quantify the microstructure characteristics. In Fig. 4.1 representative microstructures from materials MNML-1 through -8 are shown, revealing the distribution of particles at different length scales. In materials MNML-1 through -4, the two distinct particle phases (Ni and Al) can be seen with the nickel particles being the brighter more globular shaped particles. In each microstructure the grayish-contrast aluminum particle morphology is essentially spherical for both

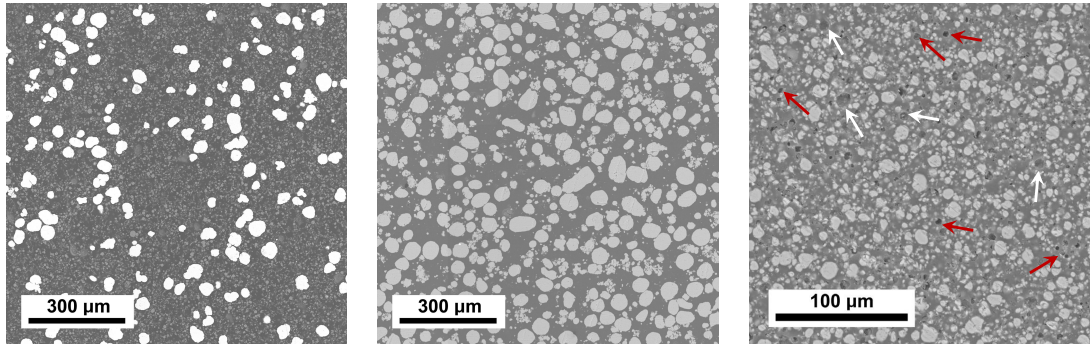
the small and large particles. These images were taken on polished specimens using a scanning electron microscope (SEM) in back scattering mode. Polishing of the composite materials often resulted in particles being “pulled out” of the epoxy matrix. This can be seen more clearly in materials MNML-3, 6, 7, and 8 where outlines of holes are more visible (highlighted by white arrows). While some of these craters may be due to porosity the likelihood of this being the case is low. In clear cases of porosity the craters are very smooth around the perimeter as well as in their interiors. MNML-6 was the only material to have an observable amount of porosity by the presence of small voids visible by the naked eye. However, the measured density for MNML-6 corresponded well with the theoretical max density indicating that the overall porosity is low and voids observed in the micrographs were due to particle pullout. The theoretical maximum density calculated using the rule of mixtures is shown in Table 4.1 along with measured densities. Even though MNML-6 had observable porosity following casting the theoretical maximum density (TMD) was almost 100% the calculated density. This is most likely due to the measured samples having a slightly higher loading fraction of aluminum. The other composites, with the exception of MNML-4, also had TMD values within 1% TMD. In the case of MNML-4, while there was no observable porosity at either the macro or micro scales, it had a fairly low TMD. Considering that the amounts of each constituent were the same as those for MNML-3, and the samples were cast using the same methods, it may be possible that some settling of the particles occurred in this mixture. Since most of the specimens used for density measurements came from the top half of the original casting, settling of the particles (as in MNML-4) can affect the density measurements.

4.1.1 Multi-Scalar Analysis of Area Fractions (MSAAF)

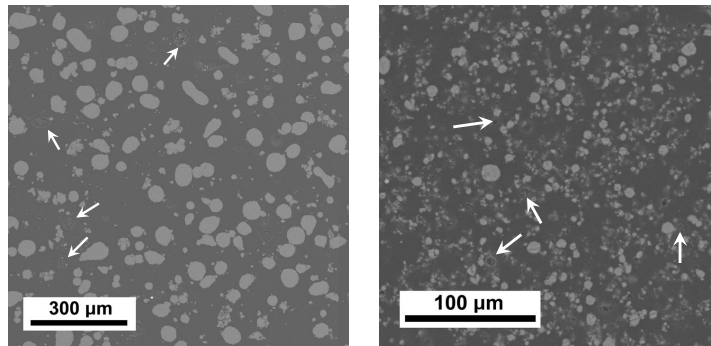
The multi-scale analysis of area fractions (MSAAF) obtains statistical information about the particle area fractions within a material as a function of length scale.



(a) MNML-1 (40% (50 μm) Al, 10% Ni), (b) MNML-2 (40% (5 μm) Al, 10% Ni), (c) MNML-3 (20% (50 μm) Al, 10% Ni)



(d) MNML-4 (20% (5 μm) Al, 10% Ni), (e) MNML-5 (40% (50 μm) Al, 10% Ni), (f) MNML-6 (40% (5 μm) Al, 10% Ni)



(g) MNML-7 (20% (50 μm) Al), (h) MNML-8 (20% (5 μm) Al)

Figure 4.1: Representative SEM microstructure images for each prepared epoxy-based composite. The white arrows in shown in images for MNML-3, 6, 7, and 8 denote examples of where particle pullout has occurred. The red arrow shown in the image for MNML-6 denotes pores/voids within the microstructure.

Table 4.1: Measured and calculated material densities using the rule of mixtures with density values of 2.70 [112], 8.90 [112], and 1.19 g/cm³ [14] for Al, Ni, and Epoxy, respectively.

Material	Theoretical Density (g/cm ³)	Measured Density (g/cm ³)	TMD (%)
MNML-1 (40% 50 μ m Al+10% Ni)	2.565	2.5581	99.73
MNML-2 (40% 5 μ m Al+10% Ni)	2.565	2.5427	99.13
MNML-3 (20% 50 μ m Al+10% Ni)	2.263	2.2465	99.27
MNML-4 (20% 5 μ m Al+10% Ni)	2.263	2.1352	94.35
MNML-5 (40% 50 μ m Al)	1.794	1.7939	99.99
MNML-6 (40% 5 μ m Al)	1.794	1.7939	99.99
MNML-7 (20% 50 μ m Al)	1.492	1.5055	100.90
MNML-8 (20% 5 μ m Al)	1.492	1.4933	100.80

From this technique, developed by Spowart et al. [116], a homogeneous length scale, as well as information about the distribution of particles can be obtained. This analysis essentially looks at the changes in area fractions (A_f) of a phase/phases in the microstructure as a function of sub-regions of length scale, Q . The homogeneous length scale, L_H , is the characteristic length for which the microstructure will exhibit statistically similar properties for all other regions examined at that length scale. Mathematically (L_H) is often defined as the length at which for a given phase/phases of interest the coefficient in variation in the area fraction $(\sigma_{A_f}/A_f) = 0.01$. Meaning the area fraction of particles for the length scale L_H varies by no more than 1.0% from one region to another within the microstructure. This can be more easily seen from a plot (see Fig. 4.2) of (σ_{A_f}/A_f) vs. Q . In this plot, known as an MSAAF plot, a dashed line is drawn to represent a trendline fit to the last three data points. The intersection of the dashed line with the horizontal axis determines the L_H value for the microstructure. This is typical of what is done for microstructures that have a homogeneous length scale larger than the sample image dimensions and/or outside the selected coefficient of variation. The values for this plot come from Eqn. 27.

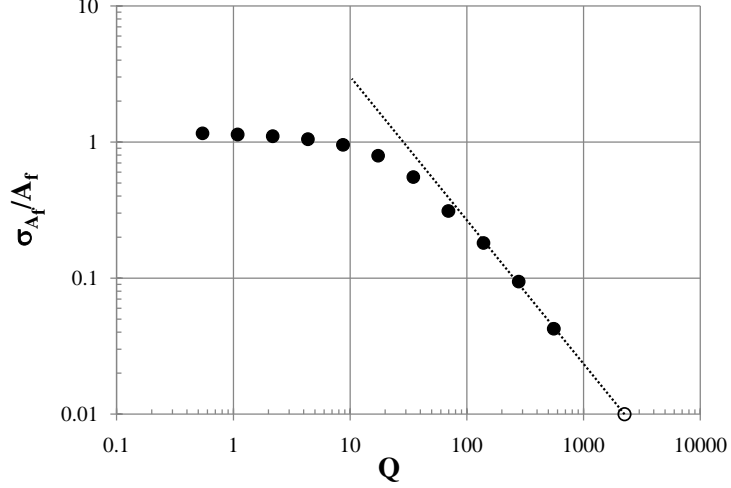


Figure 4.2: Typical MSAAF plot of an isotropic microstructure. The open circle represents the homogeneous length scale based on a 0.01 coefficient of variation and solved for using a trend analysis based on the last three data points.

$$\frac{\sigma_{A_f}}{A_f} = \left(\frac{\pi}{4A_f} \right)^{1/2} \left(\frac{Q}{d_p} \right)^{-1} \quad (27)$$

Here, A_f is the area fraction that the particles of the phase of interest cover, Q is the length of subdivided areas from A_f , and d_p the mean diameter of the particles.

As mentioned earlier information regarding the distribution of particles within the material can also be determined from the MSAAF technique. For microstructures having a random distribution of particles, the linear region of an MSAAF plot has a slope equal to -1.0. Microstructures with a more uniform distribution of particles have a slope less than -1.0 (more negative/steeper) resulting in a shorter L_H . Likewise a microstructure in which the particles are more clustered, the slope is greater than -1.0 (more positive/shallower) resulting in a longer L_H .

The original MSAAF technique was used to determine the isotropic homogeneous length scale (the direction independent value). Since then however, the MSAAF technique has been modified to look at the directional dependency of the homogeneous length scale to determine if the microstructure shows any anisotropy [117]. In this

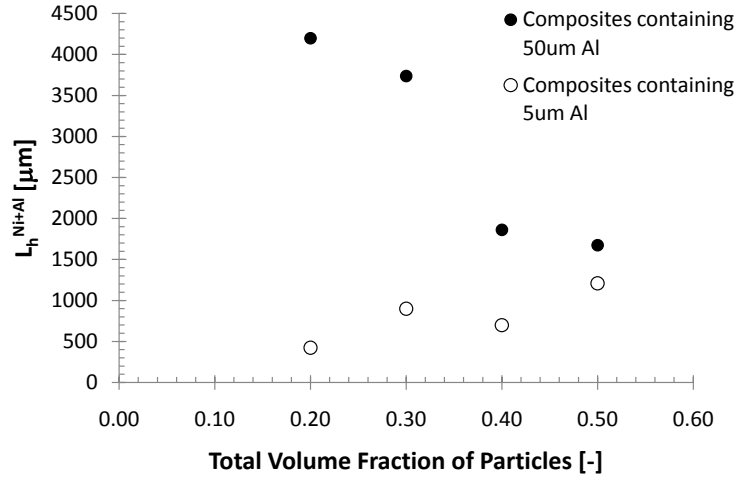


Figure 4.3: Homogeneous length scale for each epoxy-based composite determined by MSAAF. Both the nickel and aluminum particles were considered as belonging to the same phase. L_H was taken for a coefficient of variation (CV) of 0.01.

case the technique was modified to sample the microstructure by varying Q along the vertical and horizontal directions of the microstructure image.

Homogeneous Length Scale of Epoxy-Based Composites: For the composites in this study, the homogeneous length scale representing the length at which the distribution of constituents in the microstructure varies by no more than a certain amount (determined by the coefficient of variation) for different regions in the microstructure sampled at that length scale was determined using the MSAAF technique. As the volume fraction of particles in the composites increased the homogeneous length scale decreased (see Fig. 4.3). This is due to the fewer possible arrangements the particles may have. As the size of the particles increases, there is an increase in the homogeneous length scale. In Fig. 4.3 the homogeneous length scale for each composite is plotted against the total volume fraction of particles. In this plot the nickel and aluminum particles are considered as being the same phase in determining the homogeneous length scale.

Using Eqn. 27, curve fits for homogeneous length scales with different volume fractions (0.00 to 0.60) and sizes of particle diameters (52, 20, and $5.5\mu\text{m}$) (see Fig. 4.4) were generated in order to compare the results with the theory. The diameters 52 and $5.5\mu\text{m}$ correspond to the average particle sizes for aluminum. While the experimental results matched well with the curve generated using $5.5\mu\text{m}$ in which the composites contained smaller aluminum particles, for the composites with the larger aluminum particles the results fell well below the predicted values using Eqn. 27. For these larger particle containing materials a curve generated using a diameter of $20\mu\text{m}$ matched more closely with the experimental results. This may indicate that for real microstructures with large particle size distributions the smaller particles may have a larger effect on the homogeneous length scale. In the case for these composites, the diameters in the lowest 8% percentile of the particle size distribution for the H50 Valimet powder were found to be below $20.0\mu\text{m}$, which would be expected to decrease the homogeneous length scale to an extent. However, the top 8% percentile of the particle size distribution for the H50 Valimet powder ranged from $\approx 75 - 110\mu\text{m}$ signifying smaller particles have a more dramatic effect on the homogeneous length scale of particle reinforced composites. Another possibility for the data not corresponding to what is predicted by MSAAF theory is that the MSAAF technique is based on Poisson statistics with microstructures containing point particles. Since real particles have finite sizes the homogeneous length scales predicted using Eqn. 27 are not expected to match up directly with experimental data. For the composites containing smaller Al particles, as well as an addition of Ni (MNML-2 and MNML-4), there was a slight increase in the homogeneous length scale away from the model curves shown in Fig. 4.4. This is observed as a small increase in L_H at 30 and 50 vol.% total particle loading fraction. This increase is due to the 10 vol.% of nickel reinforcement which has an average, larger, particle diameter of $47\mu\text{m}$.

In Fig. 4.5 the homogeneous length of each composite was determined for the

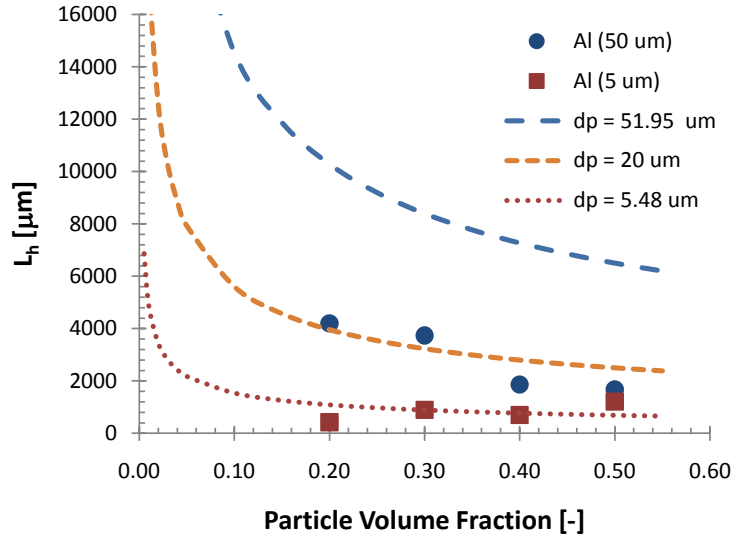


Figure 4.4: Homogeneous length scale predictions for different particle diameters plotted along with the homogeneous length scales of the epoxy-based composites.

aluminum particles where the nickel particles were considered as being part of the epoxy phase. This was done to determine the correlated spatial effects of nickel particles on the distribution of the aluminum particles and the homogeneous length scales. For the composites containing nickel there were much higher homogeneous length scales of the aluminum particles. This was expected since the nickel particles occupy volume that is now inaccessible to the aluminum particles causing a "forced" clustering effect. The nickel particles also had a noticeable effect on the homogeneous length scale of composites of different sizes. For composites with larger aluminum particles (MNML-1 and -3) there were smaller homogeneous length scales. This is due to the nickel and aluminum particles in these composites having comparable diameters disrupting fewer particles. For composite MNML-2 and -4 a much larger number of aluminum particles are displaced with the infiltration of the nickel particles which are less efficient at packing the same amount of material in as small of a space as possible. This causes a much larger effect on the possible arrangements of the smaller aluminum particles increasing their clustering and homogeneous length scale.

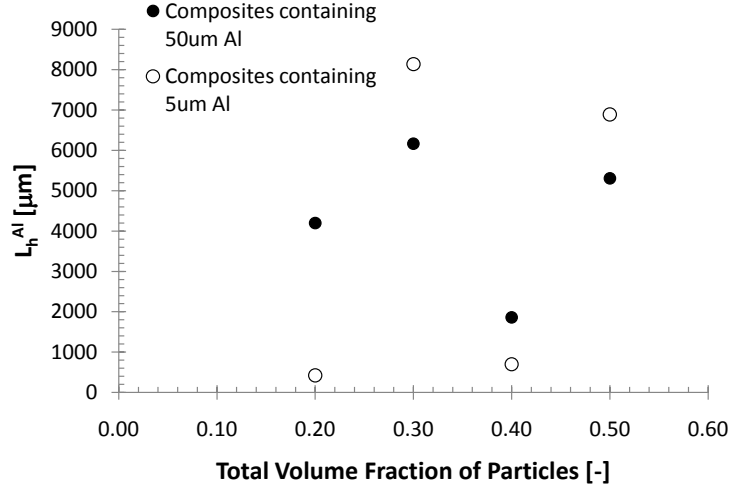


Figure 4.5: Homogeneous length scale of aluminum for each epoxy-based composite determined by MSAAF. The nickel particles were considered as belonging to the epoxy phase. L_H was taken for a coefficient of variation (CV) of 0.01.

The homogeneous length scale of nickel is also affected by the other particles, and possibly by the composite processing techniques. In Fig. 4.6 the homogeneous length scale for the nickel phase is shown as function of total loading fraction of particles in the composite. As the volume fraction of the particles increases, so do the homogeneous length scales of nickel. Also, the composites with smaller aluminum particles have shorter homogeneous length scales. If the spatial distribution of the Ni particles is not correlated with the Al particles then the homogeneous length scales for nickel would be constant. However, as the loading fraction of aluminum increases, more volume is eliminated in which the nickel can occupy, thereby lengthening L_H . This may be an indication of increased clustering at higher amounts of particle loading fraction due the higher difficulty in mixing powder into the epoxy at volume fractions near the “jamming limit” [116].

Table 4.2 lists the homogeneous length scale values for each composite determined for the Al, Ni, and the combination of Ni+Al.

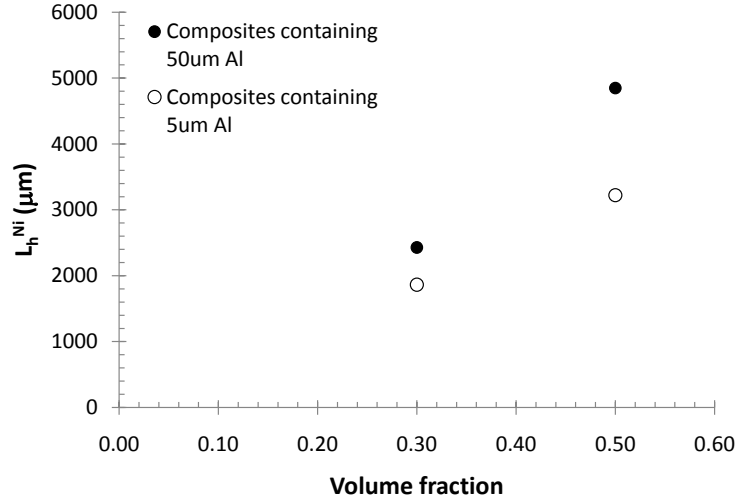


Figure 4.6: Homogeneous length scale of nickel for each epoxy-based composite plotted against the total loading fraction of particle reinforcement. The aluminum particles were considered as belonging to the epoxy phase. L_H was taken for a coefficient of variation (CV) of 0.01.

4.1.2 Nearest Neighbor Distributions

The intermixing of the constituents at the mesoscale is a key mechanism for possible reactions in these composites, which places a prime importance on understanding the distance between particles. In regards to the deformation mechanisms that take place at the mesoscale (particle level), contact interactions are also an important aspect to understand since large stress concentrations are more likely to nucleate localized extreme deformations and microdamage in the surrounding regions. Nearest-neighbor distances between particles can help reveal information about the spatial distribution of particles within the composites. Using Matlab, a program was written to identify the particles from a microstructure image and calculate their centers. The distances between each particle's center and every other particle center was then tabulated and sorted to obtain the first 19 nearest neighbor distances between particles. The average distances for each n^{th} nearest neighbor were then calculated for each composite. The results for the the Al-Al and Ni-Ni nearest neighbor distances (NND) are reported

in Table 4.2 for the first, third, fifth, and tenth nearest neighbor distances alongside the homogeneous length scales determined using the MSAAF technique.

Ni-Ni Nearest Neighbor Distances: The volume fraction of particles had the most impact on the Ni-Ni nearest neighbor distances. For distances between nickel particles in composites MNML-1 through -4 the nearest neighbor distances were smaller for the composites containing only 20% aluminum by approximately 16% for each n^{th} nearest neighbor (see Fig. 4.7). This equates to a 5.2 and 21.1 μ m difference for the first and tenth nearest-neighbor distances respectively. For both volume fractions of aluminum (20 or 40%), the nearest neighbor distances between Ni particles varied very little with changes in Al particle size (see Fig. 4.8 for a plot of nearest neighbor distances for the composites MNML-3 and MNML-4). This is an indication that the nickel is consistently distributed throughout the epoxy matrix for composites containing comparable amounts of aluminum.

Composites with larger Al particles have slightly larger Ni-Ni nearest neighbor distances. After examining the microstructures for composite MNML-1 through -4 that were threshold for the Ni particles only, some regions were observed in which the Ni particles were more clustered for composites MNML-1 and -2. This can be seen in Fig. 4.9 in which the spatial distribution of the Ni is shown for MNML-1 through -4. The increased amount of clustering which causes many of the Ni particles to have shorter nearest neighbor distances, also isolates many particles with much larger nearest neighbor distances. This results in shorter Ni-Ni nearest neighbor distances for lower n^{th} nearest neighbors and longer Ni-Ni nearest neighbor distances for higher n^{th} nearest neighbors. This effect can be seen in Fig. 4.8. The clustering found in the microstructure images was corroborated with MSAAF data. As was discussed earlier the slope of the MSAAF-plot can be used to characterize not only the homogeneous length scale, but also the type of spatial arrangement of the particle phases. In an MSAAF-plot the slope of the linear portion of the curve can be used to determine if the

Table 4.2: Homogeneous length scales for Ni, Al, and Ni+Al calculated for CV=0.01 and the 1st, 3rd, 5th, and 10th nearest-neighbor distance values between Ni-Ni, and Al-Al particles for each composite. L_H values for CV=0.05 were calculated and found to be approximately 20% the homogeneous length scales for CV=0.01.

Material	L_H^X [μm]	L_H^{Ni+Al} [μm]	1_{NND}^{st} [μm]	3_{NND}^{rd} [μm]	5_{NND}^{th} [μm]	10_{NND}^{th} [μm]
L_H^{Ni} , Ni-Ni Distances						
MNML-1 (40% 50 μm Al+10% Ni)	48666	1674	39.3	77.2	105.3	158.7
MNML-2 (40% 5 μm Al+10% Ni)	29812	1208	47.1	78.7	104.4	149.8
MNML-3 (20% 50 μm Al+10% Ni)	14940	3737	38.1	65.8	89.7	134.0
MNML-4 (20% 5 μm Al+10% Ni)	11046	899	37.6	68.3	91.1	132.3
L_H^{Al} , Al-Al Distances						
MNML-1 (40% 50 μm Al+10% Ni)	5305	1674	13.6	23.0	30.1	44.4
MNML-2 (40% 5 μm Al+10% Ni)	6892	1208	2.7	4.2	5.4	7.7
MNML-3 (20% 50 μm Al+10% Ni)	6166	3737	21.9	38.2	51.1	74.8
MNML-4 (20% 5 μm Al+10% Ni)	8138	899	3.1	5.8	7.8	11.6
MNML-5 (40% 50 μm Al)	1861	1861	17.6	27.9	35.8	51.8
MNML-6 (40% 5 μm Al)	699	699	2.9	4.6	5.9	8.4
MNML-7 (20% 50 μm Al)	4198	4198	22.1	38.3	50.6	66.0
MNML-8 (20% 5 μm Al)	424	424	2.8	5.0	6.7	10.0

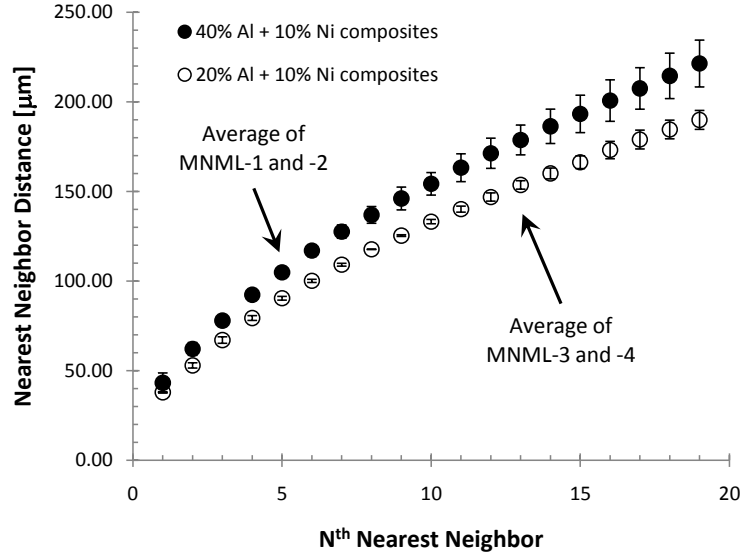


Figure 4.7: Nearest neighbor distances between nickel particles for composites MNML-1 through -4. Values for MNML-1 and -2 were averaged together as were the values for MNML-3 and -4.

particles are clustered (slopes > -1), randomly distributed (slopes $= -1$), or uniformly arranged (slopes < -1). In the case where the slopes are less negative with more clustering, there is an accompanied larger homogeneous length scale. For composites MNML-1 and -3 the slopes in the linear regions (as shown in Fig. 4.10) were found to be -0.68 and -0.80 , respectively, signifying a degree of Ni particle clustering. In composites MNML-2 and -4 the slopes were approximately -1.35 and -1.09 respectively indicating the nickel particles are more randomly/uniformly distributed throughout the epoxy matrix.

Al-Al Nearest Neighbor Distances: At first glance when comparing the Ni-Ni nearest-neighbor results with the Al-Al nearest neighbor distance results shown in Table 4.2, we find that there are shorter nearest neighbor distances for the composites with smaller diameter aluminum particles (see Fig. 4.11). Additionally, as the volume fraction of particles increased, the nearest-neighbor distances decreased. This effect is attributed to how less spread out the particles can be arranged for a finite

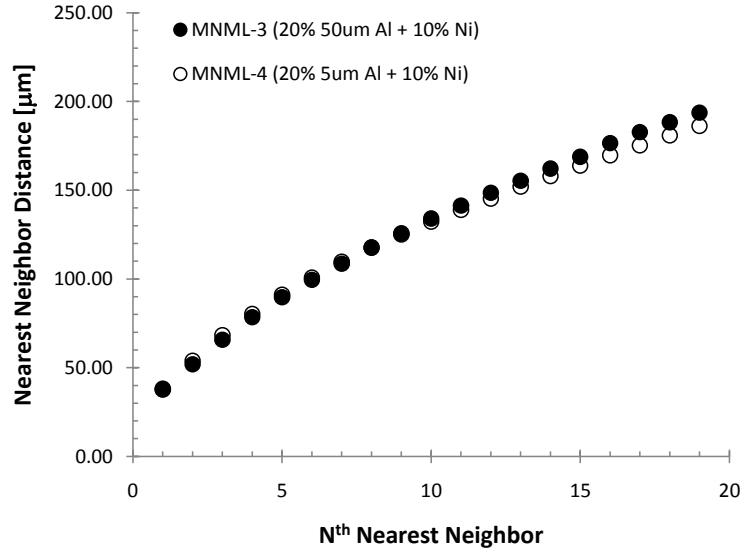
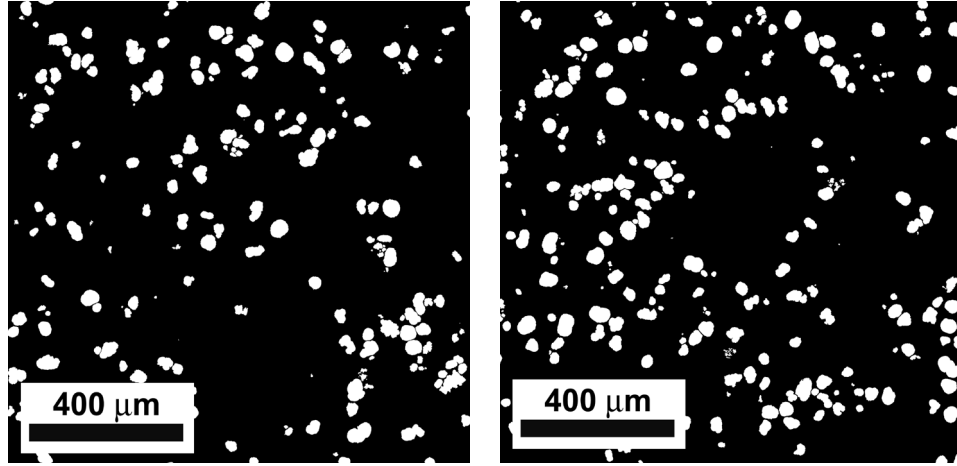
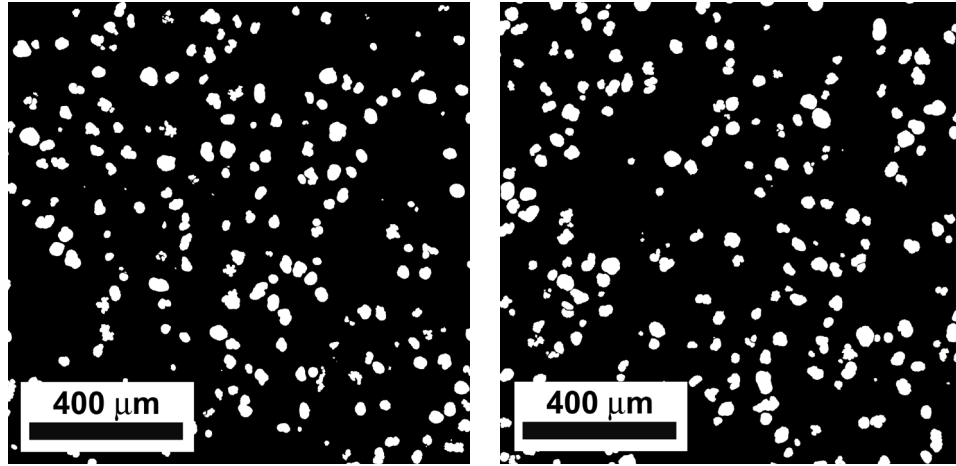


Figure 4.8: Nearest neighbor distances between nickel particles for composites MNML-3 and -4. This plot highlights the nearly identical nearest-neighbor distances between nickel particles for composites containing comparable volume fractions of aluminum.

volume of space. The composites with Ni particles have slightly shorter Al-Al nearest neighbor distances. This is due to the nickel particles “forcing” the aluminum particles to be closer to one another by occupying space that would otherwise be available to the aluminum particles. However, this effect is minimal and surprising since there was a clear effect on the lengthening of L_H for aluminum in these composites due to the enhanced clustering. Since the calculated nearest neighbor distances are an average of distances for over hundreds of particles the Ni particles may only be displacing Al particles by a relatively short amount that is distributed over the rest of the bulk matrix and hence not affecting the average Al-Al nearest neighbor distances. In the case of composites MNML-2 and -4 with small Al particles, even though from a calculation standpoint there are large regions that are free of Al where the Ni resides, there are plenty of particles in the regions away from the Ni particles that are taken into account and no large effects are expected in the Al-Al nearest neighbor

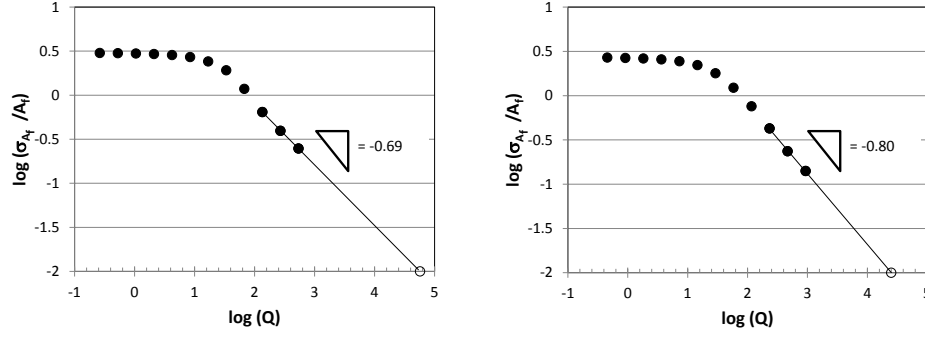


(a) MNML-1 (40% 50μm Al + 10% Ni). (b) MNML-3 (20% 50μm Al + 10% Ni).



(c) MNML-2 (40% 5μm Al + 10% Ni). (d) MNML-4 (20% 5μm Al + 10% Ni).

Figure 4.9: Microstructures for MNML-1 through -4 threshold for Ni particles, highlighting the spatial distribution of particles. In figures (a) and (b) there are regions of increased clustering of particles whereas for (c) and (d) the Ni is distributed more uniformly.



(a) MNML-1 (40% 50 μ m Al + 10% Ni). (b) MNML-3 (20% 50 μ m Al + 10% Ni).

Figure 4.10: Nickel particle MSAAF-plots with indicated slopes for composite MNML-1 (a) and MNML-3 (b). The slopes characterized as being less negative than -1.0 indicates a clustering of the nickel particles.

distances. For the composites MNML-1 and -3 with large Al particles, as was the case for MSAAF calculations, the Ni is only taking up a region that is on the order of the same particle size of the Al which would cause the average Al-Al distance calculations to only slightly be affected. Since the nearest neighbor distances were only taken up to the 19th nearest neighbor, it is possible that more significant distance differences may be observed for higher nearest neighbor distances.

4.1.3 Summary of Homogeneous Length Scales and Nearest Neighbor Distances

The homogeneous length scale calculations using MSAAF revealed composites with 50 μ m Al particles have larger L_H values than those with 5 μ m sized particles. This is consistent with the MSAAF theory; however, for the composite with the larger particles L_H values are smaller than the predicted values from the theory. L_H decreased with increasing particle loading fractions, and Ni had a tendency to increase the homogeneous length scale for the composites with smaller aluminum particles.

There was more clustering of Al in composite containing Ni with large degree of clustering in smaller Al containing composites. This was due to Ni displacing the volume which Al would normally be able to occupy with a larger number of displaced

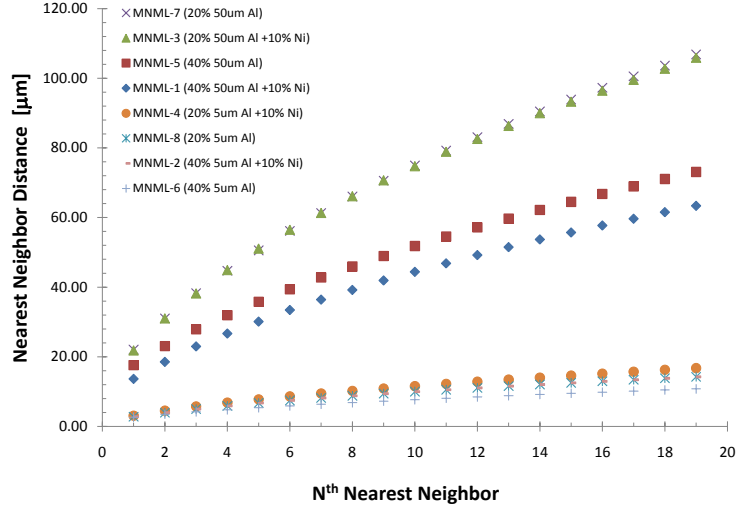


Figure 4.11: Nearest neighbor distances between aluminum particles for each composite.

particles for composites with smaller aluminum particles.

The Ni-Ni particle nearest neighbor distances were very similar for composites within the subsets containing 40% Al + 10% Ni (MNML-1 and -2) and MNML-3 and -4 which contains 20% Al + 10% Ni. Even though the particle size for Al was different for each composite within each subset the nearest neighbor distances were effected primarily by particle volume fraction with larger nearest neighbor distances for composites containing 40% Al. This was attributed to the increased difficulty in mixing the powders in higher volume fractions into the epoxy matrix to evenly distribute the constituents.

The Al-Al particle nearest neighbor distances were shorter for composites containing 5 μ m sized Al particles. This is an artifact of the particles having smaller diameters. Also, as the volume fraction of aluminum increased, the nearest neighbor distances decreased due to less matrix material available for the particles to spread out in a finite volume of space. The introduction of Ni particles forced Al particles to cluster to some degree which was corroborated with MSAAF results. This is because the Ni is displacing material that would normally be occupied by either the epoxy or

Al. However, this was found to have little effect on the average Al-Al nearest neighbor distances and therefore only very slight distance changes were observed. It is possible that if higher n^{th} nearest neighbor distances were calculated larger distances may be found for the composites containing 5 μ m sized aluminum particles.

4.2 Ultrasonic Sound Speed and Elastic Properties

An important method to characterize a material's bulk mechanical response is by measuring the ultrasonic sound speeds to determine the elastic properties of the material. Using the ultrasonic wave speed data and measured sample densities the mechanical properties were evaluated using Eqns. 8 through 13. A summary of the ultrasonic wave speed measurements for each composite and calculated materials properties are given in Tables 4.3 and 4.4.

In general, as the volume fraction of particle reinforcement increases (or as the volume fraction of epoxy decreases) the elastic moduli E , μ and K increase, while λ and ν decrease. This is a result of larger portions of the composite composed of a stiffer material than the epoxy matrix. With the exception of the composites containing 50 vol.% particle loading fractions, where MNML-1 had a Young's modulus 1.5 MPa higher than MNML-2, no noticeable particle size effects on the elastic properties were seen. This may indicate that particle size may not have large effects on the elastic properties, for the range of particle sizes employed in the present work. The elastic properties obtained from these ultrasonic sound speed measurements will be used as the baseline for comparison with those obtained from compressive loading conditions. Also, to determine if values are reasonable, elastic bounding theories are used to determine the effective elastic property values and compare the results from those obtained from ultrasonic sound speed measurements.

Table 4.3: Summary of ultrasonic sound speed measurements for each epoxy-based composites. ^a Epoxy property values are taken from averages in [3].

Material	C_l [mm/ μ s]	C_T [mm/ μ s]	C_0 [mm/ μ s]	Density (gcm ³)
MNML-1 (40% 50 μ m Al+10% Ni)	2.952 \pm 0.013	1.520 \pm 0.008	2.374 \pm 0.014	2.558
MNML-2 (40% 5 μ m Al+10% Ni)	2.886 \pm 0.009	1.442 \pm 0.005	2.357 \pm 0.010	2.543
MNML-3 (20% 50 μ m Al+10% Ni)	2.447 \pm 0.007	1.175 \pm 0.009	2.036 \pm 0.008	2.247
MNML-4 (20% 5 μ m Al+10% Ni)	2.521 \pm 0.005	1.235 \pm 0.004	2.079 \pm 0.005	2.135
MNML-5 (40% 50 μ m Al)	3.033 \pm 0.010	1.518 \pm 0.018	2.475 \pm 0.023	1.794
MNML-6 (40% 5 μ m Al)	3.002 \pm 0.009	1.534 \pm 0.007	2.424 \pm 0.015	1.794
MNML-7 (20% 50 μ m Al)	2.757 \pm 0.005	1.342 \pm 0.014	2.280 \pm 0.017	1.506
MNML-8 (20% 5 μ m Al)	2.740 \pm 0.002	1.273 \pm 0.005	2.313 \pm 0.004	1.493
<i>Epoxy</i> ^a	2.905 \pm 0.449	1.186 \pm 0.268	2.561 \pm 0.343	1.190

Table 4.4: Summary of isotropic elastic properties calculated from ultrasonic sound speed measurements for each epoxy-based composites. Errors are the reported standard deviations. ^a Epoxy property values are taken from averages in [3].

Material	μ [GPa]	λ [GPa]	E [GPa]	K [GPa]	ν [-]
MNML-1 (40% 50 μ m Al+10% Ni)	5.912 \pm 0.074	10.471 \pm 0.137	15.602 \pm 0.179	14.412 \pm 0.148	0.320 \pm 0.002
MNML-2 (40% 5 μ m Al+10% Ni)	5.291 \pm 0.037	10.594 \pm 0.137	14.110 \pm 0.089	14.121 \pm 0.121	0.333 \pm 0.002
MNML-3 (20% 50 μ m Al+10% Ni)	3.102 \pm 0.043	7.245 \pm 0.095	8.377 \pm 0.103	9.313 \pm 0.081	0.350 \pm 0.003
MNML-4 (20% 5 μ m Al+10% Ni)	3.160 \pm 0.014	6.845 \pm 0.047	8.482 \pm 0.033	8.952 \pm 0.045	0.342 \pm 0.001
MNML-5 (40% 50 μ m Al)	4.132 \pm 0.094	8.235 \pm 0.276	11.016 \pm 0.202	10.990 \pm 0.221	0.333 \pm 0.006
MNML-6 (40% 5 μ m Al)	4.221 \pm 0.039	7.726 \pm 0.153	11.171 \pm 0.081	10.540 \pm 0.136	0.323 \pm 0.003
MNML-7 (20% 50 μ m Al)	2.711 \pm 0.072	6.018 \pm 0.126	7.290 \pm 0.168	7.825 \pm 0.081	0.345 \pm 0.005
MNML-8 (20% 5 μ m Al)	2.419 \pm 0.017	6.376 \pm 0.042	6.591 \pm 0.040	7.988 \pm 0.032	0.362 \pm 0.001
<i>Epoxy</i> ^a	1.724 \pm 0.759	6.764 \pm 1.589	4.815 \pm 2.065	7.912 \pm 2.094	0.401 \pm 0.018

4.2.1 Voigt-Reuss Upper and Lower Bounds for Effective Elastic Properties

Many sets of bounding equations have been derived to predict the isotropic elastic properties of composite materials. The most simple bounding method available for determining the effective elastic property of a composite material is given by the Voigt-Reuss bounds [118, 119], which takes into account the volume fraction of the composite constituents. For a particular property of interest the value is bound by the following relation:

$$\left\langle \frac{1}{X} \right\rangle^{-1} \leq X_e \leq \langle X \rangle \quad (28)$$

where $\langle 1/X \rangle^{-1}$ and $\langle X \rangle$ are the harmonic and arithmetic averages respectively of the composite constituents' property of interest, and X and X_e the effective property values for the composite. The harmonic and arithmetic averages are defined by Eqns. 29 and 30 respectively:

$$\left\langle \frac{1}{X} \right\rangle^{-1} = \sum_{i=1}^N \frac{\phi_i}{X_i} \quad (29)$$

$$\langle X \rangle = \sum_{i=1}^N \phi_i X_i \quad (30)$$

where ϕ_i is the volume fraction of a constituent phase, and N is the number of phases in the composite.

The Voigt-Reuss bounds are often referred to as the rule of mixtures, or one-point bounds since they rely on knowledge of one-point statistics, (such as volume fraction, where ϕ_i , is equivalent to the probability of finding phase i located at a point randomly placed in a composite). Using these bounding equations and the Young's modulus values obtained from literature for the constituents the effective elastic properties of the two-phase (Ni + epoxy) and (Al + epoxy) systems were determined. These results are shown in Fig. 4.12.

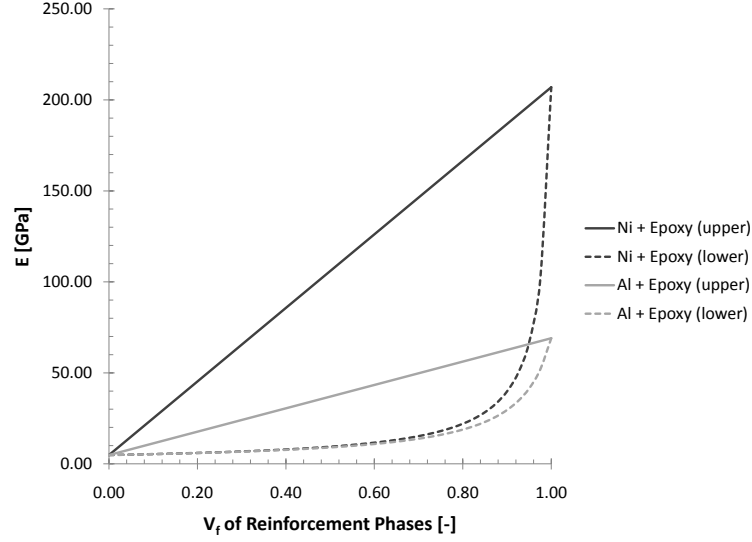


Figure 4.12: Results for the Voigt-Reuss bounds applied to the Ni+Epoxy and Al+Epoxy systems.

Right away we can begin to see, the effects that highly contrasting material properties of the constituents, can have on the bounds of the composite mixture. The Ni+epoxy system has a much wider bounds then the Al+epoxy system, which is attributed to nickel having a much higher elastic modulus. These wide bounds are typical of bounds based on the volume fractions of the individual phases. We can also see that the lower bound of the elastic modulus deviates very little from the modulus of pure epoxy until higher volume fractions ($\simeq 0.50$ - 0.60) of metal reinforcement is reached. This behavior in the plot is typical in which the lower-bound is dominated by the material phase with the lowest value of the property of interest, in this case the elastic modulus of epoxy. In contrast, the upper-bound is dominated by the material phase with the largest value of the property of interest and its volume fraction. While so far only the application of the Voigt-Reuss bounds to a two-phase system have been shown, many of the composites in this work are three-phased materials. The results of Voigt-Reuss bounds for both two and three phased materials (MNML-1 through MNML-8) in this work are shown in Fig. 4.13. Since, the Voigt-Reuss bounds only

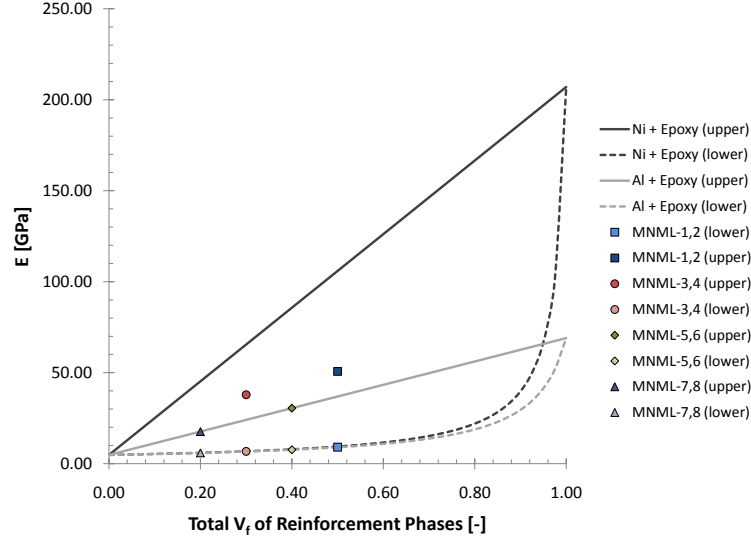


Figure 4.13: Results for the Voigt-Reuss bounds applied to the Ni+Epoxy, Al+Epoxy, and Al+Ni+Epoxy systems. Results obtained from calculations using the rule of mixtures model.

take into account the volume fraction and property value of the individual phases and not the particle sizes many of the bounds are identical for the different materials. This is a major drawback to one-point bounding equations, in not being able to take into account the microstructure. Again, in each case the lower-bound of the each composite is dominated by the epoxy phase with values lying on the Al + epoxy line for MNML-5 through MNML-8 or slightly deviating ($< 0.75\%$) from the Al + epoxy line for the equal amounts of total volume fraction of reinforcement for MNML-1 through MNML-4. This indicates that the elastic modulus of aluminum is contrasting enough in comparison to nickel, to control much of the lower-bound behavior for these types of composites. The elastic properties for MNML-1 through MNML-8 and the parameters used in the Voigt-Reuss calculations are shown in Table 4.5.

4.2.2 Hashin-Shtrikman Upper and Lower Bounds for Effective Elastic Properties

Since the Voigt-Reuss bounds have a tendency to give a wider range in terms of bounds for a given elastic property, other models have also been investigated. One

Table 4.5: Elastic properties determined from the Voigt-Reuss bounding Eqns. 29 and 30. **Bulk modulus values for Al and Ni are calculated from their other elastic properties.

Material	E $\frac{upper}{lower}$ [GPa]	G $\frac{upper}{lower}$ [GPa]	K $\frac{upper}{lower}$ [GPa]	ν $\frac{upper}{lower}$ [-]
Epoxy [3]	4.81	1.72	7.91	0.40
Aluminum [120]	69.00	26.00	66.44**	0.33
Nickel [120]	207.00	76.00	249.71**	0.31
MNML-1	$\frac{50.705}{9.072}$	$\frac{18.866}{3.253}$	$\frac{55.504}{14.361}$	$\frac{0.363}{0.357}$
MNML-2	$\frac{50.705}{9.072}$	$\frac{18.866}{3.253}$	$\frac{55.504}{14.361}$	$\frac{0.363}{0.357}$
MNML-3	$\frac{37.867}{6.715}$	$\frac{14.004}{2.404}$	$\frac{43.797}{10.881}$	$\frac{0.377}{0.373}$
MNML-4	$\frac{37.867}{6.715}$	$\frac{14.004}{2.404}$	$\frac{43.797}{10.881}$	$\frac{0.377}{0.373}$
MNML-5	$\frac{30.486}{7.661}$	$\frac{11.432}{2.746}$	$\frac{31.324}{12.214}$	$\frac{0.372}{0.369}$
MNML-6	$\frac{30.486}{7.661}$	$\frac{11.432}{2.746}$	$\frac{31.324}{12.214}$	$\frac{0.372}{0.369}$
MNML-7	$\frac{17.648}{5.910}$	$\frac{6.576}{2.115}$	$\frac{19.617}{9.602}$	$\frac{0.386}{0.384}$
MNML-8	$\frac{17.648}{5.910}$	$\frac{6.576}{2.115}$	$\frac{19.617}{9.602}$	$\frac{0.386}{0.384}$

of these is the Hashin-Shtrikman [1] model which like the Voigt-Reuss bounds uses the volume fractions of the constituents. However, the Hashin-Shtrikman bounds are based on variational principles to linear elasticity theory in order to determine the effective elastic moduli of multiphase composites irrespective of their geometry. These bounds are typically much tighter than the Voigt-Reuss bounds but still have the same drawbacks with being sensitive to large stiffness differences between phases and does not explicitly address the influence of particle size and microstructure.

The Hashin-Shtrikman bounds for the effective bulk (K^*) and shear (μ^*) moduli are found using the following equations [1]:

$$K_1^* = K_1 + \frac{A_1}{1 - \frac{3}{3K_1 + 4\mu_1}A_1} \quad (31)$$

$$K_2^* = K_n + \frac{A_n}{1 - \frac{3}{3K_n + 4\mu_n}A_n} \quad (32)$$

$$A_1 = \sum_{i=2}^{i=n} \frac{\phi_i}{\frac{1}{K_i - K_1} - \frac{3}{3K_1 + 4\mu_1}} \quad (33)$$

$$A_n = \sum_{i=1}^{i=n-1} \frac{\phi_i}{\frac{1}{K_i - K_n} - \frac{3}{3K_n + 4\mu_n}} \quad (34)$$

$$K_1^* < K^* < K_n^* \quad (35)$$

$$\mu_1^* = \mu_1 - \frac{1}{2} \frac{B}{1 - \frac{3(K_1 + 2\mu_1)}{5\mu(3K_1 + 4\mu_1)} B_1} \quad (36)$$

$$\mu_2^* = \mu_n - \frac{1}{2} \frac{B_n}{1 - \frac{3(K_n + 2\mu_n)}{5\mu(3K_n + 4\mu_n)} B_n} \quad (37)$$

$$B_1 = \sum_{i=2}^{i=n} \frac{\phi_i}{\frac{1}{2(\mu_i - \mu_1)} - \frac{3(K_1 + 2\mu_1)}{5\mu(3K_1 + 4\mu_1)}} \quad (38)$$

$$B_n = \sum_{i=2}^{i=n} \frac{\phi_i}{\frac{1}{2(\mu_i - \mu_n)} - \frac{3(K_n + 2\mu_n)}{5\mu(3K_n + 4\mu_n)}} \quad (39)$$

$$\mu_1^* < \mu^* < \mu_n^* \quad (40)$$

where, K_i through K_n , and μ_i through μ_n are the bulk and shear moduli of the composite constituents from least to highest in value, respectively, and ϕ_i is the volume fraction. Once the upper and lower bounds for K^* and μ^* have been found the isotropic elastic modulus and Poisson's ratio is determined using:

$$E_{1,2}^* = \frac{9K_{1,2}^*}{1 + 3 \frac{K_{1,2}^*}{\mu_{1,2}^*}} \quad (41)$$

$$\nu_{1,2}^* = \frac{3K_{1,2}^* - 2\mu_{1,2}^*}{6K_{1,2}^* + 2\mu_{1,2}^*} \quad (42)$$

Table 4.6: Effective elastic properties for the epoxy-based composites, calculated using the Hashin-Shtrikman bounds with the constituent property values in Table 4.5.

Material	E^*_{*1} [MPa]	E^*_{*2} [MPa]	K^*_{*1} [MPa]	K^*_{*2} [MPa]	μ^*_{*1} [MPa]	μ^*_{*2} [MPa]
MNML-1 (40% 50 μ m Al + 10% Ni)	12.98	40.16	15.82	36.68	4.76	15.24
MNML-2 (40% 5 μ m Al + 10% Ni)	12.98	40.16	15.82	36.68	4.76	15.24
MNML-3 (20% 50 μ m Al + 10% Ni)	8.62	27.51	11.61	25.50	3.13	10.42
MNML-4 (20% 5 μ m Al + 10% Ni)	8.62	27.51	11.61	25.50	3.13	10.42
MNML-5 (40% 50 μ m)	10.29	22.07	13.18	20.74	3.76	8.34
MNML-6 (40% 5 μ m)	10.29	22.07	13.18	20.74	3.76	8.34
MNML-7 (20% 50 μ m)	6.99	12.66	10.00	13.49	2.53	4.71
MNML-8 (20% 5 μ m)	6.99	12.66	10.00	13.49	2.53	4.71

Results of the Hashin-Shtrikman bounds applied to each composite in this work, are shown in Table 4.6. The results have also been plotted against the Hashin-Shtrikman and rule of mixture curves for the epoxy/aluminum composites in Fig. 4.14. It can be seen that in comparison to the rule of mixtures, the Hashin-Shtrikman curves are found to be much tighter. The lower bounds of the composites containing nickel are predicted to have moduli values approximately equal to the lower bound of the epoxy/aluminum curves. This is due to the lower bound properties being dominated by the properties of the constituent with the lowest moduli values.

Elastic modulus results obtained from ultrasound tests were compared to the predicted values from the Hashin-Shtrikman Bounds (see Fig. 4.15). Each composite was verified to be within the Hashin-Shtrikman bounds, and in each case the measured composite elastic moduli is found to lie near the lower bound of the Hashin-Shtrikman curve. This type of correlation occurs when the mechanical behavior of the composites is dominated by the response of the lower stiffness constituents. In the composites studied in this research, the contiguous phase is the epoxy matrix which would act as the primary stress transferring component of the composites.

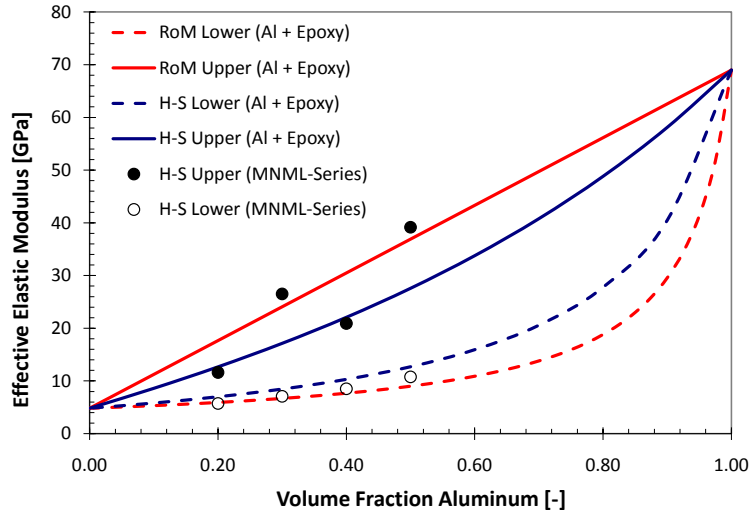


Figure 4.14: Hashin-Shtrikman upper and lower bounds for the MNML-series epoxy-based composites plotted along side the rule of mixtures and Hashin-Shtrikman curves for the two-component system of epoxy and aluminum.

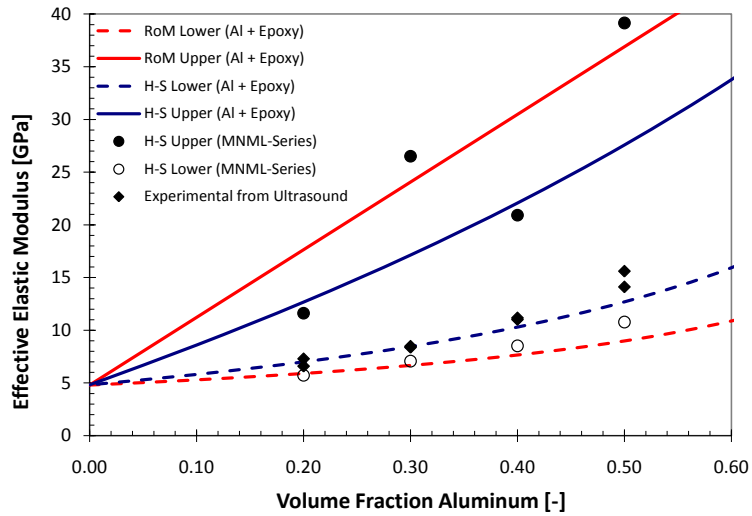


Figure 4.15: Comparison of the elastic modulus from ultrasound test to the Hashin-Shtrikman upper and lower bounds for the MNML-series epoxy-based composites. Plotted in the same figure are the rule of mixtures and Hashin-Shtrikman curves for the two-component system of epoxy and aluminum.

4.2.3 Summary of Ultrasound and Hashin-Shtrikman Bounds

The Hashin-Shtrikman bounds were tighter than those of the Voigt-Reuss bounds. Comparison between elastic properties determined from ultrasound experiments with values calculated using Hashin-Shtrikman analysis showed the composite properties to lie near the lower bound values. This is an indication of the mechanical behavior of the composite being dominated by the contiguous less stiff epoxy.

4.3 *Uniaxial Stress Quasi-Static Compression Test Results*

An understanding of the mechanical behavior of particle filled composites (used as structural energetic materials) across a wide range of strain rates is necessary to determine the effects of drops or mechanical insults on safety. This is especially true since epoxy (a main component to the composites in this study) has been shown to have rate dependent properties [2]. Therefore, quasi-static compression experiments were carried out at nominal strain rates of 10^{-4} and 10^{-3} s^{-1} . Each composite was subjected to uniaxial compression, and the mechanical properties were determined using the procedure outlined previously in Chapter 3. Tables 4.7 and 4.8 list the averages with standard deviations for peak stress, peak strain, Young's modulus, and strain-rate, for each composite system. In the following sections the stress-strain behavior, and trends observed in the mechanical properties at these quasi-static strain rates will be discussed.

Stress-Strain Behavior at Quasi-Static Strain Rates: The stress-strain curves for each composite tested at a strain rate of 10^{-4} s^{-1} are shown in Figs. 4.16 and 4.17. The amount of particle reinforcement in the epoxy was found to have a dramatic effect on the stress-strain behavior. As the volume fraction of reinforcement increased, the Young's modulus and peak stress increased as well as the amount of strain hardening. Also, at lower volume fractions of particle reinforcement a much higher degree of strain softening can be observed, which becomes less pronounced at higher loading fractions

Table 4.7: Mechanical properties for epoxy-based composites compressed at $\dot{\epsilon} = 10^{-4} s^{-1}$.

Material	σ_y [MPa]	ϵ_y [-]	E [GPa]	$\dot{\epsilon}$ ($\times 10^{-5}$) [s^{-1}]
MNML-1	88.60 ± 1.43	0.0275 ± 0.0015	10.31 ± 1.45	8.9 ± 0.4
MNML-2	94.58 ± 2.71	0.0273 ± 0.0004	13.08 ± 1.73	9.0 ± 0.3
MNML-3	85.60 ± 4.46	0.0308 ± 0.0024	7.41 ± 0.35	9.1 ± 0.4
MNML-4	85.99 ± 0.62	0.0270 ± 0.0003	7.09 ± 0.16	9.1 ± 0.3
MNML-5	82.55 ± 2.24	0.0278 ± 0.0004	8.98 ± 0.91	9.3 ± 0.4
MNML-6	92.04 ± 0.83	0.0295 ± 0.0002	8.64 ± 0.30	9.1 ± 0.4
MNML-7	83.38 ± 1.38	0.0314 ± 0.0017	5.97 ± 0.24	9.2 ± 0.3
MNML-8	85.60 ± 1.11	0.0274 ± 0.0017	6.55 ± 0.22	9.5 ± 0.5

Table 4.8: Mechanical properties for epoxy-based composites compressed at $\dot{\epsilon} = 10^{-3} s^{-1}$.

Material	σ_y [MPa]	ϵ_y [-]	E [GPa]	$\dot{\epsilon}$ ($\times 10^{-4}$) [s^{-1}]
MNML-1	100.12 ± 4.38	0.0337 ± 0.0047	11.28 ± 1.33	7.24 ± 0.12
MNML-2	103.66 ± 2.03	0.0338 ± 0.0015	12.44 ± 0.54	7.50 ± 0.04
MNML-3	92.26 ± 3.06	0.0343 ± 0.0020	6.99 ± 0.76	7.86 ± 0.04
MNML-4	98.60 ± 2.46	0.0314 ± 0.0014	7.36 ± 0.83	7.86 ± 0.04
MNML-5	94.45 ± 2.74	0.0318 ± 0.0042	8.69 ± 1.22	7.92 ± 0.03
MNML-6	100.05 ± 3.40	0.0330 ± 0.0025	10.03 ± 1.00	7.84 ± 0.05
MNML-7	97.52 ± 0.57	0.0400 ± 0.0014	5.73 ± 0.36	7.65 ± 0.03
MNML-8	99.24 ± 3.46	0.0343 ± 0.0024	6.47 ± 0.26	7.74 ± 0.05

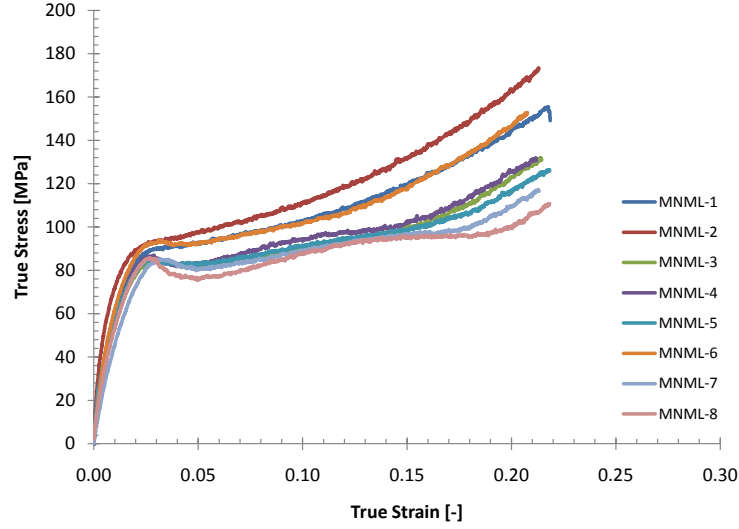


Figure 4.16: σ - ε curves for quasi-static compression tests at a strain rate of $10^{-4} s^{-1}$.

of particles. The same effects of particle loading fraction were also observed for tests conducted at strain rates of $10^{-3} s^{-1}$ as shown in Figs. 4.18 and 4.19.

Representative stress-strain curves for each of the two strain rates were plotted with one another for each composite system as shown in Figs. 4.20 and 4.21. The stress-strain response was found to have nearly identical forms for each composite at both strain rates with a few exceptions. The behavior in the elastic regime almost follows the same path, however, at higher strain rates the elastic regime is extended towards higher stresses and strains. This results in a shift of the viscoelastic- viscoplastic transition towards higher strains (and stress). The peak stress for higher strain rates also occurs at higher stresses and strains. Following the onset of yield at peak stress the stress-strain behavior of each composite has nearly the same profile as the strain rate increases with higher strain rate curves having higher flow stresses.

4.3.1 Young's Modulus at Quasi-Static Rates of Strain

Earlier it was mentioned that as the amount of total particle reinforcement increases the Young's modulus (E) increases as well. This effect can be seen in the plot of the

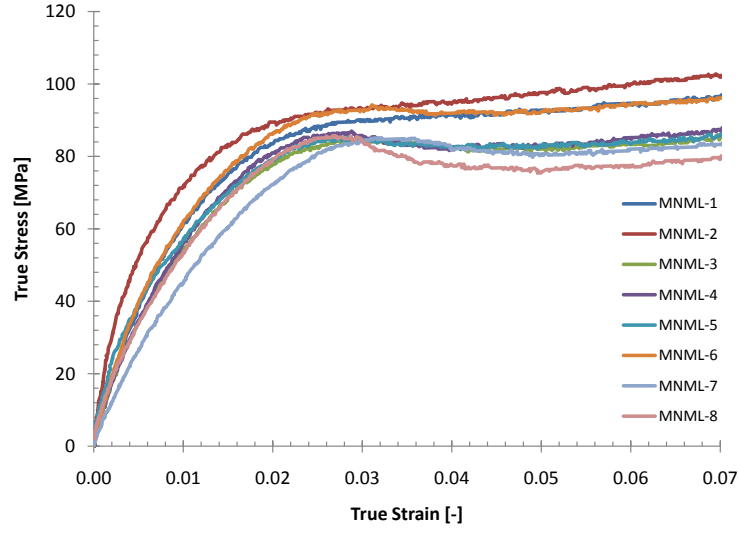


Figure 4.17: σ - ε curve plot rescaled to show the mechanical behavior in the elastic and viscoelastic-viscoplastic transition regimes at strain rates of 10^{-4} s^{-1} .

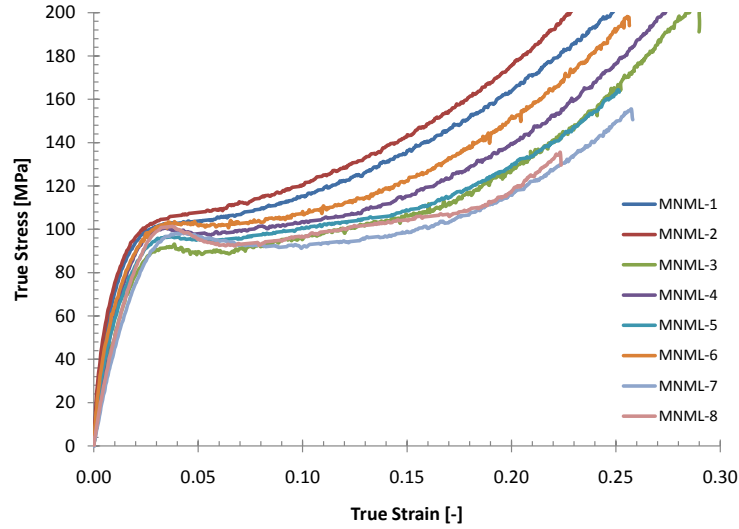


Figure 4.18: σ - ε curves for quasi-static compression tests at a strain rate of 10^{-3} s^{-1} .

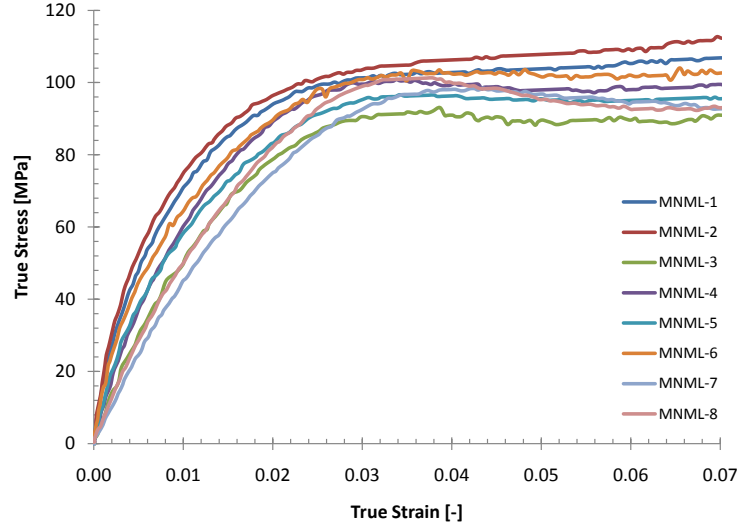
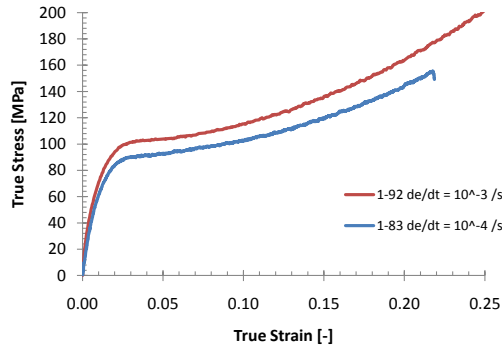
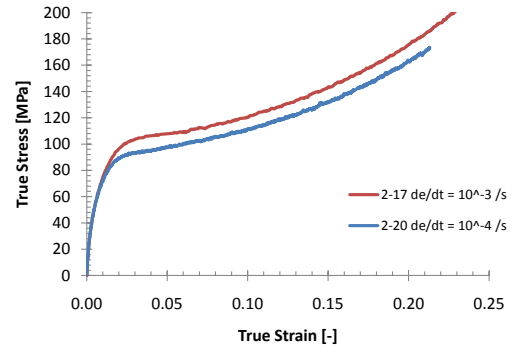


Figure 4.19: σ - ε curve plot rescaled to show the mechanical behavior in the elastic and viscoelastic-viscoplastic transition regimes at strain rates of 10^{-3} s^{-1} .

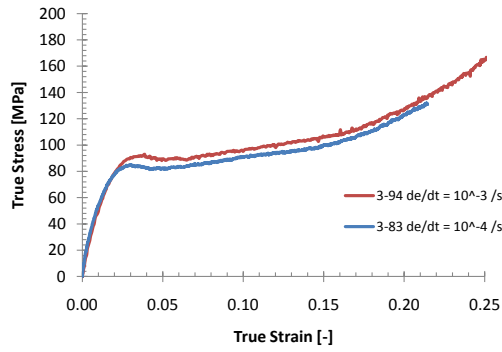
Young's modulus vs. particle reinforcement (Fig. 4.22). This increase is due to the replacement of a lower modulus material with a stiffer material. Particle size also has an effect on the Young's modulus with increases of 7.1% and 11.0% for $d\varepsilon/dt = 10^{-4}$ and 10^{-3} s^{-1} respectively. With the use of smaller aluminum particles ($5\mu\text{m}$ vs. $50\mu\text{m}$) the Young's modulus increases. This may be due to a more uniform spatial distribution of particles in the epoxy matrix that results in a more uniform distribution of stresses in the material while under load. In this strain rate regime on average, the Young's modulus decreased with an increase in strain rate. However, for each composite, the values for each strain rate were within the experimental scatter of one another. In comparison to the composite's Young's modulus values calculated from ultrasound speed measurements, their values are on average 15% smaller, which is not unexpected. The quasi-static determined values are lower due to the complex loading states that can cause particle-matrix debonding or other types of microdamage that decrease the efficiency of stress transfer between the constituents at the mesoscale, lowering the Young's modulus.



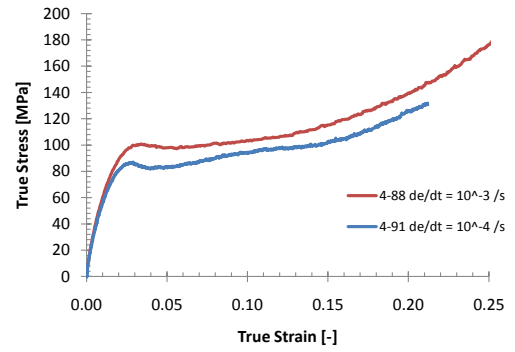
(a) MNML-1 (40% (50 μm) Al, 10% Ni)



(b) MNML-2 (40% (5 μm) Al, 10% Ni)

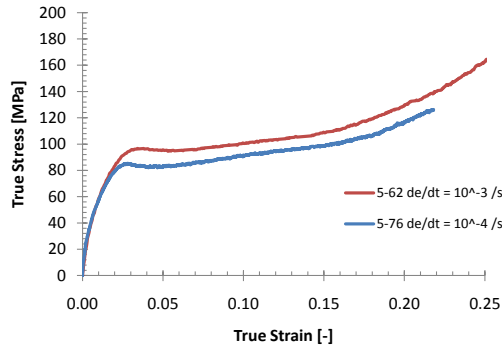


(c) MNML-3 (20% (50 μm) Al, 10% Ni)

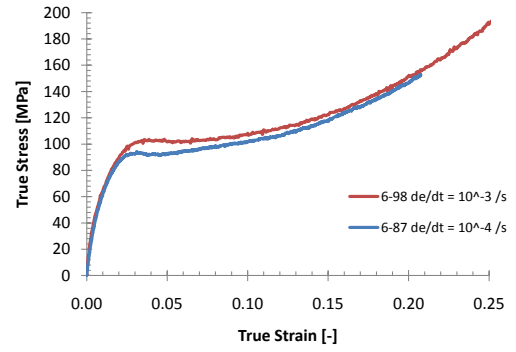


(d) MNML-4 (20% (5 μm) Al, 10% Ni)

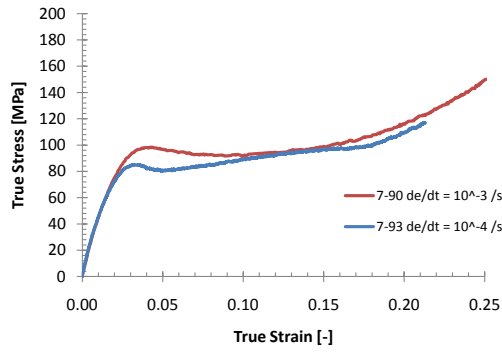
Figure 4.20: Quasi-static compression σ - ϵ curves for each composite. (CONTINUED IN NEXT FIGURE)



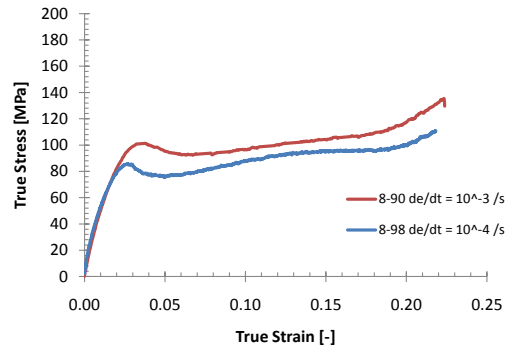
(a) MNML-5 (40% (50 μm) Al)



(b) MNML-6 (40% (5 μm) Al)



(c) MNML-7 (20% (50 μm) Al)



(d) MNML-8 (20% (5 μm) Al)

Figure 4.21: Quasi-static compression σ - ε curves for each composite.

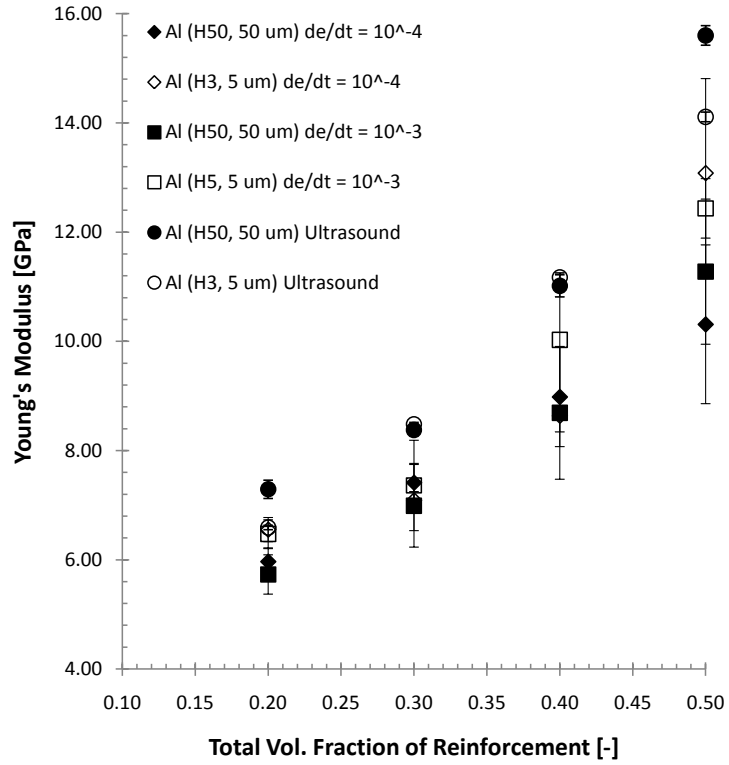


Figure 4.22: A plot of Young's modulus vs. total volume fraction of particle reinforcement for quasi-static compression experiments. Young's modulus values calculated from ultrasound speed measurements are shown for reference. The error bars shown are from standard deviation calculations.

4.3.2 Peak Stress and Peak Strain at Quasi-Static Rates of Strain

The peak stress was found to be more affected by strain rate and particle size, than the observed effect on Young's modulus. As shown in the plot of peak stress vs. volume fraction in Fig. 4.23, with an increase in strain rate a dramatic increase in the peak stress values, as much as 17.0%, is observed. Also, with a decrease in the particle size of aluminum, the peak stress increases on average by 4.9% and as much as 11.5% for a given volume fraction of reinforcement. The increase in peak stress with strain rate may be attributed to a longer relaxation time and energies needed for the polymer matrix to relax due to a decreased mobility of the polymer chains. The increase in peak stress with decreased particle size again may be related to a more uniform distribution of particles within the epoxy matrix. Many studies have shown that particles can alter the surrounding matrix material, and may therefore, alter the relaxation mechanisms to produce a strengthening effect. When the particles are smaller, there is a more uniform distribution of altered epoxy regions, which when present in a high enough concentration can decrease the percolating network of unaffected matrix regions. This causes the bulk relaxation times of the matrix material to increase, making it more difficult for the polymers to rearrange on the local level and increase the amount of energy needed to do so. Hence, the peak stress increases with the use of smaller particles.

The peak strains plotted against the total volume fraction of reinforcement can be seen in Fig 4.24. The peak strain values are found to decrease with increasing particle loading fractions for the composites containing large aluminum particles, where as the composites containing smaller particles have fairly similar peak strains with increasing loading fraction. For the composites with larger aluminum particles the distribution of particles is less uniform than for composites with smaller particles. This causes stress and strain concentrations to build up in the microstructure under load, leading to an earlier onset of yielding in the composite. At higher concentrations of particles,

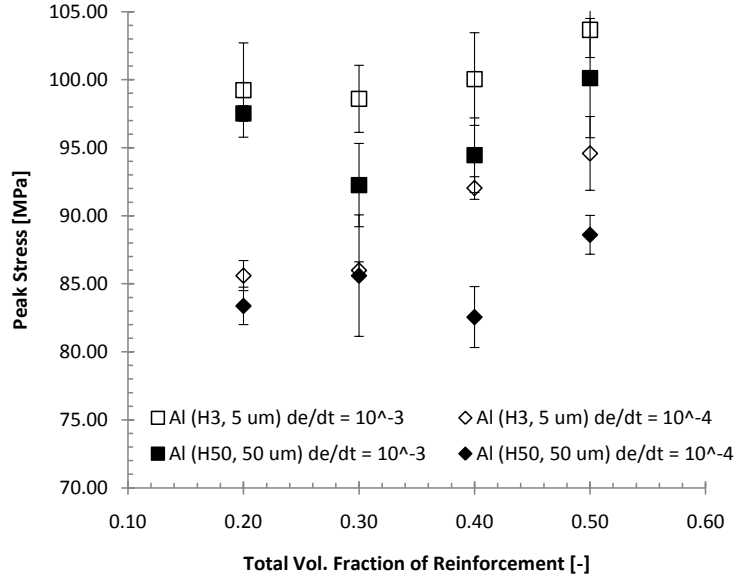


Figure 4.23: A plot of the peak stress vs. total volume fraction of particle reinforcement. The error bars shown are from standard deviation calculations and the peak stresses are calculated from a quadratic fit of the viscoelastic-viscoplastic transition.

this effect is more pronounced due to the presence of more particles in the system. Following the same argument for the composites with smaller particles there should also be a decrease in peak strain with an increase in loading fraction; however, this effect is not noticeable. This may be explained by particle arrangement having a lesser effect on the peak strain than particle size alone until a critical particle concentration is obtained at higher loading fractions. At lower volume fractions of reinforcement the peak strain is lower for composites with smaller aluminum particles. This is due to the tendency of composites with smaller particle reinforcements to have larger Young's moduli that allow higher stresses for a given strain to develop. When a critical stress level is reached there is sufficient energy for polymer chain rearrangement to occur. The peak strains are also affected by strain rate with higher strain rates resulting in a lower peak strain.

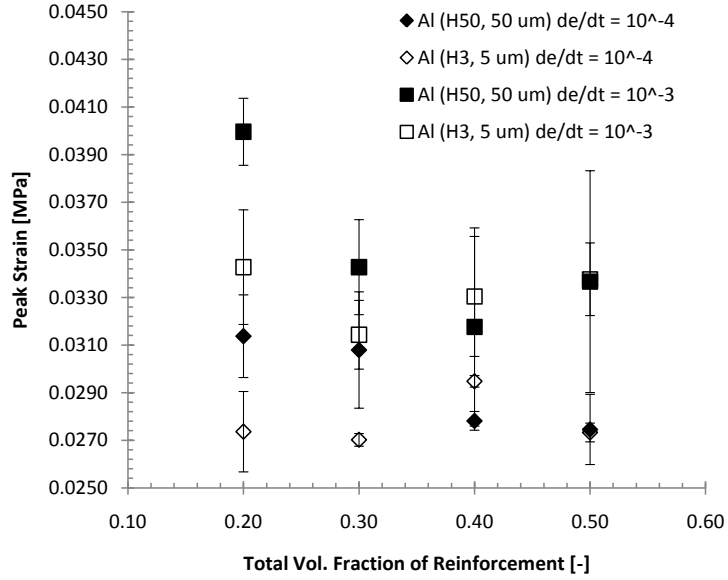


Figure 4.24: A plot of the peak strains vs. total volume fraction of particle reinforcement. The error bars shown are from standard deviation calculations and the peak strains are calculated from a quadratic fit of the viscoelastic-viscoplastic transition.

4.3.3 Recovery Strain

The amounts of total strain undergone by the composites while under load were determined from virtual strain gage data using the equations discussed in section 3.3.2. However, when the test is complete, all loads are taken off the sample and a portion of the elastically stored strain is recovered. This amount of recovered strain is dependent on both the composition of the composite and the strain history. Therefore, quasi-static tests were terminated at different degrees of strain. To determine the amount of recovered strain, each sample's dimensions were measured following testing. The measured length was converted into a plastic strain value which was then subtracted from the strain measured by the virtual strain gages. This was then divided by the amount of total strain sustained during compression to obtain the percent recovered strain value.

Figure 4.25 shows the recovered strain plotted against the true strain measured

from the virtual strain gages. It can be seen that the amount of recoverable strain decreases with the amount of true strain sustained during compression. At higher strains more plastic deformation occurs and an increased amount of damaged regions containing defects are created. This limits the amount of strain recovery possible.

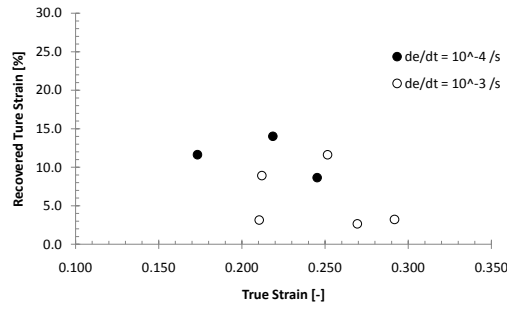
The amount of strain recovered is also dependent on the volume fraction of particle reinforcement. For higher loading fractions of particles the amount of strain recovery decreases. This effect can be more clearly observed in Fig. 4.26 with the results shown for the composites containing smaller aluminum particles (MNML-2, -4, -6, and -8).

The size of the aluminum particles was also found to have an effect on the amount of strain recovery. When smaller particles were present the amount of variability in the data decreased. Also, in comparison to the amount of strain recovery between MNML-1 with -2 and MNML-5 with -6, the amount of strain recovered was larger for the composites with smaller particles (see Fig. 4.27). Both of these effects may be due to the smaller amounts of strain and stress localization that occurs within the material under loads due to the more uniform distribution of particles in the matrix. This decreases the amount of damage that accumulates with strain.

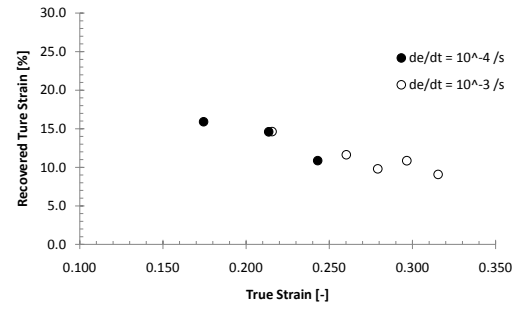
4.3.4 Damage Accumulation at Quasi-Static Rates of Strain

The methods of damage formation in particle reinforced composites leading to the decrease in the composites ability to recover strain with increased total strains, include fracture of the particle reinforcement, void nucleation and growth in the epoxy matrix, and microcracks forming due to decohesion at the particle-matrix interface. The amount of damage D due to straining is often quantified by relating the evolution of material properties such as Young's modulus and density to their original values through the following relations [121]:

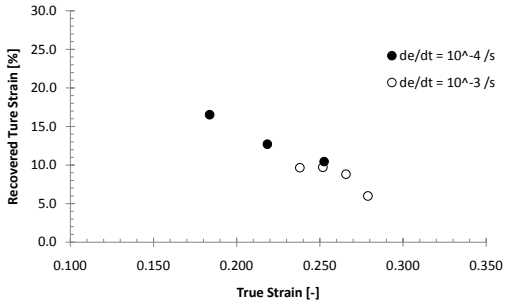
$$D_E = 1 - \frac{E}{E_0} \quad (43)$$



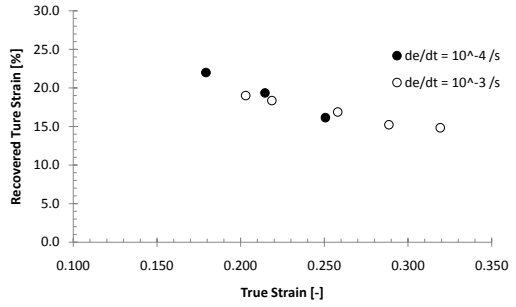
(a) MNML-1 (40% (50 μ m) Al, 10% Ni)



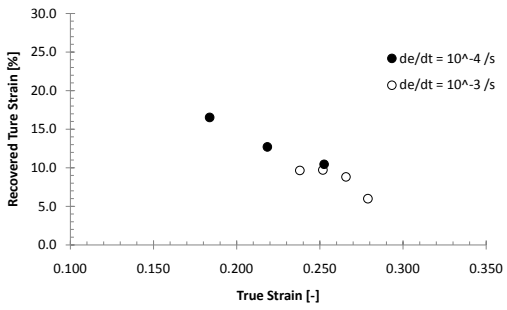
(b) MNML-2 (40% (5 μ m) Al, 10% Ni)



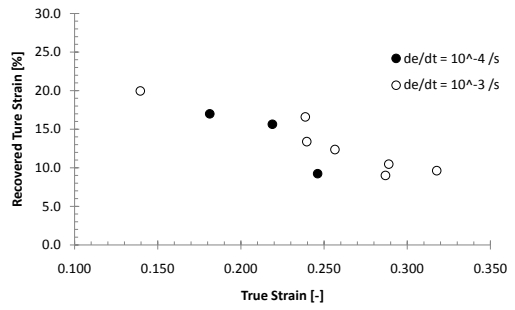
(c) MNML-3 (20% (50 μ m) Al, 10% Ni)



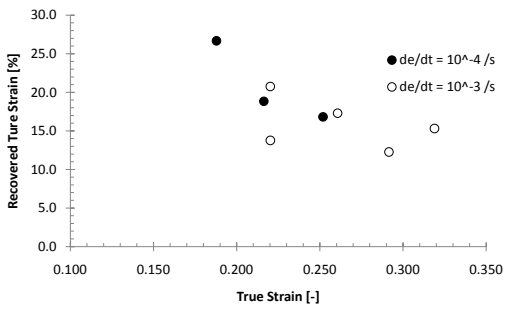
(d) MNML-4 (20% (5 μ m) Al, 10% Ni)



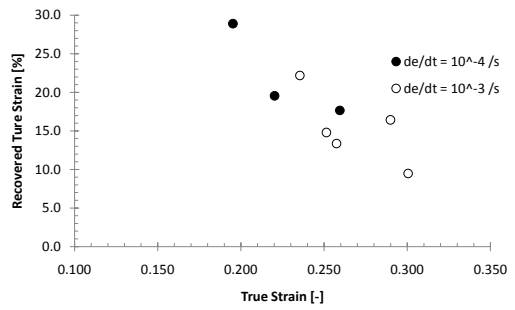
(e) MNML-5 (40% (50 μ m) Al)



(f) MNML-6 (40% (5 μ m) Al)



(g) MNML-7 (20% (50 μ m) Al)



(h) MNML-8 (20% (5 μ m) Al)

Figure 4.25: Amount of strain recovered in samples following quasi-static compression tests.

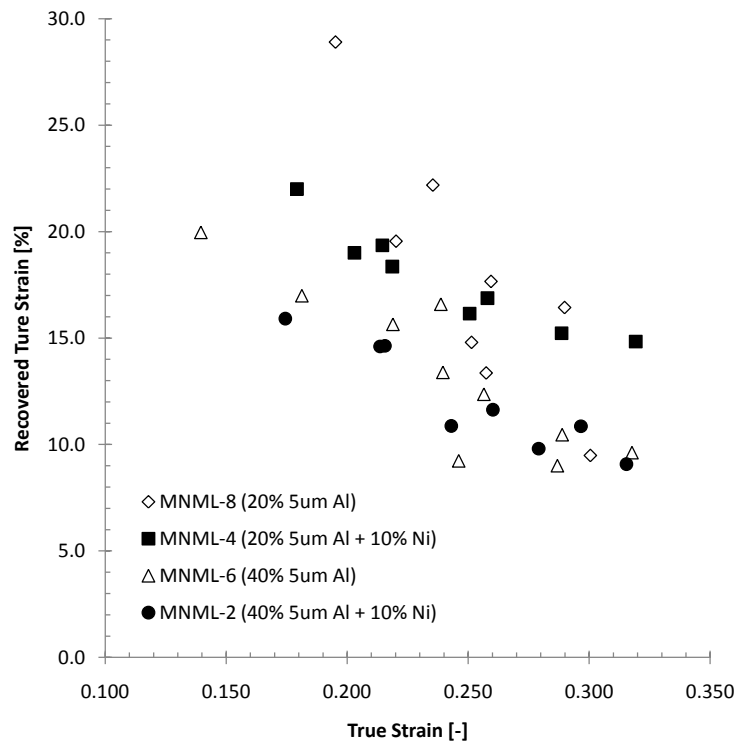
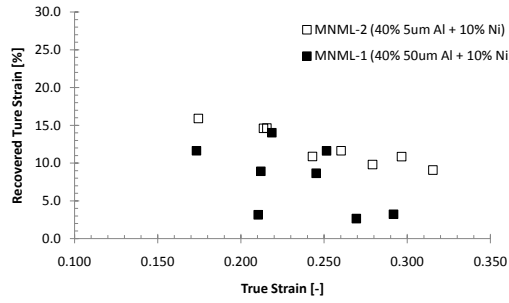
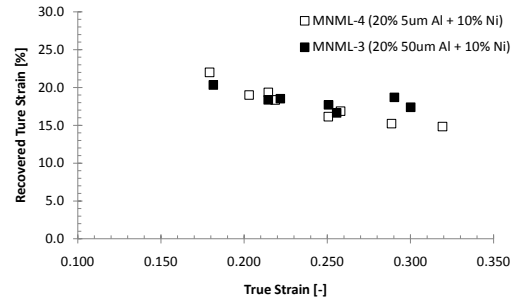


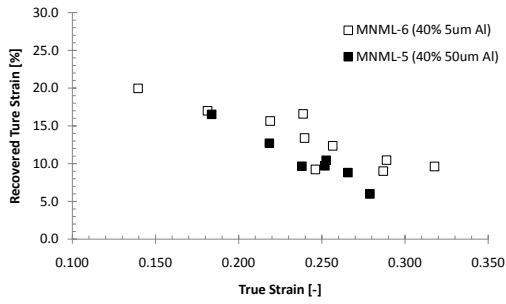
Figure 4.26: Recovered true strain as a function of plastic strain. for composites with different particles and volume fraction.



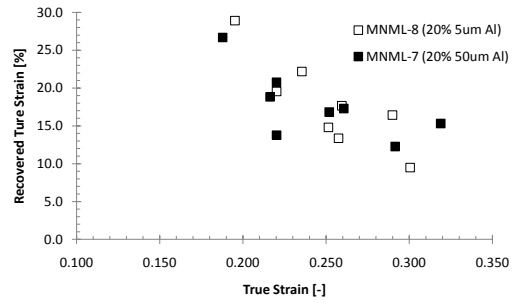
(a) Recovery strain as a function of true strain for MNML-1 and -2.



(b) Recovery strain as a function of true strain for MNML-3 and -4.



(c) Recovery strain as a function of true strain for MNML-5 and -6.



(d) Recovery strain as a function of true strain for MNML-7 and -8.

Figure 4.27: Comparison of recovery strains between composites with a change in Al particle size.

$$D_\rho = 1 - \frac{\rho}{\rho_0} \quad (44)$$

where E and ρ are the Young's modulus and density at a given level of strain, and E_0 and ρ_0 their initial values. Kouzeli et al. [121] showed a one-to-two orders of magnitude difference between the two damage parameters, with D_E being larger than D_ρ for particle reinforced aluminum composites. This was also similar to results found by Xu et al. [122] studying alumina fiber reinforced magnesium alloys. They also found the amount of accumulated damage depended on the particle size with higher amounts of damage for a given strain occurring in composites with larger sized particles. They observed this trend with two types of particle (Al_2O_3 and B_4C) reinforced aluminum systems. Both of these studies [121, 122] also developed relationships relating D_E with D_ρ . While D_E has been related to that amount of broken particles, D_ρ has been more attributed to the total accumulated damage due to matrix plasticity such as particle-matrix decohesion, and void nucleation.

For polymer bonded explosives based on β -HMX the damage mechanisms are found to be strain rate dependent [123]. At quasi-static strain rates the damage is found to be primarily interfacial debonding between the energetic crystals and polymer matrix. At higher rates of strain the fracture of the crystals becomes more prevalent.

Although the aluminum [121, 122] and β -HMX [123] matrix composites contain particles that are more brittle than the matrix, the same analysis is applied to the composites in this research, in which the matrix is more brittle than the particles. The accumulated damage as a function of the plastic deformation was therefore calculated for each composite using Equation 44. Final density measurements were obtained for samples following compression using Archimedes' principle. Qualitatively, the rate of damage accumulation was found to depend largely on the total volume fraction of the particles, and particle size. There was also a heavy influence of nickel content on the

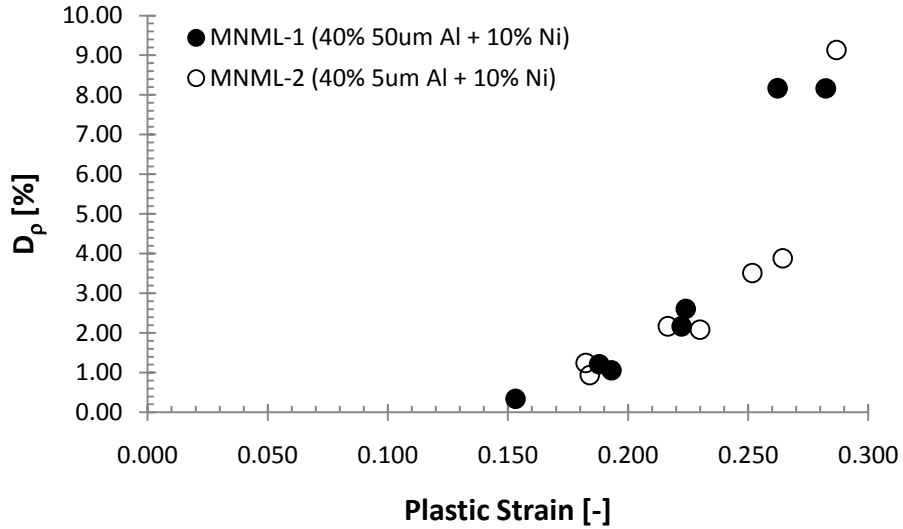


Figure 4.28: Damage-plastic strain plot for MNML-1 and -2.

rate of damage accumulation. Examining first the effects of particle size, composites containing smaller aluminum particles had decreased amounts of damage with plastic strain as shown in Figs. 4.28 to 4.31, which is consistent with results discussed of Kouzeli et al. [121]. Plastic strain measurements were taken by measuring the final specimen geometry following the completion of compression tests and strain recovery. The decreased amount of accumulated damage for composites containing smaller particles is related to the spatial distribution of particles. With the use of smaller diameter particles there is a uniform distribution of particles in the epoxy matrix, which decreases the strain and stress localizations that can lead to the damage micromechanisms such as particle-matrix decohesion. This trend was observed for each two-composite subset that differed only in aluminum particle size in the present work, with the exception of the MNML-7/MNML-8 subset which had large variations in the calculated damage values.

At lower amounts of particle reinforcement there is a greater amount of matrix material present between each particle. This would lead to lower amounts of triaxial stresses in the matrix decreasing the amounts of accumulated damage such as matrix

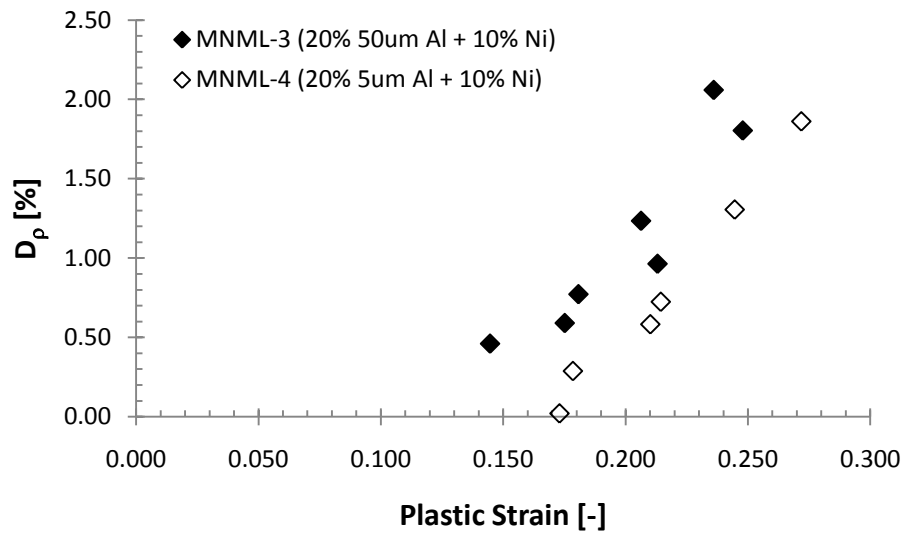


Figure 4.29: Damage-plastic strain plot for MNML-3 and -4.

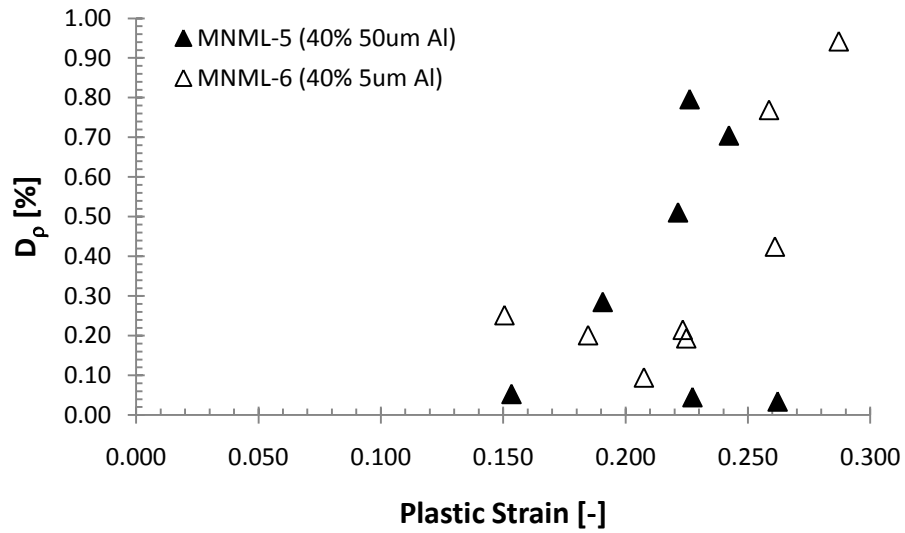


Figure 4.30: Damage-plastic strain plot for MNML-5 and -6.

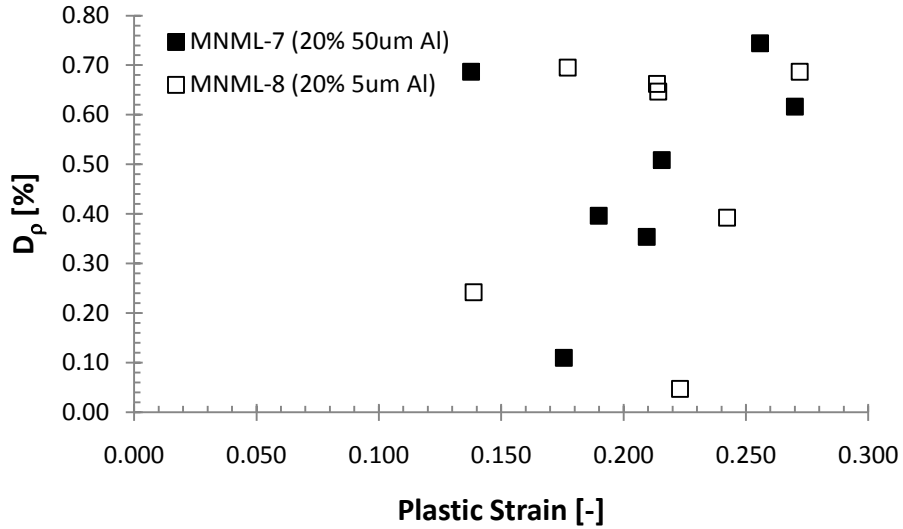


Figure 4.31: Damage-plastic strain plot for MNML-7 and -8.

voiding. Therefore, a decreased amount of damage is expected in the composites containing only 20 vol.% aluminum particles (MNML-7 and -8). However, the amounts of damage accumulation were not significantly different for the materials with 40 vol.% aluminum (MNML-5 and -6) as observed in Fig. 4.32.

However, when 10 vol.% nickel particles were introduced into the system there was a dramatic increase in the rate of damage accumulation which amplifies the effects of aluminum particle loading fractions. In Fig. 4.33 and 4.34 the two-composites subsets MNML-1/MNML-2 and MNML-3/MNML-4 are plotted against the two-composite subsets MNML-5/MNML-6 and MNML-7/MNML-8 respectively. In each case, we can see much higher levels of damage accumulation in the composites containing nickel for a given strain value, with more pronounced effects at higher strains. Where as in the case with the composites without nickel, fairly similar damage accumulation values are observed, when nickel is introduced, the composites with 40 vol.% aluminum has damage values that are as much as three to four times larger at plastic strains greater than 0.025. This can be more easily seen in Fig. 4.35 where the damage accumulation effects are plotted for all nickel containing composites. With the introduction of the

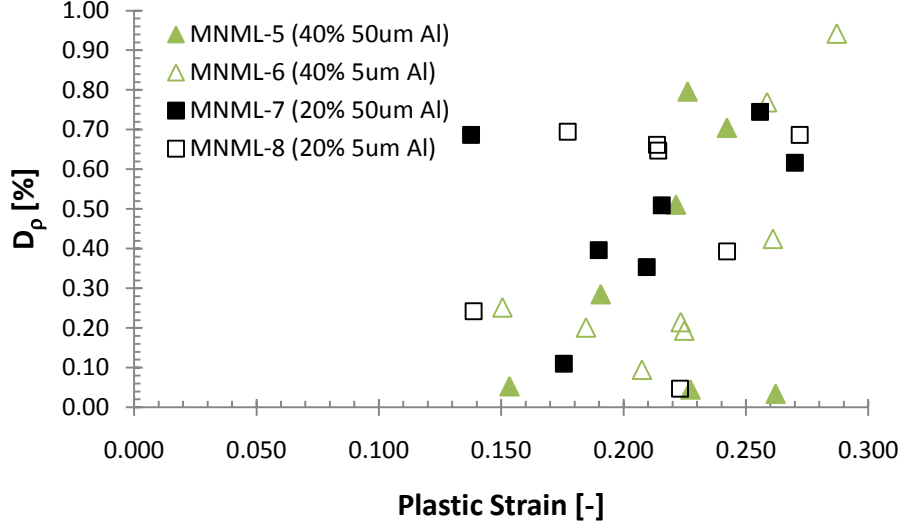


Figure 4.32: Damage-plastic strain plot for MNML-5, -6, -7, and -8.

much stiffer nickel particles a portion of the composite that would normally strain under quasi-static loading conditions now strains very little. This results in larger amounts of straining in both the epoxy and aluminum particles. Since the amount of damage accumulation in MNML-3 and MNML-4 which contains a 30 vol.% loading fraction of particles is larger than those for MNML-5 and MNML-6 which contain a total of 40 vol.% loading fraction of particles, it can be concluded that the nickel particles may have a far field effect on the amount of strain in the other constituents at the mesoscale. This would increase the stress values in both the aluminum and epoxy at larger distances from the nickel particles and enhance the accumulation of damage in a larger portion of the composite than if the nickel particles were replaced with a less stiff material.

4.3.5 Summary of Quasi-Static Compression Results

Based on the quasi-static compression test results it was found that the Young's modulus was higher for composite with 5 μ m sized Al for both strain rates ($d\varepsilon/dt = 10^{-4}$ and $10^{-3} s^{-1}$). The peak stress (σ_y) was also higher for the composites containing

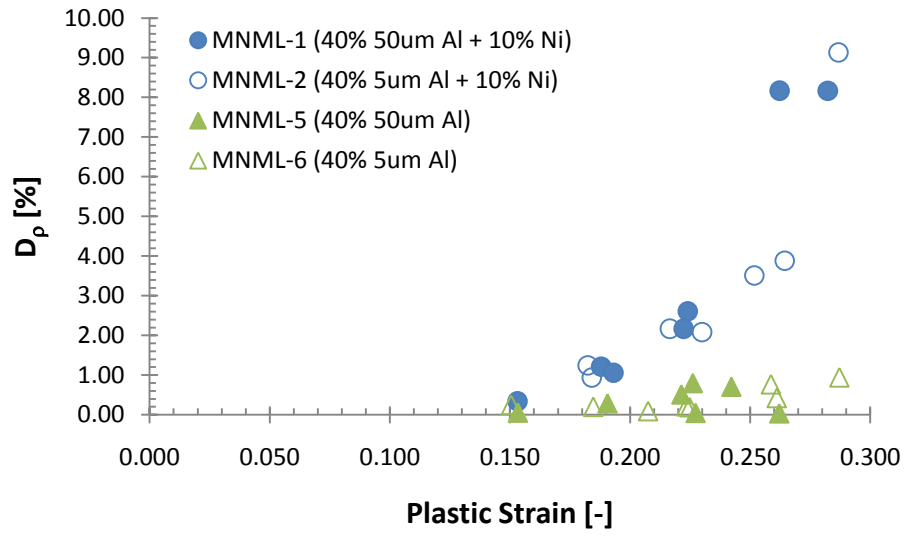


Figure 4.33: Damage-plastic strain plot for MNML-1, -2, -5, and -6.

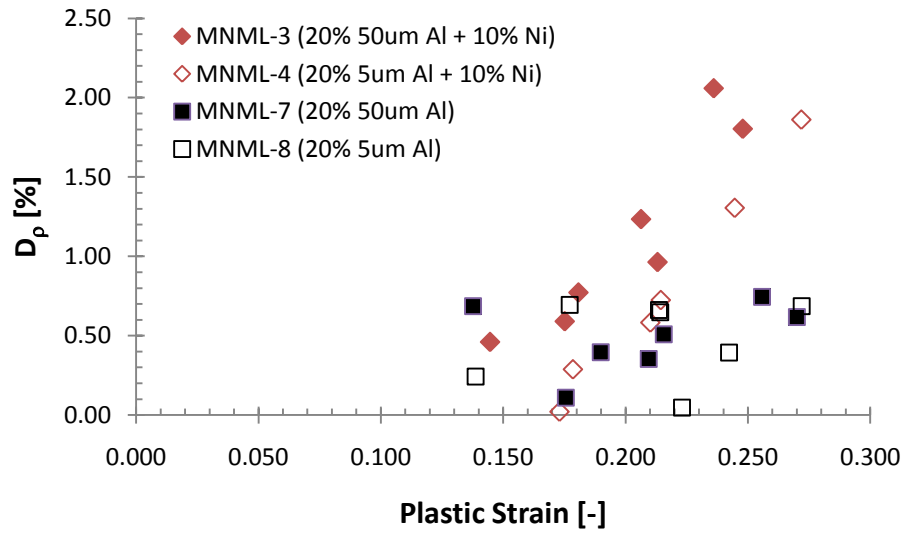


Figure 4.34: Damage-plastic strain plot for MNML-3, -4, -7, and -8.

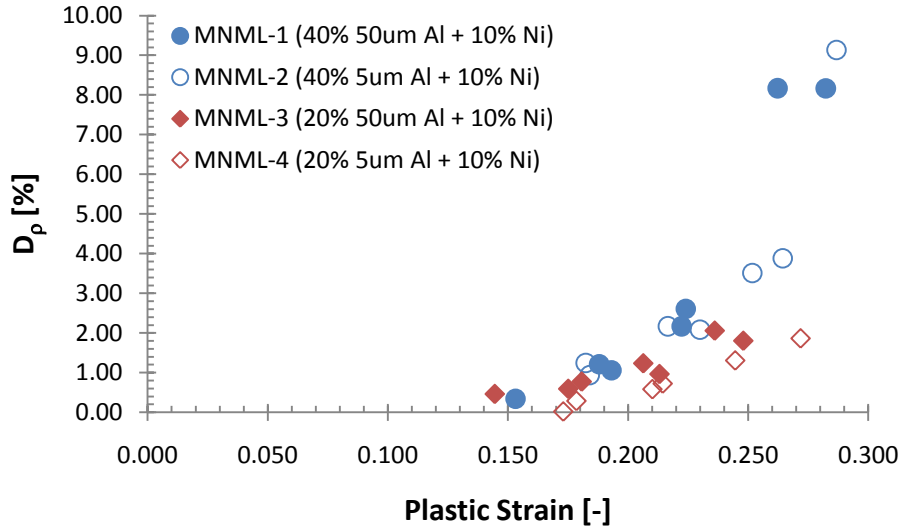


Figure 4.35: Damage-plastic strain plot for MNML-1, -2, -3, and -4.

the smaller Al particles at each rate of strain with increases as high as 17.0% with an increase in strain rate and increases of as much as 11.5% with a decrease in Al particle size from 50 to 5 μ m. Increases in strength with strain rate is a typical response of rate dependent materials and is more pronounced for polymers at low rates of strain than for metals. This alludes to the behavior of the composite having strong dependence on the mechanical behavior of the epoxy.

Along with an increase in both the Young's modulus and peak stress with increased rates of strain, there was also an accompanied increase in peak strain ϵ_y . This was more of a balance between the Young's modulus and peak stress for given composite than a material property. However, the peak strain decreased with increased amounts of particle reinforcement. This is due to an increase in the amount of stiffer constituents and resultant larger Young's modulus of the composite.

The increases in composite's Young's modulus and σ_y with decreased aluminum particle size are hypothesized to be due to a more uniform spatial distribution of particles throughout the epoxy matrix which results in a more uniform distribution of stresses and decreased amounts of stress and strain concentrations that result in

higher microdamage nucleation rates that can lower their strengths and stiffness while under load. There is also an increase in the interfacial area as particle size decreases which is expected to influence the strength and elastic modulus. If bonding between the particles with the matrix is strong then less damage is expected to occur for composites containing smaller diameter particles which would increase both Young's modulus and σ_y .

The amount of strain recovered following compression for the composites were found to be dependent on the composite composition and strain history. The amount of recovered strain decreased with increased strain levels achieved and as the volume fraction of particles increased. This is due to the increased amounts of damage incurred at higher strain and increased amounts of localized regions of extreme deformation produced by the presence of the larger amounts of particle reinforcement. Composites with smaller diameter aluminum had lower amounts of accumulated damage with plastic strain. In these composites the distribution of particles is more homogeneous which decreases the amount of stress concentrations. It may also be possible that the smaller particles produce reduced regions of affected volume and a critical volume of stress or strain concentrations need to be present for damage to accrue. The presence of Ni amplified the amount of damage accumulated in the composites, and even larger amounts of damage were produced at the higher strain levels which is indicative of a higher damage accumulation rate.

4.4 Split-Hopkinson Pressure Bar Results

Each composite was tested at dynamic strain rates using the split Hopkinson pressure bar apparatus. By varying the geometry of the specimen strain rates of $1 \times 10^3 \text{ s}^{-1}$ and $5 \times 10^3 \text{ s}^{-1}$ were achieved. Multiple tests were carried out for each strain rate to assess the experimental scatter. Each test was carried out at room temperature. The dynamic stress-strain curves and strain-rate histories were obtained for each test by

analyzing the strain gage data following the equations outlined in Chapter 3. The mechanical properties were then determined for each composite and at each strain rate. The results of the analysis for the various composite are summarized for each strain rate in Tables 4.9 and 4.10.

Table 4.9: Mechanical properties determined from split Hopkinson pressure bar experiments at a strain rate of $\dot{\epsilon} = 1 \times 10^3 s^{-1}$.

Material	σ_y [MPa]	ϵ_y [-]	E [GPa]	$\dot{\epsilon}$ [s^{-1}]
MNML-1	185.95 ± 1.86	0.0795 ± 0.0068	4.08 ± 0.51	912.45 ± 127.25
MNML-2	193.63 ± 1.14	0.0757 ± 0.0013	4.34 ± 0.40	758.48 ± 50.74
MNML-3	187.11 ± 5.13	0.0842 ± 0.0078	3.35 ± 0.32	864.05 ± 221.08
MNML-4	189.27 ± 3.38	0.0823 ± 0.0034	3.46 ± 0.28	1024.00 ± 97.33
MNML-5	171.34 ± 5.81	0.0827 ± 0.0071	3.33 ± 0.24	841.15 ± 217.57
MNML-6	184.05 ± 1.26	0.0796 ± 0.0025	3.79 ± 0.33	898.91 ± 70.47
MNML-7	182.75 ± 1.96	0.0939 ± 0.0057	2.84 ± 0.18	1161.91 ± 137.61
MNML-8	186.54 ± 1.73	0.0854 ± 0.0042	3.14 ± 0.11	1035.76 ± 189.68

Typical dynamic stress-strain curves at strain rates of $1 \times 10^3 s^{-1}$ and $5 \times 10^3 s^{-1}$ for each composite type are displayed in Figs. 4.36 and 4.37, respectively. It can be seen that the curves are characterized by a non-linear elastic behavior and a viscoelastic to viscoplastic transition that evolves into strain softening following yield. For both strain rates as the amount of particle reinforcement increases, there is an increase in the slope of the linear portion of the elastic region. The constitutive curves also demonstrate an apparently large linear range that extends up to fairly high strain levels (0.03 - 0.05). The elastic modulus was therefore determined from a linear fit at higher values, than those used in quasi-static compression experiments.

The viscoelastic-viscoplastic transition at lower strain rates were characterized to have a more abrupt change from yield to strain softening where as at the higher strain

Table 4.10: Mechanical properties determined from split Hopkinson pressure bar experiments at a strain rate of $\dot{\epsilon} = 5 \times 10^3 s^{-1}$.

Material	σ_y [MPa]	ϵ_y [-]	E [GPa]	$\dot{\epsilon}$ [s^{-1}]
MNML-1	206.12 ± 5.09	0.1662 ± 0.0217	3.03 ± 0.30	4825.51 ± 574.09
MNML-2	217.50 ± 5.66	0.1806 ± 0.0267	3.44 ± 0.55	5448.17 ± 812.16
MNML-3	211.20 ± 3.17	0.1500 ± 0.0061	3.29 ± 0.33	4175.29 ± 313.64
MNML-4	205.24 ± 2.45	0.1384 ± 0.0091	2.85 ± 0.43	4590.16 ± 859.45
MNML-5	194.79 ± 2.64	0.1408 ± 0.0156	2.70 ± 0.37	5620.83 ± 936.22
MNML-6	203.00 ± 2.40	0.1427 ± 0.0108	2.69 ± 0.42	4262.83 ± 829.64
MNML-7	197.09 ± 4.58	0.1434 ± 0.0056	2.89 ± 0.36	4765.37 ± 624.35
MNML-8	199.75 ± 4.25	0.1272 ± 0.0105	2.73 ± 0.28	4256.80 ± 760.54

rates, the transition is initially more gradual. Upon further deformation, the rate of strain softening is more gradual for the slower strain rate and persists throughout the rest of the test. For the tests conducted at higher strain rates, the rate of strain softening while initially less than that for the slower strain rate, increases and is followed by a region of perfect plastic deformation shown by the nearly zero slope in the stress strain curves. However, the region of perfect plastic deformation observed at the higher strain rate, occurs at strains greater than those achieved at the lower strain rate. Since the amount of strain attainable in a split Hopkinson test is strain rate dependent [70], the regime of perfect plastic deformation at the lower strain rate may still exist, but is not captured due to the shorter time duration of the experiments at this strain rate. The amount of strain softening also decreases with increasing amount of particle reinforcement for the higher rates. For lower rates of strain, the slope of the post yield region is largely unaffected by a change in composite composition.

While Figs. 4.36 and 4.37 show the general constitutive behavior of the composites at these high strain rates, it is hard to compare the individual curves for each

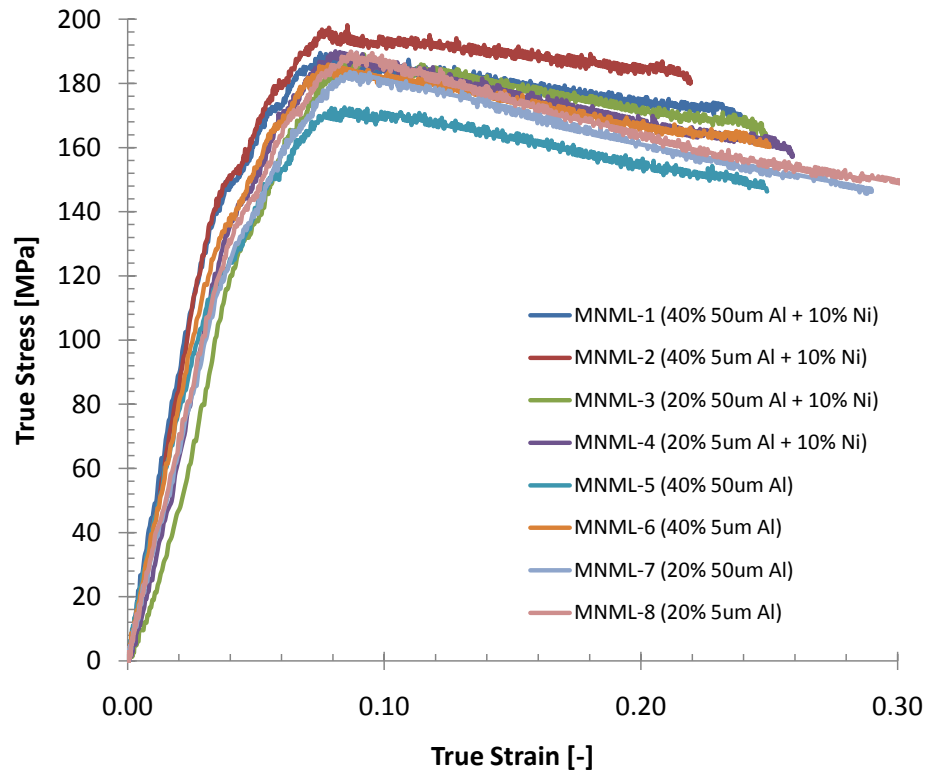


Figure 4.36: $\sigma - \varepsilon$ curves for the composites tested at a strain rate of $1 \times 10^3 s^{-1}$.

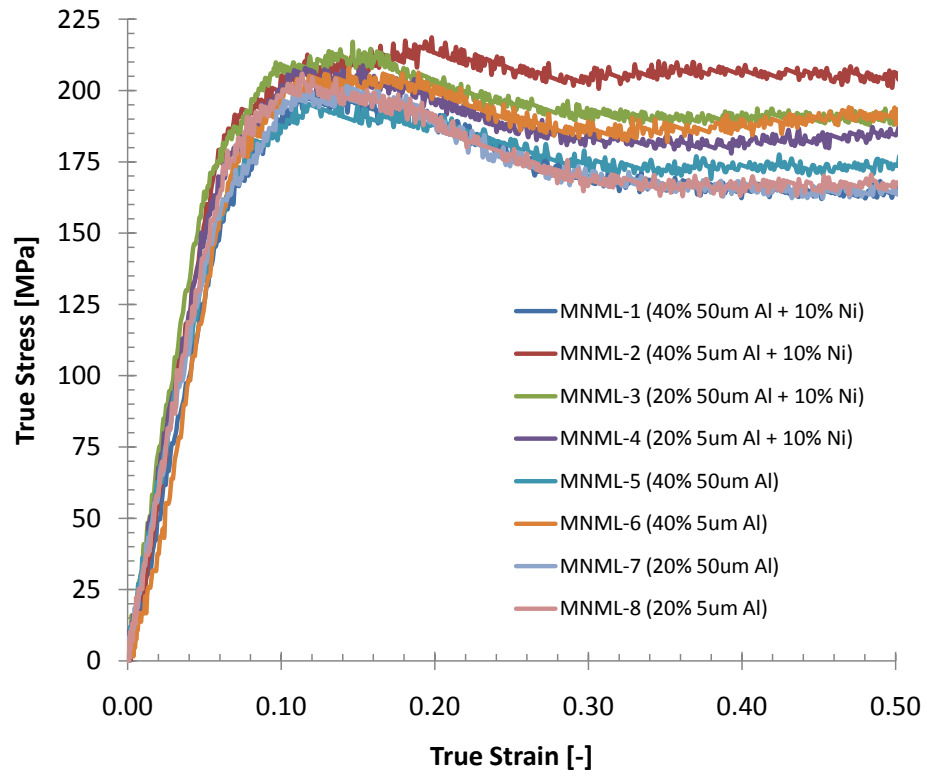


Figure 4.37: $\sigma - \varepsilon$ curves for the composites tested at a strain rate of $5 \times 10^3 s^{-1}$.

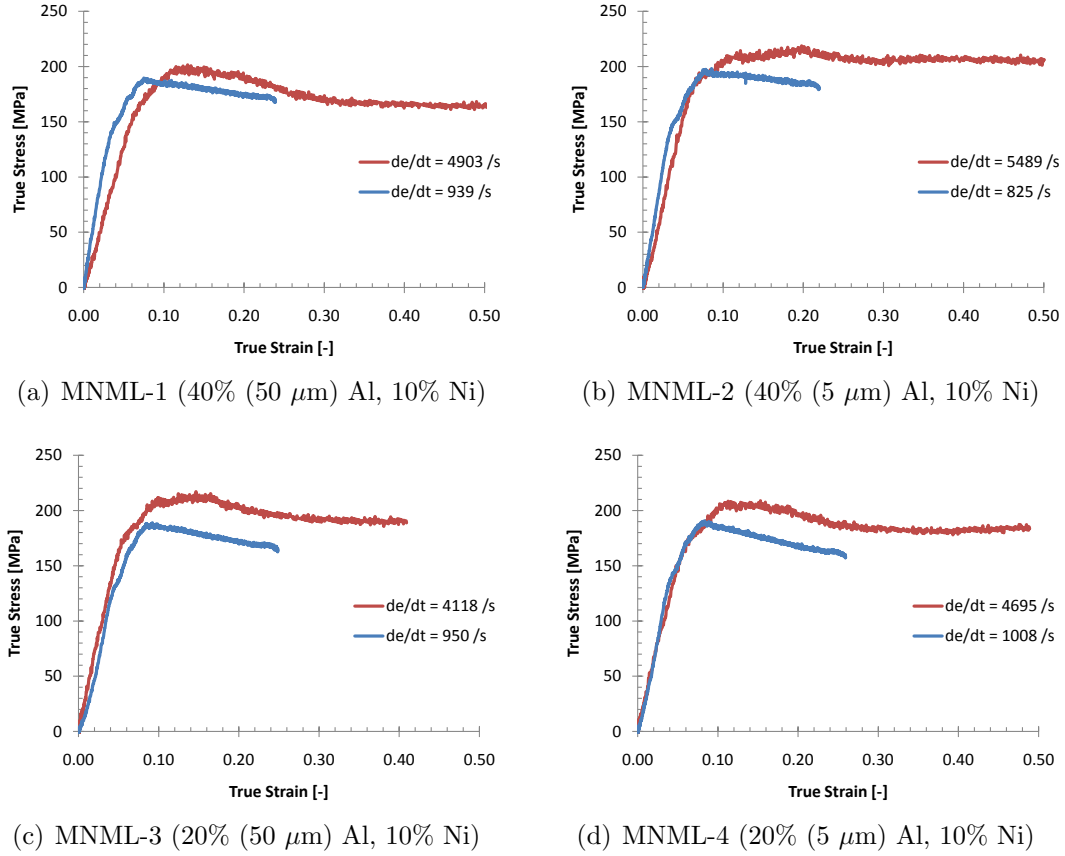
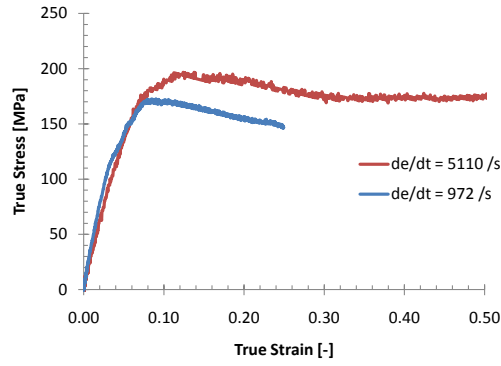
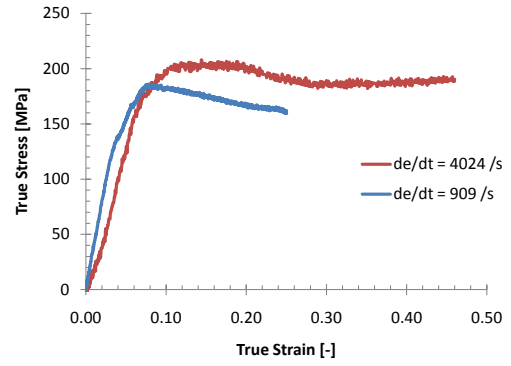


Figure 4.38: Representative split-Hopkinson pressure bar σ - ε curves for the two nominal rates of strain tested. (CONTINUED IN THE FOLLOWING FIGURE)

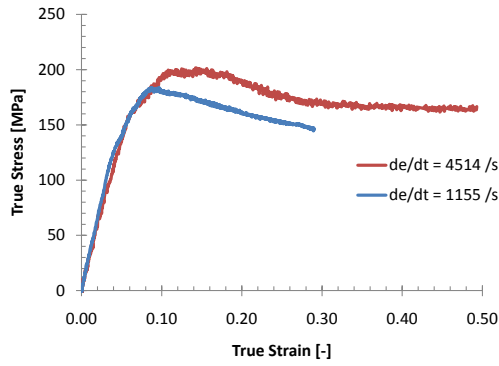
composite and how they are effected by strain rates in this regime. Therefore, representative stress-strain curves for each composite and strain rate have been plotted with one another in the Figs. 4.38 and 4.39. It can be seen from these figures that the peak and flow stresses for each composite type are found to be highly rate dependent with a shift towards higher stress values being observed with an increase in strain rate. There is also a decrease in Young's modulus with an increase in strain rate. In the following sections the peak stress, peak strain and Young's modulus will be discussed in more detail.



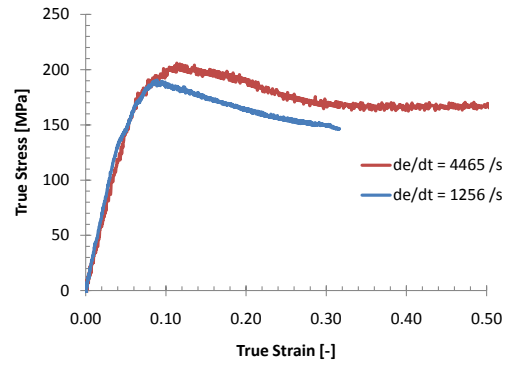
(a) MNML-5 (40% (50 μm) Al)



(b) MNML-6 (40% (5 μm) Al)



(c) MNML-7 (20% (50 μm) Al)



(d) MNML-8 (20% (5 μm) Al)

Figure 4.39: Representative split-Hopkinson pressure bar σ - ε curves for the two nominal rates of strain tested.

4.4.1 Young's Modulus at Dynamic Strain Rates

Due to the oscillations of stresses and strain prior to the development of stress equilibrium within the sample, the concept of Young's modulus is not entirely accurate, if obtained from tests conducted using a split Hopkinson pressure bar. However, since the linear portion of the elastic regime was found to extend up to relatively large strains, (as much as .05), it is not entirely out of the question to compare the "apparent" modulus at the varying strain rates within the dynamic regime, as well as between the various composites investigated. Figure 4.40 plots the Young's modulus as a function of total volume fraction of particle reinforcement for both nominal strain rates tested using the split Hopkinson pressure bar. At a strain rate of $1 \times 10^3 \text{ s}^{-1}$ the Young's modulus increases with particle loading fraction. At a higher strain rate, $5 \times 10^3 \text{ s}^{-1}$, Young's modulus appears less affected by the amount of reinforcement, and has values lower than those at the slower strain rate. While the elastic modulus often scales with volume fraction and stiffness of the constituents, it is also affected by the ability of the material to transfer and carry loads. At higher rates of strain, microdamage nucleation due to matrix-particle decohesion may be occurring that limits the composite's ability to transfer or carry these loads efficiently. Furthermore, as the strain rate is increased the polymer relaxation mechanisms occur at longer time scales than those of the experiments at lower strain rates, resulting in a more brittle material behavior that would make damage more likely to occur at the mesoscale. Correspondingly the composites with larger diameter aluminum particles were observed to have on average lower elastic moduli for both strain rates. If composites with larger particles have a nonuniform arrangement of particles in the matrix, then stress and strain localization would develop fairly early in the constitutive response of the composite at high strain rates and lead to the nucleation of microdamage prior to bulk yielding. While, it is entirely possible that early onset of microdamage may have a role in the stress-strain behavior in the elastic regime at these strain rates,

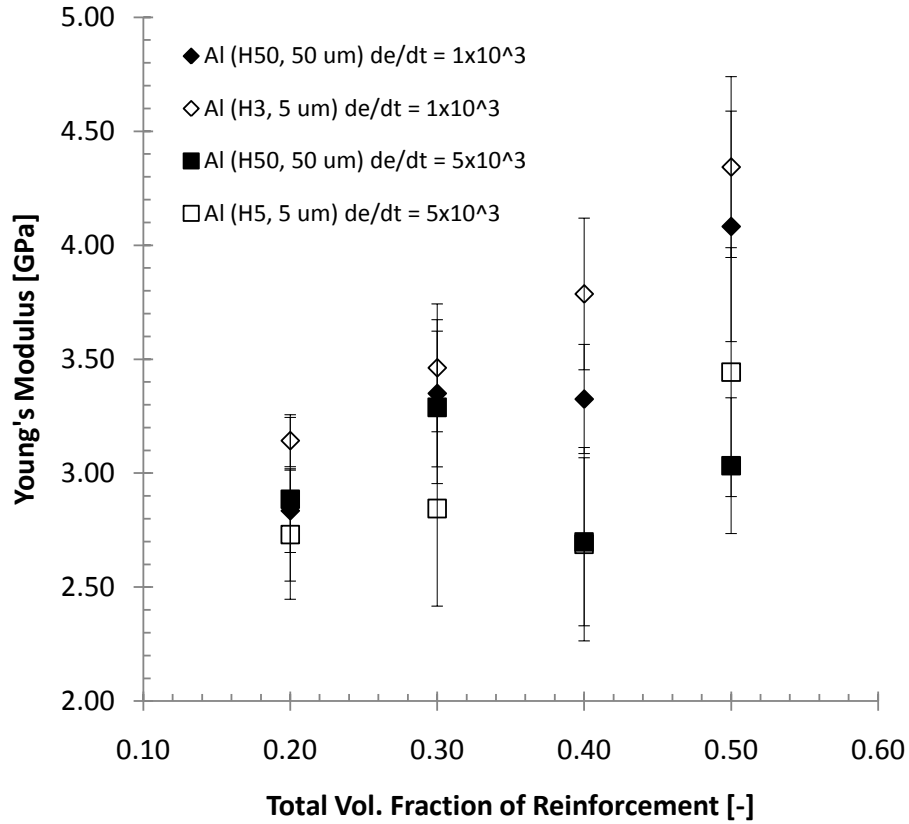


Figure 4.40: Young's modulus as a function of particle volume fraction for composites tested in uniaxial compression at dynamic rates of strain.

the stress state in the samples are highly non-uniform in the beginning stages of the loading process and as such the reported moduli should not be taken as true elastic properties.

4.4.2 Peak Stress and Strain at Dynamic Strain Rates

For materials that have applications at high rates of strain such as under impact loading conditions, it is important to have an understanding of how the composite material makeup, affects its ability to carry loads without deforming plastically. This is especially important with regards to safety concerns where any high impact insults may alter the mechanical behavior of the composite, or subsequently cause as in the

case of structural energetic materials to undergo reactions. For the composites investigated, the peak stress at high strain rates was determined for the split Hopkinson pressure bar tests using the method outlined in Chapter 3. With the addition of nickel, large amounts of strains within epoxy and aluminum constituents is expected due to its high stiffness and work hardening properties which can increase the amount of stress and strain localizations and lead to an earlier onset of yield. However, as shown in Fig. 4.41 the composites with nickel particles had peak stresses that were higher. Also the materials with smaller aluminum particles had higher stress levels as well indicating that as stress levels increase there is an increased ability for the composite to accept and transfer stresses at the mesoscale, delaying the bulk yielding. At these rates of strain, propagation of the stress waves may be aided by the presence of the more even distribution achieved with smaller particles, in comparison to composites prepared with the same volume fraction of larger aluminum particles. With increased amounts of particle reinforcement (40% particle reinforcement in comparison to 20%) there is a decrease in the load carrying capacity of the composites. This is expected due to the larger amounts of matrix-particle interfaces and possible sites for the buildup of stress concentrations.

Peak strain as affected by the volume fraction of particles is shown in Fig. 4.42. With an increase in strain rate from $1 \times 10^3 \text{ s}^{-1}$ to $5 \times 10^3 \text{ s}^{-1}$ the behavior transitions from a slightly decreasing trend in peak strain with volume fraction of particles to a slightly increasing trend. This is due to a decrease in the elastic modulus with an increase in strain rate since the peak stress-volume fraction of particle data parallel one another with an increase in value with strain rate. This also explains why the peak strains are larger for the composites subjected to the higher strain rate. The composites with smaller diameter aluminum particles had a tendency to have slightly decreased peak strain values as their counterparts. This is expected since they had greater elastic moduli than the composites with larger diameter aluminum particles.

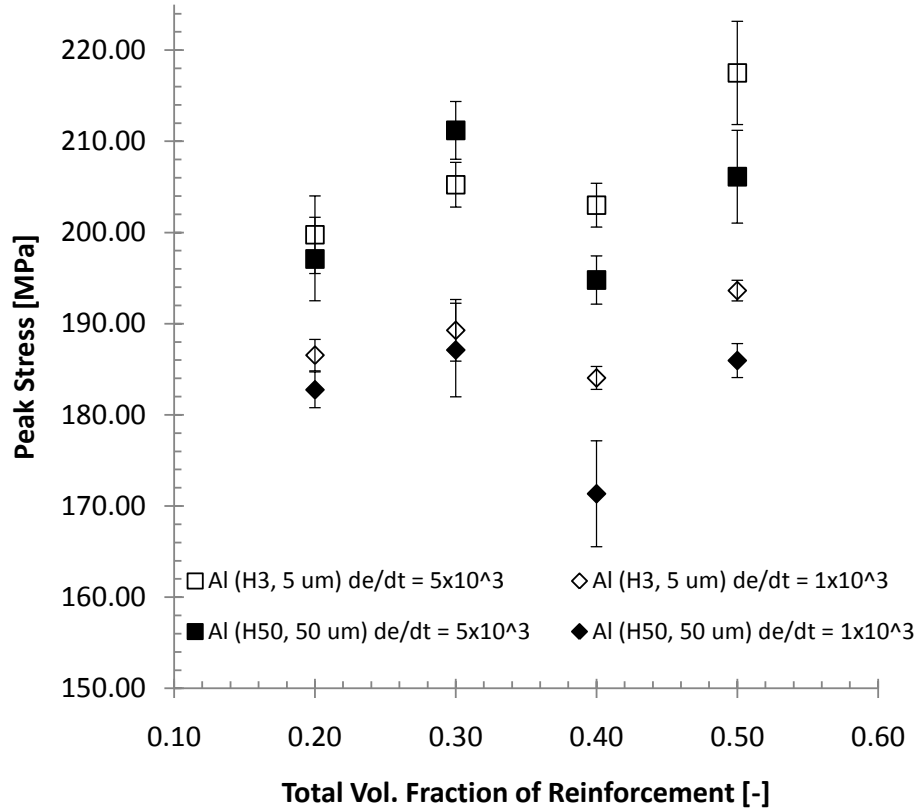


Figure 4.41: Peak stress as a function of particle volume fraction for composites tested in uniaxial compression at dynamic rates of strain. The error bars represent the standard deviation in the peak stress for the tested samples.

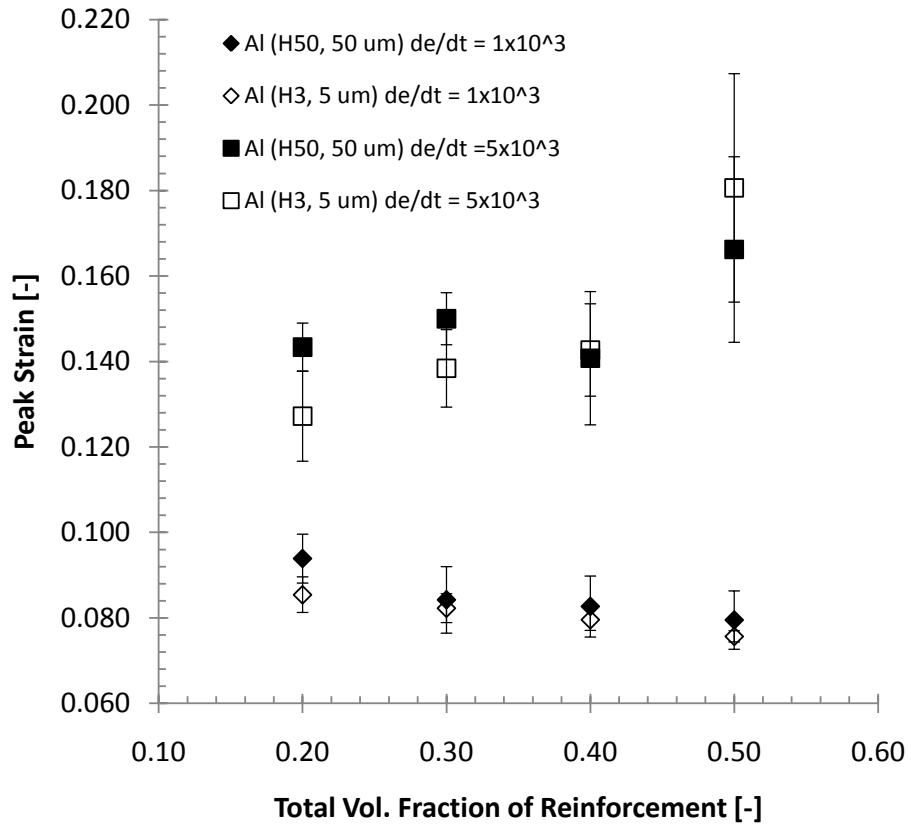


Figure 4.42: Peak strain as a function of particle volume fraction for composites tested in uniaxial compression at dynamic rates of strain. The error bars represent the standard deviation in the peak strain for the tested samples.

4.4.3 Summary of Dynamic Uniaxial Stress Compression Results

The mechanical response of the composites at dynamic rates of strain were not too different from the quasi-static strain rate results in terms of the shape of the stress-strain curve. One difference was that each composite showed strain softening following yield at a peak stress, where as at the quasi-static strain rates, MNML-1 and 2 with 50% particle loading fraction lacked this trait. As with the quasi-static strain rate results the peak stress increased with an increase in strain rate from 1×10^3 and 5×10^3 s^{-1} however, the apparent Young's modulus decreased. While the values for Young's modulus are not truly representative at these strain rates due to non-equilibrium of stress in the early stages of compression, the decreases in the apparent moduli has been related to increased amounts of damage that limits the composites ability to transfer or carry loads efficiently. The composites with larger particles were observed to have on average lower apparent elastic moduli for both strain rates due to a more nonuniform arrangement of particles that increases sites for early onset of damage. With higher loading fractions of particle reinforcement Young's modulus increased at a strain rate of 1×10^3 s^{-1} where as at a strain rate of 5×10^3 s^{-1} there was no apparent dependence on particle volume fraction.

The peak stress was shown to be highly dependent on aluminum particle size with the composites containing $5\mu m$ diameter particles having on average a 3% increase and as high as a 7% increase. There was an 10% increase in peak stress at a strain rate of 5×10^3 s^{-1} . With only an increase in strain rate by half an order of magnitude this increase is larger than that found at the quasi-static strain rates with a full order of magnitude increase from 10^{-4} to 10^{-3} s^{-1} . The introduction of Ni had a pronounced effect on the peak stress of the composites. For composites MNML-1 through MNML-4 there was an average increase in peak stress by 5% due to the addition of 10 vol.% Ni.

4.5 Taylor Rod-On-Anvil Impact Test Results

Using a gas gun, Taylor rod-on-anvil impact tests were carried out by firing cylindrical projectiles at a rigid anvil to produce dynamic deformation under nonconstant rates of strain, as described in Section 3.3.4. The final strains were calculated from impacted specimen geometry of rod-on-anvil impact test samples, performed on each composite system over a range of velocities. The strain values were then used in Hutchings's analysis to extrapolate the critical velocity (V_c) for onset of plastic deformation by conducting a linear fit of strain-velocity data as shown in Fig. 4.43. From these values the dynamic yield stress (Y) and strain (ε_y) were solved iteratively using Eqns. 22 and 23. By conducting this analysis for each test, an average dynamic yield stress and strain was determined for each composite. For each test a true strain and stress value was also calculated using the analysis. In Fig. 4.44 the stress and strain for each test is plotted with the average yield stress and strain to form dynamic $\sigma - \varepsilon$ curves for each composite. Two distinct groupings of the composites can be seen. The upper grouping consists of composites containing 20% aluminum while the lower grouping consists of the composites containing 40% aluminum. Clearly the amount of aluminum has a dramatic effect on the constitutive dynamic deformation behavior of the various composites under these loading conditions. The effect of nickel particles or use of different sized aluminum particles however, illustrate no clear trend. For composites containing 20 vol.% aluminum those with larger sized aluminum particles have higher strengths and flow stresses where as the opposite occurs for the composites with 40 vol.% aluminum. The variation in stress-strain response with varying composition indicates that interaction effects between aluminum particle size, nickel content, and aluminum volume fraction are influencing the deformation response.

The minimum velocity necessary to generate plastic deformation in the material during Taylor rod-on-anvil impact experiments, considered the critical velocity, obtained by taking the x-axis intercept of a line fitted to the respective data points.

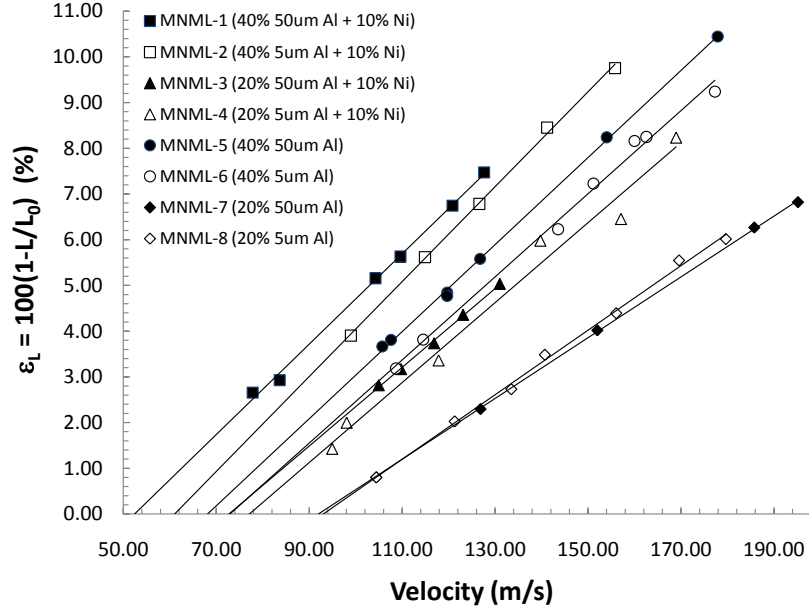


Figure 4.43: Replot of Fig. 3.18 Axial plastic strain-impact velocity plot. Critical velocities are based on intercepts of linear-fits ($R^2=0.981-0.999$) with the velocity axis.

The critical velocity was found to be highly dependent on the total volume fraction of particles present (see Fig. 4.45). As the volume fraction is increased from 0.20 to 0.50 the critical velocity decreased from 93 to 52 m/s. Also, the composites containing smaller Al particles ($5\mu\text{m}$) required a higher velocity for onset of plastic deformation (7% higher on average) than those with larger particles ($50\mu\text{m}$) of the same volume fraction.

The trends associated with the changes in volume fraction of particle, particle size, or addition of nickel on the yield stress behavior (Fig. 4.46) are not as clear as they are for the critical velocity. The most recognizable feature in the data is a sharp decrease (~ 100 MPa) in yield strength between 30 and 40% particle concentration. This indicates the possibility of a percolation threshold existing within this particle concentration range. At high enough concentrations of reinforcement the probability of particles touching or within close proximity increases, creating a threshold where the transfer of stress becomes inefficient and stress concentrations become

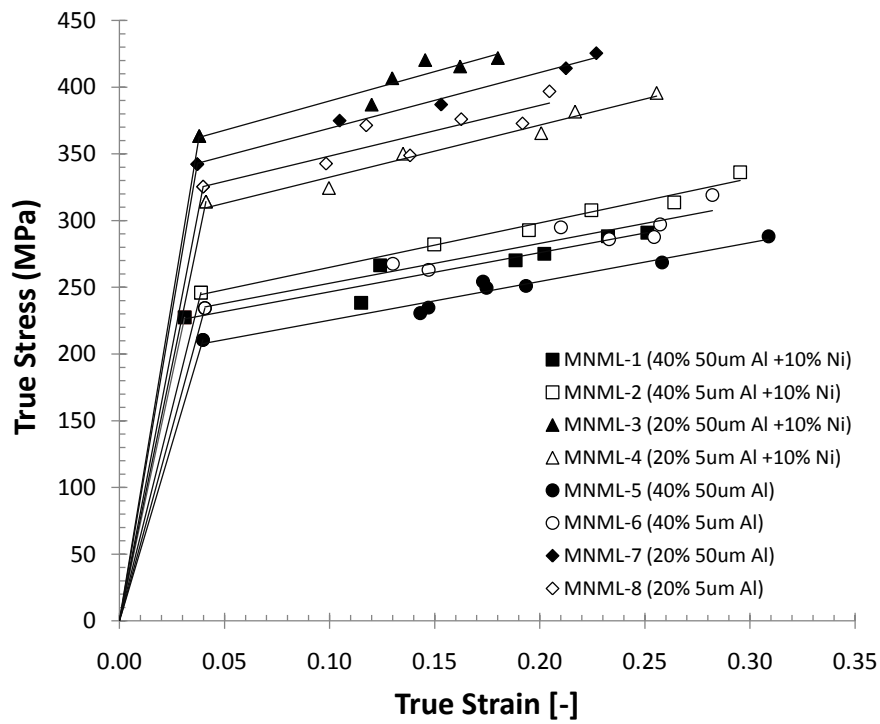


Figure 4.44: Dynamic $\sigma - \varepsilon$ curves obtained from Taylor rod-on-anvil impact experiments using Hutching's analysis.

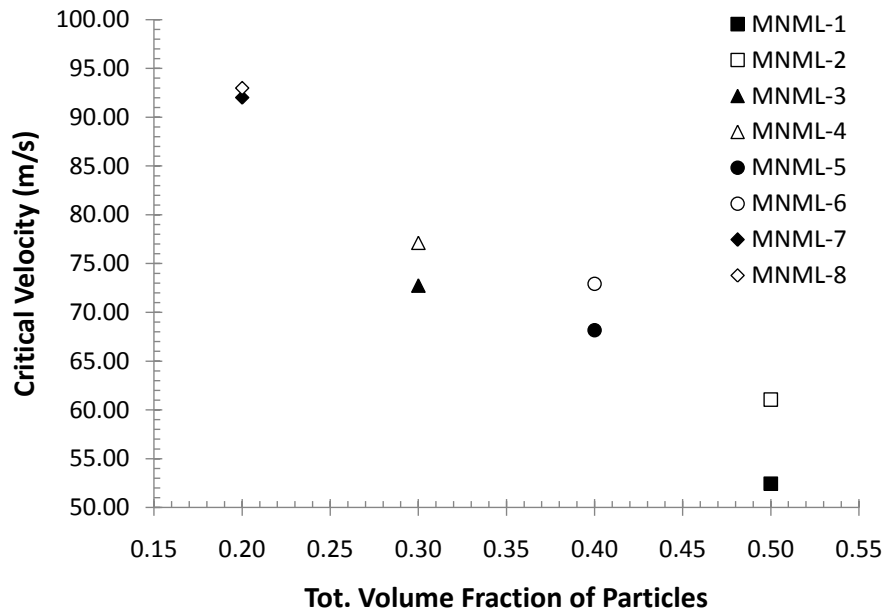


Figure 4.45: Critical velocity vs. particle concentration (50 μ m Al = closed data points, 5 μ m Al = open data points).

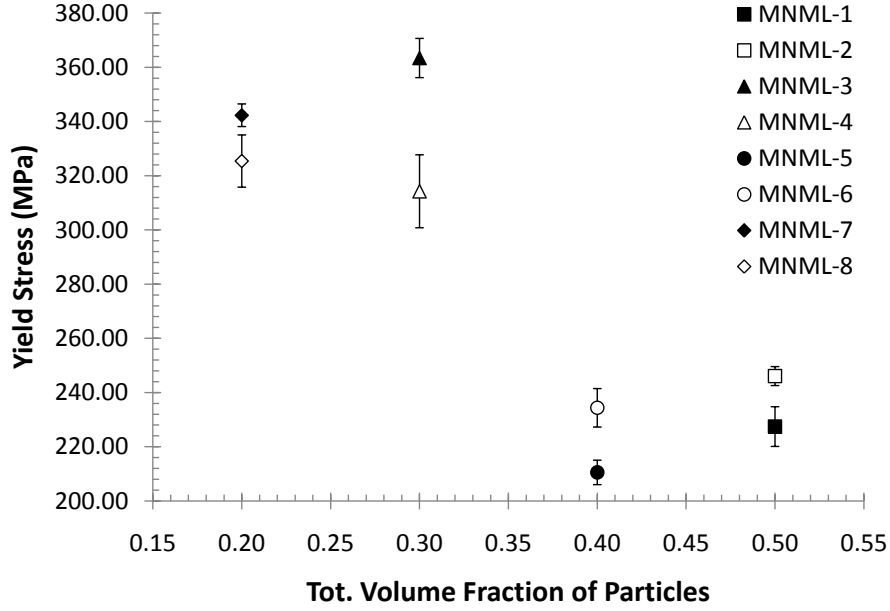


Figure 4.46: Yield stress vs. particle concentration ($50\mu\text{m}$ Al = closed data points, $5\mu\text{m}$ Al = open data points).

more prevalent due to particle-particle interactions resulting in a decrease in overall strength for the material. This is consistent with other theories [86, 102, 124]. Below this threshold, materials with larger aluminum particles have higher yield strengths than their counterparts with smaller aluminum particles. The opposite is true for particle concentrations above the percolation threshold indicating strong interaction effects. Also, upon increasing the particle concentration from 40 to 50% there is a small increase in yield strength. This increase is most likely due to the introduction of stiffer nickel particles.

The yield strains for the composites range from 3.1 to 4.1% (Fig. 4.47). While this is a fairly narrow range, trends exist for the different factors within the factorial design. The yield strain values increase slightly with increasing volume fraction up to 40% particle concentration and then decrease at levels beyond this concentration for materials with large aluminum particles and decrease slightly before this concentration for materials with small aluminum particles. This again may be due to a

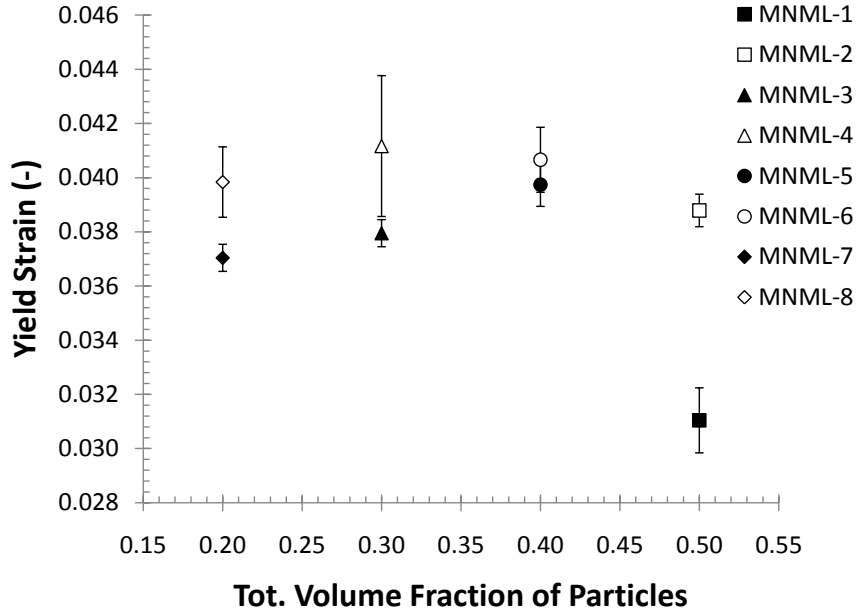


Figure 4.47: Yield strain vs. particle concentration ($50\mu\text{m}$ Al = closed data points, $5\mu\text{m}$ Al = open data points).

percolation threshold. Additionally, the composites with smaller aluminum particles have a higher yield strain than those with the same particle concentration but larger aluminum particles.

In cases where the smaller particles influence the mechanical behavior, the particles are distributed more uniformly throughout the matrix. This may help distribute the stress, deterring the formation, size, or severity of local stress concentrations that can promote early onset of damage and yielding. The composite with smaller Al particles can thus, accept higher impact velocities and reach higher elastic strains before bulk material yielding becomes measurable. This also explains the increase in the yield stress for materials MNML-2 and MNML-6 with high particle concentrations.

4.5.1 Summary of Taylor Impact Test Results

The critical velocity for plastic deformation, dynamic yield stress and yield strain all were highly dependent on the volume fraction of particles and particle size. As the volume fraction of particles increased the critical velocity decreased, the yield stress

increased up to 30% loading fraction followed by a drastic decrease at higher loading fractions, and the yield strain increased slightly up to 40% loading fractions followed by a decrease up to 50% particle loading fractions. With the use of smaller aluminum particles the critical velocity, yield stress (with the exception of MNML-4 and -8), and yield strain all had larger property values indicating that less damage occurs in composites containing smaller particles under these conditions.

4.6 Particle Strain Analysis

While quasi-static and dynamic compression experiments were carried out over a wide range of strain rates to determine the bulk mechanical behavior of each composite, the response of the composite at the mesoscale is also of key interest. In order to more fully understand the mechanical behavior of the composites at the mesoscale, compression experiments were stopped at different levels of strain.

For quasi-static compression experiments carried out at strain rates of 10^{-4} and 10^{-3} s^{-1} the samples were compressed to engineering strains of approximately .15, .20, .25, and .30 or true strains .14, .17, .22, and .28 respectively. Split Hopkinson pressure bar compression experiments were carried out at nominal strain rates of 10^3 and 5×10^3 with higher strains in the samples achieved at the higher rates of strain. Since the duration of the split Hopkinson experiments are approximately the same, the strain rate limits the level of strain achieved in each experiment. The geometry of each sample was measured following the completion of the compression experiments to determine the amounts of plastic strain.

Samples were then sectioned along their vertical axis to produce two halves. They were then mounted in epoxy and the cross-sectioned surface was polished. The microstructures were then examined using scanning electron microscopy with electron backscatter capabilities.

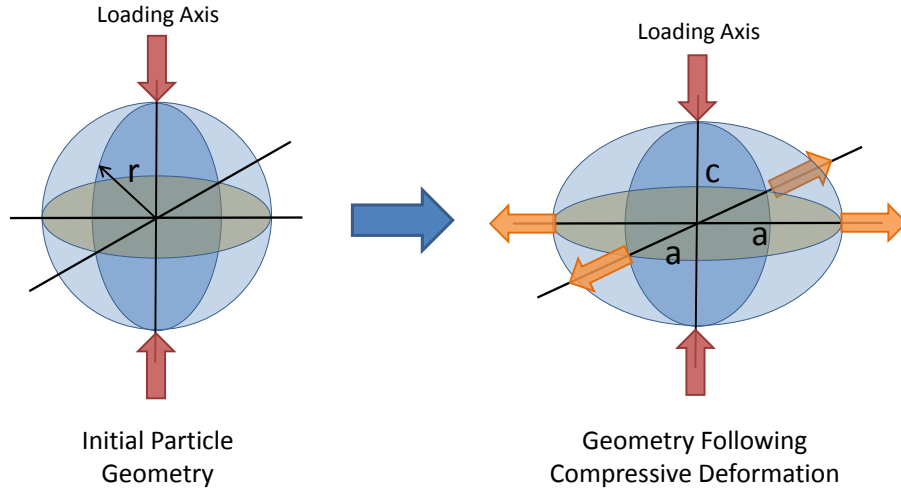


Figure 4.48: Schematic of the particle geometry before and after uniaxial compression experiments.

4.6.1 Measuring Particle Strain

As seen from microstructure images (shown in Fig. 4.1) of the bulk materials following casting for each composite, the particle morphology for both the aluminum and nickel can be considered to be spherical without any gross oversimplifications. This assumption allows the degree of particle strain to be easily measured using the following analysis.

Assuming the initial geometry of the particles is on average spherical to begin with, after compression the particles take on an oblate ellipsoidal geometry (see Fig. 4.48). With the assumption of conservation of volume during deformation, the geometry of the particles following uniaxial compression can be related to the initial particle geometry through the following equations:

$$\frac{4}{3}\pi r^3 = \frac{4}{3}\pi a^2 c \quad (45)$$

where r is the initial particle radius, a is the ellipsoidal particle's major axis length perpendicular to loading direction, and c the minor axis length parallel to the loading

direction. By simplifying Eqn. 45, an equation relating r to a and c is obtained.

$$r = \sqrt[3]{a^2 c} \quad (46)$$

The geometry of the particles can then be related to the amount of strain achieved due to uniaxial compression. The definition of true strain for a radial strain in the loading direction is defined as:

$$\varepsilon_{particle} = \int_{r_0}^{r_f} \frac{dr}{r} = -[\ln(r_0) - \ln(r_f)] \quad (47)$$

Using $r_0 = r$, $r_f = c$, and Eqn. 46 along with simple logarithmic operations, Eqn. 47 can be rewritten as:

$$\varepsilon_{particle} = -\frac{2}{3} \ln \gamma \quad (48)$$

where, γ is related to the aspect ratio of the ellipsoidal geometry through:

$$\gamma = \frac{a}{c} \quad (49)$$

Using Eqn. 48 as the basis for particle strain measurements a Matlab script was written to analyze the microstructures, to identify the particles, measure their geometry, and calculate the amount of strain. This analysis was applied to images from both the bulk starting material and post compression microstructures. Given that the starting particles have an average measure of ellipticity, an average baseline for particle strain for the as-cast material microstructures was subtracted from particle strain measurements for post compression microstructures. This allowed for the absolute particle strains to be obtained for each composite and related to the bulk plastic strain. Particle strain measurements using this method are carried out on two dimensional cross sections, as such the values obtained may not necessarily be representative of particle strains in three dimensional solids. This is due to the cross

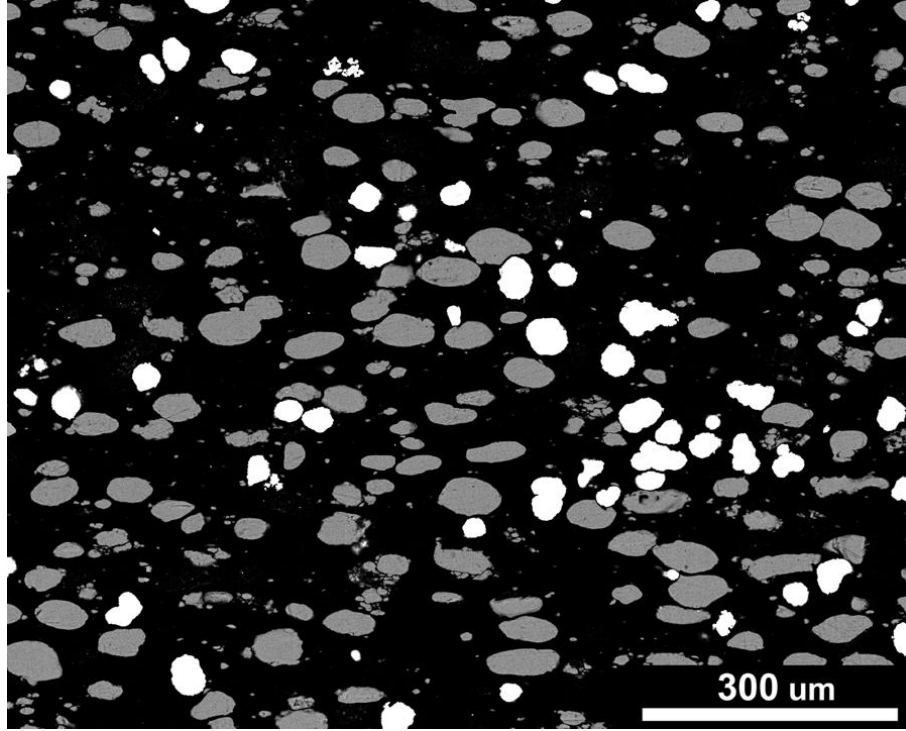


Figure 4.49: Microstructure of MNML-3 following quasi-static compression. The amount of bulk plastic strain is approximately 25%.

sectioning plane through the samples intersecting the deformed ellipsoids at random locations and not always coinciding with the particle's center axis.

The yield stress strain rate dependence of the epoxy matrix was shown earlier to have a pronounced effect on the strain rate behavior of the bulk material. Using the method outlined and the measured plastic bulk strains these same effects were also shown to have a dramatic effect on the deformation at the mesoscale of the aluminum particles. As an example of the large strain rate dependence of the particle strain on strain rate microstructures from MNML-3 (20% 50 μ m Al + 10% Ni) at bulk plastic strains of approximately 25% for quasi-static and dynamic rate of strain are shown in Figs. 4.49 and 4.50.

Results of the aluminum particle strain measurements for composites MNML-1, -3, -5, and -7 compressed at quasi-static strain rates are shown in Fig. 4.51. Two distinct deformation behavior regimes are obvious for the composites containing nickel

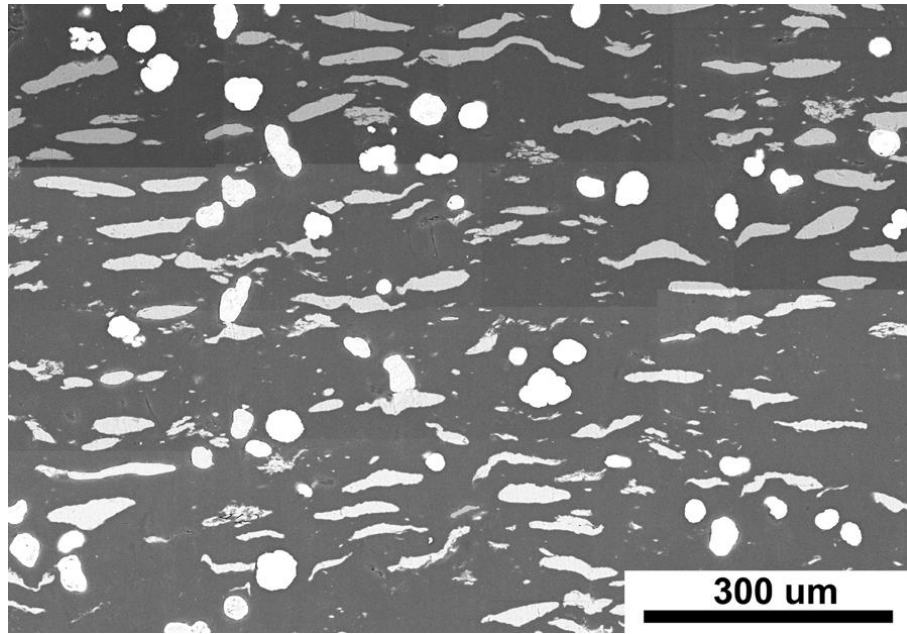


Figure 4.50: Microstructure of MNML-3 following dynamic uniaxial compression. The amount of bulk plastic strain is approximately 25%.

and those without nickel. Each type of composite is described as having a linear relationship of particle strain with the bulk strain within the range of the bulk strains tested. Also, for composites MNML-1 and 3, the rate of increase in particle strain with bulk strain was greater than those of MNML-5 and -7. For the composites containing nickel (MNML-1 and -3) the amount of straining in the aluminum was approximately .025 greater at strains around 15% and increased to as much as .150 higher at bulk strains around 28%. Despite there being a critical bulk strain, for there to be a measureable amount of aluminum particle strain, the rate of aluminum particle strain accumulation has to be greater than that of the bulk. The linear fits to the strain data can be seen in Fig. 4.51 with the critical bulk strain level determined as the intersection of the linear fit with the bulk strain axis. It should be noted that the critical bulk strain is not a real physical property of the composites. In fact, aluminum particle straining most likely begins to occur much earlier in the deformation process depending the stress localizations produced by the spatial heterogeneity of

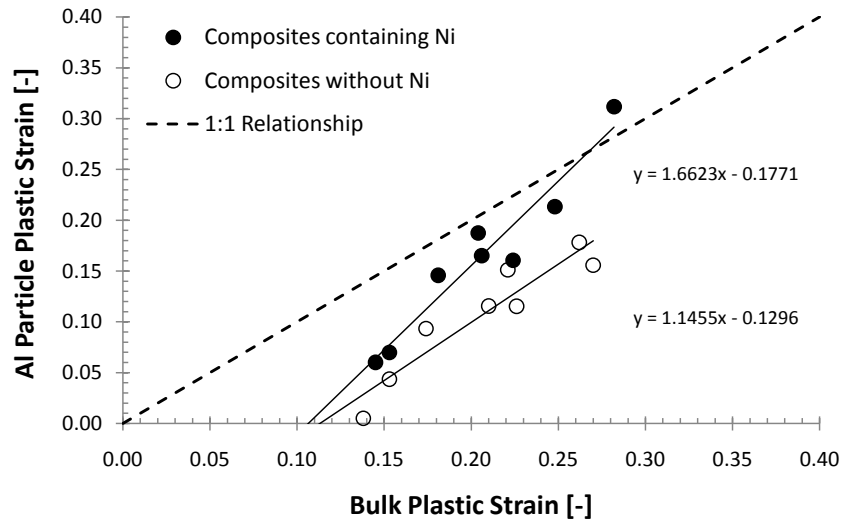


Figure 4.51: Plot of aluminum particle plastic strain against bulk plastic strain. The upper grouping of data points (filled circles) corresponds to the composites MNML-1 and MNML-3 which contain Ni. The lower grouping of data points (hollow circles) corresponds to the composites MNML-5 and MNML-7.

the particles in the matrix. The critical bulk strain however, can be thought of as a measure of the bulk response to initiation of aluminum particle plastic deformation. For both the nickel containing composites and those without nickel, the critical bulk strain for plastic deformation in the aluminum particles was determined to be 10.7 and 11.3% respectively.

Also, shown in Fig. 4.51 is a curve corresponding to a 1:1 bulk to aluminum particle plastic deformation. For both types of composites, the amount of particle deformation is primarily less than that of the bulk. This is an indication of the deformation response of the composites being dominated by the epoxy matrix at these strain rates. At large enough bulk strain levels, the aluminum plastic straining would eventually be greater than the bulk. At this point particle-particle interactions, rather than transferring of stresses from the matrix to the particles, is thought to occur due to a decrease in the flow stress of the epoxy matrix at these strain levels. Extensive microdamage would also be likely at these strain levels and composites would begin

to fail by particle-pullout before additional bulk strains can be accommodated. The crossover strain of the linear fits with the curve corresponding to a 1:1 relationship was calculated to occur at 26.7 and 89% for the composites with and without nickel respectively. For the composites in this study, extensive macrolevel cracking and failure occurred at engineering strains around 40% during quasi-static compression.

When composites MNML-1, -3, -5, and -7 were subjected to dynamic rates of strain the amount of plastic straining in the aluminum was higher than at quasi-static strain rates as shown in Fig. 4.52. As with the quasi-static compression tests the amount of aluminum plastic straining increased as the bulk plastic strain increased. However, the amount of strain accumulated by the aluminum particles is much higher than those at quasi-static strain rates with the rate of plastic deformation being approximately 60% higher (determined by slopes of linear fits). Also, the degree of plastic straining in the aluminum is greater than that of the bulk at strains larger than approximately 12%. This is an indication of a shift in the deformation behavior of the composites from quasi-static to dynamic rates of strain. From the microstructure images shown earlier for MNML-3, the aluminum particles become highly strained and deform irregularly at the dynamic rates of strain. At these strain rates the epoxy matrix is more rigid and behaves much stronger than the aluminum (indicated by the larger amounts of aluminum straining in comparison to the bulk), and therefore transfers stresses into the aluminum particles much more readily, rather than deforming and flowing with increased stress levels. This is due to a higher activation energy needed for large scale chain motions/ relaxations to occur that allow the epoxy to rearrange its structure. The critical bulk strain for plastic deformation of the aluminum is approximately half that of the quasi-static strain rate value (shown in Fig. 4.52).

It should be noted that no conclusions were attempted to be drawn between individual composite configurations. This is due to the lack of large statistical data

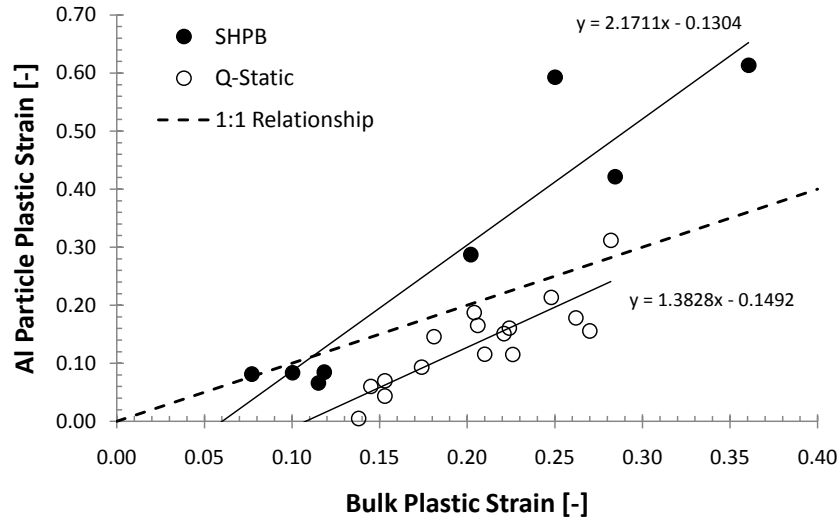


Figure 4.52: Plot of aluminum particle plastic strain against bulk plastic strain. The upper grouping of data points (filled circles) corresponds to the composites are data obtained at high dynamic strain rates. The lower grouping consists of data points (hollow circles) corresponding to particle strain measurements at quasi-static strain rates.

sets necessary for each composite to make this possible and the enormous amount of time in preparing samples and analyzing microstructures. For plots of the plastic straining in aluminum for the individual composite systems the reader is referred to Appendix D.

The measured plastic strain in the nickel particles were found to be very minimal $\epsilon_{Ni} < 3\%$ in comparison to the aluminum particles as shown in Fig. 4.53. This was the case for both the quasi-static and dynamic strain rates and was not dependent on the amount of total bulk plastic deformation for the composites. The very small amounts of strain, $\approx 2.5\%$ on average, in the nickel particles is due to the comparatively much larger Young's modulus, yield stress, and work hardening characteristics of nickel over both the aluminum and epoxy constituents. While nickel underwent very little plastic deformation, the presence of Ni particles in the epoxy caused more extensive plastic straining of the aluminum particles. As can be seen in Fig. 4.54 the microstructure of

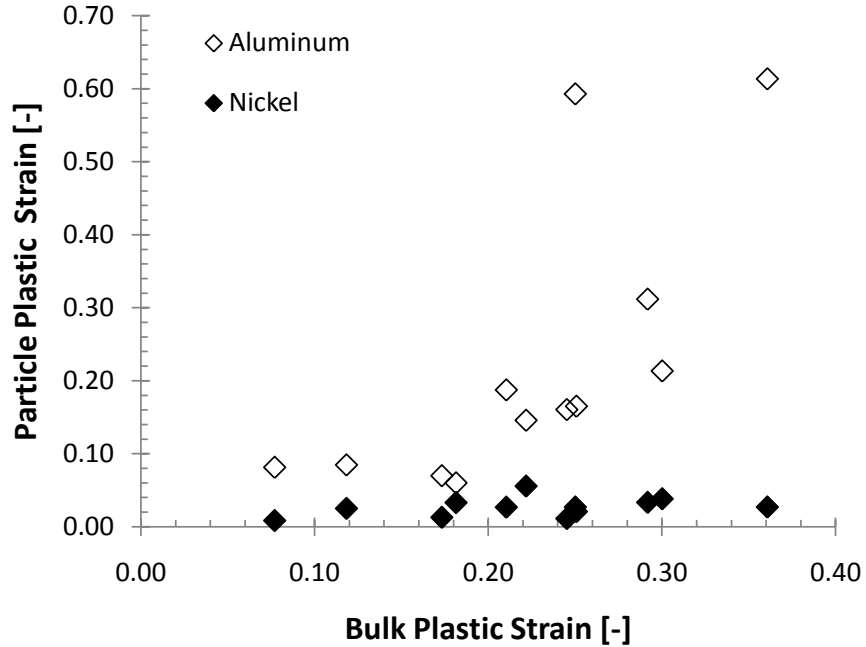


Figure 4.53: Measured amounts of particle plastic strain for Ni. On average the amount of particle plastic strain is 2.67% and has no pronounced dependence on strain-rate.

MNML-1 following a post uniaxial compression test at a strain rate of $5 \times 10^3 \text{ s}^{-1}$ shows extensive deformation of the aluminum particles while the nickel appears virtually untouched. The amount of straining in the aluminum closer to the nickel particles also appears to be more pronounced. This can be seen in Fig. 4.54 (circled regions) where the aluminum particles close to the nickel particles appear to be warped and follow the contours of the nickel particles. In this case the nickel particles act as rigid anvils within the microstructure by straining very little and transferring all of the stress to the surrounding region which results in more extensive deformation in the aluminum and epoxy regions.

To determine whether any changes in particle size affects the degree of strain in the particles, an examination of composites containing small aluminum particles was taken by analyzing the microstructures of MNML-2, -4, -6, -8 following compression at a strain rate of $1 \times 10^{-4} \text{ s}^{-1}$ and a bulk plastic strain of approximately 21.5%. This

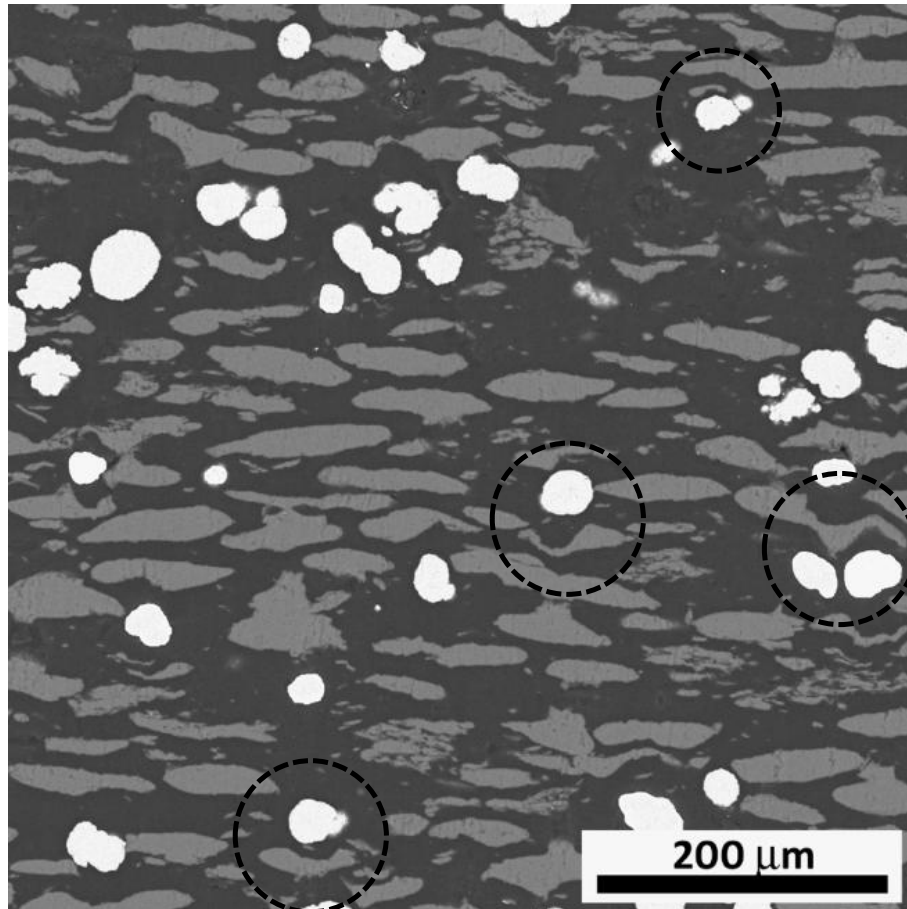


Figure 4.54: Microstructure of MNML-1 following dynamic uniaxial compression at a strain rate of $5 \times 10^3 \text{ s}^{-1}$. The amount of bulk plastic strain is approximately 36%. Dashed circles indicate regions where aluminum deformed and wrapped around the stiffer nickel particles.

strain rate and strain level was chosen due to the consistent measured post compression plastic bulk strain across each composite. With the exception of MNML-2 the levels of strain in the composites containing $5\mu\text{m}$ aluminum were within the same range as the counterpart composites with $50\mu\text{m}$ as shown in Fig. 4.55. Additionally the composites containing nickel had consistently higher rates of aluminum particle deformation for both sizes of aluminum. Therefore, the addition of a small percentage of a much stiffer material, induces larger amounts of strain in the other composite constituents, even if they are present in comparatively low volume fractions (i.e. 20% of aluminum for this composite system). In Fig. 4.55 a line dividing the two types of composites is plotted on the inset figure. The similarity in strain levels in aluminum between composites with large and small composites may be due to readily accessed states of equilibrium that the composites achieve at these rates of strain. In these states the epoxy chains are allowed to move more freely and stress transfer between the different constituents results in fewer sites of stress/strain localizations to occur. Particle strain distributions were tabulated for each composite at this strain rate and plastic bulk strain and are plotted as histograms in Fig. 4.56. While the main peaks of the distributions are fairly close to one another, the composites with Ni are found to have a wider distribution of particle strains with a slightly larger number of particles at the high end of the distribution. Aluminum particle size also had an effect on the distribution. Composites with larger particles are also more likely to have a portion of particles that achieve much larger particle strains, as shown in 4.56 where MNML-3 has particles that reach plastic strain between 120-125%. This is due to the more heterogeneous distribution of particles and greater degree of particle-particle interactions causing an increased amount of stress and strain localizations to nucleate. These particle-particle interactions result in strain gradients around the Ni particles that extend out to approximately one particle diameter (from microstructure observations). Small aluminum particles are more likely to be fully contained within the

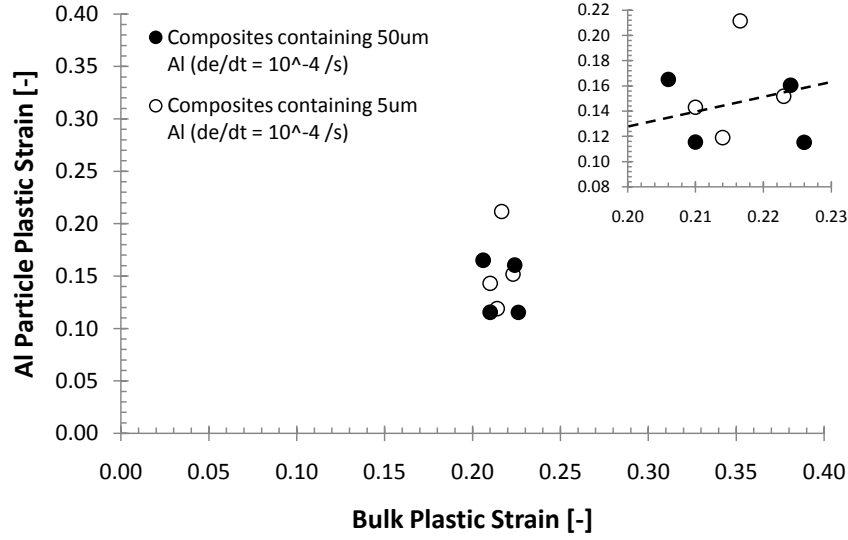
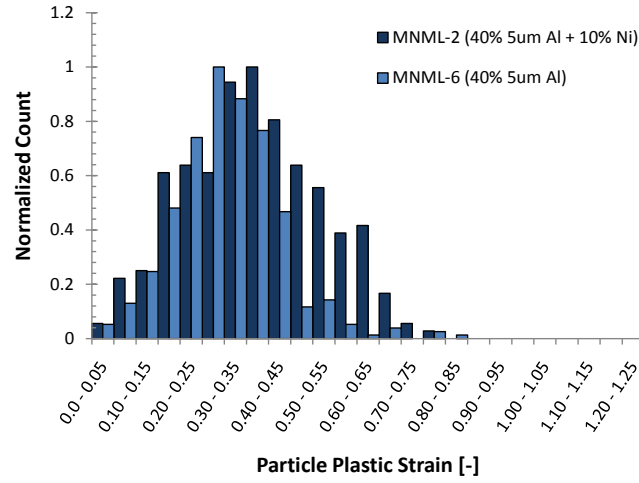


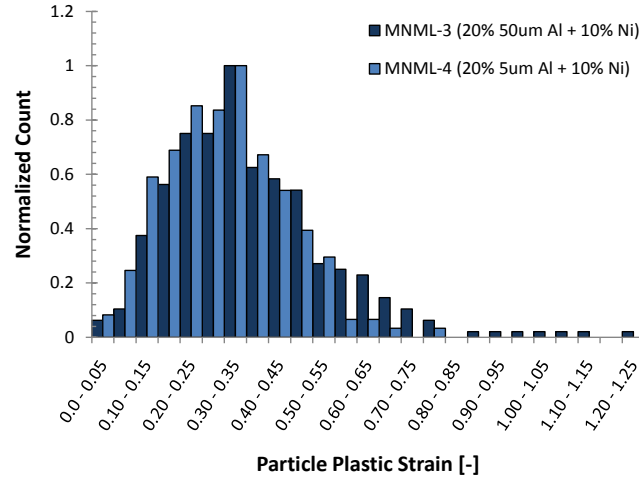
Figure 4.55: Particle strain in aluminum for MNML-2, -4, -6, and -8 at a strain rate of $1 \times 10^{-4} \text{ s}^{-1}$ and bulk strain of approximately 21.5%. Results are also plotted with those for the similar composites with larger aluminum particles. The dotted line (arbitrarily drawn with no mathematical basis) represents the divider where the data points above this level of particle strain represent materials with Ni and those below without Ni.

strain gradient surrounding the Ni particles and therefore experience a more uniform strain field due to their smaller size. Larger aluminum particles on the other hand are more likely to be partially located within the strain gradient field surrounding the Ni particles. Because of their larger size, this would cause them to experience more of the strain field and have a much larger variation of strain across the extent of the aluminum particles. For the composites containing larger aluminum particles this would result in larger and nonuniform straining of the aluminum particles.

In order to determine if particle strains in aluminum due to dynamic strain rates for composites containing small Al particles were similar to those at the lowest quasi-static strain rate, MNML-2 was chosen for further microstructure analysis at the other experimental strain rates. A microstructure of MNML-4 at a strain rate of $1 \times 10^3 \text{ s}^{-1}$ with a lower plastic bulk strain (7.2%) was also analyzed. The results of this analysis are shown in Fig. 4.57. Considering the quasi-static and dynamic strain



(a) Particle strain distribution for aluminum in composites MNML-2, and -6, at a strain rate of $1 \times 10^{-4} \text{ s}^{-1}$ and bulk strain of approximately 21.5%. The distributions are wider for the composite containing Ni and have more particles that strain to higher amounts.



(b) Particle strain distribution for aluminum in composites MNML-3, and -4, at a strain rate of $1 \times 10^{-4} \text{ s}^{-1}$ and bulk strain of approximately 21.5%. The distributions are wider for the composite containing larger aluminum particles due to the more heterogeneous distribution of particles and greater degree of particle-particle interactions causing an increased amount of stress and strain localizations to nucleate.

Figure 4.56: Particle strain distribution for aluminum in composites MNML-2, -3, -4 and -6, at a strain rate of $1 \times 10^{-4} \text{ s}^{-1}$ and bulk strain of approximately 21.5%.

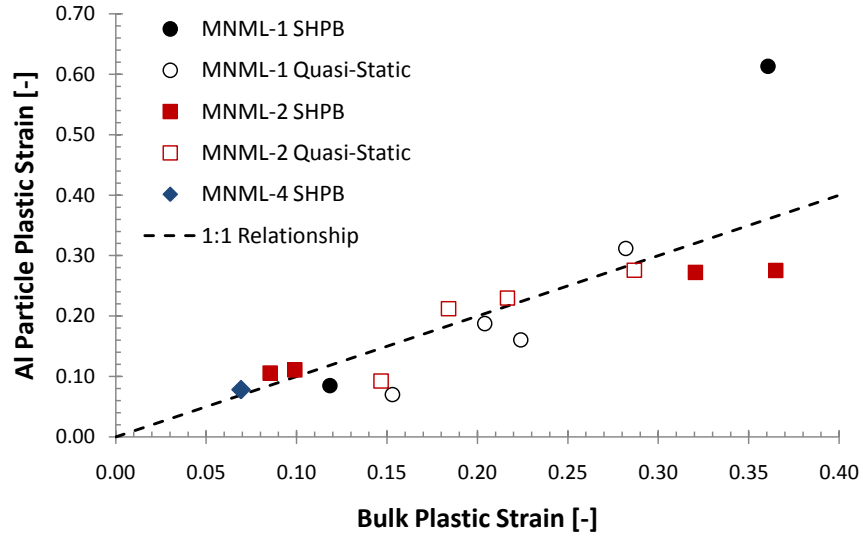


Figure 4.57: Plot of particle size effects on the degree of particle plastic strain found in epoxy based composites. Results for MNML-1 (40% 50 μ m Al + 10% Ni) are shown in black, MNML-2 (40% 5 μ m Al + 10% Ni) Red, and MNML-4 (20% 5 μ m Al + 10% Ni) Blue.

rate data for MNML-2, the particle deformation shows no pronounced changes with a change in strain rate. At low strains the deformation of aluminum is greater than the bulk strain for higher strain rates. However, at higher bulk strain levels the measured particle strains were lower than that of the bulk strain. When small particles are in the epoxy matrix there are a larger number of particles that strain for the same loading fraction of particles. These particles are more evenly distributed between the nickel particles for MNML-1 vs. MNML-2, which decreases the amount of particle-particle interactions, and has a pronounced effect on the particle strain distributions of aluminum as well. In Fig. 4.58 a much wider distribution of strains for MNML-1 can be seen with up to 162%, where as for MNML-2 the particle strains were confined below 100% for the same level of bulk strain.

Earlier it was mentioned that the nickel particles aid in the straining of the aluminum particles a great deal when they are within an affected zone surrounding the

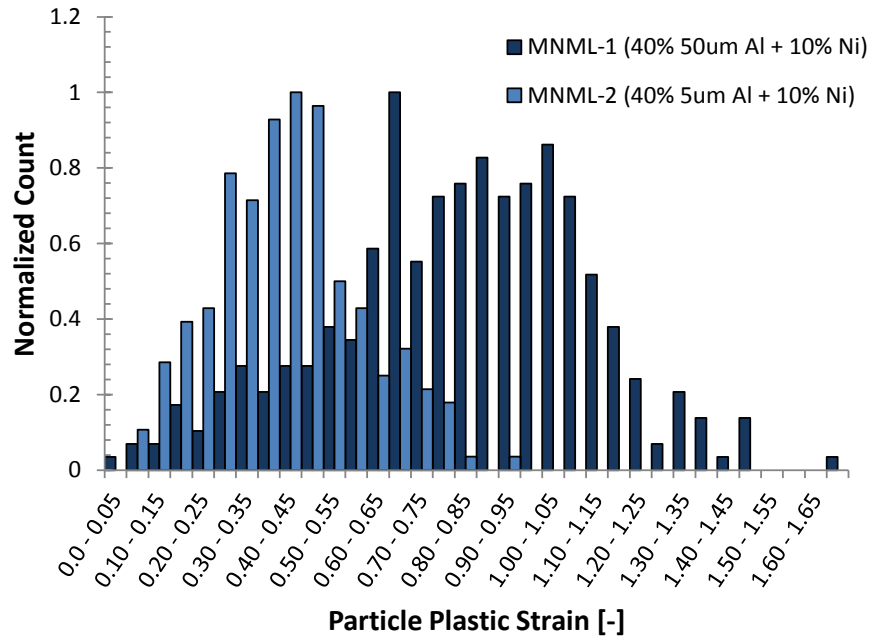


Figure 4.58: Particle strain distribution for aluminum in composites MNML-1, and -2, at a strain rate of $5 \times 10^3 \text{ s}^{-1}$ and bulk strain of approximately 36.0%. At higher strain rates the larger aluminum particles a greater degree of particle-particle interactions causes an increased amount of stress and strain localizations to nucleate at a much faster rate than composites with smaller aluminum particles.

nickel particles. To get a better idea of the extent to which the nickel particles influence the deformation of the aluminum an image mapping the strain in each particle was prepared using Matlab. Based on the amount of strain in the particles they were artificially colored, with a more red color representing a particle that has strained more. It was found that the highest degree of strain in aluminum occurs near the poles surrounding the nickel particles (see Figs. 4.59 and 4.60 for microstructures conducted at $1 \times 10^{-3} \text{ s}^{-1}$ and $1 \times 10^{-4} \text{ s}^{-1}$, respectively with the loading axis aligned in vertical direction). The particles also deform to match the contours of the nickel particle morphology. Since the nickel deforms very little, as the rest of the composite is compressed, the material above and below the nickel gets squeezed against the nickel anvils with compressive stresses aligned with the loading axis. However, the motion of the material on the sides is constrained by the nickel which limits the amounts of strain in the aluminum to lower values. This is indicated by particles colored with a more bluish hue. This constraining effect is even more pronounced in regions between two horizontally aligned nickel particles within close proximity (see Fig. 4.60). In between the Ni particles the strain fields constrain the deformation of the aluminum thereby decreasing their overall strain levels and help prevent excess damage from being generated in that region.

The deformation of the particles has a similar morphology for the composites containing large aluminum particles, such as can be observed in Fig. 4.61 for a particle strain mapping for MNML-1 at a bulk strain of $\approx 36.0\%$ and strain rate of $5 \times 10^3 \text{ s}^{-1}$. For the composites containing larger aluminum particles, while the Al particles in close proximity to Ni still wrap around and conform to the contours of the Ni particles, in the regions between the Ni particles they are elongated and have high aspect ratios. The difference is that for composites containing small Al particles this extreme elongation is distributed amongst many particles. Also by observation of the resulting microstructure from these tests the radius of the affected region around the

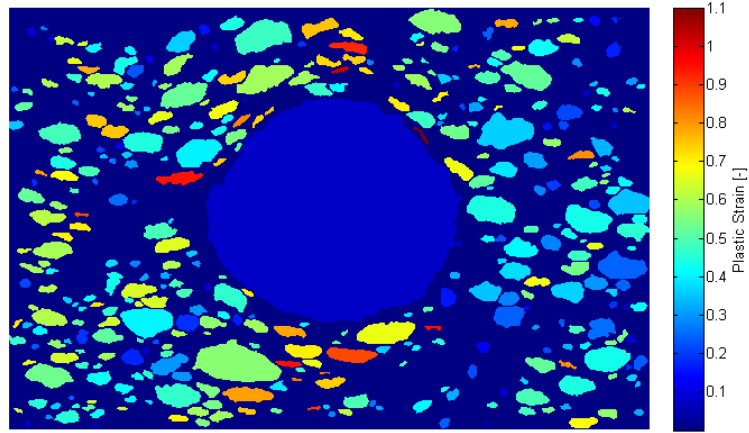


Figure 4.59: Particle strain mapping for MNML-2 (40% 5 μ m Al + 10% Ni) with a bulk plastic strain of 28.7%. In this figure the aluminum particles with the largest strains are located near the poles of the Ni particle (large particle located in center of image). As the Ni-Al particle distance increases the Al particle strain decreases magnitude. Image is from a compression test conducted at a strain rate of $1 \times 10^{-3} \text{ s}^{-1}$.

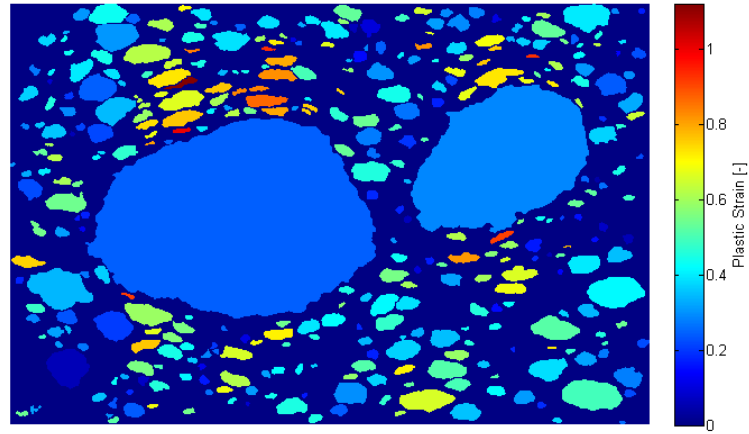


Figure 4.60: Particle strain mapping for MNML-2 (40% 5 μ m Al + 10% Ni) with a bulk plastic strain of 21.7%. In this figure the aluminum particles with the largest strains are located near the poles of the Ni particle (two larger particles). As the Ni-Al particle distance increases the Al particle strain decreases magnitude. Also, in between the Ni particles the strain fields overlap placing a constraint on the deformation of the aluminum. This decreases their overall strain levels which would also prevent excess damage from being generated in that region. Image is from a compression test conducted at a strain rate of $1 \times 10^{-4} \text{ s}^{-1}$.

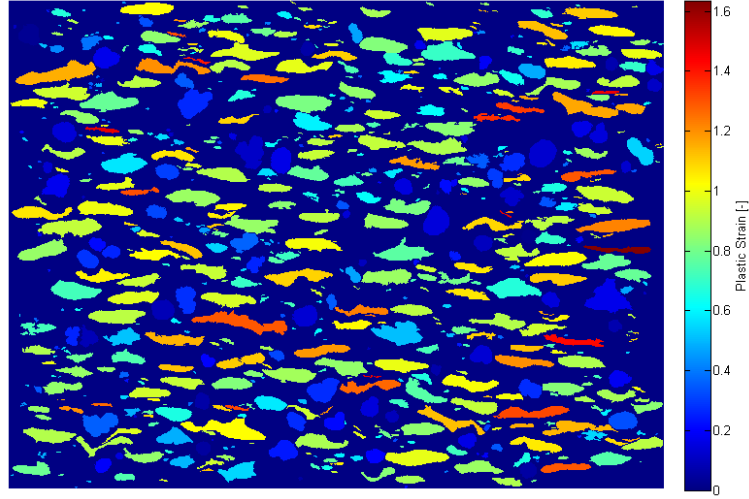


Figure 4.61: Particle strain mapping for MNML-1 (40% 50 μ m Al + 10% Ni) with a bulk plastic strain of 36.0%. In this figure the aluminum particles strain the most near the poles of the Ni particles (small darker blue particles located throughout image). The strain fields around the Ni particles has been estimated to be as thick as 0.5 - 1.0 Ni diameters by measuring distances between the Ni particles and matching contoured regions of the Al particles.

Ni particles is estimated to have a thickness as much as 0.5 - 1.0 times the diameter of the nickel particles. This translates to roughly 24 - 48 μ m respectively.

4.6.2 Summary of Particle Strain Analysis from Microstructures

From post-mortem examination of the composite microstructures following compression at quasi-static and dynamic strain rates, the aluminum was found to strain at higher rates in comparison to the bulk for the dynamic strain rate regime. This was due to the epoxy exhibiting a strong bilinear yield strength dependence on strain rate with a transition that occurs at intermediate rates of strain. At dynamic strain rates the epoxy therefore has a higher strength which in this case makes it stronger than aluminum. This causes the aluminum to deform to higher extents. Aluminum also had higher strains for composites containing Ni, which strained very little. This was due to Ni acting as small anvils distributed throughout the epoxy matrix. Because of this aspect, the aluminum in close proximity to nickel had higher strain levels than in

the bulk regions. They were also higher for Al particles located near the poles aligned with the axis of uniaxial compression. Aluminum particle strains were found to be as high as 170% for some aluminum particles in composites containing 40% 50 μ m Al and 10% Ni. The Al particle strains were also higher for the composite MNML-1 as opposed to MNML-2. This is due to decreased particle-particle interactions in composites containing small aluminum particles which have a more homogeneous aluminum particle distribution.

4.7 Thermomechanical Behavior of Epoxy-Based Polymer Composites

4.7.1 Effect of Particle Reinforcement on T_g and $\tan \delta$

Differential scanning calorimetry was used to characterize the glass transition temperature of the various composites at two heating rates 10 and 20 °C/min. As the heating rate increases the glass transition temperature often increases [125]. This effect has also been shown for bulk metallic glasses [126]. As described earlier the glass transition temperature is an important material property for polymers as it marks the transition from glassy (high storage modulus) to rubbery (low storage modulus) behavior. Therefore any change in the glass transition temperature due to particle reinforcement could potentially have dramatic effects on the deformation behavior of the composites at high rates of strain where temperatures can rise adiabatically. The results of the DSC tests are tabulated in Table 4.11. With an increase in heating rate the glass transition temperature increases, and as much as 24% for MNML-2.

The glass transition temperatures are plotted against the volume fraction of particle reinforcement in Fig. 4.62. For both heating rates there is an increase in T_g from 0.20 to 0.30 particle loading fraction. Beyond this amount of reinforcement the glass transition temperature begins to decrease with particle loading. At 0.50 the glass transition temperature increases again for the composites tested at 20 °C/min. This type of behavior has been seen in epoxy/carbon nanotube composites where the drop

Table 4.11: Glass transition temperatures determined from DSC measurements at two different heating rates.

Material	T_g 10 °C/min [°C]	T_g 20 °C/min [°C]	Increase [%]
Epoxy	67.72 ± 0.97	72.40 ± 0.97	6.9
MNML-1 (40% 50 μ m Al + 10% Ni)	70.67 ± 0.49	74.78 ± 0.44	5.8
MNML-2 (40% 5 μ m Al + 10% Ni)	76.41 ± 2.04	83.35 ± 0.50	7.8
MNML-3 (20% 50 μ m Al + 10% Ni)	75.55 ± 1.39	77.70 ± 0.76	2.8
MNML-4 (20% 5 μ m Al + 10% Ni)	71.32 ± 0.61	75.32 ± 0.62	5.6
MNML-5 (40% 50 μ m Al)	63.39 ± 1.29	71.50 ± 0.45	12.8
MNML-6 (40% 5 μ m Al)	70.25 ± 0.44	74.64 ± 0.54	6.2
MNML-7 (20% 50 μ m Al)	71.21 ± 0.71	74.68 ± 0.48	4.9
MNML-8 (20% 5 μ m Al)	67.36 ± 1.64	73.52 ± 0.43	9.2

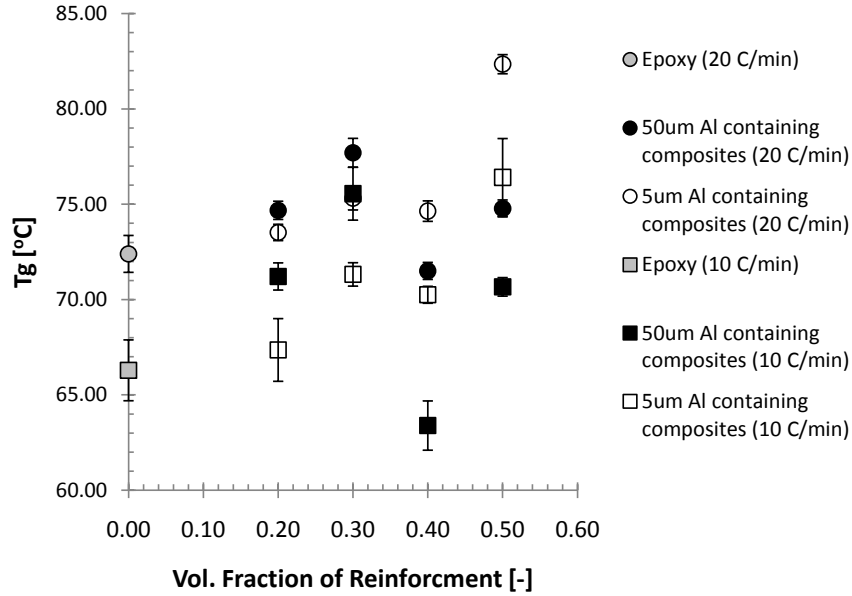


Figure 4.62: Glass transition temperatures for each composite determined at two different heating rates using a DSC. The upper grouping of data points are for the glass transition temperatures measure at a heating rate of 20 °C/min, and the lower grouping 10 °C/min.

in T_g corresponded to the volume fraction of nanotubes coinciding with a percolation threshold that offered the greatest mobility of the polymer chains [127].

At this point it should be mentioned that the glass transition temperatures are lower than that of the pure epoxy for MNML-5 (40% particle loading fraction) at the lower heating rate indicating that the particles may be acting as plasticizers in certain configurations. Also, the variability of the glass transition temperature was fairly high in these tests due to the small sample size associated with the experimental procedure. Therefore, the glass transition temperature will be taken as those determined by DMA as the sample sizes were much larger and more representative of the bulk.

Using dynamic mechanical analysis the glass transition temperature was taken as the temperature at which the $\tan \delta$ has a maximum value which corresponds to the mid-point of the glass transition in the composites. As with the glass transition temperature determined from DSC measurements, T_g increases with volume fraction

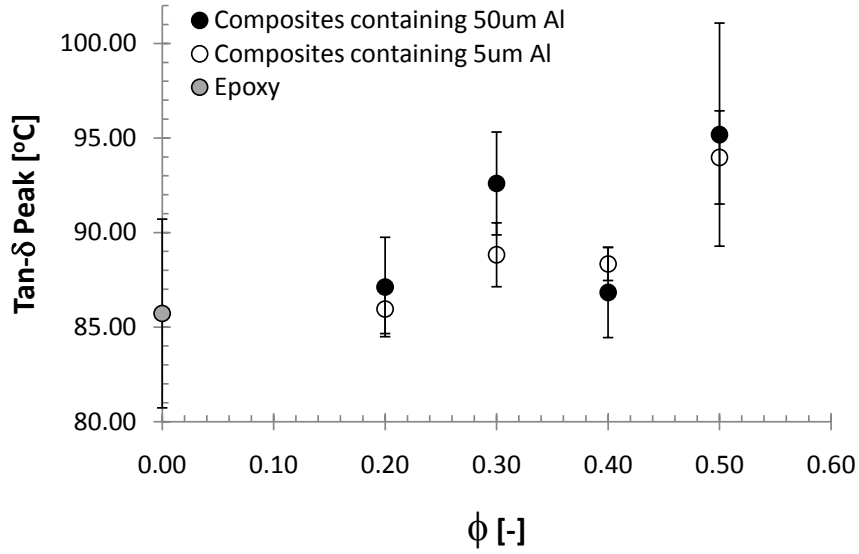


Figure 4.63: Glass transition temperature determined from $\tan \delta$ peaks.

of particles indicating the particles are constraining the polymer chain motion required for the glass relaxation to occur (see Fig. 4.63). The affected regions around the particles may extend far enough into the epoxy matrix disrupting the percolation of unaffected epoxy. This alters the bulk relaxation behavior by increasing the amount of energy needed for the relaxation to occur. There were also noticeably higher glass transition temperatures for the composites containing nickel. This indicates a stronger interaction of the nickel particles with the epoxy matrix through either increased bonding or physical constraints caused by the rougher surface characteristics of nickel particles than that of aluminum. The glass transition temperatures from $\tan \delta$ measurements have been summarized in Table 4.12 along with temperature values corresponding to the loss modulus (E'') peaks for comparison. See Appendix C.2 for representative $\tan \delta$ and loss modulus curves for epoxy and each epoxy composite.

As discussed in Chapter 2, the introduction of particles into a polymer matrix often produces a shift not only in the $\tan \delta$ peak temperature but decreases the height and broadens the width of the peak as well. These same effects were observed for the

Table 4.12: Glass transition temperatures from loss modulus and $\tan \delta$ peak temperatures. The $\tan \delta$ peak height is also shown in the table.

Material	$T_g(\text{E'' Peak})$ [°C]	$T_g(\tan \delta \text{ Peak})$ [°C]	$\tan \delta$ Peak Height [-]
Epoxy	78.2 ± 3.6	85.7 ± 5.0	0.978 ± 0.084
MNML-1 (40% 50 μm Al + 10% Ni)	85.8 ± 5.2	95.2 ± 5.9	0.681 ± 0.043
MNML-2 (40% 5 μm Al + 10% Ni)	85.7 ± 3.2	94.0 ± 2.5	0.651 ± 0.011
MNML-3 (20% 50 μm Al + 10% Ni)	85.4 ± 2.6	92.6 ± 2.7	0.876 ± 0.030
MNML-4 (20% 5 μm Al + 10% Ni)	81.2 ± 2.2	88.8 ± 1.7	0.877 ± 0.022
MNML-5 (40% 50 μm Al)	78.5 ± 2.5	86.8 ± 2.4	0.889 ± 0.028
MNML-6 (40% 5 μm Al)	80.9 ± 0.7	88.3 ± 0.9	0.782 ± 0.029
MNML-7 (20% 50 μm Al)	81.4 ± 0.8	87.1 ± 2.6	1.017 ± 0.045
MNML-8 (20% 5 μm Al)	77.8 ± 0.6	86.0 ± 1.3	0.945 ± 0.010

epoxy composites in this study. As the volume fraction of the particles increased the effects of peak broadening and decrease in peak height were enhanced as shown in Fig. 4.64. The effect of particle volume fraction on the $\tan \delta$ peak height can be seen in Fig. 4.65. At volume fractions above 0.20 the peak height decreases monotonically with an increase in particle volume fraction. The decrease in peak height is related to the increase in elastic response as opposed to viscoelastic response. When more metallic fillers are used an increase in the reduction of matrix mobility near the particles occurs due to the adsorption of the epoxy on the particle surface, which reduces the free volume and increases the stiffness at the particle-matrix interface. This also causes T_g to increase incrementally with an increase in particle loading fraction. $\tan \delta$ is related to the storage (E') and loss modulus (E'') through the following equation:

$$\tan \delta = \frac{E''}{E'} \quad (50)$$

Since the loss modulus is related to the viscosity and amount of energy converted to heat, when a portion of the viscoelastic constituent is replaced with the relatively rigid elastic particles this decreases the amount of material that can flow, thereby decreasing the amount of energy loss. An increase in the amount of crosslink junctions from the influence of particles also could contribute to this effect. Considering a mechanical coupling, rather than chemical, $\tan \delta$, can also be thought of as the ability of the polymer to bear loads, which due to an increase in elastic material response with higher loading fraction of metal particles, would increase the storage modulus and therefore decrease the $\tan \delta$ peak height according to Eqn. 50. The broadening effect is related to the dispersive characteristics of the particles in the epoxy matrix. Due the variability associated with the spatial distribution of particles different regions will contribute different activation energies towards the overall glass transition. In regions where defects may be present such as with microcracks at the

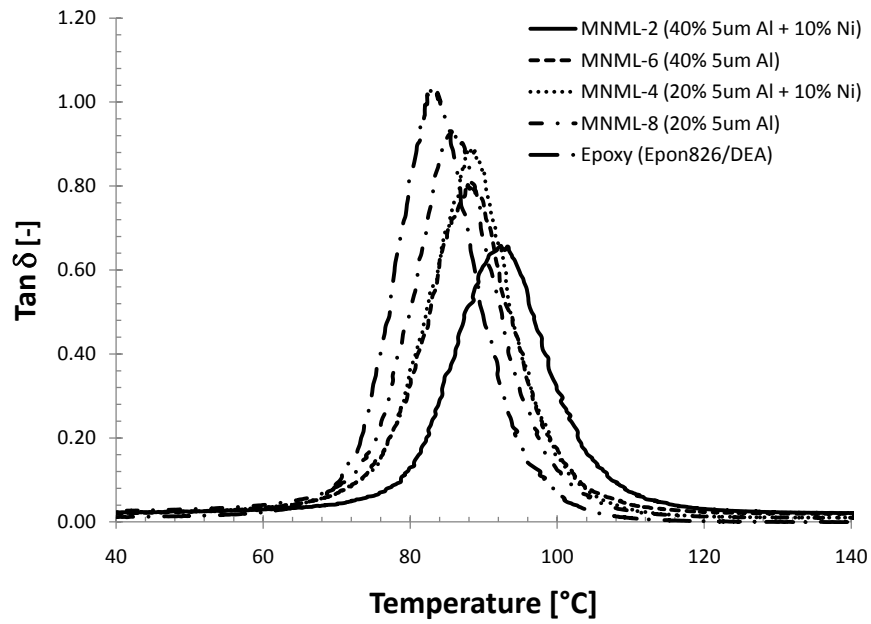


Figure 4.64: Comparison of $\tan \delta$ curves for epoxy-based composites containing 5 μm sized aluminum particles. As the volume fraction of particles increases the $\tan \delta$ peak decreases in height and broadens.

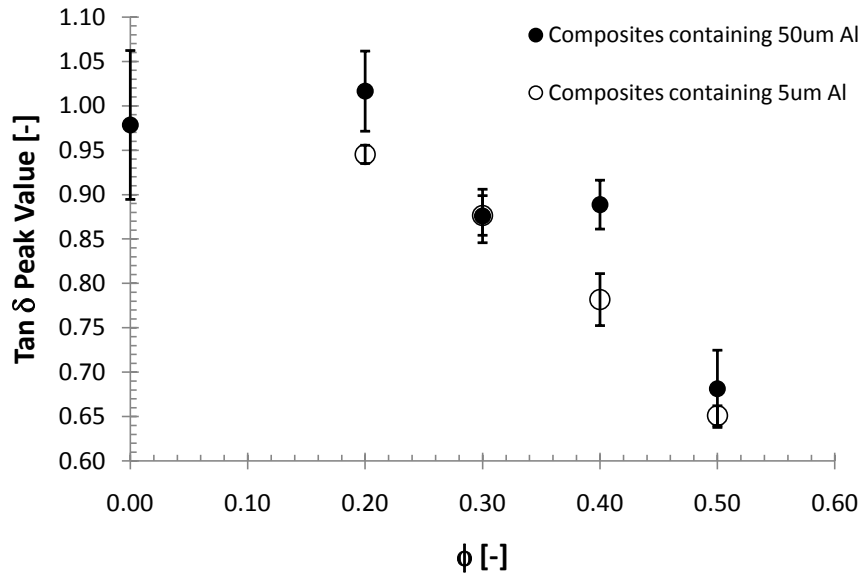


Figure 4.65: Plot of the decrease in $\tan \delta$ peak height as the volume fraction of particle reinforcement increases.

particle matrix interface or weak triaxial stress due to the stress fields formed during the curing of the epoxy, a plasticization effect or decrease in the activation energy for relaxation to occur. Conversely, if there is strong adsorption of epoxy molecules on the surfaces of the particles and strong triaxial stress fields are created, then epoxy mobility is limited and requires larger activation energies. Ultimately the total amount of activation energy required for the glass transition is a balance of the two extremes and for this system the activation energy is higher.

4.7.2 Effects of Particle Reinforcement on Crosslink Density

The crosslink density can have a dramatic effect on the mechanical behavior of polymers, particularly in the rubbery regime. As the crosslink density increases the storage modulus in the rubbery regime increases. Following the theory of rubber elasticity the crosslink density (N) is calculated using Eqn. 51.

$$N = \frac{E'}{3kT} \quad (51)$$

The storage modulus was measured using dynamic mechanical analysis (DMA) techniques. By increasing the volume fraction of particles in the epoxy matrix the storage modulus was shown to increase in the rubbery regime (see Figs. 4.66 and 4.67). This indicated that the chemistry of the epoxy matrix may be altered by the presence of particles. This effect was also observed for each composite regardless of the size of aluminum particles used. To determine whether or not the size of the aluminum particles or use of nickel had any varying effects on the crosslink density, the storage modulus values were measured at 140 °C and then used to find the crosslink density of the composites. The results of the analysis are summarized in Table 4.13 and plotted in Fig. 4.68. Using the crosslink density values the crosslink spacing was calculated, and is summarized in the same table.

Table 4.13: Crosslink density for epoxy-based composites in this research and for those studied by Martin et al. [14] and Ferranti et al. [3]

Material	ϕ [-]	E' at 140 °C [MPa]	ν_e at 140 °C [nm ⁻³]	$\nu_e^{spacing}$ at 140 °C [nm ⁻¹]
Epoxy	0.00	21.09 ± 2.82	0.58 ± 0.16	1.20 ± 0.04
MNML-1 (40% 50 μ m Al+10% Ni)	0.50	139.94 ± 46.36	9.50 ± 0.42	0.47 ± 0.01
MNML-2 (40% 50 μ m Al+10% Ni)	0.50	183.04 ± 24.24	10.44 ± 1.38	0.46 ± 0.02
MNML-3 (20% 50 μ m Al+10% Ni)	0.30	68.82 ± 1.93	3.93 ± 0.11	0.63 ± 0.01
MNML-4 (20% 50 μ m Al+10% Ni)	0.30	67.93 ± 4.04	3.88 ± 0.23	0.64 ± 0.01
MNML-5 (40% 50 μ m Al)	0.40	83.39 ± 4.81	4.76 ± 0.27	0.59 ± 0.01
MNML-6 (40% 50 μ m Al)	0.40	109.88 ± 3.13	6.27 ± 0.18	0.54 ± 0.01
MNML-7 (20% 50 μ m Al)	0.20	44.38 ± 0.32	2.53 ± 0.02	0.73 ± <0.00
MNML-8 (20% 50 μ m Al)	0.20	41.43 ± 3.33	2.36 ± 0.19	0.75 ± 0.02
Epoxy ^[14]	0.00	11.69 ± 1.69	0.68 ± 0.10	1.14 ± 0.06
21 μ m Ni+17 μ m Al+20wt.% Epoxy ^[14]	0.45	146.13 ± 20.75	8.54 ± 1.21	0.49 ± 0.02
21 μ m Ni+56.3nm Al+20wt.% Epoxy ^[14]	0.45	233.25 ± 93.22	13.6 ± 5.45	0.43 ± 0.05
Epoxy ^[3]	0.00	11.00 ± 1.00	0.64 ± 0.08	1.17 ± 0.05
3.2 μ m Al+ <i>F</i> <i>e</i> ₂ <i>O</i> ₃ +78vol.% Epoxy ^[3]	0.22	61.00 ± 4.00	3.47 ± 0.23	0.66 ± 0.02
3.2 μ m Al+ <i>F</i> <i>e</i> ₂ <i>O</i> ₃ +70vol.% Epoxy ^[3]	0.30	97.00 ± 3.00	5.56 ± 0.16	0.56 ± 0.01
56.3nm Al+ <i>F</i> <i>e</i> ₂ <i>O</i> ₃ +70vol.% Epoxy ^[3]	0.30	97.00 ± 3.00	5.56 ± 0.16	0.56 ± 0.01
3.2 μ m Al+ <i>F</i> <i>e</i> ₂ <i>O</i> ₃ +60vol.% Epoxy ^[3]	0.40	77.00 ± 8.00	4.41 ± 0.48	0.61 ± 0.02
3.2 μ m Al+ <i>F</i> <i>e</i> ₂ <i>O</i> ₃ +47vol.% Epoxy ^[3]	0.53	321.00 ± 32.00	18.31 ± 1.81	0.38 ± 0.01

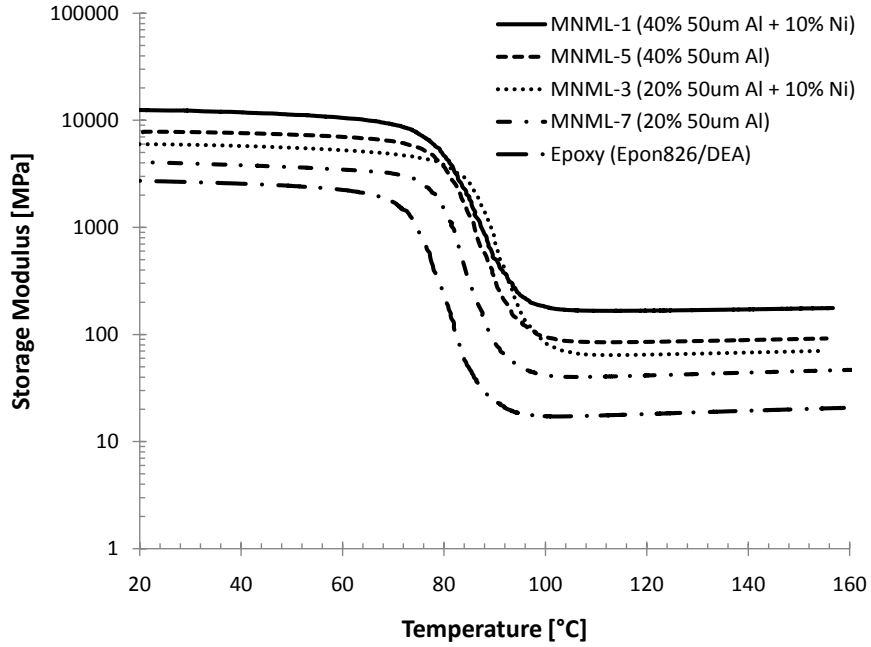


Figure 4.66: Effect of particle loading fraction on the storage modulus for the materials containing $50\mu\text{m}$ sized aluminum particles. Notice how the storage modulus in the rubbery regime increases more than in the glassy regime.

As expected the crosslink density, ν_e , increased with the volume fraction of particles. However, there were no noticeable effects of particle size on the crosslink density until volume fractions of particles greater than 30% were used. At these higher loading fractions the crosslink density was lower for composites containing larger aluminum particles by approximately 30% and 10% for the composites MNML-5 and MNML-1 respectively. The difference between MNML-1 with MNML-2 was also less than the difference between MNML-5 with MNML-6. This may be due to MNML-2 having larger nickel particles within the matrix obscuring a portion of the effects due to the smaller aluminum particles. The nickel particles have a rougher surface than the aluminum particles that could cause an increase in the apparent crosslink density due to an increase in physical entanglements between the epoxy with the nickel. The effects of particle volume fraction and particle size on crosslink density are greater than that of the use of nickel. However, for composites MNML-3 and MNML-4, influences due

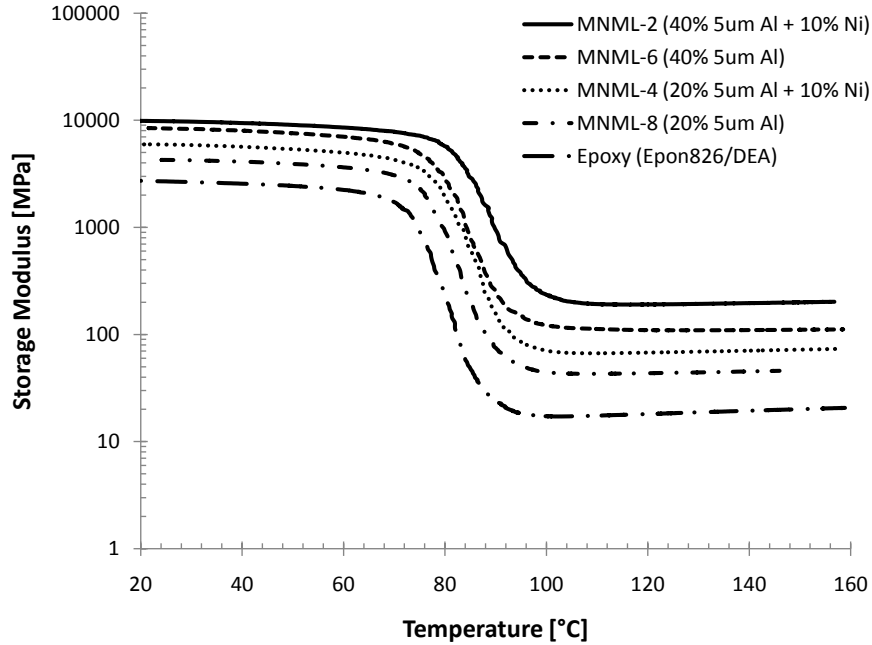


Figure 4.67: Effect of particle loading fraction on the storage modulus for the materials containing $5\mu\text{m}$ sized aluminum particles. Notice how the storage modulus in the rubbery regime increases more than in the glassy regime.

nickel are shadowed by the effects of aluminum particle size and volume fraction. Also shown in Fig. 4.68 are the crosslink spacings between network junctions, which are found to decrease with increased volume fraction for each composite.

Epoxy cast composites prepared with globular nickel and micron/nano sized aluminum particles by Martin et al.[14] and with hematite and micron/nano-sized aluminum particles by Ferranti [3], have also shown similar increases in crosslink density with an increase in volume fraction of particles. The authors also reported dramatic increases in the crosslink density when nano sized aluminum particles were used over micron sized particles. Increases in the crosslink density were as much as 100% in Ni+nano-Al +20wt.% composites containing 45 vol.% of particle reinforcement. For a lower volume fraction of reinforcement (22%) this increase was approximately 27% higher for Fe_2O_3 +nano-Al+78 vol.% epoxy composites in comparison to the equivalent composite system prepared with micron sized aluminum. To understand the

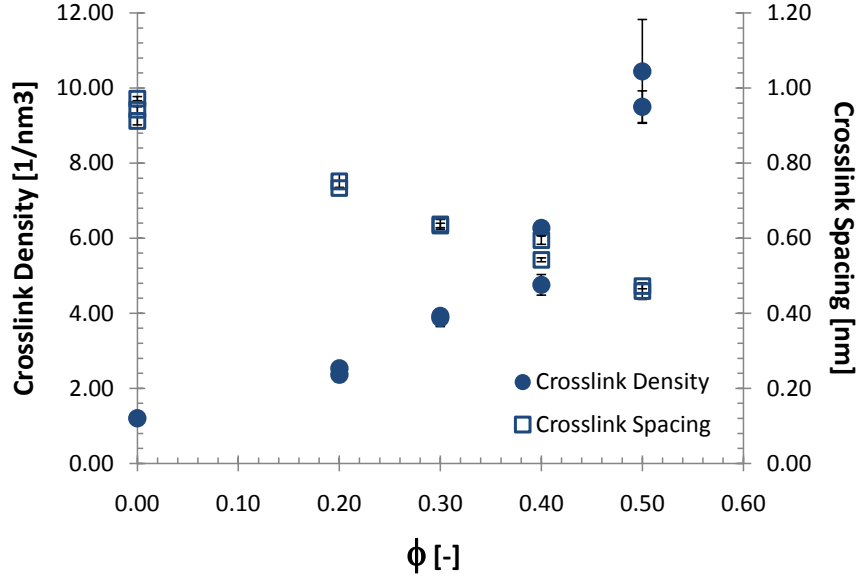


Figure 4.68: Effect of particle loading fraction on the crosslink density and spacing in epoxy-based composites.

effects of particle size on the crosslink density their findings are plotted with results on the composites used in this research, and are shown in Fig. 4.69. It can be seen that as expected the data for composites containing nano-sized particles have much larger increases in crosslink density than those containing micron sized particles indicating that surface area has a large role in the observed ν_e increases by providing additional sites for enhanced bonding or chain entanglement.

4.7.3 Estimate of Interphase Thickness

A more important utility of the DSC experiments to this research is the relation of heat capacity with the interphase thickness in these types of composites. The altered heat capacity ΔC_p across the glass transition temperature was used in calculations that estimate the interphase thickness surrounding the particles. Using the methodology developed by Lipatov [38], discussed in Chapter 2, the interphase thickness is calculated from Eqns. 52 and 53 which is then related to the volume of the interphase through Eqn. 54 (equations are shown here again for readers ease).

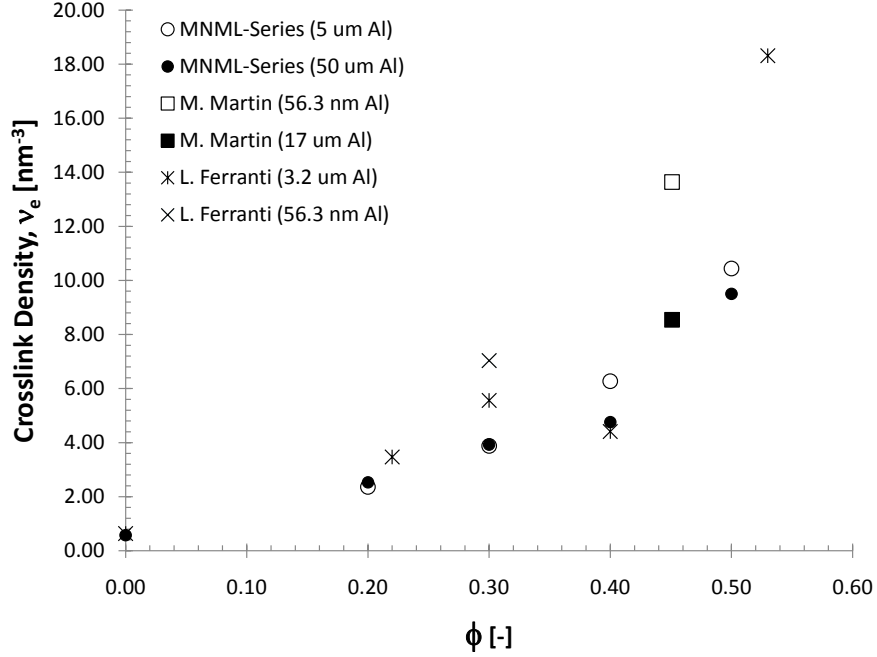


Figure 4.69: Comparison of the effect of particle loading fraction and size on the crosslink density and spacing in epoxy-based composites from multiple studies.

$$\Delta r_i = r_f \left(\frac{\lambda_i \phi}{1 - \phi} + 1 \right)^{1/3} - r_f \quad (52)$$

where,

$$\lambda_i = 1 - \frac{\Delta C_p^{fill}}{\Delta C_p^{Unfill}} \quad (53)$$

$$\nu_i = \left(\left(\frac{\Delta r_i}{r_f} + 1 \right)^3 - 1 \right) \phi \quad (54)$$

The heat capacity was determined at temperatures of $T_g \pm 10^\circ\text{C}$, $T_g \pm 20^\circ\text{C}$, 50°C , and 100°C . Since the rate of heat flow with temperature have fairly constant slopes before and after the glass transition temperature the change in heat capacity across T_g was found to be very similar and averaged for each ΔT values. Results of the calculations are summarized in Tables 4.14 and 4.15.

Table 4.14: Parameter values used in calculation of the interphase thickness and volume.

Material	ϕ [-]	$\Delta C_p^{T_g \pm 10}$ [$\frac{J}{gK}$]	$\Delta C_p^{T_g \pm 20}$ [$\frac{J}{gK}$]	$\Delta C_p^{50/100}$ [$\frac{J}{gK}$]	$\lambda^{T_g \pm 10}$ [-]	$\lambda^{T_g \pm 20}$ [-]	$\lambda^{50/100}$ [-]
Epoxy	0.00	0.480	0.623	0.780	—	—	—
MNML-1	0.50	0.129	0.200	0.199	0.731	0.678	0.745
MNML-2	0.50	0.131	0.182	0.193	0.727	0.707	0.753
MNML-3	0.30	0.187	0.260	0.283	0.611	0.583	0.637
MNML-4	0.30	0.186	0.262	0.286	0.614	0.580	0.634
MNML-5	0.40	0.215	0.315	0.318	0.552	0.495	0.592
MNML-6	0.40	0.189	0.276	0.298	0.607	0.556	0.618
MNML-7	0.20	0.311	0.429	0.447	0.352	0.312	0.427
MNML-8	0.20	0.356	0.483	0.500	0.258	0.225	0.359

Table 4.15: Interphase thickness and volume calculated from changes in heat capacity measured using a DSC.

Material	ϕ [-]	$\Delta r^{T_g \pm 10}$ [μm]	$\Delta r^{T_g \pm 20}$ [μm]	$\Delta r^{50/100}$ [μm]	$\nu_i^{T_g \pm 10}$ [-]	$\nu_i^{T_g \pm 20}$ [-]	$\nu_i^{50/100}$ [-]
MNML-1	0.50	5.12	4.81	5.20	0.30	0.28	0.31
MNML-2	0.50	1.39	1.35	1.43	0.30	0.29	0.31
MNML-3	0.30	2.03	1.94	2.11	0.07	0.07	0.08
MNML-4	0.30	0.79	0.75	0.81	0.07	0.07	0.08
MNML-5	0.40	2.86	2.59	3.05	0.13	0.12	0.14
MNML-6	0.40	0.33	0.30	0.33	0.14	0.13	0.15
MNML-7	0.20	0.74	0.60	0.89	0.02	0.02	0.02
MNML-8	0.20	0.06	0.05	0.08	0.01	0.01	0.02

The interphase thickness calculations are dependent on particle size and volume fraction. As a result, with increases in particle diameter or volume fraction, the interphase thickness increases. The particle size and volume fraction dependence on interphase thickness can be clearly seen in Fig. 4.70. For the composites containing $5\mu\text{m}$ sized aluminum particles, there is a slight increase in the interphase thickness at volume fractions of 0.30 and 0.50. This is due to the presence of the nickel particles which have sizes around $48\mu\text{m}$. Even though the interphase thickness is different for the $5\mu\text{m}$ and $50\mu\text{m}$ sized aluminum particle composites, the interphase volume is nearly the same as shown in Fig. 4.71. At particle loading fraction $V_f \leq 0.20$ the interphase volume fraction is less than 2.0% of the total microstructure. At a higher loading fraction however, the interphase volume fraction increases dramatically on upwards of 30.0% for composites with 0.50 loading fractions of particles. This indicates that the influence of particle reinforcement on the chemistry and mechanical behavior of the epoxy matrix has a far field effect that extends well into the bulk matrix. This can disrupt the percolation of the unaffected epoxy matrix throughout the composite at these high loading fractions of particles and in some instances be the dominant matrix phase. The effects of the interphase on the percolation of the epoxy matrix can be seen in a two-dimensional microstructure for MNML-1 (see Fig. 4.72). Here a Matlab code has been used to artificially create the interphase layer around each particle.

4.7.4 Decomposition Temperature of Epoxy-Based Composites

Thermogravimetric analysis (*TGA*) was used to measure the decomposition temperature, defined as $T = T(98 \text{ wt}\%)$. Measurements show that addition of nickel and aluminum particles into the epoxy matrix improves the thermal stability of the composites. As the amount of filler was increased the thermal stability increased as well, as indicated by shifts of the TGA curves towards higher temperatures (See Figs. 4.73

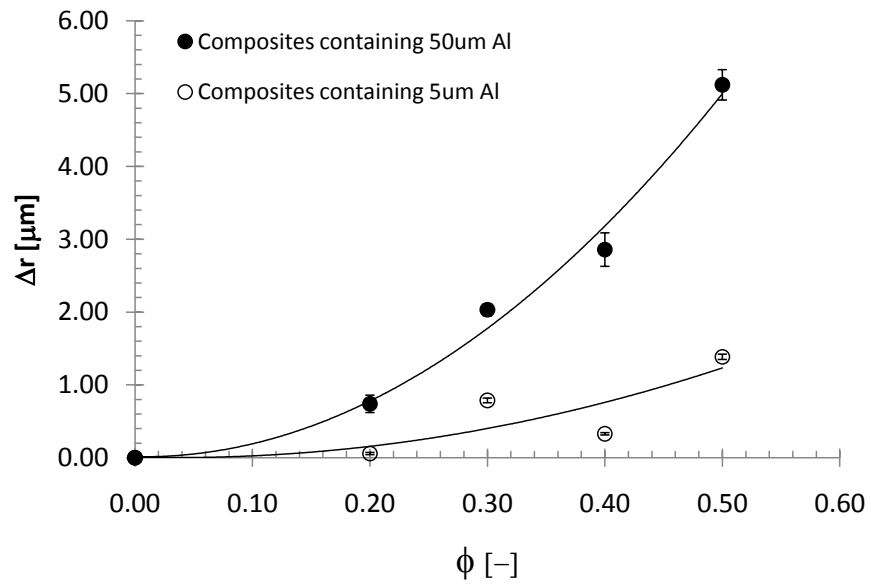


Figure 4.70: Plot of interphase thickness against the total volume fraction of particles. Lines are quadratic fits to the data to aid in guiding the eye.

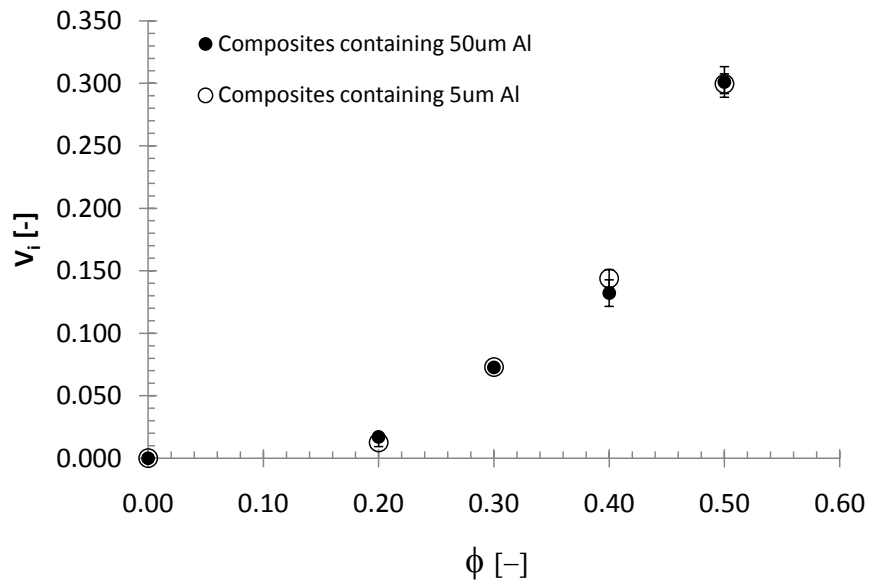


Figure 4.71: Plot of interphase volume fraction against the total volume fraction of particles.

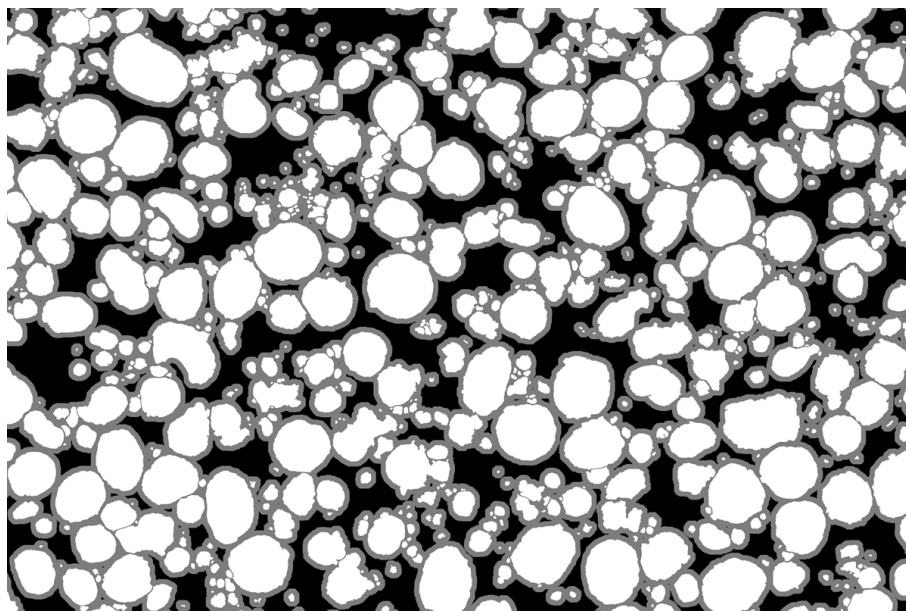


Figure 4.72: Figure showing the interphase (gray) surrounding the particles in a 2D microstructure for MNML-1. In this figure there is no distinction between the Ni and Al particles. Both particle types were threshold to have the same pixel color (white).

and 4.74. This is a common effect that has been observed in other thermoset matrix composites such as epoxies reinforced with carbon black [128] or epoxy reinforced with $TiO_2 - SiO_2$ nanoparticles [129]. The neat epoxy decomposes at 282°C while at 20, 30, 40 and 50% particle loading fraction, the decomposition temperature increases to approximately 307 , 333 , 325 and 337°C respectively. A summary of the TGA results is given in Table 4.16 and plotted in Fig. 4.75. Interestingly at 30% particle loading fraction the composites have dramatic increase in T_{decomp} from the composites with 20% and 40% particle loadings. This indicates the possibility of a preferential loading fraction of particles in the matrix that interact with the polymer chains optimally due to a combination of chemical and physical interactions of the constituents. These interactions form an interphase region at the particle-matrix interface. This may also be an interaction effect of the Ni with epoxy in which the increased surface roughness or thermal conductivity of the Ni particles alter the chemistry of transfer of heat through the composite more efficiently from particle to particle rather than from the

particles to the matrix. This would keep most of the higher temperatures present within the composite in the particle phases and delay the increase in temperature of the epoxy matrix. Since the composites that contain Ni (30 and 50% total particle volume fraction) have large increases in T_{decomp} it would stand to reason that Ni has a strong influence on the stability of the epoxy at higher temperatures. Additionally at higher particle loading fractions positive physical interactions, such as the spatial arrangement of particles and associated stress fields from matrix curing may decrease due to interacting stress fields. As the number of particles increase within the matrix, more surface area is created that would allow for more chemical interactions to occur and increase the bonding and thermal stability of the composites.

Table 4.16: Decomposition temperature of each composite measured from TGA data at $T = T(98 \text{ wt}\%)$.

Material	T_{decomp} [°C]
Epoxy	282.50
MNML-1 (40% 50 μ m Al + 10% Ni)	338.93
MNML-2 (40% 5 μ m Al + 10% Ni)	335.52
MNML-3 (20% 50 μ m Al + 10% Ni)	332.882
MNML-4 (20% 5 μ m Al + 10% Ni)	331.56
MNML-5 (40% 50 μ m Al)	332.21
MNML-6 (40% 5 μ m Al)	325.45
MNML-7 (20% 50 μ m Al)	307.27
MNML-8 (20% 5 μ m Al)	306.78

4.7.5 Summary of Thermomechanical Behavior and Influence of Particles on Epoxy

Thermomechanical analysis allowed for changes to the epoxy matrix to be determined. Using DSC, DMA, and TGA experimental techniques, changes in the glass transition

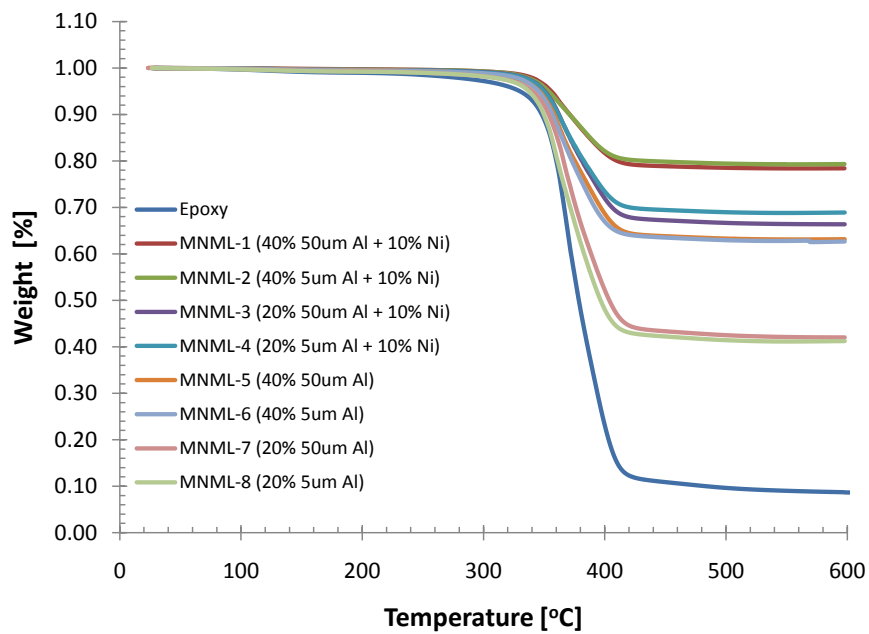


Figure 4.73: Thermogravimetric analysis curves of epoxy-based composites.

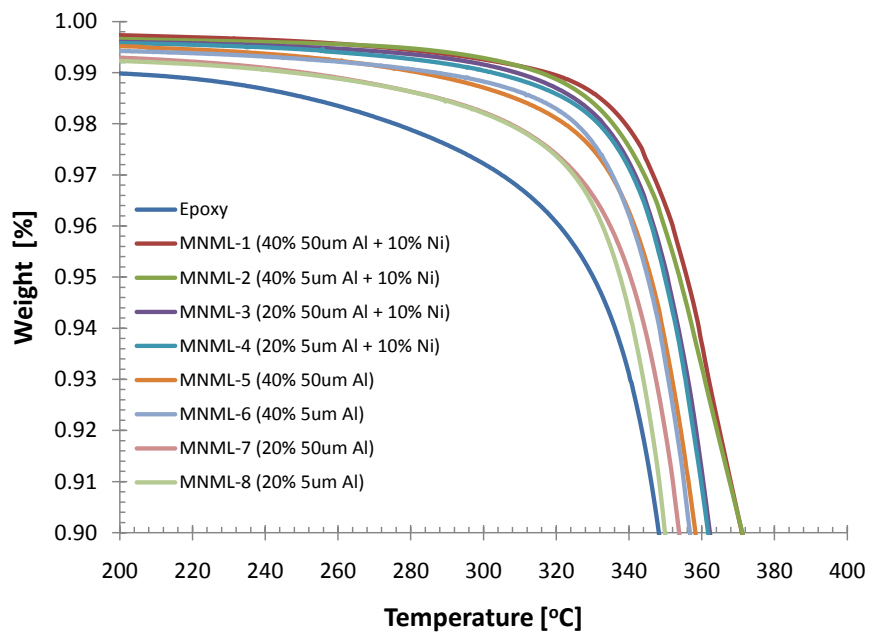


Figure 4.74: Thermogravimetric analysis curves of epoxy-based composites rescaled to show the region decomposition begins.

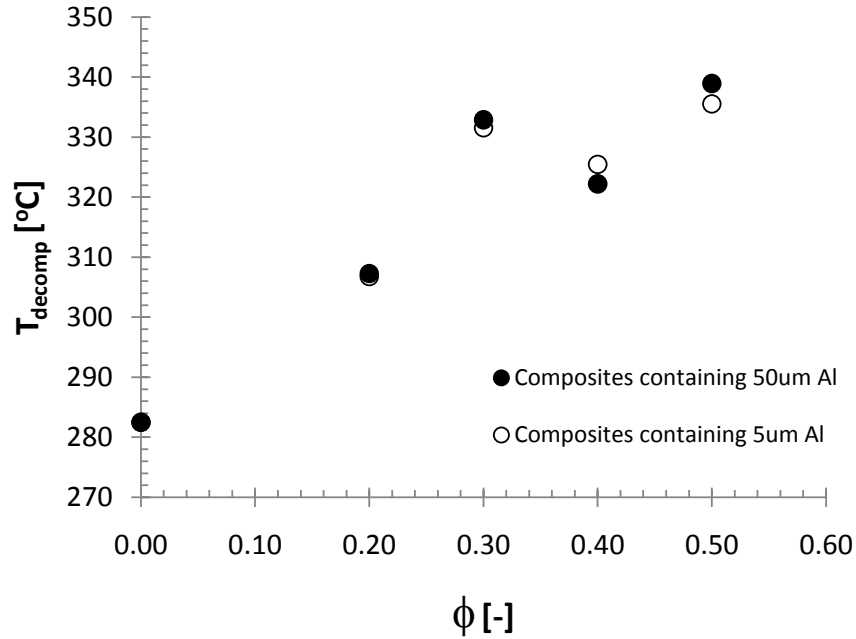


Figure 4.75: Decomposition temperature as a function of volume fraction of particle reinforcement.

temperature T_g , decomposition temperature T_{decomp} , and crosslink density ν_e were all measured for the various composites. T_g increased towards higher temperatures as the amount of filler increased. This gives more mechanical advantage to the epoxy by keeping it in the glassy regime longer as the temperature increases in the composite allowing it to contribute to the deformation of aluminum over longer durations until epoxy transitioned into its rubbery state.

The decomposition temperature increased with composite filler percentage by increased bonding or physical entanglements at the epoxy-particle interfaces or other changes in chemistry. Increases between 14 and 56 °C were found for 20 and 50 particle loading fractions respectively. The effect of this is increased thermal stability which as with increased T_g temperatures places a key role in the deformation behavior of the composites at the mesoscale, especially at high rates of strain where

large increases in temperature due to adiabatic heating are possible. With the increased thermal stability the epoxy network stays intact longer which gives more cohesive composite strength and ability to transfer stresses between constituents at these higher temperatures.

The crosslink density also increased by as much as 1800% over that of pure epoxy with increasing particle volume fraction as determined from the increased storage moduli values measured in the rubbery regime for each composite. This change in chemistry effects the epoxies ability to relax, its strength, T_g and T_{decomp} . With shorter distances between epoxy network junction points, the epoxy has greater back stresses and resistance to stretching as deformation of the composite takes place while under load. The sources of the increased crosslink junctions are most likely with particle surfaces. Thus, it is suspected that composites with particles of smaller diameter but same total volume fraction would result in higher crosslink densities. This effect was not observable in this system until particle loading fractions reached levels above 30%. This is probably due to the particles lying in the micron scale regime since other studies have shown that for epoxy composites containing nano-sized particles [3], the effect was more pronounced at lower volume fractions.

This increased crosslinking or bonding of the epoxy with particles, alters the natural configuration of the network near and at the matrix-particle interface to create an interphase region. The interphase region characterized using heat capacity data based on an analysis developed by Lipatov [38], showed that the interphase thickness and volume increase with particle size and volume fraction. For MNML-1 and -2 this interphase volume was as much as 30% of the total composite volume with thickness surrounding the particles of approximately 5.0 and 1.4 μm respectively.

CHAPTER V

MESO-SCALE SIMULATIONS OF EPOXY-BASED COMPOSITES USING ALE3D

Details regarding the evolution of the deformation behavior at the particle level are not practically attainable through experimental techniques other than by means of post-mortem microstructure analysis on tested samples. From the particle strain measurements detailed in the previous section, the amount of strain measured for the particles was found to be dependent on the bulk plastic strain and compressive strain rate.

For uniaxial compression tests conducted at quasi-static rates of strain, the tests are easily terminated at different strain levels. However, at higher strain rates the task of stopping the tests at different levels of strain is very difficult; hence, no attempts were made to do so.

Computational efforts are an alternative approach to examining the material behavior and can be more cost effective and lead to a greater understanding of mechanisms taking place during high rate impact loading conditions. This is due to the vast amount of additional data available at each time step of calculation that is not available in an experimental setup. In a sense each time step calculation is equivalent to an experiment that was stopped at the same time during a loading process and becomes a snap shot of the evolution of a material's state. Computational studies on materials also allow for the simulation at scales on the particle level. Therefore, in order to more fully understand the contributions of each composite constituent towards the overall bulk mechanical and deformation behavior at the mesoscale, computational

studies implementing three dimensional microstructure domains were carried out using ALE3D [130], which is an Arbitrary Lagrangian Eulerian hydrocode developed by Lawrence Livermore National Laboratory. More specifically explicit simulations examining the high strain rate behavior of the composites are investigated.

5.1 Microstructure Generation

One of the first steps in conducting simulations at the mesoscale is to import or generate microstructures for the microstructure domain. Although there are a variety of methods that are often used to generate microstructures, the program Particle Pack 2.4 [131] was chosen for the simulations conducted in this research. Particle Pack 2.4 allows the user to import a particle size histogram with a corresponding volume fraction for each bin to create a set of particles that are then randomly distributed in a volume defined by the user. The user can also assign a material type to each bin that is later used by ALE3D to assign them their material properties. Since the particles are approximately spherical, as has been discussed previously the geometry for the particles created by Particle Pack 2.4 were chosen to be spheres. This is not expected to yield unrealistic stress-strain behavior or dramatic differences in particle strain measurements. A couple of microstructure generations using Particle Pack 2.4 are shown in Fig. 5.1 without the presence of an epoxy matrix.

An advantage to using Particle Pack is the ability to generate three dimensional microstructures in a fraction of the time it takes using other methods, such as collecting a stack of images from serial sectioning or by using X-ray computed tomography (CT). However, by doing so fine features of the particles such as surface roughness and undulations or ellipticity are lost since an idealized perfect sphere geometry is used when generating the particles. Another disadvantage of using Particle Pack, is that it does not generate truly randomized microstructures. Instead, Particle Pack places particles in the domain in order of those with the largest diameters to those with

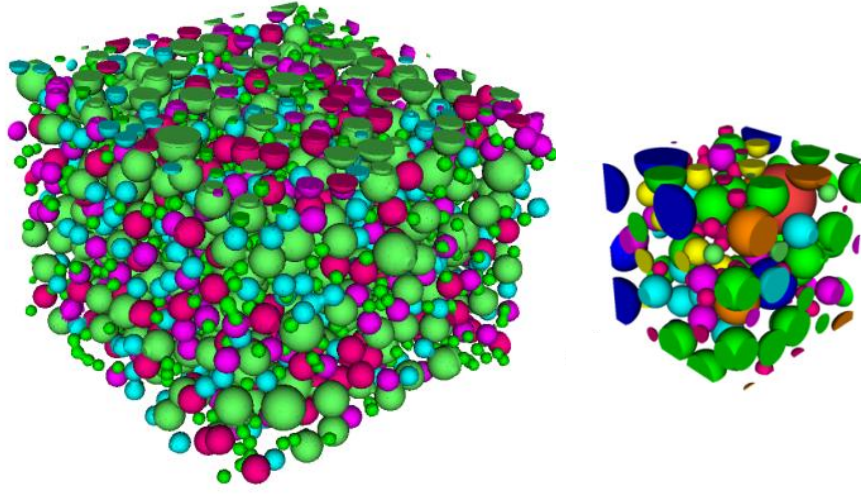
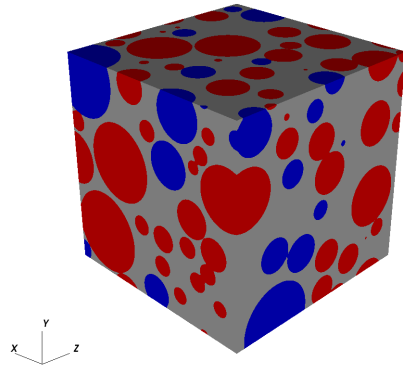


Figure 5.1: Two instances of microstructures generated using Particle Pack 2.4.

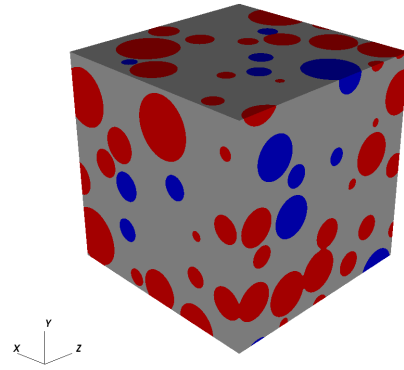
the smallest diameters. This introduces a correlation between particle size and type with their spatial distribution, which may have an effect on the simulated composite behavior. Two-point correlation and higher order n -point correlation functions would be advantageous to compare generated microstructures with the real microstructures. However, in this research, correlation functions were not implemented.

For composites experimentally measured properties are representative of the bulk material and are not typically the same property value that would be calculated from computational studies at the mesoscale. However, by using representative microstructural volumes that are large enough to capture the response of the material properties of interest this can be circumvented, but at a cost of computational resources and time. In the following computation studies, the microstructure domains were therefore made as large as reasonably possible taking into account the mesh resolution and time required to run the simulations. The size of the microstructure domain was chosen for the composites MNML-1, 3, 5, and 7 to be $250 \times 250 \times 250 \mu\text{m}$ with mesh resolution of $4 \mu\text{m}$. For composites MNML-4 and 8 the microstructure domain was

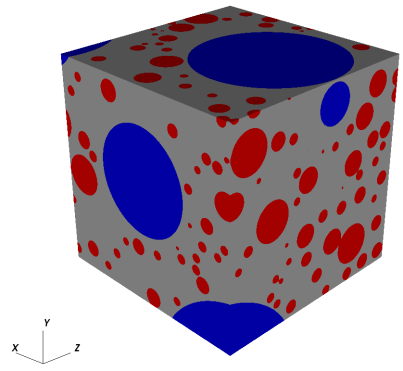
chosen to be $50 \times 50 \times 50 \mu\text{m}$ with mesh resolution of $0.4 \mu\text{m}$. In Fig. 5.1 the resultant microstructures for MNML-1, 3, 4, 5, 7 and 8 are shown with particles embedded in an epoxy matrix. From the exterior surfaces a randomized spatial distribution of the particles and range of particle sizes can be seen.



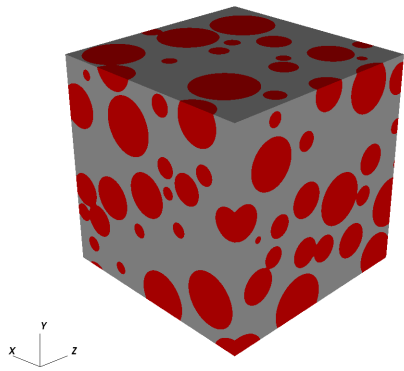
(a) MNML-1 (40% (50 μm) Al, 10% Ni).



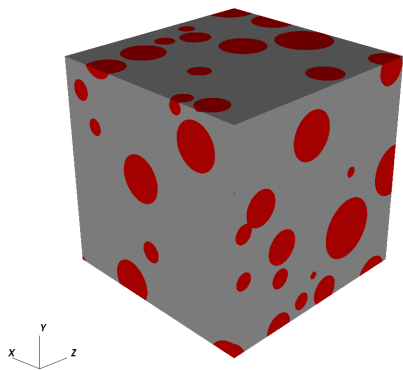
(b) MNML-3 (20% (50 μm) Al, 10% Ni).



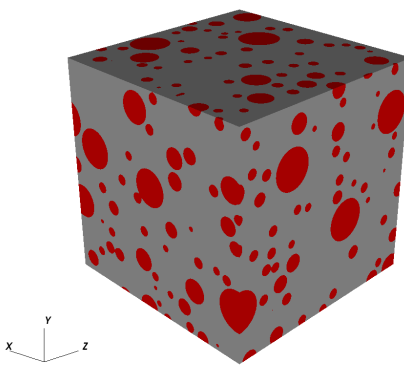
(c) MNML-4 (20% (5 μm) Al, 10% Ni).



(d) MNML-5 (40% (50 μm) Al).



(e) MNML-7 (20% (50 μm) Al).



(f) MNML-8 (20% (5 μm) Al).

Figure 5.2: Composite microstructure domains. Aluminum is shown in red, nickel in blue, and epoxy gray.

5.2 Mesoscale Simulation Boundary Conditions

Once the microstructure domains were established, symmetry boundary conditions were placed on the bottom and two adjacent sides as shown in Fig. 5.3. For the top a rigid steel plate with a velocity loading condition was used to apply a compressive load at a strain rate of 4620 s^{-1} . This strain rate was chosen so as to better correlate results with uniaxial compression experiments using the split Hopkinson pressure bar carried out at nominal strain rates of 5000 s^{-1} , which had an actual experimental average strain rate of 4620 s^{-1} . Between the rigid steel plate and the composite a sliding surface was used with zero friction between the steel plate and microstructure domain. For the remaining two sides a region of air borders the microstructure. This is to allow the advection of material at the boundaries to take place without causing too much element distortion that would cause the simulation to abort early. To ensure the air region did not influence the behavior of the composite constituents, it was given no strength which essentially made this region act as a void.

5.3 Simulation Material Models

In epoxy-based structural energetic materials, the elastic properties of the individual constituents are highly contrasting, meaning that they differ from one another by large amounts. This requires that the materials used in the simulations have well defined material models to ensure as accurate of a material response as possible.

For nickel and aluminum the constitutive behavior of the material was defined by the Steinberg-Guinan rate independent strength model [132] This model is ideal for the strain rates used in these simulations and the material model parameters are well characterized for both nickel and aluminum. In this model, the yield strength is a function of pressure, temperature, and strain hardening through the following equation:

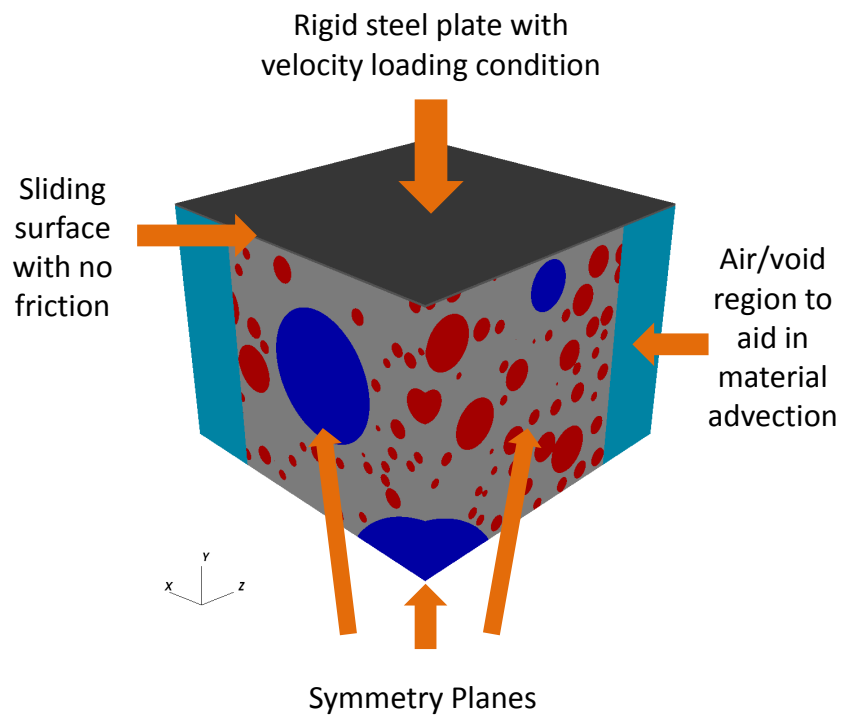


Figure 5.3: Boundary conditions implemented in the three dimensional ALE3D simulations of composite microstructures uniaxially compressed at a strain rate of 4620 s^{-1} .

$$Y = Y_0 [1 + \beta (\varepsilon_p + \varepsilon_i)]^n \frac{G(P, T)}{G_0} \quad (55)$$

where Y_0 is the initial yield stress, β a work hardening constant, ε_p the equivalent plastic strain, ε_i the initial plastic strain, and G_0 the initial shear modulus. $G(P, T)$ is then defined by the relation:

$$G = G_0 \left[1 + \frac{AP}{\eta^{1/3}} - B (T - T_0) \right] \quad (56)$$

where, A and B are material constants that define the pressure and temperature dependence of the shear modulus respectively, η the amount of compression, and T_0 room temperature. The melting is based on a modified Lindemann law with T_m defined as:

$$T_m = T_{m0} \exp \left[2a \left(1 - \frac{1}{\eta} \right) \right] \eta^{2(\gamma_0 - a - 1/3)} \quad (57)$$

where T_{m0} is the melt temperature at constant volume, and a is the Lindemann melting law parameter. When $T \geq T_m$ the yield strength and shear modulus are set to zero.

Very few models exist in ALE3D that are available for describing the constitutive behavior of polymers. While this is the case for ALE3D, there are also very few models that exist in the open literature that can adequately be used to characterize polymers. The few models that do exist also are limited to application in a set strain rate regime and are developed with a certain type of polymer in mind. Therefore, for epoxy, the constitutive behavior used in the simulations was defined based on a tabular rate hardening model where the flow stress is a function of the equivalent plastic strain with a power law strain rate dependence defined by the following equation:

$$Y(\bar{\varepsilon}_p, \dot{\bar{\varepsilon}}_p) = Y(\bar{\varepsilon}_p) [a + b\dot{\bar{\varepsilon}}_p]^m \quad (58)$$

Here, $\bar{\varepsilon}_p$ is the equivalent plastic strain, $\dot{\bar{\varepsilon}}_p$ the equivalent plastic strain rate, a and b hardening model material constants and m the power law strain rate parameter. Using data from Jordan et al. [2], this model was applied to the stress strain curves from strain rates of 134 to $1.4 \times 10^4 \text{ s}^{-1}$. By using a strain rate of $3.9 \times 10^3 \text{ s}^{-1}$ as a reference curve a set of values for the parameters were found by iteratively solving the equation that minimized the differences in the peak stress between the experiments and model curves. These values are shown in Table 5.1 with the tabular hardening model and experimental stress strain curves shown in Fig. 5.4.

Table 5.1: Tabular hardening parameters for Epoxy (Epon826/DEA). Reference curve for data at a strain rate of $1.3 \times 10^3 \text{ s}^{-1}$ was used to find the parameters in the dynamic strain rate regime.

Material	a	b	m
Epon826/DEA	0.085	249.0	0.14

5.4 Mesh Resolution Effects

The mesh resolution in computational studies plays a key role in the simulation outcome. Therefore mesh resolution studies are often carried out to monitor the convergence of key material properties as the mesh size changes. In the current mesh resolution study a microstructure domain $240 \times 240 \times 240 \text{ }\mu\text{m}$ for MNML-3 (20 vol.% $50\mu\text{m}$ Al + 10 vol.% Ni + Epoxy) was used with individual elements varying from 2, 3, 4, 6, 8, 12, and $16\mu\text{m}^3$ in size. Since stress is a major component of the simulation interpretations, the von Mises stress was considered at a location directly in the center of the composite domain following compression for the length time of $t = 21.6\mu\text{s}$. To track the variation in composite response as a function of mesh density this procedure was carried out for each mesh resolution in an increasing element density and normalized by the previous 'smaller' mesh density. From the results shown in Fig. 5.5 there were only slight changes in the composite response at that location for

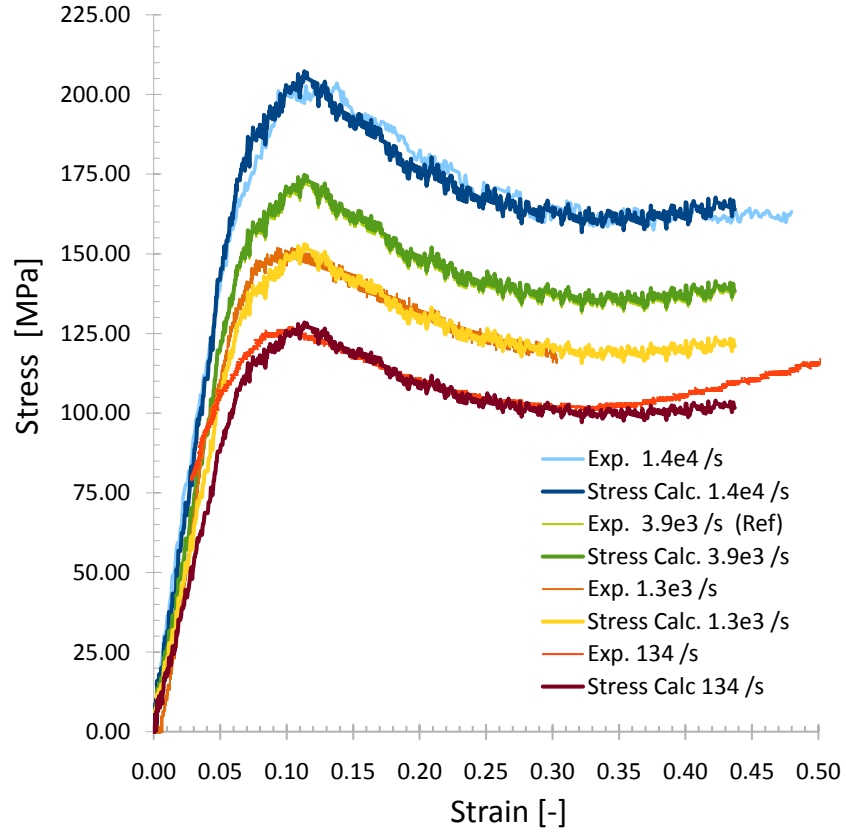


Figure 5.4: Results of tabular hardening model parameter determination for epoxy at strain rates from 134 to $1.4 \times 10^4 \text{ s}^{-1}$. Experimental stress strain curves are taken from data by Jordan et al. [2].

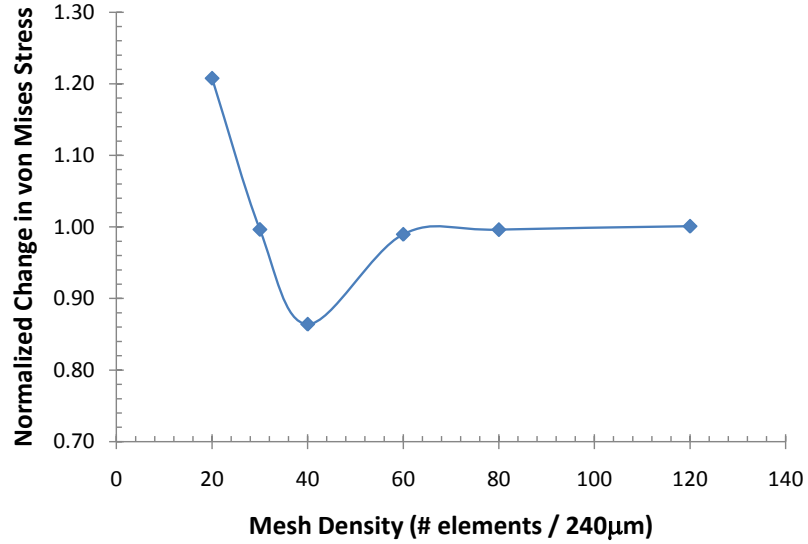


Figure 5.5: Mesh resolution optimization for particle reinforced epoxy composites. The von Mises stress was determined at the center location of the composite domain after a compressive loading duration of $21.6\mu s$ at a strain rate of $4620 s^{-1}$.

element densities greater than 60, corresponding to an element size of $4\mu m$.

Strain is also an important parameter in these studies and as such the strain fields needed to be visually resolved to better understand the evolution of the mechanical behavior. Snapshots of the computation domain were taken at the same loading duration used in the von Mises stress calculations as seen in Fig. 5.6. As the element size decreased from 16 to $2\mu m$ the strain fields became more defined with no significant changes from a mesh size of 4 to $2\mu m$. This gave further confidence in choosing $4\mu m$ as an appropriate resolution for these computational studies. For composites containing the smaller sized aluminum particles ($5\mu m$ vs. $50\mu m$) the element size was decreased by an order of magnitude to $0.4\mu m$ in order to keep the number of elements across the smallest particles approximately equal. This amounted to approximately 5 elements across the smallest particle diameters.

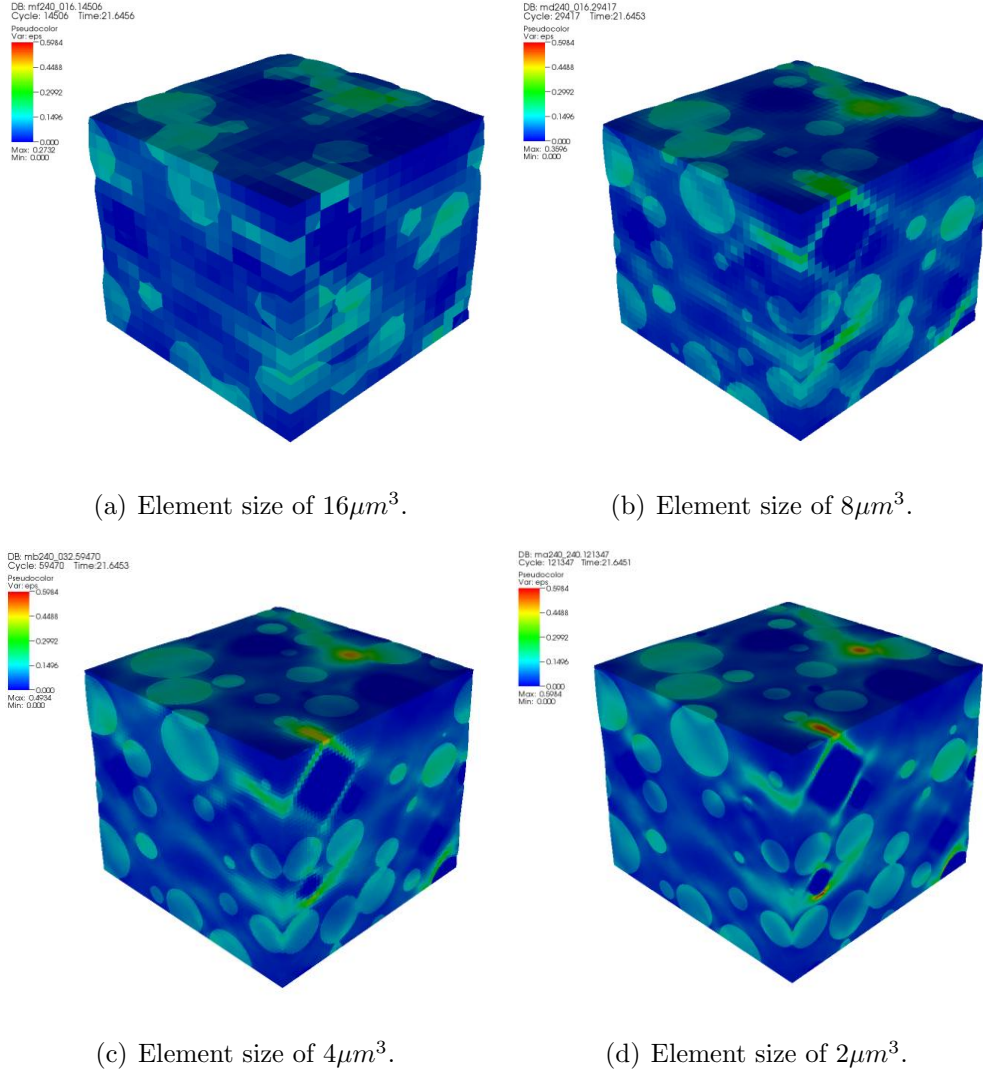


Figure 5.6: Snapshot of MNML-3 at a time step of $21.6\mu s$ for different element sizes.

5.5 Composite Material Behavior from Simulations

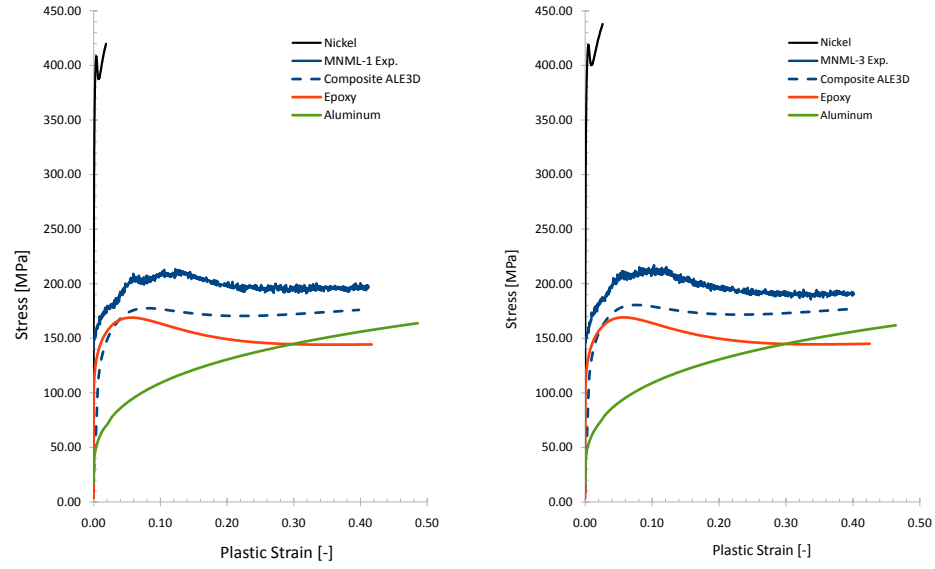
An advantage of conducting mesoscale simulations is the ability to track the stress and strain of not only the entire bulk, but the individual constituents at the particle scale. This is important for understanding the role of interactions of the constituents on the bulk mechanical behavior and effects on one another. Since there was no incorporation of interface cohesion or friction between the constituents the results are of their interaction under perfect bonding conditions. In Fig. 5.7 the stress is plotted

against the effective plastic strain for the bulk, nickel, aluminum, and epoxy, in the case of each composite (MNML-1, 3, 5, and 7) and compared to the experimental results for split Hopkinson pressure data at the same strain rate. The differentiation of elastic and plastic strain from experimental data was determined from the point at which the stress strain curves begin to deviate from linear behavior.

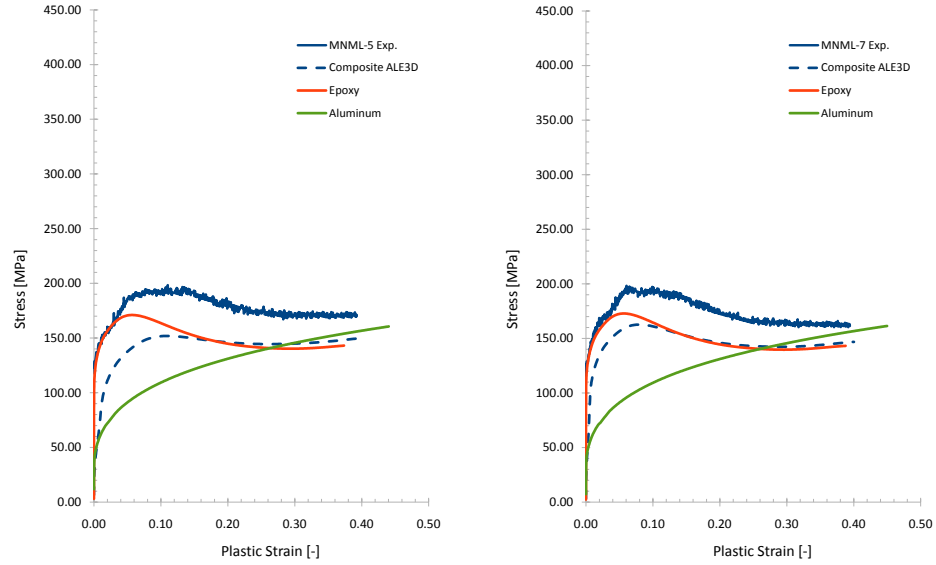
In each case, the simulation was not able to predict the experimental bulk response. While the general shape of the bulk simulation stress-strain curves matched the experimental results with less strain softening in materials with higher amounts of particle loading (and more strain softening in composites with less particle loading) the stress values achieved were much lower than those measured from experiments. From the constituent stress-strain curves, the epoxy was found to be initially much stiffer than aluminum indicating that it is capable of carrying a larger portion of load during the early stages of deformation. The aluminum also deformed to larger strains than epoxy and in the nickel reinforced composites there was an increase in the amount of strain for aluminum by approximately 10 and 3% (with the values derived from ratio of Al strain for MNML-1 with MNML-5 and MNML-3 with MNML-7 respectively) at a bulk strain of 40%. For the epoxy phase the increase in strain was also higher in the composites containing Ni with increase of 12 and 9% (from calculations of ratio of epoxy strain for MNML-1 with MNML-5 and MNML-3 with MNML-7 respectively) at a bulk strain of 40%. From experiments this was also shown to be the case where composites that contained Ni had larger measured particle strains for the aluminum phase. This is due to the nickel acting as rigid anvils within these types of composites and only straining to approximately 2%, at a total composite strain of 40%. The stress levels in nickel also reached loads of over 400 MPa at these strain rates, which coupled with the low strain values is a result of the high stiffness and work hardening characteristics of Ni.

The high work hardening characteristics of Ni also play an important role in the

evolution of the stress strain behavior of aluminum and epoxy. When a portion of the composites are replaced with a material such as Ni, that percentage of the composite strains very little in comparison to the other less stiff materials. This induces the epoxy and aluminum to strain more to keep an overall equivalent bulk composite strain rate. By having higher rates of strain the epoxy and aluminum have higher induced flow strengths. In Fig. 5.7 epoxy and aluminum are observed to have a cross-over point in their stress-strain curves in which the flow stress of epoxy is overtaken by the flow stress of aluminum. In MNML-1 and -3 this transition point occurs at plastic strains of approximately 30%, while in MNML-5 and -7 the value is around 25%. While each phase reaches this stress or strain at different times throughout the deformation process it reveals some information about how the overall constitutive response of the individual composite components may alter the behavior of the others. In MNML-1 and -3 this transition comes at a later strain due to the epoxy having a higher strain rate dependence on flow stress than Al which is fairly rate independent until much higher rates of strain than those attained by Al in the simulations for these loading conditions. This means that in addition to the Ni particles directly affecting the deformation behavior of the Al through more frequent particle-particle interactions or strain fields produced by the Ni particles, they indirectly affect the straining of aluminum by altering the strength of epoxy. In terms of the bulk behavior these effects are accompanied by a lower amount of strain softening in the epoxy which can account for a portion of the lower amounts of strain softening observed by the bulk for composites containing Ni.



(a) MNML-1 (40% 50 μ m Al + 10%Ni). (b) MNML-3 (20% 50 μ m Al + 10%Ni).



(c) MNML-5 (40% 50 μ m Al). (d) MNML-7 (20% 50 μ m Al).

Figure 5.7: Composite mechanical behavior comparison of experimental results with simulations.

When the larger sized aluminum particles were replaced with a smaller diameter, there was virtually no difference in the composites stress-strain behavior. In one such

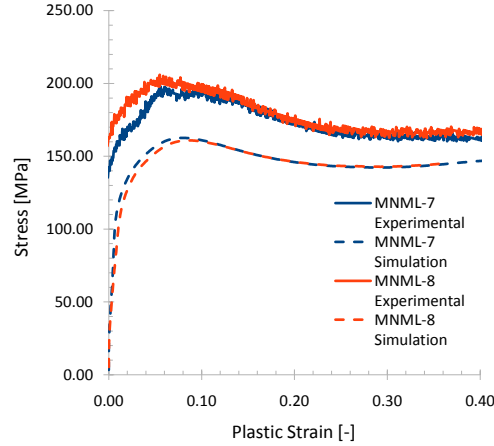


Figure 5.8: Examination of effects on simulation results with a change in particle size. MNML-7 (20 vol.% 50 μ m Al) simulation results are compared with MNML-8 (20 vol.% 5 μ m Al) results.

example, comparing the experimental and simulations stress strain curves for MNML-7 (20% 50 μ m Al) and MNML-8 (20% 5 μ m Al), the curves from each simulation coincide directly on top of one another as shown in Fig. 5.8. Since the material models used in the simulations have no dependence on particle size the simulations are primarily affected by the volume fractions of the composite constituents.

5.6 Decomposing the Strain into Composite Constituents and Examination of Strain Rate Behavior

While the stress strain curves for the composites and their constituents are beneficial for obtaining information about the total deformation process and allowing for a comparison of the final strain levels, they reveal only a limited amount of information of how their behavior and interactions may change in relation to one another over time. Therefore, to more fully understand the affects of composite design on the evolutionary process of aluminum and epoxy deformation, the bulk strain of the composites was decomposed into their components and further analyzed to determine their individual strain rates. In Fig. 5.9(a) the strain is plotted against time for

composite MNML-5 (40 vol.% 50 μ m Al). In the initial stages of the deformation, aluminum has a much larger strain rate (indicated by the steeper slope) than epoxy which has a much shallower slope that is essentially zero until approximately 10 μ sec into the loading event. At larger times the strain rate of epoxy increases until it stabilizes with a strain rate of 4920 s^{-1} from $t = 24\mu$ s onward. By contrast, aluminum has a steady strain rate of 5500 s^{-1} and reaches this state almost immediately. It should be noted that the values for the rates of strain are for the plastic contribution to strain rate and are expected to be at the very least initially different from the prescribed strain rate placed by a velocity loading condition on the rigid steel plate at the top of the simulation domain.

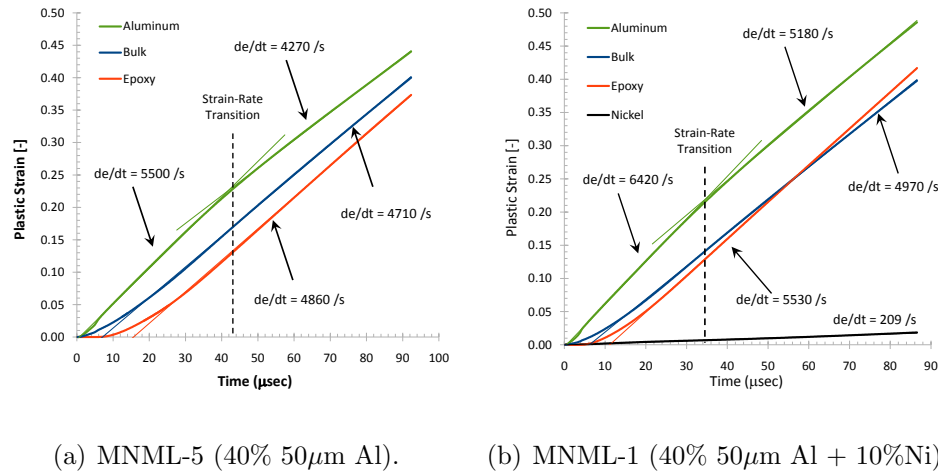


Figure 5.9: Bulk, aluminum, epoxy, and nickel plastic strains as a function of time for 3D simulations conducted on (a) MNML-5 and (b) MNML-1.

In Fig. 5.9(b) a representative plot of strain vs. time for a composite containing Ni (40 vol.% 50 μ m Al + 10 vol.% Ni) is shown as a counterpart for the composite without nickel. The most obvious difference in the strain rate behavior is the quicker plastic strain response of epoxy, that appreciably strains after approximately 3 μ s. Additionally, the aluminum plastic strain rates are much larger than in the composite without Ni. In this case the strain rate for Al increases by 980 s^{-1} (16.7%) to 6420 s^{-1}

over the composite without Al, while for epoxy there is a relatively small difference with an increase of only 2.3% to 4970 s^{-1} . These increases in strain rate are a result of the stiffer Ni particles causing regions of high strain surrounding them. This was seen in earlier results of particle strain analysis for the composites at different rates of strain. Another contribution to the change in epoxy may be due to an increased work hardening of Al by interactions with Ni. In these simulations the higher rates of strain for epoxy and Al are balanced by the relatively low rates of plastic strain of Ni which has a strain rate of 209 s^{-1} .

In both examples shown, the slope for the aluminum goes through a transition in which the slope decreases after an extended period of loading. As shown in Fig. 5.9 the time at which this occurs is around 43 and $35\mu\text{sec}$ for MNML-5 and -1, respectively. It is at this point that the epoxy has strain softened enough that the work hardened aluminum starts to behave stronger than epoxy and decrease its rate of strain. The time at which this occurs is higher for composites without Ni which again is an indication of the interactions of the rigid Ni particles with epoxy and Al particles exhibiting a strong effect on the deformation behavior of the composite at the mesoscale.

As another example of determining the effects of constituent volume fraction, attempts were made to model composite MNML-4 with the appropriate volume fractions of Al and Ni to match the experimental volume fractions. Finding a region that was representative of the experimental volume fractions while still maintaining a reasonable sized microstructure domain was unsuccessful. However, a domain with 20 vol.% of Al and 20 vol.% of Ni was found. This higher volume fraction of Ni increased the strength of the composite as would be expected with a composite containing higher concentrations of a stiffer material but still had the traits of underpredicted peak and flow stress levels (see Fig. 5.10 (a)). With just an additional

10 vol% increase in Ni, the strain rate behavior of the composite is even more dramatically affected. The strain rate of Ni drops off by two orders of magnitude down to 7.25 s^{-1} while the strain rate of epoxy and aluminum increases by approximately 1000 s^{-1} for other Ni containing composites. This was enough to increase the amount of strain of aluminum and epoxy up to 58 and 54% which is approximately 10-12% higher than the levels reached in composites MNML-1 and -3.

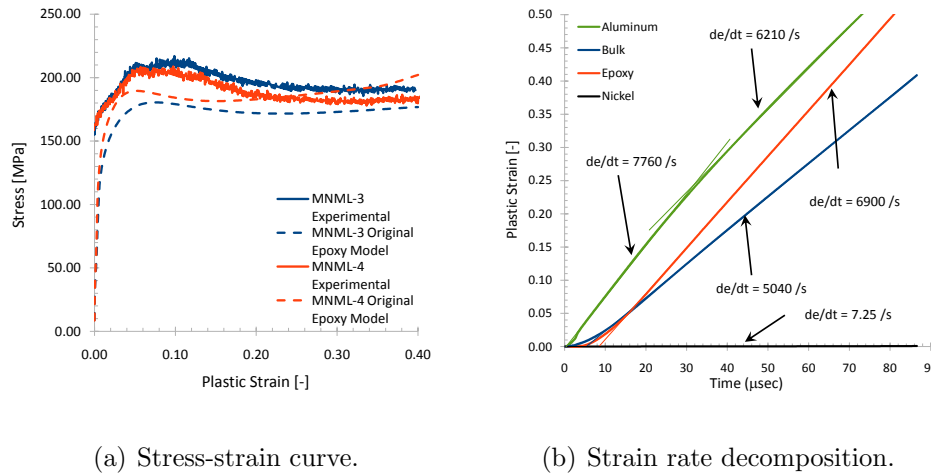


Figure 5.10: Examination of effects on simulation results with a change in particle size and volume fraction Ni. In (a) MNML-3 (20 vol.% $50\mu\text{m}$ Al + 10% Ni) simulation results are compared with a region of MNML-4 containing a high concentration of Ni (20 vol.% $5\mu\text{m}$ Al + 20% Ni) results. In (b) the strain-time decomposition for MNML-4 is depicted. Note the change in scale of from previous strain-time plots. This was done to be able to observe the higher strains due to the much higher strain rates produced in the Al and epoxy phased from increased amounts of Ni.

The aluminum and epoxy plastic strains were then compared with that of the bulk strain for composites MNML-1, 3, 5, and 7 (see Fig. 5.11) to better understand the effects of composite design on the evolution of the mechanical deformation. This is important to understand since aluminum is a primary reactant in oxidation and

intermetallic formation of nickel-aluminide reactions which are the most likely reactions to occur in the composites used in this study. Since the reactions are influenced by the mechanical mixing, the plastic strain of the aluminum and epoxy phases can offer good insight into any possible mechanical mixing involved in the initiation of reaction.

Up until bulk plastic strain values around 10-12%, the curves for each composite vary by very little. Beyond these bulk strain levels the curves become more differentiable by separating into regions with composites that contain Ni and those without Ni. For the composites with Ni the aluminum plastic strains are higher as discussed previously. However, in this plot we can see that there is only slight influence of the volume fraction of Al on the overall strains that aluminum undergoes. This indicates that the Al-Al particle interactions by particle-particle contact and Al-Epoxy-Al interactions through developed strain fields directly between the aluminum particles are not as influential on the overall deformation of the aluminum, as the influence of Ni particles. In all cases the strain levels of aluminum are larger than the bulk strains. This is due to its lower strength than either Ni or epoxy at these rates of strain.

In the case of epoxy there is a clear division in the plastic strains of epoxy with bulk strain for the composites into two regions, those with and without Ni. As was observed for Al, epoxy had higher strain levels for composites containing Ni. Also, there were no large differences in plastic strains between composites containing 20 and 40 vol.% Al for each type of composite (those with and without nickel). This is again an indication that Al-Al particle interactions are not a primary source of deformation of the aluminum particle deformation. However, one interesting observation can be made with regards to volume fraction effects of aluminum. For the composites containing 20 vol.% Al, the amount of plastic strains in the epoxy phase

are higher than those with 40 vol.% Al. If there is an interparticle interaction effect between individual Al particles on the behavior of the other phases, one possible explanation for this may be due to constraint effects on the contiguous epoxy matrix. Within a particle reinforced polymer matrix the distribution of particles changes from one region to the next. These different particle distributions can cause regions to have configurations in which the particles inhibit the flow/plastic deformation of the matrix phase to act as a constraining effect. This effect arises from the aluminum particles straining that subsequently work harden enough locally to become stronger than epoxy. In composites that contain larger amounts of aluminum, there will be an increased probability of formation of these types of regions. This would increase the amount of epoxy regions between the Al particles that deform to a lower amount and decrease the overall epoxy plastic strain for a given bulk strain level.

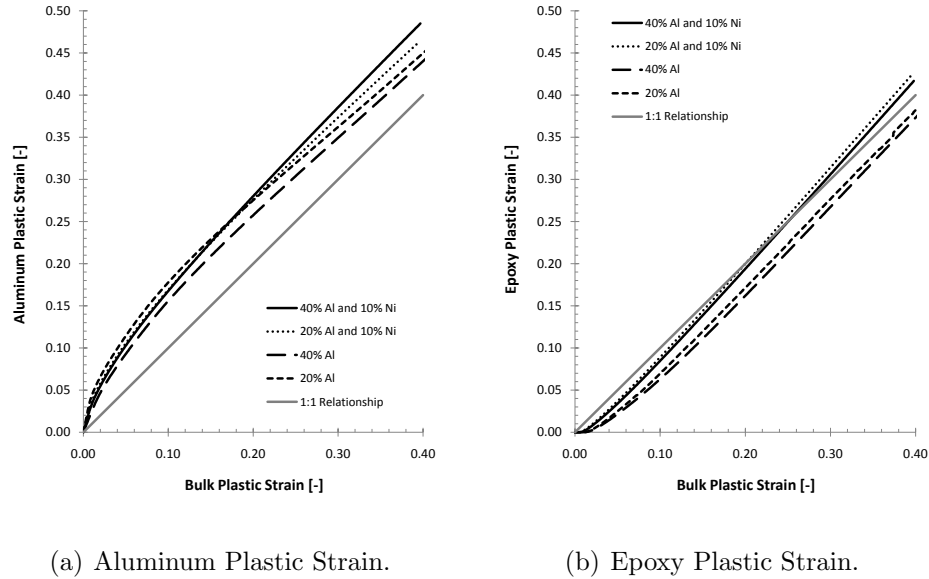


Figure 5.11: Aluminum (a) and epoxy (b) plastic strains as a function of bulk plastic strains up to 40% for 3D simulations conducted on MNML-1, 3, 5, and 7. Plotted along with the composites is a 1:1 correspondance curve of the individual phase strain with bulk strain.

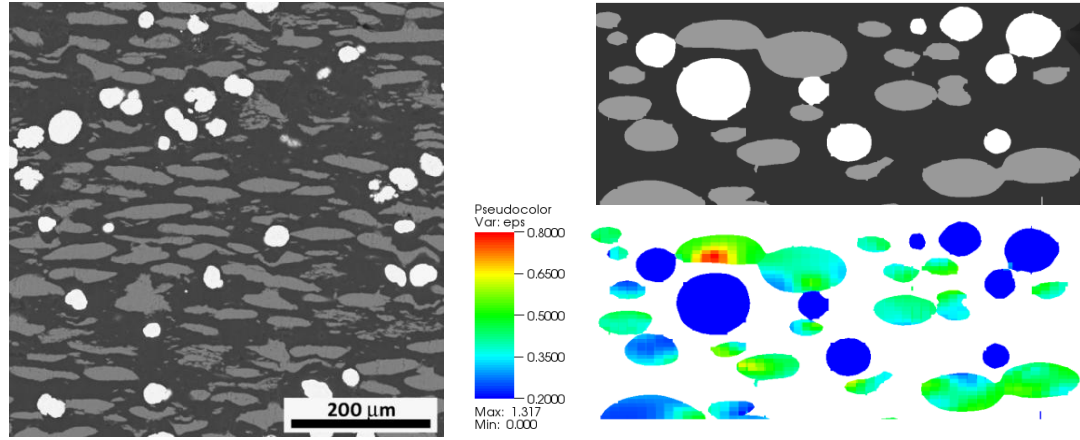


Figure 5.12: Comparison of Al particle strains in simulations (right) with resultant real microstructure (left) following dynamic compression to 35% for MNML-1 (40 vol.% 50μm Al + 10% Ni).

5.7 *Comparison of Simulation Microstructures with Experiments*

In comparing the simulated microstructures following compression with real microstructures the underpredicted bulk stress from the simulations resulted in lower aluminum particle strains as expected. As a representative example of the aluminum particle strains found following compression to 36% bulk plastic strain, the real and simulated microstructures of MNML-1 (40 vol.% 50μm Al + 10% Ni) are shown in Fig. 5.12. At 36% bulk strain MNML-1 had average Al particle strains of 62% whereas the simulation showed average Al plastic strains of 45%. As was illustrated from experimentally obtained microstructures Al strain is more pronounced in the regions surrounding the Ni particles. A similar type of behavior is observed in the simulations. The differences in the particle strain additionally suggests that alternate material models need to be investigated to more accurately predict the bulk response of the composites.

5.8 Characterization of Strain Localization Effects

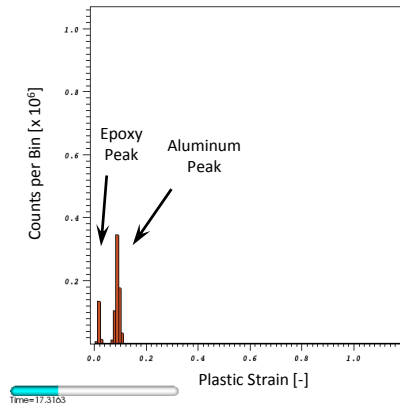
In the previous discussions of simulations only averaged results have been taken into consideration. Due to the local heterogeneities of different regions at the mesoscale the local strains are going to be distributed over a range of values and will behave according to the following equation:

$$\varepsilon = \bar{\varepsilon} + \varepsilon' \quad (59)$$

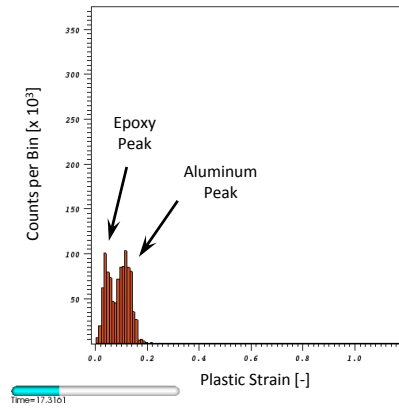
where, $\bar{\varepsilon}$ is the average strain and ε' the perturbation about the average. This equation describes the local strains as being equal to the average bulk value with some perturbation away from that average. This means some regions will have larger strains than the average while other regions will have lower values. However, the totals when summed up over the entire volume will still be equivalent to the average bulk value. The deviation in strains arise from the local heterogeneity in the microstructures such as high contrasting constituent properties or differences in particle clustering.

In order to characterize the strain localization effects at the mesoscale, plastic strain histogram data for each element of the epoxy and aluminum phases were obtained throughout the simulations at bulk plastic strain values from 0-40% in 2% strain increments. On the vertical axes in Fig. 5.13 are the histogram counts for plastic strain bins shown on the horizontal axes. For MNML-5 (40 vol.% 50 μ m Al) on the lefthand side we can see a clear distinction in the strain distribution from that of MNML-1 (40 vol.% 50 μ m Al + 10% Ni) on the righthand side at the different bulk strain levels. In the early stages of bulk deformation (8% bulk strain) there is strain partitioning of the epoxy and aluminum phases into two different peaks. However, the peaks for MNML-1 are more broad and have larger strain values than those of MNML-5. As the bulk strain has progressed towards larger strain values, at 20% the peaks become more distributed in nature. For MNML-5 these peaks are still well defined where as for MNML-1 the peaks begin to overlap quite substantially to the

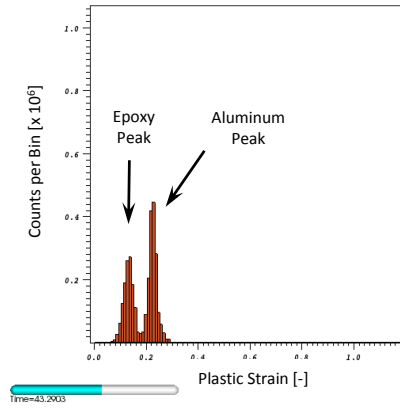
point that only the very top portions of the histogram can be seen. At bulk strains of 40% these effects become even more pronounced for MNML-1. For MNML-5 the distribution of strain is no more broader than at the other bulk strain levels however more elements have undergone deformation such that the peaks are much higher. This is also true for MNML-1 but with many more strain states that have been reached. The epoxy and aluminum peaks were determined by examining the histogram data of the individual phases separately.



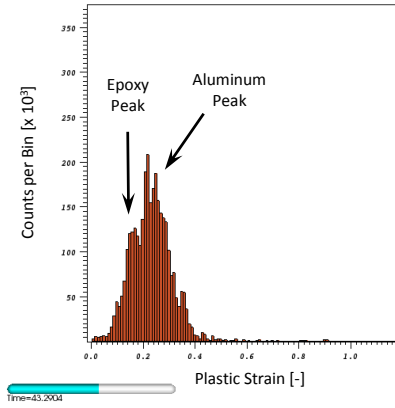
(a) MNML-5 at 8% bulk strain.



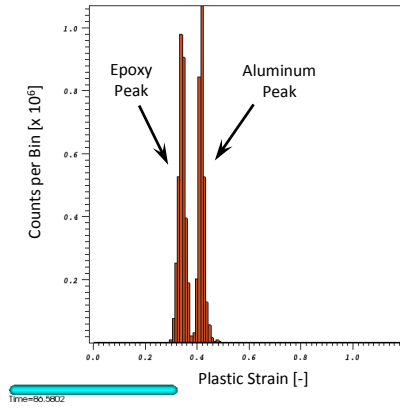
(b) MNML-1 at 8% bulk strain.



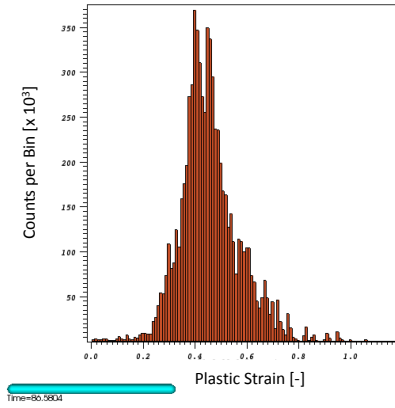
(c) MNML-5 at 20% bulk strain.



(d) MNML-1 at 20% bulk strain.



(e) MNML-5 at 40% bulk strain.



(f) MNML-1 at 40% bulk strain.

Figure 5.13: Plastic strain histogram data for a composite MNML-5 (left) and MNML-1 (right).

The large differences in behavior stem from differences in the degree of contrast in the material properties between Ni, Al, and epoxy which have as an example Young's moduli values of 222, 72, and 2.5 GPa respectively. For MNML-5 which only contains epoxy and aluminum the strengths and Young's moduli are much closer in value than they are for nickel and aluminum or nickel and epoxy. The strength differences are exemplified in the stress strain curves for each phase of the composites in Fig 5.7 with epoxy and Al behavior more closely resembling one another than that of epoxy with Ni or Ni with Al.

5.9 Epoxy Material Model Sensitivity

As seen in the previous section large differences in the simulated composite behavior, underpredicting the stresses and strains from that of experiments, is observed. It is speculated that these differences are due to the interactions between the different composite constituents that alter the mechanical behavior and/or chemistry of the epoxy matrix so that it no longer is the same material that would be found in a neat epoxy.

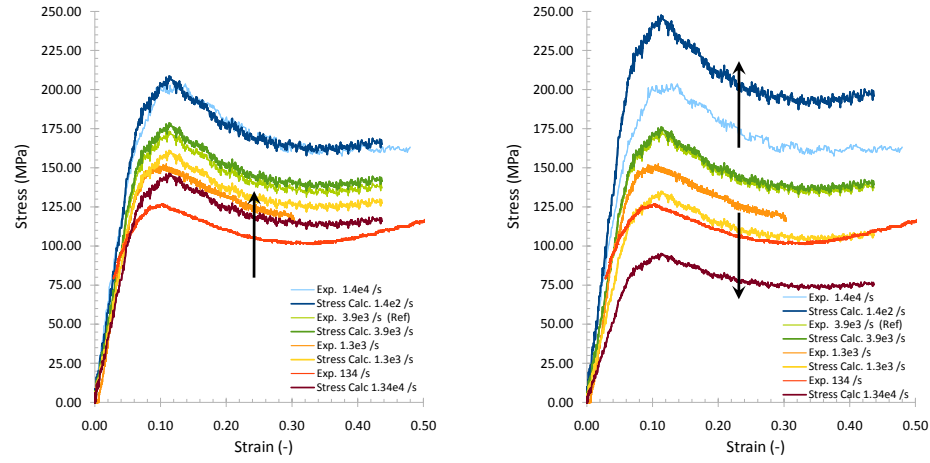
As has been shown in the simulations, the average strain rate for epoxy is less than $0.6 \times 10^4 \text{ s}^{-1}$. If the epoxy is unaffected by the presence of either the Ni or Al particles then a modification of the parameters would be a fruitless task. However, previous studies have shown that an interphase exists at the particle-matrix interface region in polymer composites. This interphase would be characterized as having a different orientation or conformation of the polymer chains with different mechanical properties. The interphase has been calculated from DSC analysis to have an effective thickness as large as $7 \text{ }\mu\text{m}$ around micron sized embedded particles [37], and it accounts for more than 10% of the overall microstructure. In a study by Martin [14] an increase in the crosslink density was measured for epoxy reinforced with Ni and Al particle in comparison to neat epoxy. There is evidence to support the claim that the

epoxy may be strengthened by changes in the mechanical properties and chemistry by enhanced crosslink densities or arrangement of the polymer chains to produce such an interphase.

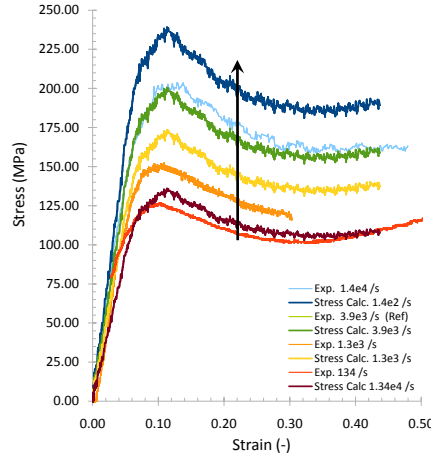
To determine if the model parameters for epoxy used in the simulations have an effect on the overall stress strain behavior of the composites, a parameter sensitivity study was conducted on the tabular hardening model (shown again for clarity).

$$Y(\bar{\varepsilon}_p, \dot{\bar{\varepsilon}}_p) = Y(\bar{\varepsilon}_p) [a + b\dot{\bar{\varepsilon}}_p]^m \quad (60)$$

The tabular hardening model has three parameters that were fine tuned to be able to match the experimental data for pure epoxy at different strain rates in the dynamic strain rate regime up to $1.4 \times 10^4 \text{ s}^{-1}$ with $a = 0.085$, $b = 249.0$, and $m = 0.14$. The goal of modifying the parameters was to increase the overall composite strength to more closely match the experimental results. Three cases were found in which this might be possible. In the first case more strength is given to the epoxy regions straining at lower rates by increasing a (see Fig 5.14 (a)). In the second case more strength can be given to the regions straining at higher rates through an increase in m (see Fig 5.14 (b)). However, this also comes with detrimental decrease in strengths for regions straining at decreased rates. Since, there are expected to be fewer regions that strain at lower rates, this may be overcome by the added strength given to the regions straining at higher rates. In the third case increased epoxy strength is given to all regions regardless of their rate of strain by increasing the parameter b (see Fig 5.14 (c)). This has the affect of increasing the strengths of epoxy by increasing amounts, as the strain rate increases. Table 5.2 lists the parameters used to alter the behavior of the epoxy.



(a) Effect of increasing a by giving lower strain rates more strength. Parameters $a=0.267$, $m=249.0$, $b=0.14$.
(b) Effect of increasing m by giving lower strain rates more strength. Parameters $a=0.085$, $m=249.0$, $b=0.28$.



(c) Effect of increasing b by giving all strain rates a higher strength. Parameters $a=0.085$, $m=704.7$, $b=0.14$.

Figure 5.14: The effect of changing the tabular hardening parameters on the epoxy stress-strain behavior. The stress strain curves shown are the experimental results plotted along side the calculated curves using the tabular hardening model. Experimental data taken from [2].

Table 5.2: Modified tabular hardening parameters for Epoxy (Epon826/DEA).

Simulation Designation	a	b	m
original	0.085	249.0	0.14
hm200a	0.267	249.0	0.14
hm200b	0.0297	249.0	0.14
hm200c	0.085	704.7	0.14
hm200d	0.085	83.0	0.14
hm200e	0.085	249.0	0.28
hm200f	0.085	498.0	0.14

Applying the parameters to the epoxy regions in MNML-3 (20% 50 μ m Al + 10% Ni), the overall composite was found to have a large variation in its response (see Fig. 5.15). By modifying a , as was done for case one, there was only a slight increase in the stresses achieved in comparison to the original epoxy model parameters. This curve is represented as hm200a. This indicates that there are very few regions strain-ing at rates less than the strain rate curve ($3.9 \times 10^3 \text{ s}^{-1}$) used as a reference in the calculations that would be able to contribute to an overall stress increase. Similarly there was a only a small effect by giving the lower strengths to the lower strain rate regions (curve hm200b) and only shifted the curve down by approximately 2 MPa.

For case two, there was an increase in the strength of the composite due to an increase in exponential factor used in the hardening model (curve hm200e). However, the increase was not large enough to accurately predict the response of MNML-3 even though for the neat epoxy there was an increase in strength of 50 MPa for the strain rate of $1.4 \times 10^4 \text{ s}^{-1}$. Additionally, a change in m also has an affect on the horizontal peak stress position. With an increase in the exponential factor m there was a slight shift of the peak towards the right. This is surprising since there was no observable shift in the modified curves for neat epoxy shown in Fig 5.14 (b). The underlying cause of this response is still under investigation.

For case three, where the epoxy was given more strength for all strain rates (curves

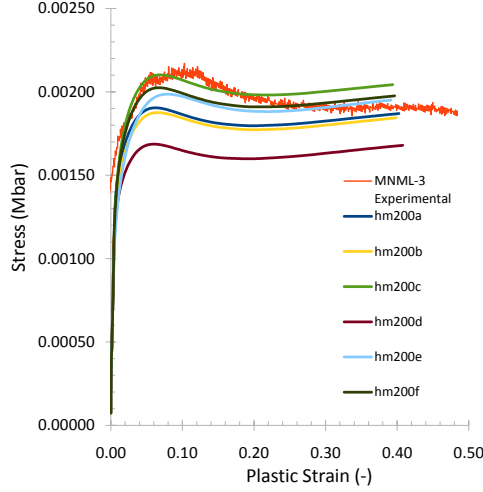
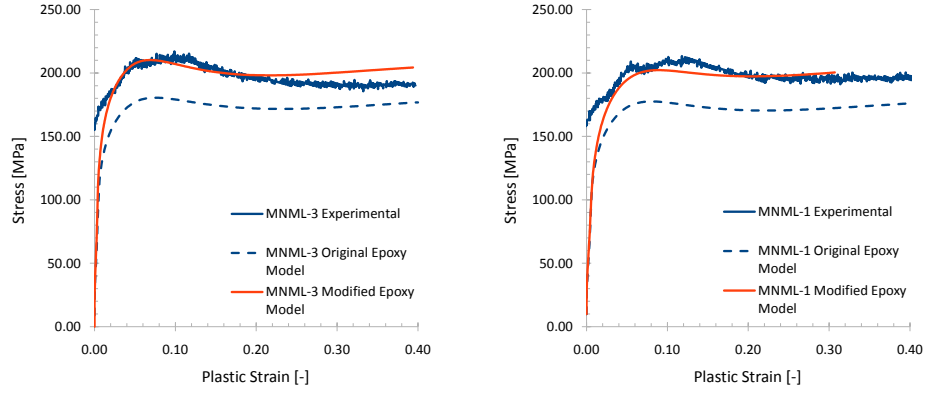


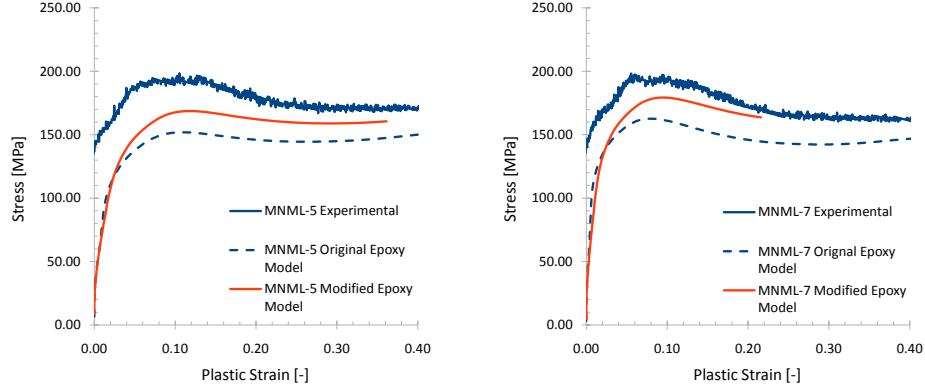
Figure 5.15: Comparison of different modification to the epoxy model on the behavior of MNML-3 (20 vol.% 50 μ m Al + 10% Ni).

hm200c and hm200f), there was a pronounced effect on the composite stress strain response. Both sets of parameters increased the overall strength to more closely match the peak stress of MNML-3. The parameters used in simulation hm200c were able to predict the experimental curve more closely with an increase in the strength of epoxy at the highest strain of 40 MPa. Since this increase in strength is for the strain rate of $1.4 \times 10^4 \text{ s}^{-1}$ for neat epoxy, these set of parameters were chosen for implementation into the epoxy model used for composite MNML-5.

In Fig. 5.16 the modified composite stress strain responses for MNML-3, -1, -5, and -7 are compared to those of the original epoxy model and experimental data. The parameters chosen for the epoxy were optimized to most accurately match the mechanical response of MNML-3. While the modified parameters were able to more accurately predict the behavior for MNML-3, when they were applied to other composites the response still underpredicted the experimental curves. The modified epoxy modeled worked well for predicting the response of composite MNML-1 which contains Nickel, although with a slightly underpredicted peak stress. This difference is suspected to be due to an increased loading fraction of Al. For MNML-5 and -7 the



(a) MNML-3 (20% 50 μ m Al + 10% Ni). (b) MNML-1 (40% 50 μ m Al + 10% Ni).



(c) MNML-5 (40% 50 μ m Al).

(d) MNML-7 (20% 50 μ m Al).

Figure 5.16: Using the epoxy model parameters: $a=0.085$, $m=704.7$, $b=0.14$, determined from optimization of the mechanical response for MNML-3 to examine the effects on other composite systems.

simulation response was still quite low in comparison to the experimental stress-strain behavior. However there was a good improvement with results for MNML-7 being more promising. The better results for MNML-7 as opposed to MNML-5 are most likely due to the parameters being optimized for MNML-3 which has a similar loading fraction of aluminum as MNML-7. The modified epoxy model was able to match experimental results for MNML-1 and MNML-3 more closely since the presence of the Ni particles induce higher strain rates in the epoxy which therefore maximizes the effect of the hardening model used for epoxy.

Although, the epoxy tabular hardening model can be fine tuned to achieve more accurate results, the parameters only work for those individual composites. In the simulation results the composites without nickel reinforcement have large discrepancies in the simulation and experimental stress strain curves, where as those with nickel matched fairly well. There were also differences in the response based on the loading fraction of aluminum with higher loading fractions having larger differences in experimental and simulation peak stresses. Thus, there is a need for a better model that can incorporate microstructure characteristics such as volume fraction of particles, or particle type and size that can consider the effects on change in the chemistry and mechanical behavior of the epoxy matrix. While there is clear mechanical enhancement of the epoxy matrix due to the presence of nickel, there is also an enhancement to the epoxy due to the presence of aluminum. The tabular hardening model is strain rate dependent. Since epoxy is initially stronger than the pure aluminum phase there is no contribution to the strength enhancement by aluminum. This was exhibited in the response of the modified epoxy model underpredicting the experimental results more for the composites containing a larger loading fraction of aluminum. In addition to the mechanical advantage given to the epoxy due metal particle reinforcement, a change in the epoxy chemistry may explain the possible enhancement to the strength of epoxy by metal particle reinforcement.

5.10 Summary of Mesoscale Modeling

Mesoscale simulations were conducted on epoxy composites at compressive strain rates of 4620 s^{-1} . Simulations were found to underpredict the stress levels found from experiments for each composite. They also revealed that the strain rates for aluminum were initially higher than those of epoxy by around 700 to 900 s^{-1} until around 30 - 40 μsec . Afterwards the strain rate of aluminum decreased such that the strain rate of aluminum was higher for the composites containing only Al and

almost equal (but still higher for Al) in the composites containing Ni. The change in behavior was due to the work hardening of Al. The epoxy was slow to ramp up to a steady rate of strain and took approximately 18 to 28 μsec to reach this state. Aluminum on the other hand had reached a steady strain rate almost immediately after the start of the simulations.

By examining the plastic strain of both the aluminum and epoxy phases in comparison to the bulk plastic strain, aluminum accounted for a large portion of the composite deformation by straining to much larger amounts than the bulk (approximately 5-10%). Epoxy on the other hand strained slightly less than the composite bulk for the composites without any Ni present and approximately the same amount for those with Ni. Strain histograms for epoxy and aluminum showed that for composites containing Ni there was a much larger distribution of strains found in each phase and the strains were much higher than those found in the composites without Ni. For the composites without Ni the epoxy and Al strain distributions were much tighter partitioned enough to distinguish the individual peaks throughout the entire duration of the simulation with Al having larger strains than epoxy. Since the simulations underpredicted the stress for the composites at the prescribed strain rate the strain levels found in Al were lower than those found from microstructure particle strain analyses. Therefore, the strength model for epoxy was investigated as the source of the discrepancies.

A tabular strain rate hardening model was used for epoxy and found to match the response of pure epoxy at strain rates up to $1.4 \times 10^4 \text{s}^{-1}$. However, when the pure epoxy model was used in a composite mesoscale simulation where the epoxy acts as a binder for aluminum and nickel particles the result was a lower predicted stress response for the composite under compressive loads at a strain rate of 4620s^{-1} . Since the strength models for nickel and aluminum are well known for the tested rate of strain an epoxy model sensitivity study on the bulk composite behavior was

conducted by changing the model parameter values. Results found that parameters that gave the epoxy more strength for a given strain rate was able to produce results that better predicted the experimental stress strain curves. While the new set of parameters resulted in a stress-strain behavior that matched the experimental curve for the particular composite they were optimized for, they failed to capture the experimental results of other composites. These results along with experimental particle strain measurements lead to the conclusion that the epoxy is altered differently for different composite configurations, i.e. variations in different particle sizes, particle volume fractions, and particle types.

CHAPTER VI

MECHANICAL BEHAVIOR DEPENDENCE ON MICROSTRUCTURE AND EPOXY-MATRIX COMPOSITES

Epoxy matrix composites reinforced with varying loading fractions of particle reinforcement and sizes were prepared for studies of the mechanical behavior at the bulk and mesoscale (particle) levels, and over a range of strain rates. The composites were shown to be well mixed with few areas of particle agglomeration. For both aluminum particle sizes the composites showed a decreases in their homogeneous length scales and nearest neighbor distances as the volume fraction of particle reinforcement increased. However, those with smaller Al particles had shorter composite homogeneous length scales. The nickel phase also influenced the spatial distribution of the aluminum phase for composites containing smaller particles by causing them to be more clustered resulting in an increase in the overall composite homogeneous length scales. Samples from the various compression experiments were analyzed following the completion of the tests to characterize the mesoscale response of the composites by measuring the particle strain as a function of bulk strain and strain rate. To further characterize the mesoscale response three dimensional computational simulations of nickel and aluminum particles dispersed throughout an epoxy matrix were carried out at dynamic rates of strain. From these computational studies the bulk response of the composites were decomposed into the individual constituent response so that the evolution of strain and strain rate of each phase could be analyzed. From both the experimental and computational thrusts of this research the bulk and mesoscale behavior of particle reinforced epoxy matrix composites were related to the overall

effects of microstructure in terms of particle loading fraction, size, and type. Further studies using thermomechanical analyses were also conducted to characterize the effects of particle reinforcement on the epoxy matrix. In the following sections, the effects of strain rate and homogeneous length scale on the mechanical behavior of epoxy matrix composites reinforced with Ni and Al, are discussed.

6.1 Mechanical Behavior Across a Wide Range of Strain Rates

The Epon 826/DEA epoxy matrix used in the composites studied in this research is known to have a strong bilinear strain-rate dependence on the peak/yield stress as shown in Fig. 6.1 with a transition strain rate occurring around 10^2 s^{-1} . Representative stress strain curves for each strain rate range are shown in Fig. 6.2. At strain rates below 10^2 s^{-1} the yield stress increases at a much slower rate than at strain rates above 10^2 s^{-1} . This type of transition in polymer yield behavior has been linked to β and α relaxation mechanisms for PC and PVDF respectively[70]. For these relaxations, enough energy becomes available for large scale polymer main chain and side chain motions to occur, at these strain rates. For epoxy this transition in behavior is believed to be due to the β transition which involves motion of hydroxyether groups in the epoxy main chain. The composite peak stresses were shown to have a similar bilinear relationship when tested over a wide range of strain rates under compressive loads (discussed in the following section). This signifies the epoxy matrix has a predominant control over the mechanical behavior and deformation. As was shown with calculated effective elastic properties the epoxy has a dominant roles in the elastic mechanical behavior of the composites with the elastic moduli lying near the lower bound of the Hashin-Shtrikman analysis which is common for particle reinforced composites in which the contiguous phase is the lower modulus constituent.

In Figs. 6.3 and 6.4 the stress strain curves for the various composites are plotted for different rates of strain. Each composite has a similar trend in which the peak

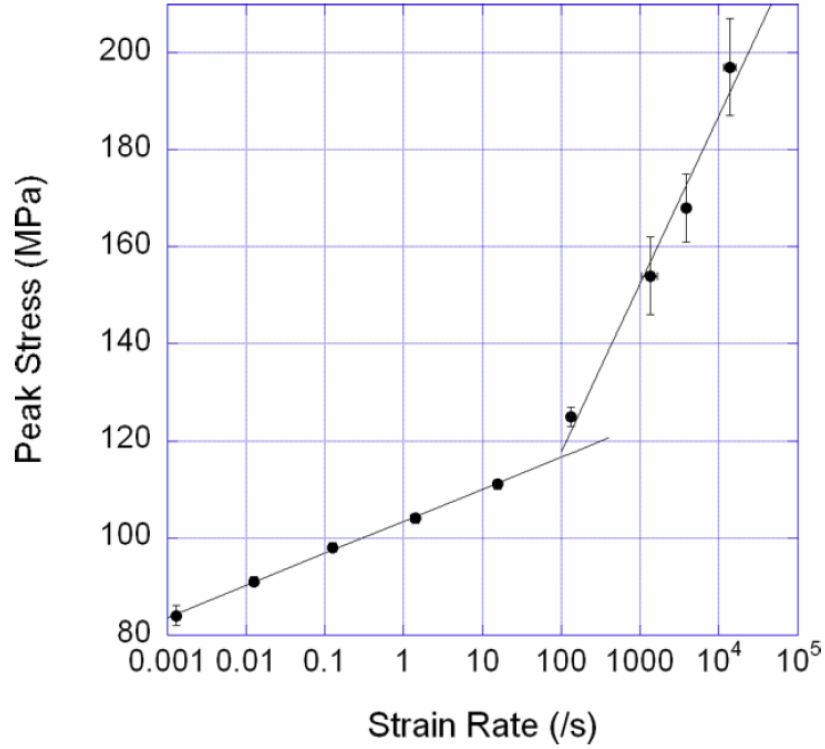


Figure 6.1: Peak stress for epoxy (Epon 826/DEA) across a wide range of strain rates from 10^{-3} to $10^4 s^{-1}$. Figure is from [2].

stress is higher for the higher rates of strain and the difference in peak stress height within each strain rate range is larger for the higher strain rates. Also, the elastic moduli appears to decrease with increasing strain rate and the strain at which the peak stress is achieved shifts towards higher strains, with the exception of the Taylor impact data for both properties.

6.1.1 Peak Stress and Transition Strain Rates for Epoxy-Based Composites

For pure polymeric materials many instances of transitions in the strain rate dependence on peak stress behavior have been documented. In this research the effects of the epoxy matrix on the composites overall behavior at different rates of strain is of prime importance. This is because the behavior of the materials under storage loading conditions and application loading conditions are of interest. However, little research

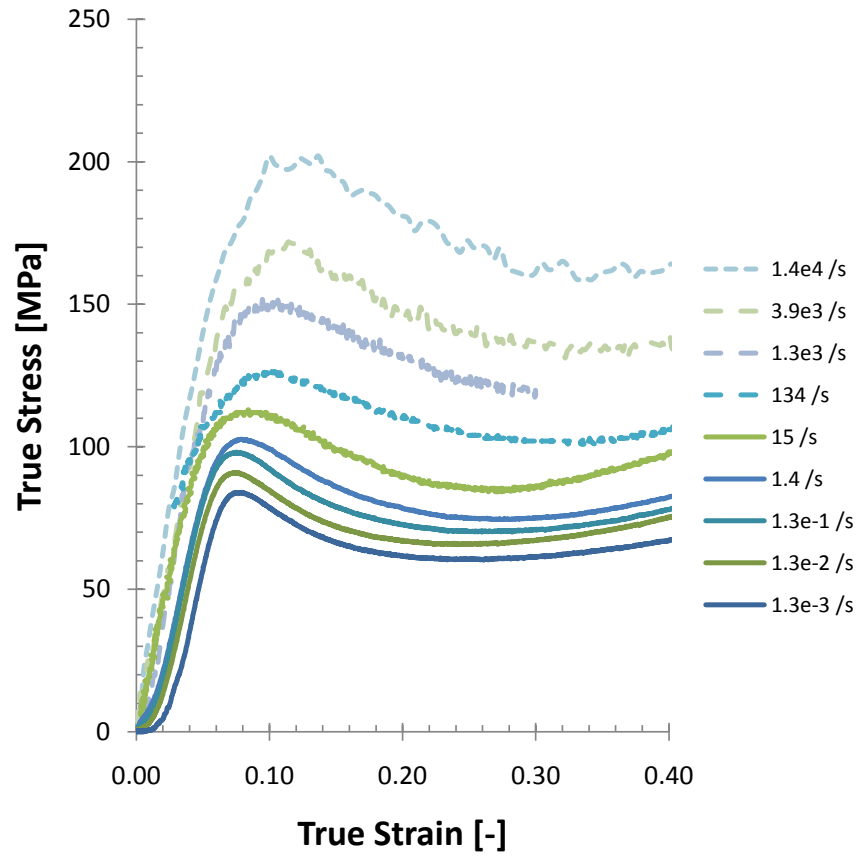
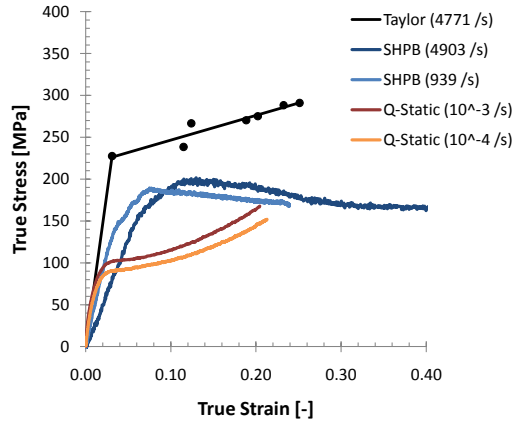
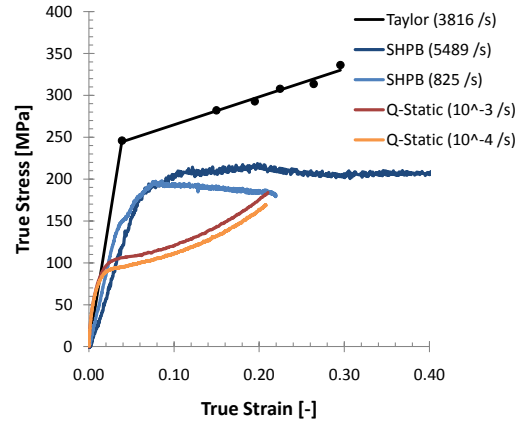


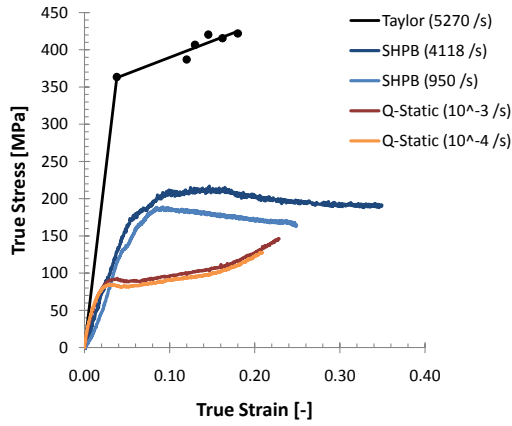
Figure 6.2: Compressive stress-strain curves for epoxy (Epon 826/DEA) across a wide range of strain rates from 10^{-3} to 10^4 s^{-1} . Data was taken from [2].



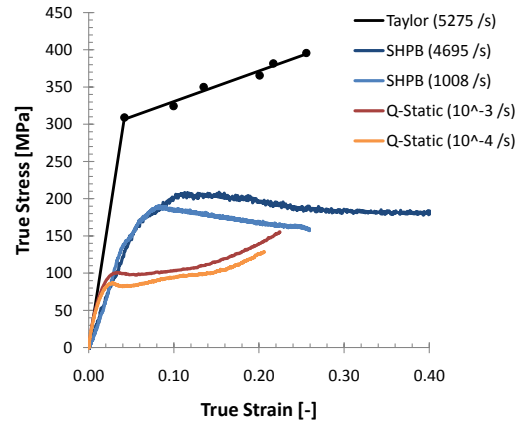
(a) MNML-1 (40% (50 μm) Al, 10% Ni)



(b) MNML-2 (40% (5 μm) Al, 10% Ni)

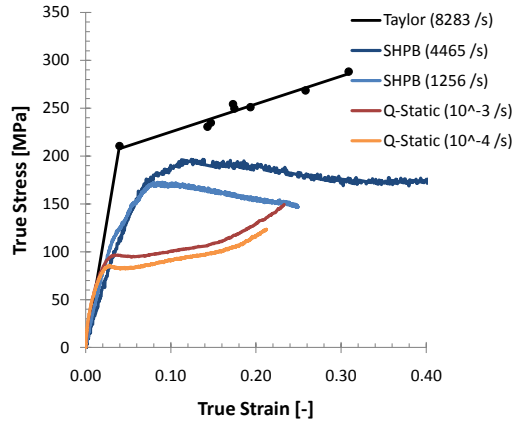


(c) MNML-3 (20% (50 μm) Al, 10% Ni)

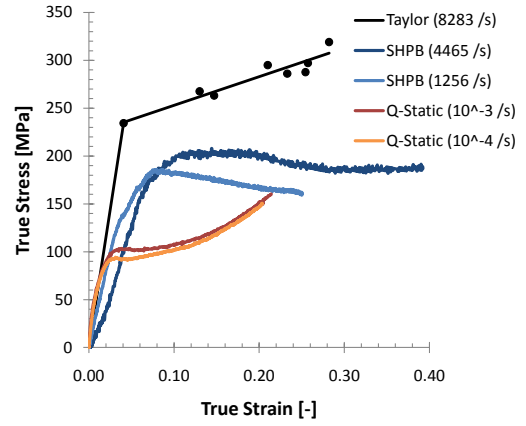


(d) MNML-4 (20% (5 μm) Al, 10% Ni)

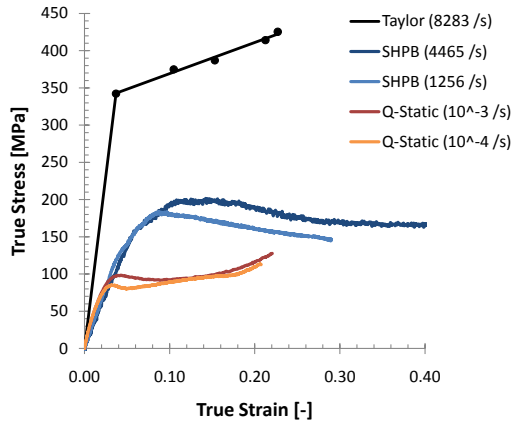
Figure 6.3: Representative σ - ϵ curves for each composite tested under a wide range of compressive strain-rates. (CONTINUED IN THE NEXT FIGURE)



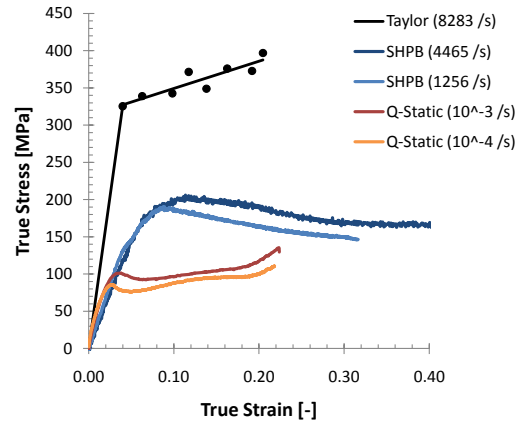
(a) MNML-5 (40% (50 μm) Al)



(b) MNML-6 (40% (5 μm) Al)



(c) MNML-7 (20% (50 μm) Al)



(d) MNML-8 (20% (5 μm) Al)

Figure 6.4: Representative σ - ε curves for each composite tested under a wide range of compressive strain-rates.

has shown a shift from lower strain rate dependence of peak stress to a higher dependence on strain rate for polymer based composites. In pure epoxy this transition occurs around a strain rate of approximately 100 s^{-1} and is easily identifiable. This is not the case for the composites studied, and in fact there are no clear trends as to how differences in composite makeup effects the change in the observed strain rate dependence as seen in Figs. 6.5 and 6.6. This may largely be due to the lack of data for compressive loads at intermediate strain rates between $1 \times 10^{-3}\text{ s}^{-1}$ and $1 \times 10^3\text{ s}^{-1}$. One thing that is clear though is that at the mesoscale different regions of epoxy are going to experience transitions at different strain rates due to the varied distribution of particles within the matrix. This would cause the overall bulk transition to occur over a much wider range of strain rates. This would help explain the difficulty in defining a transition strain rate for these composites.

Considering there is a lack of data at intermediate strain rates, a few additional statements can be made about the effects of particle size and loading fractions on the transition strain rates for each composite. If the transition strain rate takes place at lower rates, this would signify there is an enhanced strain rate strengthening effect of the polymer matrix at earlier bulk strain rates. Composites containing smaller particles have more surface area per total volume fraction of particles than those with larger aluminum particles. If a strong enough bond between the matrix and particles exists then the increased particle surface area would result in an increase in the amount of activation energy needed for polymer chains to relax or move and hence a more rigid composite. This could also create an interphase region at the particle-matrix interface that has reduced mobility due to the bonding nature or disruption of the natural polymer network structure from the presence of the particles. These would result in a polymer structure that is 'locked in' at decreased strain rate levels and give the polymer more strength at lower rates of strain. There are also shorter distances between particles in the composites with smaller aluminum particles due to

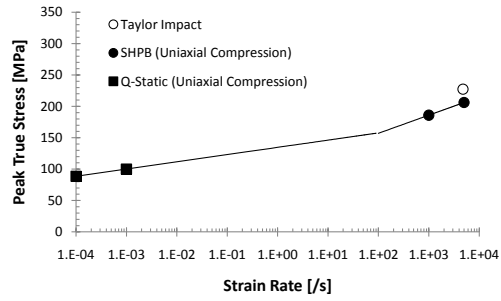
a more uniform spatial distribution (smaller L_H). If an interphase is produced with a large enough thickness then any affected regions stand a chance of contributing to the formation of a percolation network of modified epoxy that would effect the overall bulk response in which a transition strain rate would decreased to lower levels.

If a decreased bonding nature between the polymer matrix and metal particles existed there would be a large effective increase in internal free surfaces. With the introduction of the free surfaces, regions of increased epoxy mobility can exist which increases the ability of the network to rearrange itself more readily at higher rates of strain. This would not only increase the strain rate at which this transition to a higher strain rate dependencies occurs but, also the lowering of the composite strength. In terms of the effects of particle loading fraction, if there is strong bonding between the matrix and particles, then as the volume fraction of particles increases, a larger portion of the polymer matrix would inhibit chain motion and decrease the transition strain rate. Conversely, increases in the transition strain rate would occur with increased volume fractions of particles, due to increases in the amount of effective internal free surfaces.

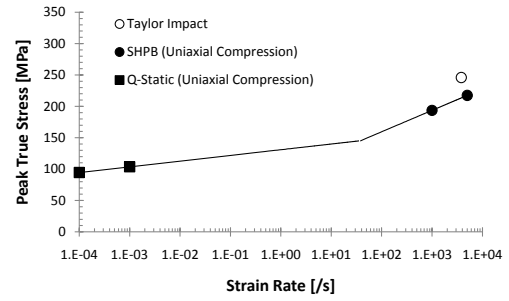
In Figs. 6.5 and 6.6 the peak stress values for the Taylor impact experiments are found to be higher than those measured from split Hopkinson pressure bar experiments at comparable strain rates. This is due to strain rates calculated for Taylor impact experiments are a measure of the mean strain rate. Upon impact the initial strain rates are much higher than the calculated strain rates which would give the composite a higher yield strength.

6.1.2 Strain-Rate Effects on Apparent Elastic Modulus

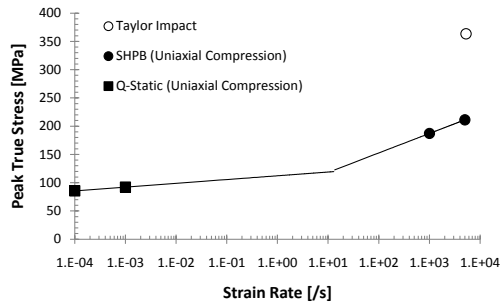
There was a marked decrease in the elastic response of the composites as the strain rate increased from quasi-static to dynamic rates of strain (See Fig. 6.7). As discussed earlier the dynamic moduli cannot be taken as true values of the elastic moduli for



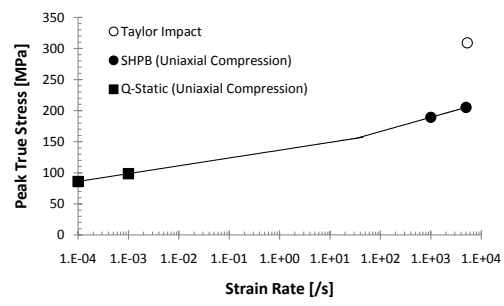
(a) MNML-1 (40% (50 μm) Al, 10% Ni)



(b) MNML-2 (40% (5 μm) Al, 10% Ni)

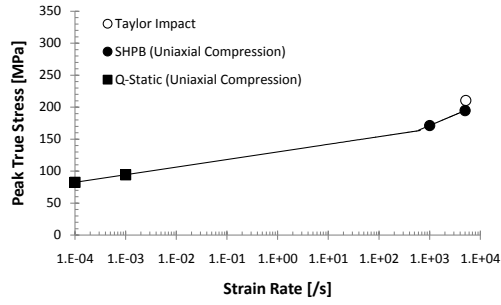


(c) MNML-3 (20% (50 μm) Al, 10% Ni)

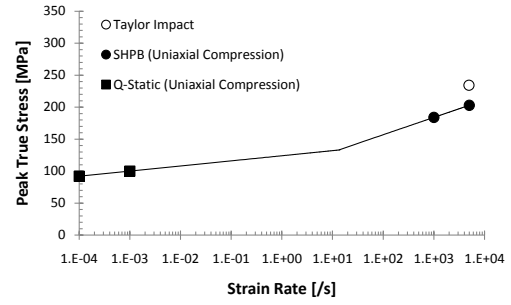


(d) MNML-4 (20% (5 μm) Al, 10% Ni)

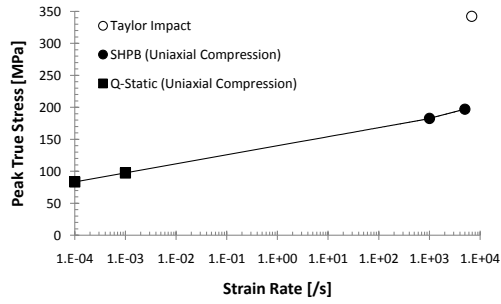
Figure 6.5: Peak stress dependence on strain rate for quasi-static compression, dynamic compression, and Taylor impact loading conditions. (CONTINUED IN THE NEXT FIGURE)



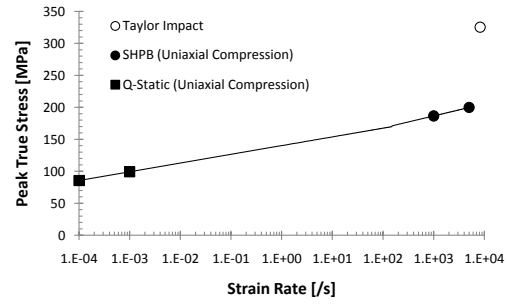
(a) MNML-5 (40% (50 μm) Al)



(b) MNML-6 (40% (5 μm) Al)



(c) MNML-7 (20% (50 μm) Al)



(d) MNML-8 (20% (5 μm) Al)

Figure 6.6: Peak stress dependence on strain rate for quasi-static compression, dynamic compression, and Taylor impact loading conditions.

the composites due to a heterogeneous stress state in the split Hopkinson pressure bar samples in the early stages of the loading process. With that being said, it is quite possible for mechanical behavior differences to occur as a result of the effects of strain rate rather than the mechanical behavior of the epoxy matrix.

Studies have shown that damage in PBX is responsible for a decrease in the global modulus [133] of the composite. In this study on PBX the researchers related the decrease to microdamage mechanisms such as crystal-matrix debonding using a model based on Griffith's failure criterion. In another study a drop in the storage modulus was related to a change in the beta relaxation of the polymer [25]. If the polymer is influenced by the presence of particles or strain-rate then this would alter the overall response of the composite.

Young's modulus may be thought of as a material's ability to transfer stresses efficiently and resist permanent deformation under prescribed loads. Therefore, any change in the elastic behavior can be related to a change in the efficiency of these processes. If microdamage nucleates at very early stages of the loading process there would be an effect on Young's modulus. One scenario in which this can occur is at high stress concentration initiation sites such as those due to interparticle contact. This would help explain why Young's modulus is typically lower for materials containing larger aluminum particles regardless of strain rate. In the composites with larger aluminum particles the spatial distribution of particles is less homogeneous.

From the quasi-static and dynamic strain rate compression tests, a similar mechanical behavior as that of pure epoxy was observed in which there is a large dependence of peak stress on strain rate. This indicates that epoxy controls much of the mechanical behavior in these composites. For Taylor impact tests on the composites the peak stresses were higher than for those determined from split Hopkinson pressure bar experiments at similar rates of strain. This is due to the non-equilibrium states in stress that occur during a Taylor impact experiment. The strain rate for which

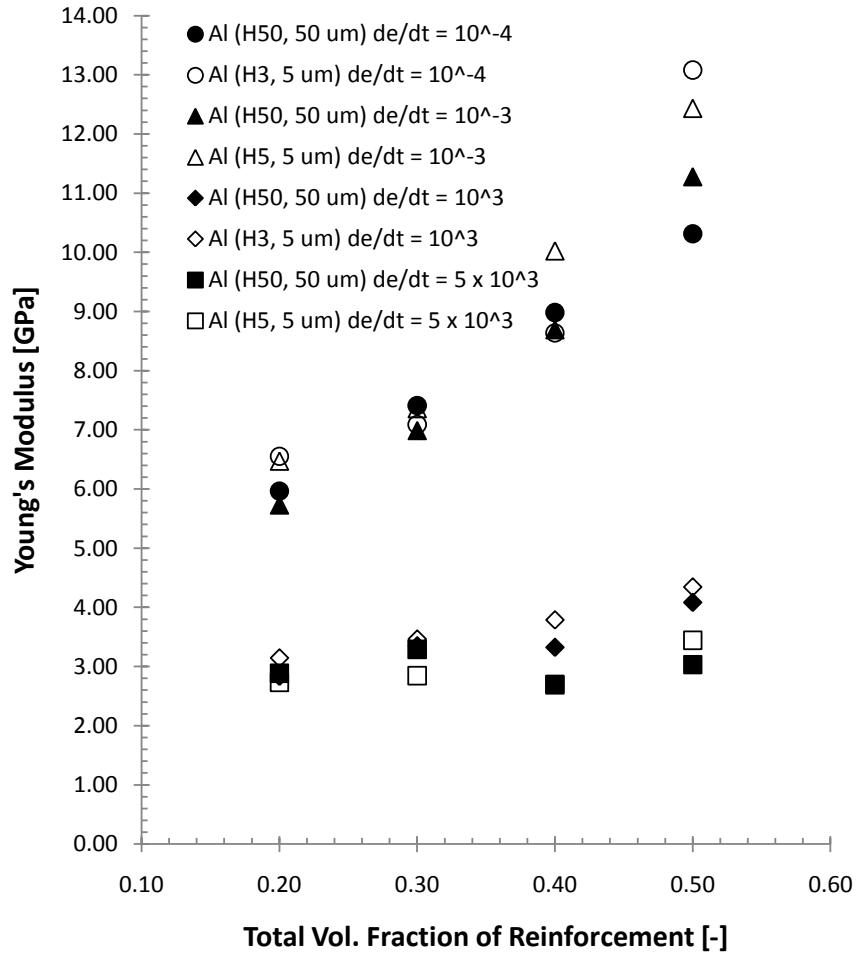


Figure 6.7: Summary of Young's modulus values across a wide range of strain rates. Filled symbols represent composites with 50 μm aluminum particles, open symbols 5 μm aluminum particles.

the peak stress transitions to high strain rate dependence were also determined and were found to have no consistent trend with variations in the composite configuration. These values are hard to claim as being absolute for each composite since only two average strain rates were sampled in the quasi-static and dynamic strain rate regimes. Tests at intermediate strain rates would be highly beneficial in resolving the range of strain rates for which the transition occurs.

6.2 Effects of Homogeneous Length Scales on Composite Mechanical Properties

One of the goals of this research is to correlate the mechanical behavior of the composites to the microstructure characteristics. The homogeneous length scale is a good measure of how the different volume fractions and size of the particle constituents affect the spatial characteristics of the microstructure. As such the composite properties may be in part controlled by the homogeneous length scale of either the individual particle types or the combination of Ni+Al.

6.2.1 Dependence of Elastic Modulus on L_H

When plotting the Young's modulus (E) for the composites against the homogeneous length scales for the Al (L_H^{Al}) and Ni+Al (L_H^{Ni+Al}) phases, a strong dependence was observed for E on L_H^{Ni+Al} . This is not too surprising since the representative homogeneous length scale depends on the volume fraction of particles and models have shown that the elastic properties of composites are primarily determined by the amount of each constituent in the composite. However, depending on the size of the aluminum particles the Young's modulus had different dependencies on the homogeneous length scales. In Figs. 6.8 and 6.9 the dependence of E on L_H^{Ni+Al} is shown for the composites containing $5\mu\text{m}$ and $50\mu\text{m}$ aluminum particles respectively for each rate of strain. For the composites containing small aluminum particles there was a positive dependence on Young's modulus with L_H^{Ni+Al} , where as for the composites with large aluminum

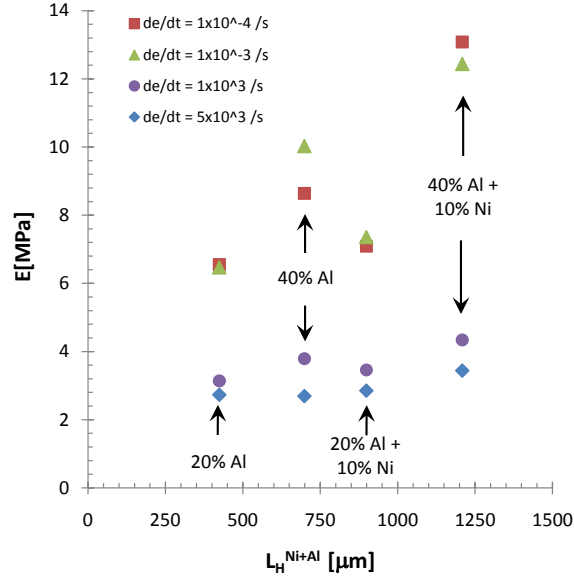


Figure 6.8: Dependence of E on L_H^{Ni+Al} for composites containing $5\mu\text{m}$ diameter aluminum particles.

particles a negative dependence was observed.

The different trends in particle size are related to differences in L_H^{Ni+Al} with changes in particle volume fraction. For the composites with small aluminum particles, noticeable increases in L_H^{Ni+Al} were observed with increases in particle volume fraction. Out of these composites MNML-2 and -4 the addition of 10 vol.% of Ni particles, which have a much larger particle size than the aluminum particles, resulted in longer L_H^{Ni+Al} values. This creates two different regimes in the plot of Young's modulus vs. L_H^{Ni+Al} with the composites containing Ni shifted towards the longer length scales, as shown in Fig. 6.10. According to MSAAF theory increases in the particle volume fractions from 20 to 40 vol.% should result in a decrease (although by very little) in the homogenous length scale for composites with an average particle size of $5\mu\text{m}$ (see Fig. 4.4). However, there was still a measured increase in L_H^{Ni+Al} from an increase in Al loading fraction from 20% to 40% for composite MNML-6 and -8 and for MNML-2 and -4. This is most likely due to experimental variability since

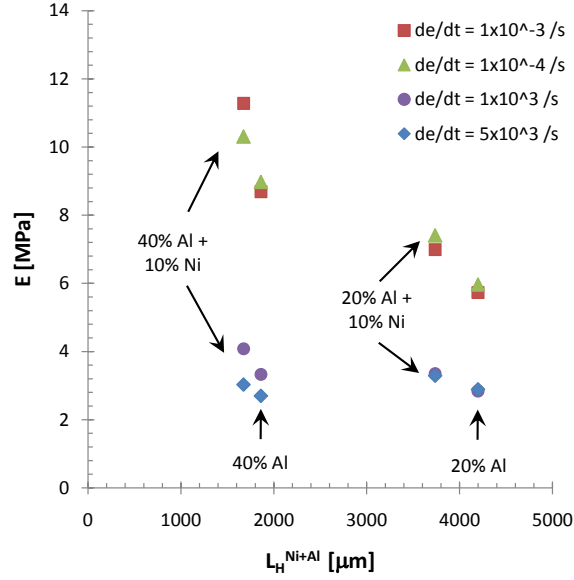


Figure 6.9: Dependence of E on L_H^{Ni+Al} for composites containing 50μm diameter aluminum particles.

L_H should decrease with higher particle loading fractions but may be an artifact of the inefficient packing of smaller aluminum particles to fit the same amount of material in a similar quantity of space as a single larger particle of equivalent volumetric diameter (meaning a single particle with a diameter that equates to the same volume fraction of material as the sum of volumes for particles of smaller diameter).

These trends for small aluminum particles are in contrast to the negative dependence of Young's modulus with L_H^{Ni+Al} found for the composites containing larger aluminum particles. For these composites there was an observed "almost linear" decrease in L_H^{Ni+Al} with increasing amounts of total particle loading fraction, which translates to a decrease in Young's modulus. Other than the Young's modulus having a negative dependence on L_H^{Ni+Al} the largest difference in comparing the trends for the composites with small Al particles with those containing large Al particles is that there were no strong deviations in L_H^{Ni+Al} for composites containing Ni particles since

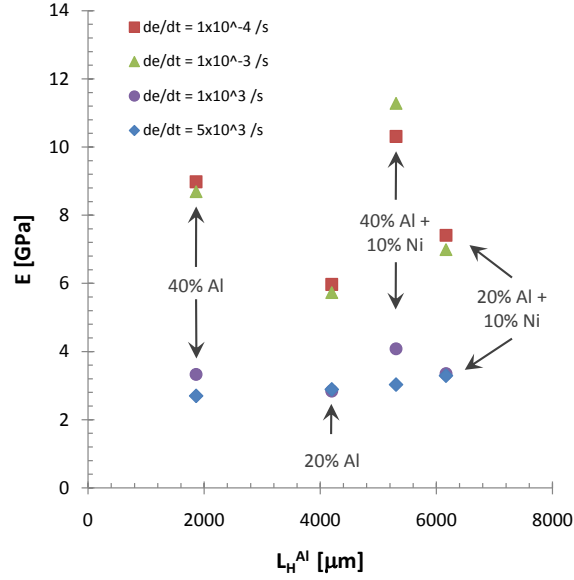


Figure 6.10: Dependence of E on L_H^{Al} for composites containing 50 μm diameter aluminum particles. Notice how the plot is divided into two distinct regions based on composite composition. Composites containing Ni are shifted towards longer L_H^{Al} values.

nickel and aluminum have similar diameters. However, when plotting Young's modulus against L_H^{Al} the two distinct regions were again produced in which case composites containing Ni have larger homogeneous length scales (see Fig. 6.10).

Since the volume fractions of constituents have a clear affect on the homogeneous length scales of composites and the elastic properties also depend on constituent volume fractions, it may be possible to develop an effective elastic properties model based on homogeneous length scales for particle composites of the type studied in this research. However, there would be some limitations in which it would not be an effective approach without some model modifications. One major limitation would be to take into account different particle sizes for different particle types. As was shown for composite MNML-2 and -4, there were large deviations in L_H^{Ni+Al} . Also, the change in homogeneous length scales with volume fraction slows down at different levels of particle volume fraction depending on the particle size. The homogeneous

length scale also increases very rapidly at dilute volume fractions. This would limit the model to a range of volume fractions above the very dilute amounts and below the point at which the homogeneous length scale begins to change very little. A model based on the homogeneous length scales using the MSAAF technique would also need to take into account their particle size, for these same reasons.

6.2.2 σ_y Dependence on L_H

At first glance in determining whether or not there were any peak stress σ_y dependencies on L_H there appeared to be a trend of increasing peak stress with homogeneous length scale at dynamic strain rates. After further examination however, it was observed that there was again a two regime dependence in which the behavior can be divided into those with and without Ni (see Fig. 6.11 for a plot of data at high strain rates for composites containing small Al particles). For the composites containing Ni there is a greater σ_y dependence on L_H^{Ni+Al} . This difference in the dependence for the two regimes show that homogeneous length scale may be used as an alternate method to distinguish the effects of different particle types on composite mechanical behavior. This is exemplified for composite peak stress data at low strain rates as shown in Fig. 6.12.

6.3 Implications of Mesoscale Effects on Mechanical Behavior of Polymer Matrix Composites

In this research chemical influences of the reinforcing particles on the epoxy matrix were found through both thermomechanical analyses and indirectly from computational efforts. Since there are changes in the epoxy due to the presence of particles, changes in the epoxy mechanical behavior occur, which vary based on particle loading fraction and size. These results suggest that the material models for polymers need to take into account additional effects when used in composites of the type where a polymer matrix is reinforced with metallic particles such as those in this research.

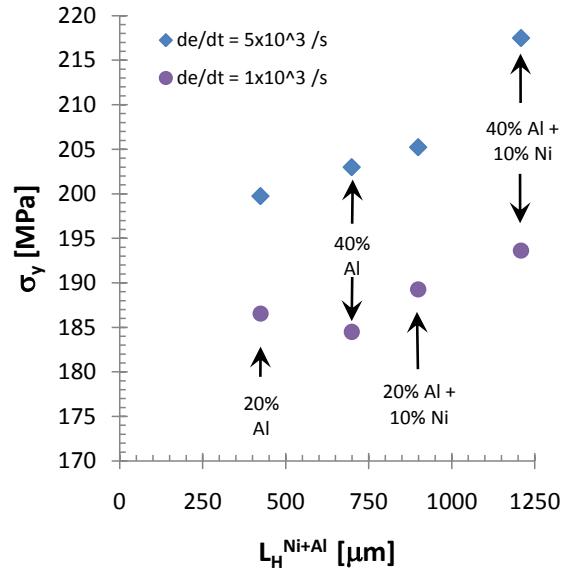


Figure 6.11: Dependence of σ_y on $L_H^{\text{Ni+Al}}$ for composites containing $5\mu\text{m}$ diameter aluminum particles subjected to compression at dynamic strain rates.

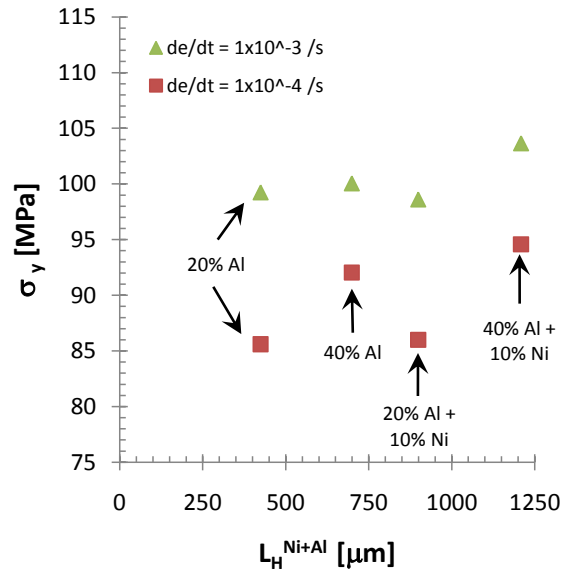


Figure 6.12: Dependence of σ_y on $L_H^{\text{Ni+Al}}$ for composites containing $5\mu\text{m}$ diameter aluminum particles subjected to compression at quasi-static strain rates.

From mesoscale simulations in which the polymer model was altered to have enhanced strain rate strengthening, more accurate results were obtained. However, modifications were not universally successful for all of the composites in this research. This, along with thermomechanical behavior results where changes in crosslink density, T_g , T_{decomp} , and formation of an interphase region were found, are the basis for the need to develop polymer models that take into account changes in the chemistry that alter the polymer's mechanical behavior in these types of composite configurations. By incorporating the effects of changes in particle size, volume fraction, and type, on a polymer matrix, it would lead to more accurate predictions from simulations at the mesoscale in which the behavior of the individual constituents are taken into account. This approach would be different from characterizing the bulk mechanical behavior and developing empirically based bulk continuum strength models (such as a tabular strength model) for the composites.

The amounts of plastic strain for particles embedded in a polymer matrix were measured as a function of bulk plastic strain and strain rate. This is the first time that this type of analysis has been reported (to the author's knowledge) for the type of composite used in this research. From these analyses increased amounts of aluminum particle strain were found in composites subjected to higher rates of strain than at lower strain rates for similar bulk strain levels. This indicated a strong effect of the epoxy matrix on the overall deformation of individual constituents in the composite and is related to the bi linear strain rate dependence of the epoxy yield stress.

This strain rate dependence on the behavior of the particles can have a dramatic impact on the understanding of these types of composite for use at high rates of strain such as those of structural energetic materials, or composite blast panels. For example, in structural energetic materials, in which a polymer is used as the matrix material, the polymer is used for two main purposes. The first is to act as a binder and provide contiguous structural strength to the composite. In composite formulations

that take advantage of the high oxygen or fluorine content of the polymer chain the other purpose of the polymer is to provide material for certain reaction pathways by way of fluorination and oxidation to enhance the overall reactive strengths and capabilities of the composites. However, one additional purpose of the polymer matrix that needs to be considered is to take advantage of the polymers mechanical properties in order to help increase the deformation of the reacting constituents, leading to enhanced mixing which is considered to be a necessary mechanism for reactions to take place in these types of composites. For polymers that have a strong yield strength dependence on strain-rate (with increases in strength with increased rates of strain) and initial high strengths that are comparable to low strength reinforcing metals such as pure aluminum, the matrix can exhibit high amounts of deformation into the metal particles during high rate loading conditions. In this research we have seen this effect, in which the amount plastic strain of the aluminum particles, were found to be larger than the strains measured for the composite bulk at strain rates greater than 10^3 s^{-1} . If the strain rate dependence of the polymer matrix strength can be tailored to have either increased or decreased strengths at high rates of strain then the particle deformation could be potentially tailored as well. This would then enable greater control over necessary strain rates and loads for reactions in structural energetic materials.

Another advantage of the polymer's mechanical behavior is the transition from a glassy to rubbery state at the glass transition temperature. As the temperature of the polymer increases through the glass transition, polymers exhibit a large decrease in storage modulus over a short temperature range that is often greater than two orders of magnitude in value. When this occurs the polymer matrix can more easily deform and begin to flow between the particles. As this process occurs particle-particle interactions are more likely to occur and opens up another particle deformation mechanism by direct interparticle contact. In this research the crosslinked nature of the

epoxy matrix can limit much of the interparticle contact to events occurring after large amounts of internal damage or fracturing of the matrix. The dominant failure method of the reinforced epoxy composites in these studies occur due to decohesion of the epoxy from the particles at the particle-matrix interface. The microcracks that form can then allow for the reinforcing particles to move through these regions more freely. However, this would not fully limit the effect of particle-particle interactions from developing. This is because the presence of particles can cause increased rates of strain in the surrounding materials which can then cause either the matrix as well as other particle types to strain-rate harden. For epoxy, the strength increases with increased strain rate, where beyond a transition strain rate there is a more pronounced strengthening effect. When epoxy and aluminum are used in composites, this has can have an additional effect of the epoxy exhibiting mechanical strengths higher than the aluminum allowing more stress to be transferred to the particles causing more deformation.

CHAPTER VII

CONCLUSIONS AND FUTURE WORK

7.1 *Key Conclusions*

The key conclusions of this work investigating the effects of microstructure, including particle size, and volume fraction of particle reinforcement, and the introduction of a second particle of dissimilar properties, on the mechanical response of epoxy-matrix composites can be briefly summarized as follows:

- The epoxy matrix has a dominant effect on the mechanical behavior of the composites studies in the research. From elastic property bounding theories, the Young's moduli (obtained using ultrasonic sound speed measurement techniques and stress-strain curves) is found to lie near the lower bounds, which is common for polymer-matrix composites that are heavily influenced by the polymer behavior. Additionally, a bilinear strain rate dependence for peak stress, similar to that of epoxy, was found for the composites. This is in contrast to the strain rate independent mechanical behavior of nickel and aluminum for the range of strain rates carried out in this work.

- The influence of the highly strain rate dependent nature of epoxy, was found to have a strong effect on the deformation response of the composites at the mesoscale level. For low rates of strain ($< 10^{-3} \text{ s}^{-1}$) the deformation rate of the aluminum particles with strain is smaller than at high rates of strain ($> 10^3 \text{ s}^{-1}$). This has previously not been shown for particle reinforced polymer-matrix composites. The influence of a second, harder particle phase (Ni) on the deformation of the aluminum particles was also investigated. For the composites containing Ni, the aluminum strain levels achieved are increased dramatically for the particles and more so for those in the vicinity of the Ni particles. This is attributed to the rapid strain hardening of Ni,

that causes them to act as "rigid anvils" distributed throughout the epoxy matrix.

- Using computational simulations to further investigate the mesoscale mechanical behavior of these composites, the epoxy matrix was found to behave differently than a pure epoxy material. For these composites the epoxy is altered by the presence of the particles, causing it to have a higher strain rate dependency than pure epoxy. This results in the epoxy having more strength than aluminum which allows it to impart more stress into aluminum causing increased amounts of deformation. From a sensitivity study conducted on epoxy it was determined that the increased strain rate dependency of the epoxy matrix is dependent on the amounts and types of particle reinforcement. This highlights the need for new polymer models to be developed that incorporate the strengthening effects of particles.

- The altered mechanical behavior of epoxy due to the presence of particles is a result of changes to the epoxy network. From DMA tests the epoxy was found to have a higher degree of crosslinking, and DSC analyses revealed the formation of an interphase in the epoxy matrix. These are clear indications that the chemistry of the epoxy matrix has been modified and is different from neat epoxy. The glass transition temperature and decomposition temperature were also found to be different.

For the first time, the influence of the strain rate dependent strength for epoxy matrix has been shown to cause a strain rate dependent deformation response of reinforcement particle phases that are typically strain rate independent (for the strain rates tested in this work). Particle reinforced polymer matrix composites, for use at high strain rates, therefore, need to have the strain rate dependencies of the polymer matrix incorporated into their design. This is important, not only for their bulk strength and deformation characteristics, but for their mesoscale characteristics, in which the polymer matrix can have large changes in their strain rate sensitivities. By taking advantage of polymer strain rate sensitivities, this can aid in the preferential deformation of certain particle phases for increases in reactivity (as in the case of

structural energetic composites), or as a dissipation of energy from unwanted loads by transferring stresses from the matrix to more ductile particle phases. With this in mind the polymer matrix needs to be formulated to have the required rate dependent characteristics for their intended application.

7.2 *Future Work*

7.2.1 Dynamic Response of Composites Under Additional Loading Conditions

A bilinear dependence of the peak stress with strain rate was observed for the epoxy-based composites in this study. However, a large gap of experimental data for intermediate rates of strain exist between 10^{-3} and $10^3 s^{-1}$. Drop weight impact experiments and implementation of servo-hydraulic compression frames capable of achieving these strain rates would be very beneficial for pinpointing the transition strain rate between the peak stress exhibiting a low strain rate dependence to a high strain rate dependence. Experiments at these rate would also lead to better insights into the polymer-particle interactions and particle deformation mechanisms.

The current study only examined the effects of composite configuration on the mechanical behavior at strain rates up to $5 \times 10^3 s^{-1}$ however, many of these types of materials are designed for use at higher strain rates where shock waves are generated due to the extreme pressures produced during loading. A study examining the effects of particle reinforcement type, loading fractions, and size on strain rates $> 10^3 s^{-1}$, corresponding to shock wave propagation through these materials would enable equations of state describing the composites under these loading conditions to be developed and lead to a better understanding of the reactivity and mechanical behavior of polymer matrix structural energetic materials.

7.2.2 Effects of Epoxy Structure on Particle Strain

In Chapter 1, the relation between the epoxy chemical structure and polymer properties were briefly discussed. Also, from particle strain measurements as well as mesoscale simulations the epoxy was found to have a higher strength than aluminum at high strain rates. By changing the length of the epoxy chain as well varying the curing agent, changes in the glass transition temperature, degree of crosslinking, and relaxation behavior of the epoxy can be modified and possibly tailored to preferentially cause particles within the matrix to deform to different extents at varying strain rates. Additionally, by altering the chemistry of the epoxy system, the cohesion of the epoxy with the particles may also be modified. This would lead to changes in the interphase characteristics at the particle-matrix interface and therefore changes in the mechanical behavior of the composites. Using surfactants the effects of cohesion on the interphase and mechanical behavior can be examined without changing the epoxy system.

Another method of examining the effects of epoxy structure on the mechanical behavior of the composites is to change the particle size, type, or loading fraction. In present work the particle size has been shown to affect the crosslink density as well as the interphase thickness calculated from differential scanning calorimetry and dynamic mechanical analysis techniques respectively. In the composite design space used in this research there were only two particle sizes chosen for the aluminum particles and one particle size for nickel. Further studies that expand on the two factorial design space would yield a better understanding of not only the interplay between particle size, loading fraction, or type with the epoxy matrix but the resultant bulk mechanical behavior as well. By including a set of composites that contain only the nickel particles the mechanical response of composites containing aluminum and nickel can be more easily decomposed into the contributions of the individual constituents. As a starting point for expansion on the investigated design space,

additional recommended composite configurations are shown in Table 7.1.

Table 7.1: Material configurations determined from a two-factorial design of experiments with suggested initial configurations to expand the design space.

Material	Al Particle Size (μm)	Al Vol. Fraction (%)	Ni Particle Size (μm)	Ni Vol. Fraction (%)
MNML-1	50	40	50	10
MNML-2	5	40	50	10
MNML-3	50	20	50	10
MNML-4	5	20	50	10
MNML-5	50	40	N/A	0
MNML-6	5	40	N/A	0
MNML-7	50	20	N/A	0
MNML-8	5	20	N/A	0
Expanded-1	5	40	5	10
Expanded-2	5	40	5	10
Expanded-3	5	20	5	10
Expanded-4	5	20	5	10
Expanded-5	N/A	0	50	10
Expanded-6	N/A	0	5	10

In Table 7.1 the expanded set of material configurations focus on the inclusion of composites with smaller sized nickel particles and those containing only nickel with epoxy. Often composite properties increase with increased loading fractions of reinforcing particles. However, there is also a trend where the property of interest increases up to a certain point with increased loading fractions of particles and then begins to decay or stabilize with further increases in loading fractions of particles. There is also the possibility that at low loading fractions for properties to decrease initially and then begin to increase at higher loading fractions. Therefore, an investigation of composite configurations focused on determining the effects of particle volume fraction for a set particle size would lead to a greater understanding of the interaction of the particles with the epoxy matrix and the bulk/mesoscale mechanical behaviors.

7.2.3 Alternative Matrix Materials for Enhanced Structural Properties

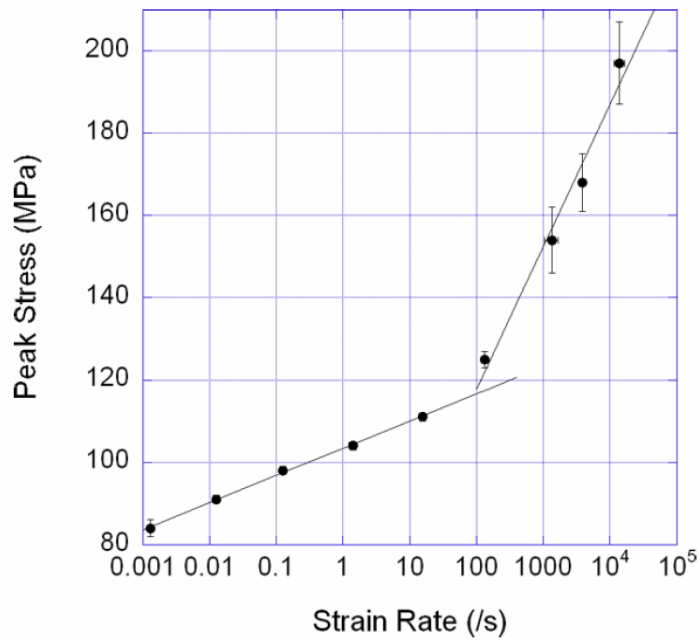
One of the overall goals for structural energetic materials is for the composite to exhibit high elastic modulus and strength properties. In this research the strength and elastic modulus were found to be rate dependent and have values of approximately 83 to 103 MPa and 6 to 13 GPa respectively at quasi-static strain rates. However, there is potential for much improvement in these properties. By considering other matrix materials improved structural properties may be achieved.

One such matrix material that may be of benefit is poly(ether-ether-ketone) (PEEK). PEEK has been characterized as an ultrapolymer with large strength values for a polymer. PEEK exhibits a bilinear dependence in flow stress/strength that is similar to that of epoxy (see Fig. 7.1). However, the transition from low strain rate dependence to high strain rate dependence occurs at a lower strain rate that is between $10^{-1}s^{-1}$ and 10^0s^{-1} , where as epoxy has a transition at approximately 10^2 . This increase in strength at lower strain rates has the potential to cause the matrix surrounding higher strain rate inducing particles (such as Ni) to strengthen quicker than epoxy and cause larger amounts of deformation in other particles. In the low strain rate dependence regime PEEK has strengths that are roughly 30 MPa higher than epoxy. In the high strain rate dependence regime the strength of PEEK is still higher than that of epoxy but appears to have a shallower strain rate dependence. By examination of the slopes this causes epoxy to eventually have strengths at strain rates greater than $\sim 10^4s^{-1}$. It should be noted that the data for PEEK does not go about $10^{-1}s^{-1}$ which would not rule out the possibility of PEEK still having higher strengths at much larger strain rates. With that being said the higher strengths for PEEK below 10^4s^{-1} would still cause a higher degree of particle deformation in particle reinforced PEEK composites to occur, as well as at earlier stages in the loading process at the higher rates of strain. While it is left to be seen how they perform

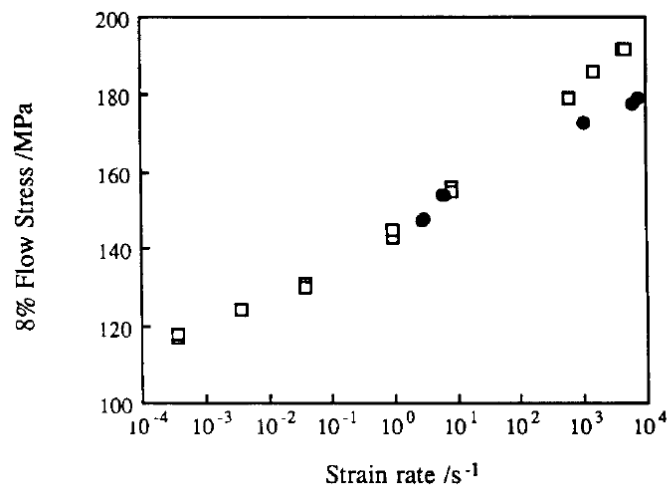
with reinforcement particles such as nickel and aluminum as was the case in this research, from a rule of mixtures point of view PEEK's more ideal structural properties in comparison to epoxy would produce a composite with preferred mechanical properties than those found in epoxy-based composites.

Another material of beneficial interest for a matrix material is self reinforcing polyphenylene (SRP). While few studies have examined the properties of SRP, the tensile and flexural strengths have both been shown to be higher than other performance thermoplastics such as PEEK and PEI [135]. A graph comparing the flexural strength of an SRP PX-1000 to other high performance polymers is shown in Fig. 7.2. The mechanism behind the large increase in strength over other polymers is due to a reinforcing rigid-rod effect of the chain backbone being comprised of multiple phenylenes (di-substituted benzene rings). The chemical structure of an SRP with and without substitute side chains are shown in Fig. 7.3. The tensile and flexural strengths and moduli values of 200-350 MPa and 8-10 GPa [135, 136, 137] respectively are fairly large in comparison to the epoxy used in this research with a modulus < 4 GPa and strength values < 100 MPa (compressive) [2]. Additionally the compressive strength for Tecamax SRP measured according to the ASTM D 695 standard was found to be > 620 MPa [137]. This would undoubtedly give a composite comprised of SRP much higher strengths than epoxy-based composites. However, to the authors knowledge no studies have been conducted on particle reinforced SRP and any effects of particles on the mechanical behavior of SRP are left to be determined.

Both PEEK and SRP are thermoplastics and therefore have strong differences in their mechanical and thermal behavior than that of epoxy (a thermoset). While increased strain rate loading conditions typically make polymers behave more brittly and hence more like an epoxy their lack of chemical crosslinking would most likely change how any reinforcing particles within the polymer matrix deform particularly in the dynamic regime. The increased temperatures at higher strain rates can cause



(a) Replot of the peak stress for epoxy (Epon 826/DEA) across a wide range of strain rates from 10^{-3} to 10^4 s^{-1} . Figure is from [2].



(b) Peak stress for PEEK across a wide range of strain rates. Figure is from [134].

Figure 7.1: Peak stress for PEEK and Epon826/DEA across a wide range of strain rates.

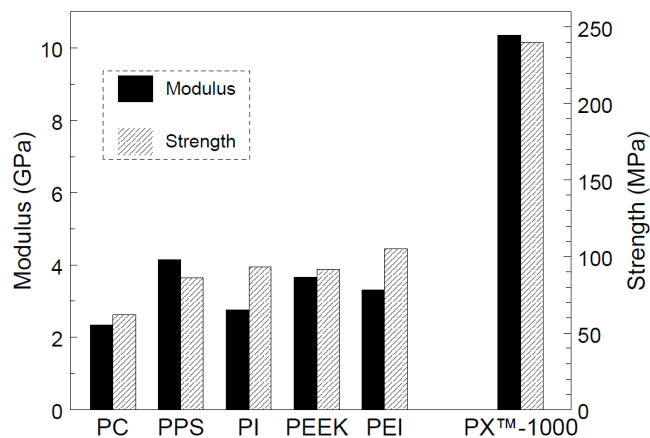


Figure 7.2: Comparison of tensile properties for various engineering thermoplastics. Figure taken from [135].

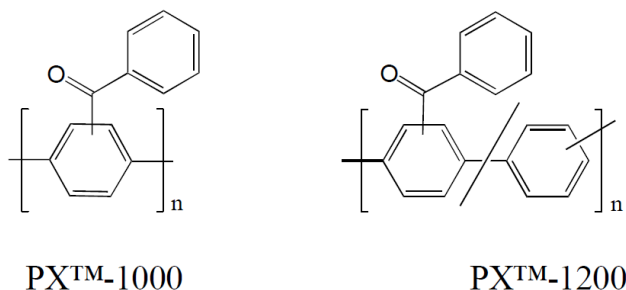


Figure 7.3: Chemical structures of and self reinforcing polyphenylene. Figure taken from [135].

the polymer matrix to melt and flow more readily under loads that can open up different deformation mechanisms to take place. This would lead to more particle-particle contact and fluid like flow of the polymer that could enhance mixing between the constituents.

7.2.4 Alternative Matrix Materials for Increased Energetics

The previous two alternative matrix materials were discussed to increase the mechanical properties of the composite. For increased energetics while still maintaining the use of an epoxy matrix as the binder a fluorinated epoxy may be used. One example

of a fluorinated epoxy system is shown in Fig. 7.4. This system was studied by Ge et al. [138] to examine the flexural and thermal properties of a fluorinated epoxy resin and compare the results to the more commonly used epoxy resin, DGEBA, which has a similar chemical structure. Their findings show the flexural modulus and strength properties of the fluorinated epoxies to be on par with the DGEBA resins (see Table 7.2).

Table 7.2: Mechanical properties of the thermal-cured fluorinated (BEF) and DGEBA epoxy resins with different curing agents. Data taken from [138].

Samples	Resin/Curing Agent	Flexural Strength (MPa)	Flexural Modulus (GPa)
EP-1	BEF/HMPA	119	2.09
EP-2	BEF/6FAPB	79	2.13
EP-3	BEF/TMDA	92	2.09
EP-4	DGEBA/HMPA	126	1.95
EP-5	DGEBA/6FAPB	82	2.23
EP-6	DGEBA/TMDA	105	1.86

The absorption of moisture can often lead to a plasticization effect. A fluorinated epoxy has an additional advantage of decreased moisture absorption than an epoxy without fluorine as a member of the polymer chain structure as shown by [138]. This would help stabilize the mechanical behavior of the epoxy matrix used in composites over longer periods of storage in a wider range of conditions.

By functionalizing SRP with fluorine it may be possible to have combined energetic benefits with higher strength characteristics. Poly(p-phenylene), due to their rigid backbone chain and exceptional thermal and chemical stability that do not dissolve easily, have been functionalized in a study by Wright et al. [139] to increase polymer solubility for easier synthesis. The poly(p-phenylene) was functionalized with many types of side chains (fluorinated as well as nonfluorinated) indicating the wide range of possible chain structures available for study as viable matrix materials in structural energetic materials with high strength and energetic formulations. The chemical structure of poly(p-phenylene) with studied functional groups can be seen in

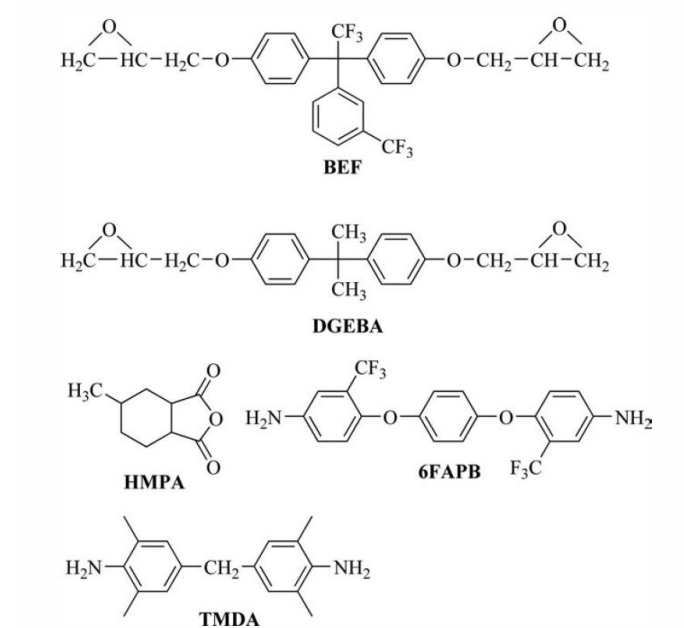


Figure 7.4: Chemical structures of fluorinated and non-fluorinated epoxy resins (BEF and DGEBA) and curing agents (HMPA, 6FAPB, and TMDA). Figure taken from [138].

Fig. 7.5. Having the capability of varying the side chain length would also present the opportunity to characterize the effect of side chain group length on the mechanical behavior and relaxation mechanisms of the polymer at high rates of strain. One note regarding the mechanical behavior of functionalized polyphenylenes should be made. By introducing the side chain groups the mechanical behavior will be altered due to a change in the chain-chain interactions. Therefore, parallel investigations of the SRP and functionalized SRP's would be highly beneficial.

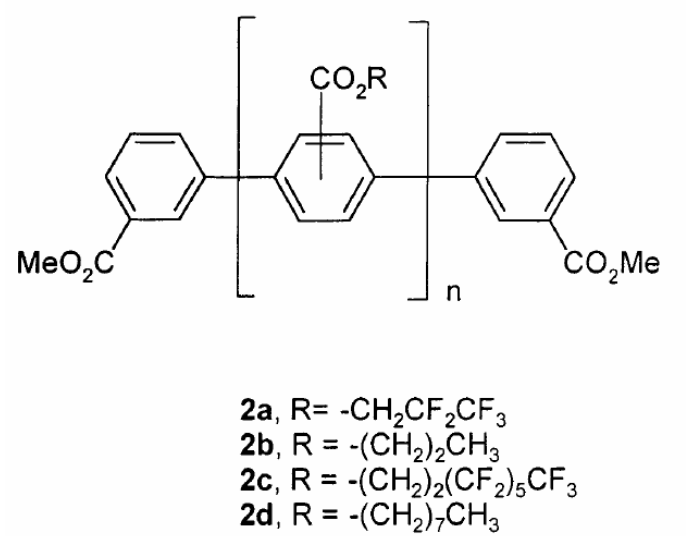


Figure 7.5: Chemical structure of functionalized poly(p-phenylene) and investigated side groups. Figure taken from [139].

APPENDIX A

EPOXY RESIN AND CURING AGENT SYSTEM

A.1 Curing of Epoxy Resins

To begin to understand epoxy one must first understand their processing and curing mechanisms. Epoxy systems are usually comprised of a resin and a curing agent, that when mixed together form a physically and more importantly chemically cross-linked molecular network of polymer chains that is irreversible and cannot be re-shaped from the original geometry of the mold without machining. This system is part of a much broader type of polymer known as a thermoset, which is different from a thermoplastic that can be melted and re-shaped after curing. This makes thermoset polymers more thermally stable and better suited for high-temperature applications up to their decomposition temperature, which for epoxy is around 380 °C. However, the cross-linked nature of thermosets also makes them more brittle. The most common resin used in epoxies is diglycidylether of bisphenol-A (DGEBA) which is synthesized from the reaction between epichlorohydrin and bisphenol-A (BPA) through a step-growth polymerization. In Fig. A.1 the structures of BPA and epichlorohydrin are shown in the reaction diagram to produce the most basic unit of DGEBA (degree of polymerization of essentially one) with epoxide groups on the ends and two phenyl groups in the center. The epoxide ($\text{CH}_2\text{-CH-O}$) three member ring groups act as the primary reaction sites for cross-linking when curing agents are introduced.

Amines are often used in the curing of epoxies. They yield a high degree of cross-linking and produce good strength and chemical resistance. For these types of amine based curing agents the amine group bonds to the DGEBA by first opening epoxide end groups between the oxygen and end carbon. The amine nitrogen then forms a new

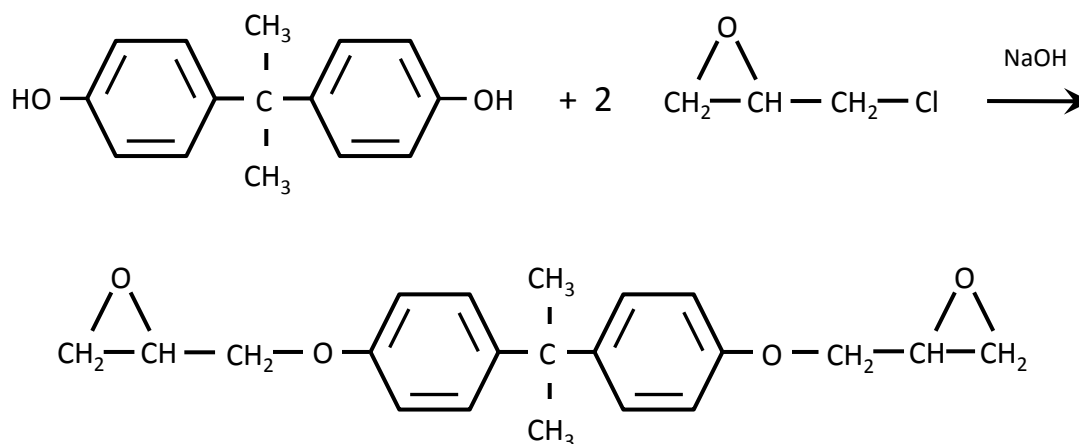


Figure A.1: Reaction of bisphenol-A (BPA) with epichlorohydrin to form the basic structure of diglycidylether of bisphenol-A (DGEBA), a common resin used in epoxy systems.

bond with the carbon atom, while the hydrogen moves to the electronegative oxygen creating a hydroxyl group. The number of amine groups with available hydrogen atoms present in the molecules of the curing agent affects, the degree of cross-linking in these systems. By using diethylamine, for example, only one amine group (with one hydrogen atom) is available to create an end capped DGEBA molecule [17, 18]. The reaction for this system is shown in Fig. A.2.

In systems with curing agents containing more than one amine group (polyamine) such as ethylenediamine (two amines with two hydrogen atoms each) , diethylenetriamine (two amine groups with two hydrogen atoms each, and one amine with one hydrogen), or triethylenetetramine (two amines with two hydrogen atoms each, and two amines with one hydrogen) the amount of available sites for bonding with DGEBA can be increased from one to four, five and six respectively thereby increasing the degree of cross-linking in the final cured epoxy system (see Fig. A.3. There are many different types of curing agents available and oftentimes more than one type is used in an epoxy system.

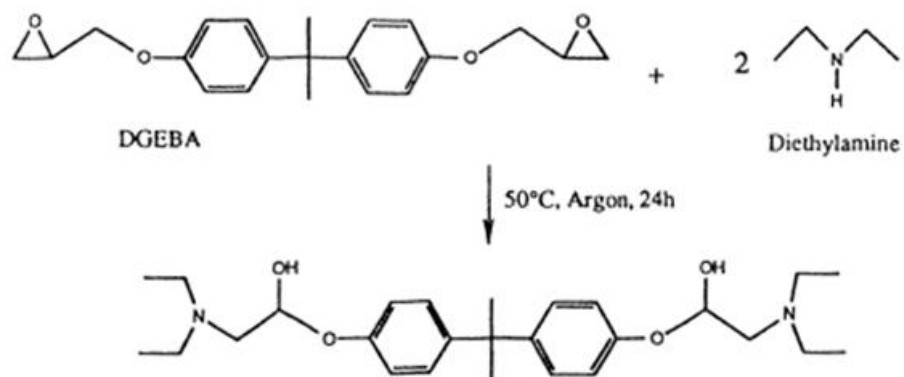


Figure A.2: Reaction of diglycidylether of bisphenol-A (DGEBA) and diethylamine. Figure taken from [17].

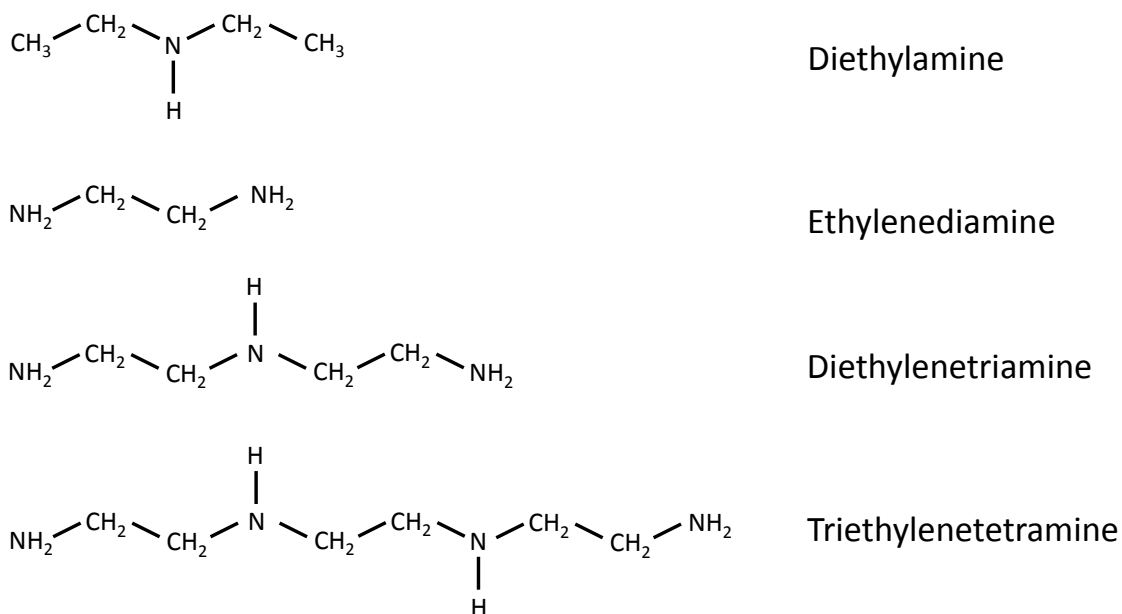


Figure A.3: Amine-based curing agents for curing epoxy resins with different amounts bonding sites, altering the amount degree of cross-linking that is possible for a given epoxy system.

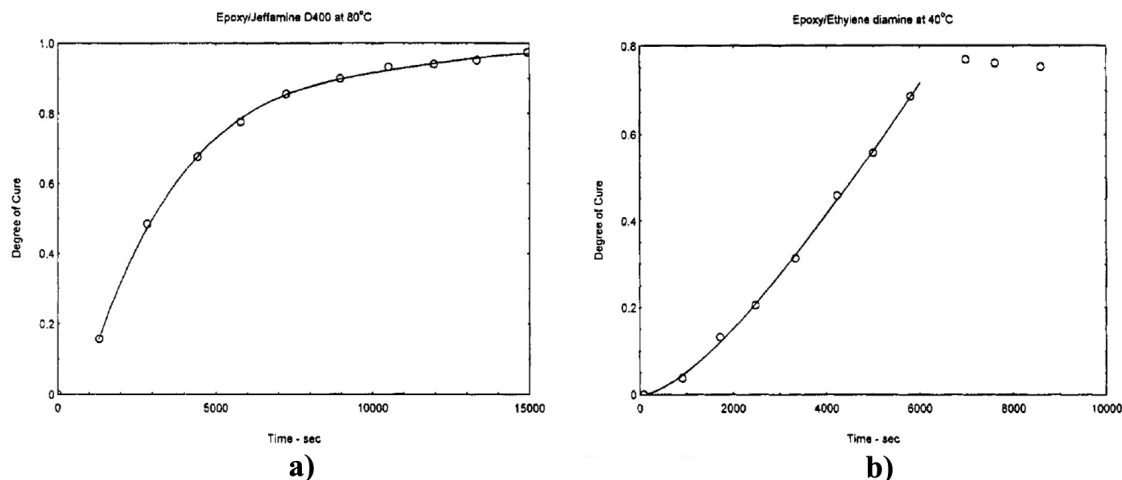


Figure A.4: Variation of the degree of cure with time for DGEBA cured with Jeffamine D400 at 80 °C a), and Ethylene at 40 °C b). Experimental data points are shown as circles and the solid curve represents a best-fit, fourth-order polynomial. Images were taken from [19].

Many researchers have investigated the effects of curing temperature [17, 18, 19, 20] on the curing times of amine-cured DGEBA epoxy. In these studies many different amines based curing agents were used such as: polyoxypropylendiamine (Jeffamine D400) [19], ethylenediamine [19], diethylamine [17, 18], and diethanolamine [19, 20] to name a few. For these systems the time to reach full cure decreased with increased curing temperatures. In [19] epoxy/polyoxypropylene-diamine cured at 80 °C reached approximately full cure within 5 hours whereas epoxy/ethylenediamine reached about 75% cure after 3 hours and showed no additional reactions of curing afterwards. They attributed the stalling of the curing reaction in the ethylenediamine cured system to the curing temperature being lower than the glass transition temperature for this system ($T_g = 105^\circ\text{C}$). At the point of leveling off ($\approx 75\%$ of cure) the reacting system 'vitrifies' slowing down the reaction rates between the curing agent and the resin (see Fig. A.4). The authors noted that for the Jeffamine D400 system with a T_g of 40°C and cured at 40°C , the curing properties were similar to that of the ethylenediamine system cured at 40°C .

In other work by [17], they showed that Raman spectroscopy can be used to investigate the cure mechanisms of amine-cured epoxy and results were compared with near-infrared (NIR) absorbance spectrum. They used diethylamine to end cap the DGEBA molecules by curing them at 50 °C and monitoring the NIR absorbance spectrum, and found the reactions in the mixture to be completely consumed after 24 hours, indicated by the disappearance of the epoxide peak (4525 /cm). In normalized Raman spectroscopy the ratio of the epoxide peak and phenyl ring peak was also shown to be linearly related to the epoxide concentration. Other researchers [18] investigating DGEBA cured with diethylamine first made a stoichiometric solution of DGEBA with the diethylamine cured at 51 °C for 48 hours and then added DGEBA in increments of 10% to the DGEBA/diethylamine solution from 0% to 100% DGEBA. They then used NIR and Raman spectroscopy to monitor any reactions within these mixtures. For 70% (w/w) DEGEBA/diethylamine they monitored the absorbance spectrum for approximately 80 hours and noticed that after approximately 6 hours the epoxide peak began to decrease dramatically, as shown in Fig. A.5. Since there should be no high degree of cross-linking due to the end capped nature of this system they suggested this phenomenon to be due to the formation of a tertiary amine between the DGEBA/diethylamine solution and the added neat DGEBA resin.

For DGEBA cured with diethanolamine (DEA) in a 100:11.65 ratio (DGEBA:DEA by wt.), Lundberg et. al [20] found that the epoxy is sufficiently cured within in 8 days at a curing temperature of 24 °C, 3 days at 40 °C and 18 hours at 75 °C. Whereas other researchers have used Raman and NIR spectroscopy, or variations in dynamic shear modulus to name a few, they examined the glass transition temperature, hardness, and linear shrinkage as indicators of chemical changes or degree of cure. By using this method they noticed the glass transition of the epoxy to be dependent on the curing temperature. When they used a curing temperature of 100 °C T_g increased with curing time to around 93 °C to 100 °C after about one week of curing. For the

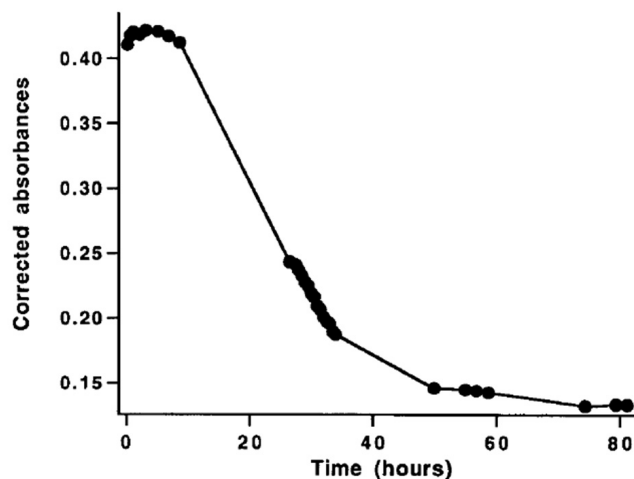


Figure A.5: Stability plot of 70% (w/w) DGEBA/diethylamine. Plot shows a decrease in the epoxide peak absorbance as curing time increases despite having an end-capped crosslinking agent. Figure taken from [18].

case of when a 40 °C curing temperature was used T_g after one week was around 60 °C and continued to increase to about 70 °C with curing times up to 100 days with no further data points taken beyond 100 days for this curing method. Results showing a comparison of the two curing methods can be seen in Fig. A.6.

They also noticed that the glass transition temperature would change when a higher post-cure temperature was used. When they cured the epoxy at 40 °C, the final glass transition temperature was around 55 °C to 60 °C after 3 days and with post curing at 100 °C for an additional 3 days yielded a glass transition temperature of 97 °C and 103 °C after additional post curing at 125 °C. In both cases the glass transition temperature reached a plateau at around 100 °C. In this study the researchers also found the durometer, D , hardness to be insensitive in the degree of cure after the epoxy had gelled and developed its initial cure indicating that it is not a suitable method for measuring the degree of cure. The hardness for this system while not reported was estimated to be around 90 from Figure 21 in [20].

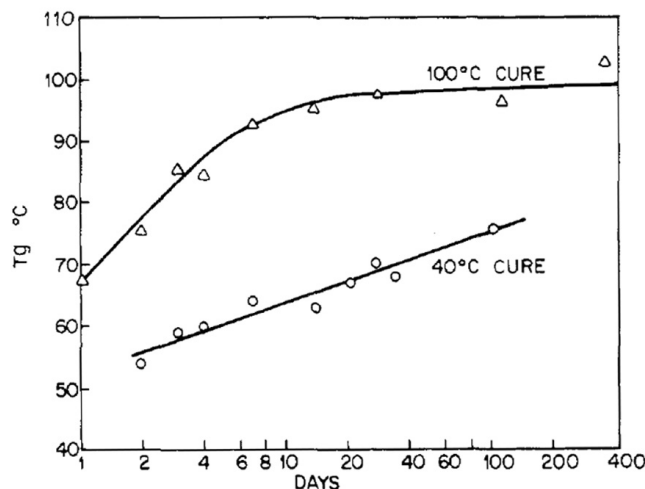


Figure A.6: Glass transition temperature as a function of curing times for DGEBA cured with diethanolamine DEA. Figure taken from [20].

A.2 Alternate Curing Method in Amine-Cured Epoxies

In the present work diethanolamine (DEA) is used as a curing agent, which is similar in structure to diethylamine. Whereas diethylamine has a terminating methyl (R-CH₃) group on each end, diethanolamine has a carbon atom with hydroxyl group (R-CH₂OH) in place of one of the hydrogen atoms. This can influence the matrix properties due to a difference in the curing method of amine-cured epoxies and interactions of diethanolamine with the metal particles dispersed throughout the matrix.

In the case of cross-linking mechanisms the diethanolamine allows the epoxy to behave to a small degree as an end capped DGEBA similar to the diethylamine cured epoxies, but also opens up the possibility for etherification with additional epoxide end groups to increase the degree of cross-linking within the system and increased hydrogen bonding. This reaction of epoxide with the hydroxyl to form an ether group (the reaction shown in Fig. A.7) is most likely to occur in cases where the amine is present in less than stoichiometric concentrations.

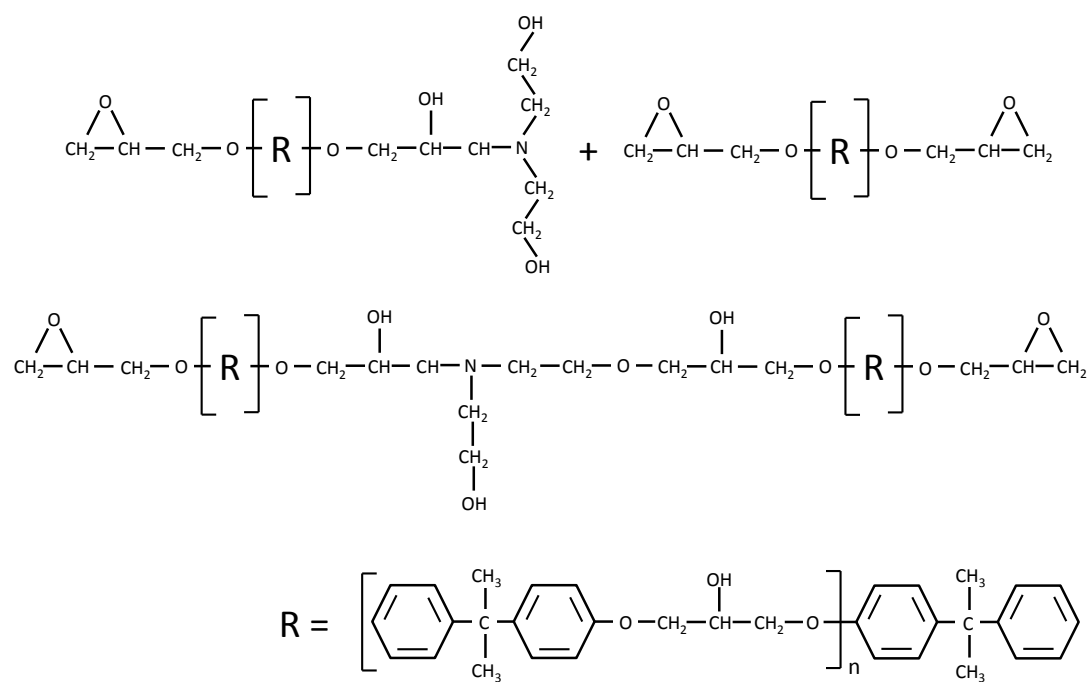


Figure A.7: Possible reaction pathway for creating additional cross-links in an epoxy system.

One possible explanation for amines being present in less than stoichiometric concentrations is the local variation of the epoxy and curing agent at the molecular scale during the curing process. Another possibility is the interaction of the diethanolamine with the surfaces of the metal particles (discussed in section 2.3.1), which can cause a less than stoichiometric ratio between the amine and epoxide groups.

A.3 Effect of Water Molecules on Relaxation Mechanisms in Epoxy

In an amine-cured epoxy there are two main polar groups that are present, the hydroxyl groups and the nitrogen groups from the amines. When water infiltrates in epoxy it will have a tendency to form a hydrogen bond between these groups first [140]. Other likely hydrogen bonding of water can occur between two hydroxyl groups as well as hydrogen bonding of water between hydroxyl and ether groups (less likely due relatively weak hydrogen bonding with ether). As discussed earlier, as the epoxide bonds with the amines in the curing agent a hydroxyl group is formed which can be a potential hydrogen bonding site with water. The amount of water that can then be absorbed therefore varies with the amount of bonding sites with the curing agent in a DGEBA system as well as the ratio of amine in the system. In epoxide rich epoxies there will be fewer available hydrogen bonding sites while in amine rich epoxies there will be more. When the water infiltrates the epoxy matrix, the water molecules act as a plasticizer and decreases the temperature at which relaxation mechanisms in epoxy occur. In work carried out by Feng et al. [140], T_g , was found to decrease by approximately 9°C in epoxies that were cured with sulfanilamide. The activation energies of the gamma relaxation were also lower as an indication of a plasticization effect. These results for the glass transition and activation energies are shown in Figures A.8 and A.9 which are taken from [140].

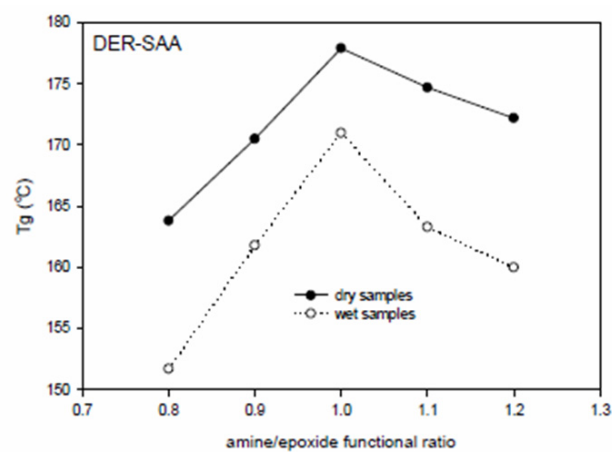


Figure A.8: Water effect on glass transition temperature of DER-SAA system. Figure taken from [140].

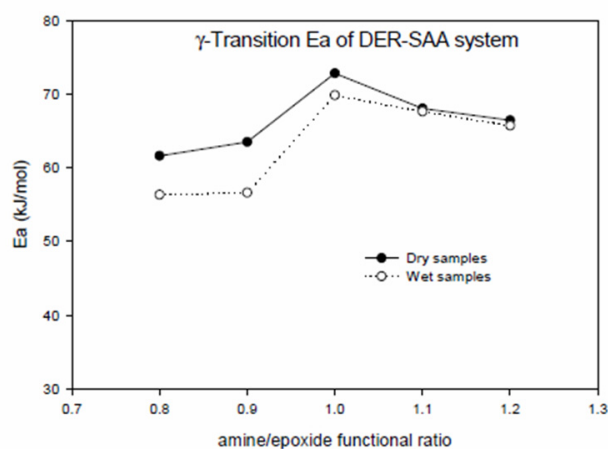


Figure A.9: Effect of amine/epoxide functional ratio on the activation energy of the gamma relaxation of DER-SAA system. Figure taken from [140].

APPENDIX B

SPLIT-HOPKINSON PRESSURE BAR EQUATIONS

In the following section equations are derived which are used for determining the stress and strain in samples during loading using a split-Hopkinson pressure bar (SHPB). The derivation is based on the assumption of one dimensional wave propagation and follows the derivation found in [104].

Assuming there are only elastic waves in the pressure bars a 1-D wave propagation analysis is used to relate strain in the bars to the stresses and strains in a sample placed between the incident and transmission bars. The subscripts *1* and *2* refer to the bar ends on the incident and transmission side of the specimen respectively. Additionally the subscripts *i*, *r*, and *t* refer the variables pertaining to the incident, reflected, and transmission waves respectively.

Starting with the general form of an equation for 1-D wave propagation:

$$\frac{\partial^2 u}{\partial t^2} = \frac{1}{C_{bar}} \frac{\partial^2 u}{\partial t^2} \quad (61)$$

where C_{bar} is the speed of sound of the bars used in the SHPB apparatus. The general solution to Eqn. 61 for waves traveling in the incident and transmission bars have the form:

$$u(x, t) = f(x - ct) + g(x + ct) = u_i + u_r \quad (62)$$

and,

$$u(x, t) = h(x - ct) = u_t \quad (63)$$

The strains in the bars can be found for the incident and transmission bars using:

$$\varepsilon = \frac{\partial u}{\partial x} = \frac{\partial u}{\partial f} \frac{\partial f}{\partial x} + \frac{\partial u}{\partial g} \frac{\partial g}{\partial x} = f' + g' = \varepsilon_i + \varepsilon_r \quad (64)$$

and,

$$\varepsilon = \frac{\partial u}{\partial x} = \frac{\partial u}{\partial h} \frac{\partial h}{\partial x} = h' = \varepsilon_t \quad (65)$$

Similarly the velocities of the bars are found using:

$$\dot{u}_1 = \frac{\partial u}{\partial t} = -C_{bar}\varepsilon_i + C_{bar}\varepsilon_r \quad (66)$$

and,

$$\dot{u}_2 = \frac{\partial u}{\partial t} = -C_{bar}\varepsilon_t \quad (67)$$

Looking at the specimen between the bars we know that the rate of strain in the specimen will be related to the bar end velocities and specimen length through the following relation:

$$\dot{\varepsilon}_{sample} = \frac{\dot{u}_1 - \dot{u}_2}{l_s} = \frac{-C_{bar}\varepsilon_i + C_{bar}\varepsilon_r + C_{bar}\varepsilon_t}{l_s} \quad (68)$$

$$\dot{\varepsilon}_{sample} = \frac{C_{bar}}{l_s} (-\varepsilon_i + \varepsilon_r + \varepsilon_t) \quad (69)$$

Eqn. 69 is used for a three-wave analysis of the strain in the sample. If we now take a look at the forces at the bar ends, then on either side of the specimen we know:

$$\sigma = \frac{F}{A_{bar}} = E_{bar}\varepsilon \quad (70)$$

or upon rearranging,

$$F_{bar} = A_{bar}E_{bar}\varepsilon \quad (71)$$

Upon substitution of the strain for the incident and transmission bars the forces on either side of the sample become:

$$F_1 = A_{bar}E_{bar}(\varepsilon_i + \varepsilon_r) \quad (72)$$

and,

$$F_2 = A_{bar}E_{bar}(\varepsilon_t) \quad (73)$$

Assuming force equilibrium has been reached in the sample following an initial ringup and the sample deforms uniformly then $F_1 = F_2$. From this relation we can now relate the strain from the transmission wave in the transmission bar the strains from the incident and reflected waves in the incident bar through the following equation:

$$\varepsilon_t = \varepsilon_i + \varepsilon_r \quad (74)$$

Substituting Eqn. 74 into Eqn. 69 a one-wave analysis equation for the rate of strain in the specimen is related to the strain due to the reflected wave by:

$$\dot{\varepsilon}_{sample} = \frac{C_{bar}}{l_s}(-\varepsilon_i + \varepsilon_r + \varepsilon_i + \varepsilon_r) = \frac{C_{bar}}{l_s}(2\varepsilon_r) \quad (75)$$

The stress within the specimen still needs to be derived. Assuming that volume is conserved in the sample while deforming we can write:

$$A_0l_0 = A_sl_s \quad (76)$$

where the left hand side of the equation is the initial sample geometry and the right hand side the instantaneous sample geometry. The instantaneous sample area is then found using:

$$A_s = \frac{A_0l_0}{l_s} \quad (77)$$

where l_s is found from either Eqn. 69 or 75

Using the definition of stress, (F/A_s) , a derivation of the stress in the sample is related to the forces at the bar ends through the following equation. Since the forces are assumed to be equal on either end of the sample then either F_1 or F_2 can be used in the calculations.

$$\sigma_{sample} = \frac{A_{bar}E_{bar}}{A_s} (\varepsilon_i + \varepsilon_r) \quad (78)$$

or,

$$\sigma_{sample} = \frac{A_{bar}E_{bar}}{A_s} (\varepsilon_t) \quad (79)$$

Eqn. 78 is used for a two-wave analysis of the sample stress while Eqn. 79 a one-wave analysis. For a three-wave analysis an average of the two are taken using:

$$\sigma_{sample} = \frac{A_{bar}E_{bar}}{2A_s} (\varepsilon_i + \varepsilon_r + \varepsilon_t) \quad (80)$$

APPENDIX C

THERMOMECHANICAL LOSS MODULUS AND TAN- δ CURVES

C.1 Loss Modulus, E'' , Curves for MNML-Series Composites

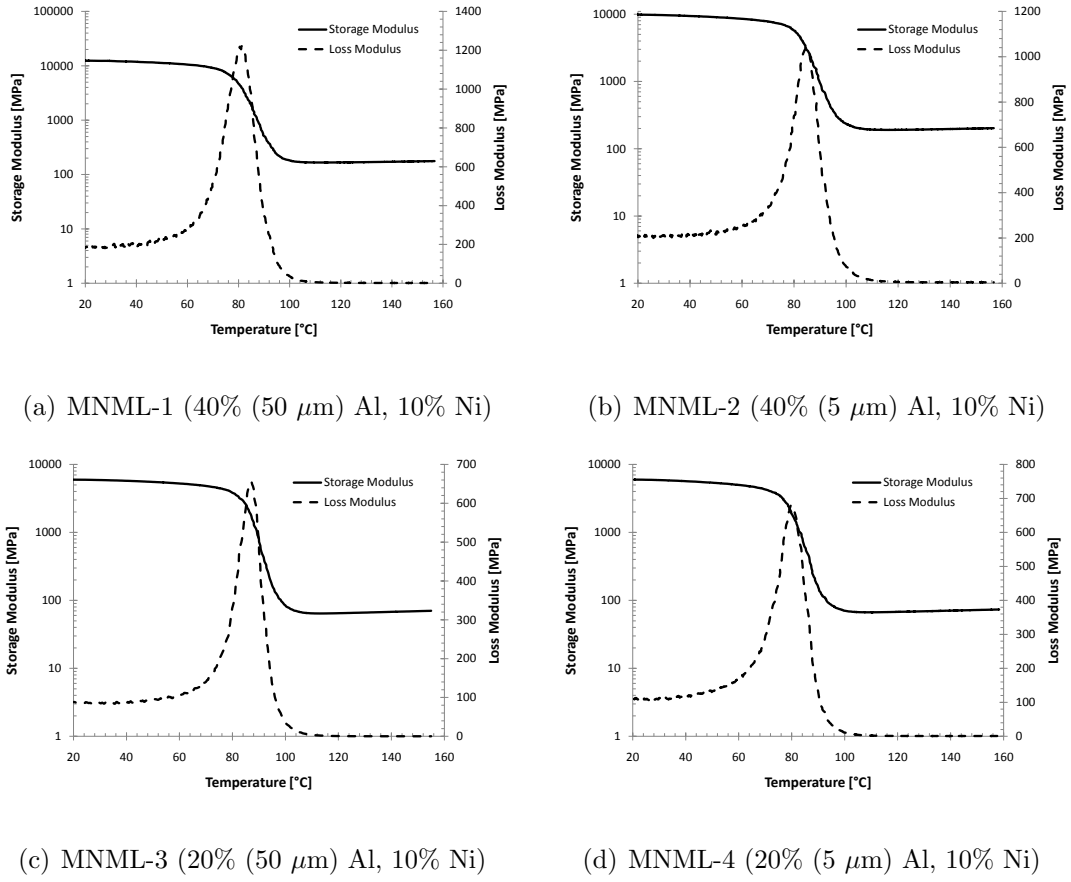
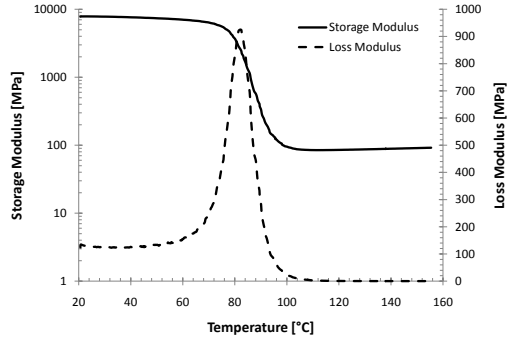
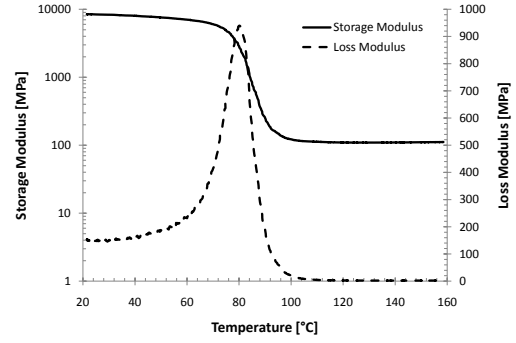


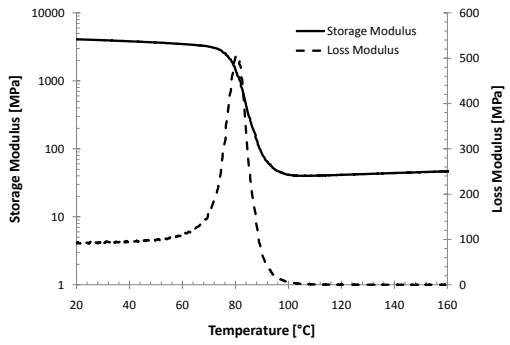
Figure C.1: Loss modulus temperature plots for composites MNML-1 through 4.



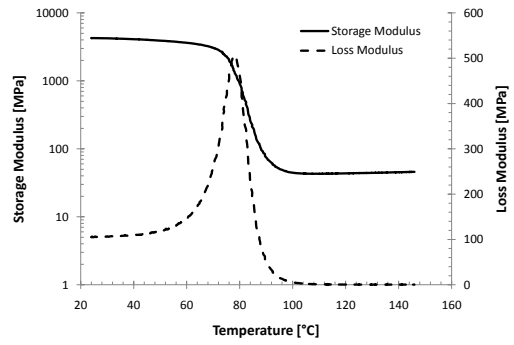
(a) MNML-5 (40% (50 μm) Al)



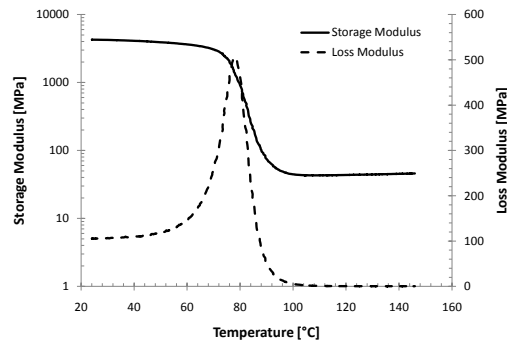
(b) MNML-6 (40% (5 μm) Al)



(c) MNML-7 (20% (50 μm) Al)



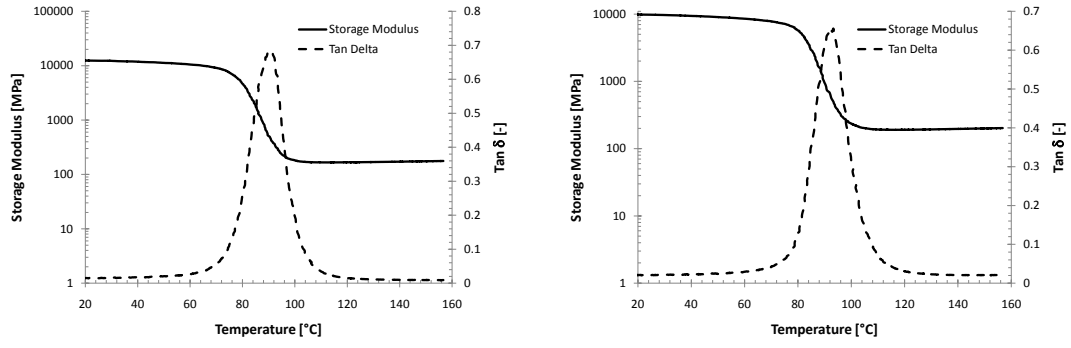
(d) MNML-8 (20% (5 μm) Al)



(e) Epoxy (Epon826/DEA)

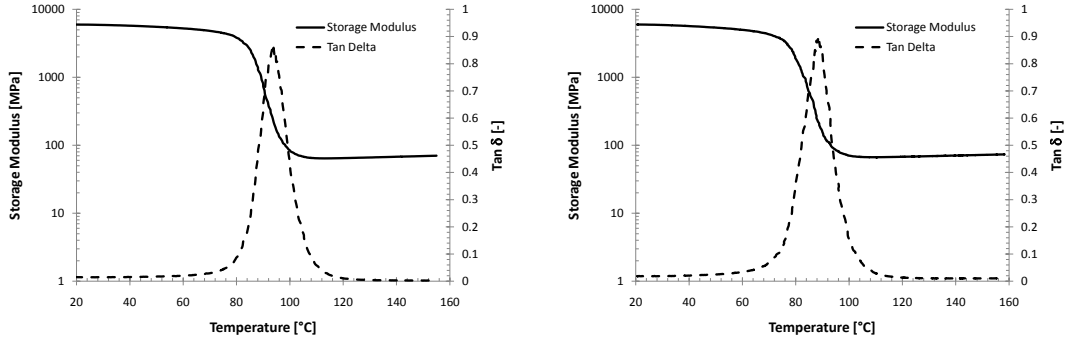
Figure C.2: Representative loss modulus curves for each composite MNML-5 through 8 plotted along side the storage modulus. (Continuation of previous figures.)

C.2 $\tan \delta$ Curves for MNML-Series Composites



(a) MNML-1 (40% (50 μm) Al, 10% Ni)

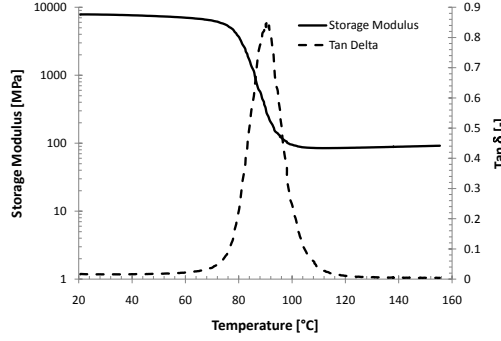
(b) MNML-2 (40% (5 μm) Al, 10% Ni)



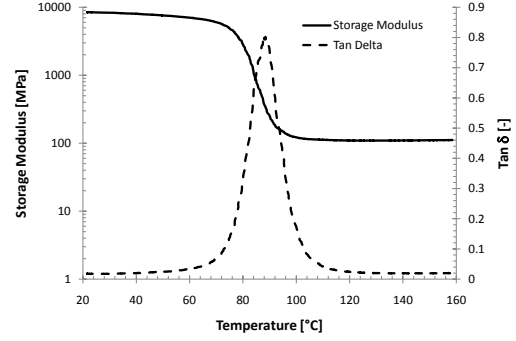
(c) MNML-3 (20% (50 μm) Al, 10% Ni)

(d) MNML-4 (20% (5 μm) Al, 10% Ni)

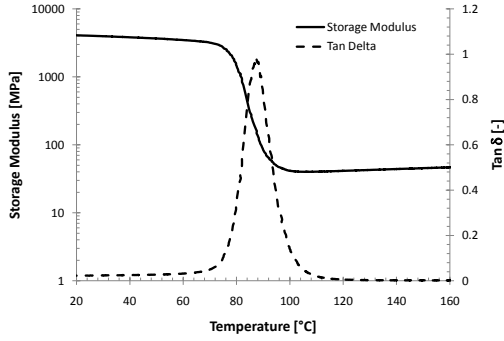
Figure C.3: Representative $\tan \delta$ curves for each composite MNML-1 through 4 plotted along side the storage modulus.



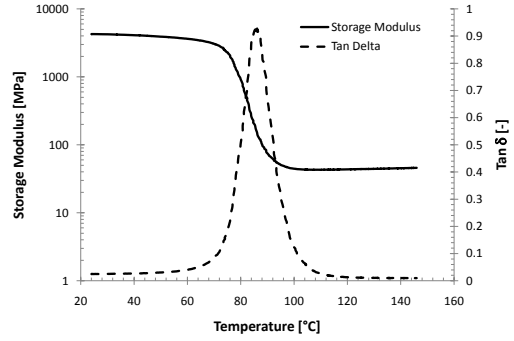
(a) MNML-5 (40% (50 μm) Al)



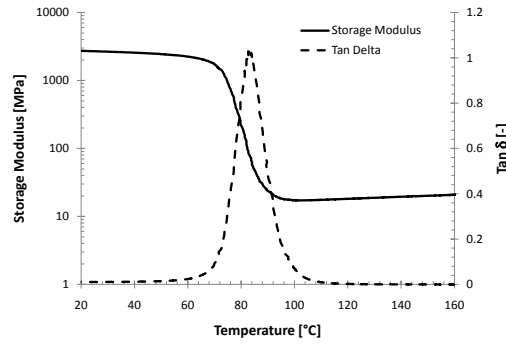
(b) MNML-6 (40% (5 μm) Al)



(c) MNML-7 (20% (50 μm) Al)



(d) MNML-8 (20% (5 μm) Al)

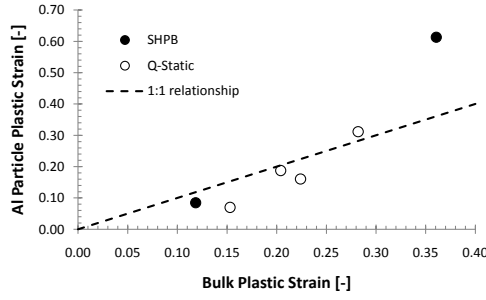


(e) Epoxy (Epon826/DEA)

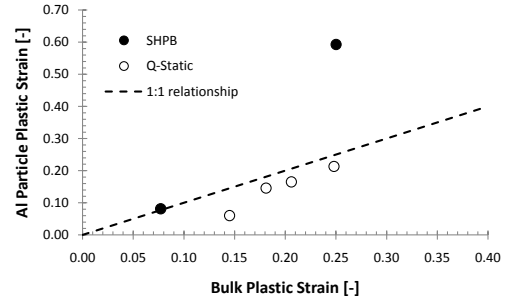
Figure C.4: Representative $\tan \delta$ curves for each composite MNML-5 through 8 plotted along side the storage modulus. (Continuation of previous figures.)

APPENDIX D

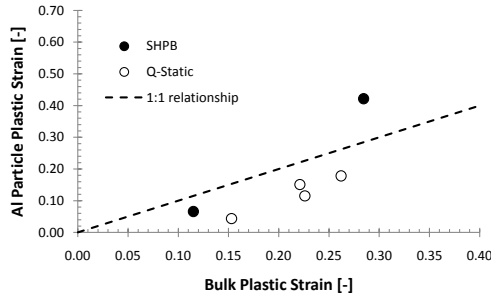
PARTICLE STRAIN PLOTS FOR MNML-1, -3, -5, AND 7



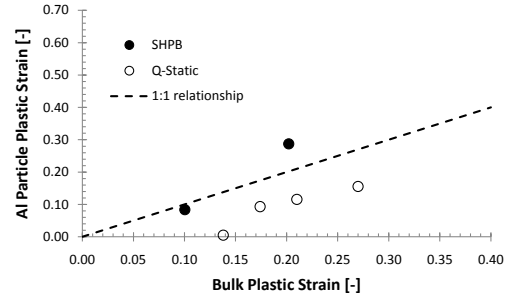
(a) MNML-1 (40% (50 μm) Al, 10% Ni)



(b) MNML-3 (20% (50 μm) Al, 10% Ni)



(c) MNML-5 (40% (50 μm) Al)



(d) MNML-7 (20% (50 μm) Al)

Figure D.1: The average amount of plastic strain in the aluminum particles for composites MNML-1, -3, -5, and -7 plotted against the bulk plastic strain.

REFERENCES

- [1] Z. Hashin and S. Shtrikman, “A variational approach to the theory of the elastic behavior of multiphase materials,” *J. Mech. Phys. Solids*, vol. 11, pp. 127–140, 1963.
- [2] J. L. Jordan, J. R. Foley, and C. R. Siviour, “Mechanical properties of Epon 826/DEA epoxy,” *Mech Time-Depend Mater*, vol. 12, pp. 249–272, 2008.
- [3] L. Ferranti Jr., *Mechanochemical reactions and strengthening in epoxy-cast aluminum iron-oxide mixtures*. PhD thesis, Georgia Institute of Technology, 2007.
- [4] E.-C. Koch, “Metal-fluorocarbon-pyrolants: III. Development and application of magnesium/Teflon/Viton (MTV),” *Propellants, Explosives, Pyrotechnics*, vol. 27, pp. 262–266, 2002.
- [5] K. K. Kuo, G. A. Risha, B. J. Evans, and E. Boyer, “Potential usage of energetic nano-sized powders for combustion and rocket propulsion,” *Materials Research Society Symposium Proceedings*, vol. 800, pp. 3–14, 2004.
- [6] K. Blobaum, M. Reiss, J. P. Lawrence, and T. Weihs, “Decomposition and characterization of a self-propagating CuO_x/Al thermite reaction in a multilayer foil geometry,” *Journal of Applied Physics*, vol. 94, pp. 2915–2922, 2003.
- [7] R. G. Ames, “Energy release characteristics of impact-initiated energetic materials,” *Materials Research Society Symposium Proceedings*, vol. 896, pp. 123–132, 2006.
- [8] J. Cai, S. Walley, R. Hunt, W. Proud, V. Nesterenko, and M. Meyers, “High-strain, high-strain-rate flow and failure in PTFE/Al/W granular composites,” *Materials Science and Engineering A*, vol. 472, pp. 308–315, 2008.
- [9] A. Rai, L. Zhou, A. Prakash, A. McCormick, and M. Zachariah, “Understanding and tuning the reactivity of nano-energetic materials,” *Materials Research Society Symposium Proceedings*, vol. 896, pp. 99–110, 2006.
- [10] E. B. Herbold, N. N. Thadhani, and J. L. Jordan, “Observation of a minimum reaction initiation threshold in ball-milled Ni+Al under high-rate mechanical loading,” *Journal of Applied Physics*, vol. 109, p. 066108, 2011.
- [11] S. Du, B. Aydelotte, D. Fondse, C.-T. Wei, F. Jiang, E. Herbold, K. Vecchio, M. Meyers, and N. Thadhani, “Explosive compactions of intermetallic-forming powder mixtures for fabricating structural energetic materials,” in *Shock Compression of Condensed Matter-2009* (M. L. Elert, W. T. Buttler, M. D. Furnish,

- W. W. Anderson, and W. G. Proud, eds.), pp. 498–501, American Institute of Physics, Melville, New York,, 2009.
- [12] S. Du and N. Thadhani, “Impact initiation of pressed Al-based intermetallic forming powder mixture compacts,” in *Shock Compression of Condensed Matter-2009* (M. L. Elert, W. T. Buttler, M. D. Furnish, W. W. Anderson, and W. G. Proud, eds.), pp. 470–473, American Institute of Physics, Melville, New York,, 2009.
 - [13] J. Addiss, J. Cai, S. Walley, W. Proud, and V. Nesterenko, “High strain and strain-rate behaviour of PTFE/aluminum/tungsten mixtures,” in *Shock Compression of Condensed Matter-2007* (M. L. Elert, M. D. Furnish, R. Chau, N. Holmes, and J. Nguyen, eds.), pp. 773–776, American Institute of Physics, Melville, New York,, 2007.
 - [14] M. Martin, S. Hanagud, and N. Thadhani, “Mechanical behavior of nickel+aluminum powder-reinforced epoxy composites,” *Materials Science and Engineering A*, vol. 403, pp. 209–218, 2007.
 - [15] J. L. Jordan, L. Ferranti, R. A. Austin, R. D. Dick, J. R. Foley, N. N. Thadhani, D. L. McDowell, and D. J. Benson, “Equation of state of aluminum-iron oxide-epoxy composite,” *Journal of Applied Physics*, vol. 101, p. 093520, 2007.
 - [16] A. Fredenburg, A. Jakus, T. McCoy, J. Cochran, and N. Thadhani, “Processing and dynamic properties of high-energy-density linear cellular alloy (LCA) coupled structural energetic materials,” *JANNAF Conference Proceedings*, pp. 1–7, 2009.
 - [17] K. Hong, T. Vess, R. Lyon, K. Chike, J. Aust, and M. Myrick, “Remote cure monitoring of polymeric resins by laser Raman spectroscopy,” *International SAMPE Symposium and Exhibition (Proceedings)*, vol. 38, pp. 427–435, 1993.
 - [18] K. Chike, M. Myrick, R. Lyon, and S. Angel, “Raman and near-infrared studies of an epoxy resin,” *Applied Spectroscopy*, vol. 47, pp. 1631–1635, 1993.
 - [19] M. L. Huang and J. G. Williams, “Mechanisms of solidification of epoxy-amine resins during cure,” *Macromolecules*, vol. 27, pp. 7423–7428, 1994.
 - [20] C. Lundberg, “Diethanolamine as a hardener for epoxy resins,” *Ind. Eng. Chem. Prod. Res. Dev.*, vol. 19, pp. 319–326, 1980.
 - [21] I. Ward and J. Sweeney, *An Introduction to the Mechanical Properties of Solid Polymers*. The Atrium, Southern Gate, Chichester, West Sussex PO19 8SQ, England: John Wiley & Sons, Ltd, 2004.
 - [22] G. Adam and J. H. Gibbs, “On the temperature dependence of cooperative relaxation properties in glass-forming liquids,” *The Journal of Chemical Physics*, vol. 43, pp. 139–146, 1965.

- [23] "Huntsman Corporation, Jeffamine D-400 Polyetheramine." http://www.huntsman.com/performance_products/Media/JEFFAMINE_D-400_US.pdf.
- [24] "Huntsman Corporation, Jeffamine D-230 Polyetheramine." [http://www.huntsman.com/performance_products/Media/JEFFAMINE_D-230_Polyoxypropylenediamine_\(05-09\).pdf](http://www.huntsman.com/performance_products/Media/JEFFAMINE_D-230_Polyoxypropylenediamine_(05-09).pdf).
- [25] S. Cukierman, J.-L. Halary, and L. Monnerie, "Molecular analysis of the viscoelastic properties of epoxy networks as deduced from the study of model systems," *Journal of Non-Crystalline Solids*, vol. 131-133, pp. 898-905, 1991.
- [26] J. A. Schroeder, P. A. Madsen, and R. T. Foister, "Structure/property relationships for a series of crosslinked aromatic/aliphatic epoxy mixtures," *Polymer*, vol. 28, pp. 929-940, 1987.
- [27] M. Ochi, M. Okazaki, and M. Shimbo, "Mechanical relaxation mechanism of epoxide resins cured with aliphatic diamines," *Journal of Polymer Science: Polymer Physics Edition*, vol. 20, pp. 689-699, 1982.
- [28] M. Ochi, H. Iesako, and M. Shimbo, "Relaxation mechanism of epoxide resin cured with acid anhydrides. III. Effect of alkyl side chains on mechanical and dielectric β relaxations," *Journal of Polymer Science: Part B: Polymer Physics*, vol. 24, pp. 1271-1282, 1986.
- [29] M. Ochi, Mitsukazu and Yoshizumi and M. Shimbo, "Mechanical and dielectric relaxations of epoxide resins containing the spiro-ring structure. II. Effect of the introduction of methoxy branches on low-temperature relaxations of epoxide resins," *Journal of Polymer Science: Part B: Polymer Physics*, vol. 25, pp. 1817-1827, 1987.
- [30] M. Gettings, F. Baker, and A. Kinloch, "Use of auger and x-ray photoelectron spectroscopy to study the locus of failure of structural adhesive joints," *Journal of Applied Polymer Science*, vol. 21, pp. 2375-2392, 1977.
- [31] P. Bebin and R. E. Prud'homme, "Comparative XPS study of copper, nickel, and aluminum coatings on polymer surfaces," *Chem. Mater.*, vol. 15, pp. 965-973, 2003.
- [32] J. Kelber and R. Brow, "Model epoxy/metal-oxide chemical interactions: Diethanolamine on oxidized copper and aluminum," *Applied Surface Science*, vol. 59, pp. 273-280, 1992.
- [33] P. Rosso and L. Ye, "Epoxy/silica nanocomposites: Nanoparticle-induced cure kinetics and microstructure," *Macromolecule Rapid Communications*, vol. 28, pp. 121-126, 2007.
- [34] A. Marzocca, A. Somoza, S. Goyanes, W. Salgueiro, and P. Konig, "Characterization of free volume in particulate-filled epoxy resin by means of dynamic

- mechanical analysis and positron annihilation lifetime spectroscopy,” *Polymer International*, vol. 51, pp. 1277–1284, 2002.
- [35] G. W. Brassell and K. B. Wischmann, “Mechanical and thermal expansion properties of a particulate filled polymer,” *Journal of Materials Science*, vol. 9, pp. 307–314, 1974.
 - [36] I. Low, “Effects of residual stresses on the failure micomechanisms in toughened epoxy systems,” *Journal of Materials Science*, vol. 25, pp. 2144–2148, 1990.
 - [37] S. Tognana, W. Salgueiro, and A. Somoza, “On the matrix-particle interphase in epoxy-based composites,” *Journal of Alloys and Compounds*, vol. 495, pp. 588–591, 2010.
 - [38] Y. Lipatov, *Physical Chemistry of Filled Polymers, Translated from the Russian by R.J. Moseley*, ch. 3. Shawbury Shrewsbury Salop SY4 4NR England: Rubber and Plastics Research Association of Great Britain, 1979.
 - [39] G. Spathis, E. Sideridis, and P. Theocaris, “Adhesion efficiency and volume fraction of the boundary interphase in metal-filled epoxies,” *International Journal of Adhesion and Adhesives*, vol. 1, pp. 195–201, April 1981.
 - [40] P. S. Theocaris, S. G.E., and P. Panagiotopoulos, “Calculation of effective transverse elastic moduli of fiber-reinforced composites by numerical homogenization,” *Composites Science and Technology*, vol. 57, pp. 573–586, 1997.
 - [41] E. Vassileva and K. Friedrich, “Epoxy/alumina nanoparticle composites. I. Dynamic mechanical behavior,” *Journal of Applied Polymer Science*, vol. 89, pp. 3774–3785, 2003.
 - [42] W.-D. Hergeth, U.-J. Steinau, and H.-J. Bittrich, “Polymerization in the presence of seeds. Part IV: Emulsion polymers containing inorganic filler particles,” *Polymer*, vol. 30, pp. 254–258, 1989.
 - [43] K. Iisaka and K. Shibayama, “Mechanical α -dispersion and interaction in filled polystyrene and polymethylmethacrylate),” *Journal of Applied Polymer Science*, vol. 22, pp. 3135–3143, 1978.
 - [44] K. Iisaka and K. Shibayama, “Effect of filler particle size on dynamic mechanical properties of poly(methyl methacrylate),” *Journal of Applied Polymer Science*, vol. 22, pp. 1321–1330, 1978.
 - [45] D. Brown, V. Marcadon, P. Mele, and N. Alberola, “Effect of filler particle size on the properties of model nanocomposites,” *Macromolecules*, vol. 41, pp. 1499–1511, 2008.
 - [46] T. Lewis and L. Nielsen, “Dynamic mechanical properties of particulate-filled composites,” *Journal of Applied Polymer Science*, vol. 14, pp. 1449–1471, 1970.

- [47] N. Alberola and P. Mele, "Interface and mechanical coupling effects in model particulate composites," *Polymer Engineering and Science*, vol. 37, pp. 1712–1721, 1997.
- [48] N. Bleach, S. Nazhat, K. Tanner, M. Kellomaki, and P. Tormala, "Effect of filler content on mechanical and dynamic mechanical properties of particulate biphasic calcium phosphate-polyactide composites," *Biomaterials*, vol. 23, pp. 1579–1585, 2002.
- [49] P. Cousin and P. Smith, "Dynamic mechanical properties of sulfonated polystyrene/alumina composites," *Journal of Polymer Science: Part B: Polymer Physics*, vol. 32, pp. 459–468, 1994.
- [50] S. Goyanes, P. Konig, and J. Marconi, "Dynamic mechanical analysis of particulate-filled epoxy resin," *Journal of Applied Polymer Science*, vol. 88, pp. 883–892, 2003.
- [51] S. Goyanes, J. Marconi, P. Konig, M. Martin, and I. Mondragon, "Dynamic properties of epoxy composites filled with quartz powder," *Journal of Alloys and Compounds*, vol. 310, pp. 374–377, 2000.
- [52] R. Jain, A. Narula, and V. Choudhary, "Studies on epoxy/calcium carbonate nanocomposites," *Journal of Applied Polymer Science*, vol. 114, pp. 2161–2168, 2009.
- [53] J. Liang, "Viscoelastic properties and characterization of inorganic particulate-filled polymer composites," *Journal of Applied Polymer Science*, vol. 114, pp. 3955–3960, 2009.
- [54] G. Papanicolaou, A. Xepapadaki, A. Kotrotsos, and D. Mouzakis, "Interphase modeling of copper-epoxy particulate composites subjected to static and dynamic loading," *Journal of Applied Polymer Science*, vol. 109, pp. 1150–1160, 2008.
- [55] G. Sui, S. Jana, A. Salehi-khojin, S. Neema, W. Zhong, H. Chen, and Q. Huo, "Thermal and mechanical properties of epoxy composites reinforced by a natural hydrophobic sand," *Journal of Applied Polymer Science*, vol. 109, pp. 247–255, 2008.
- [56] B. J. Ash, J. Stone, D. F. Rogers, L. S. Schadler, R. W. Siegel, B. Benicewicz, and T. Apple, "Investigation into the thermal and mechanical behavior of PMMA/alumina nanocomposites," *Mat. Res. Soc. Symp. Proc.*, vol. 661, pp. KK2.10.1–KK2.10.6, 2001.
- [57] B. J. Ash, D. F. Rogers, C. J. Wiegand, L. S. Schadler, R. W. Siegel, B. Benicewicz, and T. Apple, "Mechanical properties of Al_2O_3 /polymethylmethacrylate nanocomposites," *Polymer Composites*, vol. 23, pp. 1014–1025, 2002.

- [58] B. J. Ash, R. W. Siegel, and L. S. Schadler, "Mechanical behavior of alumina/poly(methyl methacrylate) nanocomposites," *Macromolecules*, vol. 37, pp. 1358–1369, 2004.
- [59] B. J. Ash, R. W. Siegel, and L. S. Schadler, "Glass-transition temperature behavior of alumina/PMMA nanocomposites," *Journal of Polymer Science: Part B: Polymer Physics*, vol. 42, pp. 4371–4383, 2004.
- [60] A. Bansal, H. Yang, C. Li, B. C. Benicewicz, S. K. Kumar, and L. S. Schadler, "Controlling the thermomechanical properties of polymer nanocomposites by tailoring the polymer-particle interface," *Journal of Polymer Science: Part B: Polymer Physics*, vol. 44, pp. 2944–2950, 2006.
- [61] C. Hub, S. E. Harton, M. A. Hunt, R. Fink, and H. Ade, "Influence of sample preparation and processing on observed glass transition temperatures of polymer nanocomposites," *Journal of Polymer Science: Part B: Polymer Physics*, vol. 45, pp. 2270–2276, 2007.
- [62] K. Yung, B. Zhu, T. Yue, and C. Xie, "Effect of the filler size and content on the thermomechanical properties of particulate aluminum nitride filled epoxy composites," *Journal of Applied Polymer Science*, vol. 116, pp. 225–236, 2010.
- [63] A. Bergeret and N. Alberola, "A study of the interphase in styrene-methacrylic acid copolymer/glass bead composites," *Polymer*, vol. 37, pp. 2759–2765, 1996.
- [64] K. Iisaka and K. Shibayama, "Molecular motion in cured epoxy resin filled with mica flakes," *Journal of Applied Polymer Science*, vol. 22, pp. 1845–1852, 1978.
- [65] R. Goyal, A. Tiwari, U. Mulik, and Y. Negi, "Effect of aluminum nitride on thermomechanical properties of high performance PEEK," *Composites: Part A*, vol. 38, pp. 516–524, 2007.
- [66] B. A. Nelson, W. P. King, and K. Gall, "Shape recovery of nanoscale imprints in a thermoset "shape memory" polymer," *Applied Physics Letters*, vol. 86, p. 103108, 2005.
- [67] S. Lee and G. Swallowe, "Quasi-static and dynamic compressive behaviour of poly(methyl methacrylate) and polystyrene at temperatures from 293 K to 363 K," *Journal of Materials Science*, vol. 41, pp. 6280–6289, 2006.
- [68] A. Mulliken and M. Boyce, "Mechanics of the rate-dependent elastic-plastic deformation of glassy polymers from low to high strain rates," *International Journal of Solids and Structures*, vol. 43, pp. 1331–1356, 2006.
- [69] C. Siviour, S. Walley, W. Proud, and J. Field, "The high strain rate compressive behaviour of polycarbonate and polyvinylidene difluoride," *Polymer*, vol. 46, pp. 12546–12555, 2005.

- [70] C. Siviour, S. Walley, W. Proud, and J. Field, "Mechanical behaviour of polymers at high rates of strain," *J. Phys. IV*, vol. 134, pp. 949–955, 2006.
- [71] J. L. Jordan, J. R. Siviour, Clive R. and Foley, and E. N. Brown, "Compressive properties of extruded polytetrafluorethylene," *Polymer*, vol. 48, pp. 4184–4195, 2007.
- [72] F. Zerilli and R. Armstrong, "A constitutive equation for the dynamic deformation behavior of polymers," *Journal of Materials Science*, vol. 42, pp. 4562–4574, 2007.
- [73] S. Ahmad, "Flow stress of high density polyethylene and nylon 66 at high rates of strain," *Polymer International*, vol. 28, pp. 291–294, 1992.
- [74] J.-L. Tsai and J.-C. Huang, "Strain rate effect on mechanical behaviors of nylon 6-clay nanocomposites," *Journal of Composite Materials*, vol. 40, pp. 925–938, 2006.
- [75] J. Roetling, "Yield stress behaviour of poly(ethyl methacrylate) in glass transition region," *Polymer*, vol. 6, pp. 615–619, 1965.
- [76] S. Chou, K. Robertson, and J. Rainey, "The effect of strain rate and heat developed during deformation on the stress-strain curve of plastics," *Experimental Mechanics*, vol. 13, pp. 422–432, 1973.
- [77] A. Mulliken and M. Boyce, "Polycarbonate and a polycarbonate-POSS nanocomposite at high rates of deformation," *Journal of Engineering Materials and Technology*, vol. 128, pp. 543–550, 2006.
- [78] B. Briscoe and I. Hutchings, "Impact yielding of high density polyethylene," *Polymer*, vol. 17, pp. 1099–1102, 1976.
- [79] N. Al-Maliky, J. Fernandez, D. Parry, and G. Swallowe, "Drops in the flow stress of semi-crystalline polymers at very high rates of strain," *Journal of Materials Science Letters*, vol. 17, pp. 1141–1143, 1998.
- [80] S. Hamdan and G. Swallowe, "The strain-rate and temperature dependence of the mechanical properties of polyetherketone and polyetheretherketone," *Journal of Materials Science*, vol. 31, pp. 1415–1423, 1996.
- [81] J. Richeton, S. Ahzi, L. Daridon, and Y. Remond, "A formulation of the co-operative model for the yield stress of amorphous polymers for a wide range of strain rates and temperatures," *Polymer*, vol. 46, pp. 26035–6043, 2005.
- [82] C. Bauwens-Crowet, "The compression yield behaviour of polymethyl methacrylate over a wide range of temperature and strain-rates," *Journal of Materials Science*, vol. 8, pp. 968–979, 1973.

- [83] F. Rietsch and B. Bouette, “The compression yield behaviour of polycarbonate over a wide range of strain rates and temperatures,” *Eur. Polym. J.*, vol. 26, pp. 1071–1075, 1990.
- [84] G. Swallowe and S. Lee, “A study of the mechanical properties of PMMA and PS at strain rates of 10^{-4} to 10^3 over the temperature range 293–363,”
- [85] J. Richeton, S. Ahzi, K. Vecchio, F. Jiang, and R. Adharapurapu, “Influence of temperature and strain rate on the mechanical behaviour of three amorphous polymers: Characterization and modeling of the compressive yield stress,” *International Journal of Solids and Structures*, vol. 43, pp. 2318–2335, 2006.
- [86] C. Verbeek, “Effect of percolation on the mechanical properties of sand-filled polyethylene composites,” *Journal of Thermoplastic Composite Materials*, vol. 20, pp. 137–149, 2007.
- [87] H. Unal and A. Mimaroglu, “Influence of filler addition on the mechanical properties of nylon-6 polymer,” *Journal of Reinforced Plastics and Composites*, vol. 23, pp. 461–469, 2004.
- [88] P. Vollenberg and D. Heikens, “Particle size dependence of the young’s modulus of filled polymers: 1. Preliminary experiments,” *Polymer*, vol. 30, pp. 1656–1662, 1989.
- [89] B. Pukanszky and G. Voros, “Stress distribution around inclusions, interaction, and mechanical properties of particulate-filled composites,” *Polymer Composites*, vol. 17, pp. 384–392, 1996.
- [90] N. R. Patel, “Intermediate strain rate behavior of two structural energetic materials,” Master’s thesis, Georgia Institute of Technology, 2004.
- [91] G. Taylor and H. Quinney, “The latent energy remaining in a metal after cold working,” *Proceedings of the Royal Society of London. Series A, Containing Papers of a Mathematical and Physical Character*, vol. 143, pp. 307–326, 1934.
- [92] I. Hutchings, “Estimation of yield stress in polymers at high strain-rates using G.I. Taylor’s impact technique,” *J. Mech. Phys. Solids*, vol. 26, pp. 289–301, 1979.
- [93] J. Lee and O. Min, “Effect of thermal-softening in rod impact test for the determination of dynamic mechanical properties of polycarbonate,” *KSME Journal*, vol. 9, pp. 29–40, 1995.
- [94] O.-K. Min, C.-H. Nam, and J.-M. Lee, “Effect of aspect ratio in rod impact test for the determination of dynamic mechanical properties of polycarbonate at high-strain-rate,” *Polymer (Korea)*, vol. 16, pp. 375–382, 1992.

- [95] S. Sarva, A. Mulliken, and M. Boyce, "The mechanics of large-strain inhomogeneous deformation of polymeric materials under dynamic loading conditions," *J. Phys. IV France*, vol. 134, pp. 95–101, 2006.
- [96] S. Sarva, A. Mulliken, and M. Boyce, "Mechanics of Taylor impact testing of polycarbonate," *International Journal of Solids and Structures*, vol. 44, pp. 2381–2400, 2007.
- [97] P. J. Rae, E. N. Brown, B. E. Clements, and D. M. Dattelbaum, "Pressure-induced phase change in poly(tetrafluoroethylene) at modest impact velocities," *Journal of Applied Physics*, vol. 98, p. 063521, 2005.
- [98] M. Raftenberg, W. Mock Jr., and G. Kirby, "Modeling the impact deformation of rods of a pressed PTFE/Al composite mixture," *international Journal of Impact Engineering*, vol. 35, pp. 1735–1744, 2008.
- [99] W. Mock Jr. and W. H. Holt, "Impact initiation of rods of pressed polytetrafluoroethylene (PTFE) and aluminum powders," in *Shock Compression of Condensed Matter-2005* (E. M. L. Furnish, Michael D., T. Russel, and C. White, eds.), pp. 1097–1100, American Institute of Physics, Melville, New York,, 2006.
- [100] J. Millett, N. Bourne, and G. Stevens, "Taylor impact of polyether ether ketone," *International Journal of Impact Engineering*, vol. 38, pp. 1086–1094, 2006.
- [101] D. He and B. Jiang, "The elastic modulus of filled polymer composites," *Journal of Applied Polymer Science*, vol. 49, pp. 617–621, 1993.
- [102] J. Segurado and J. LLorca, "Computational micromechanics of composites: The effect of particle spatial distribution," *Mechanics of Materials*, vol. 38, pp. 873–883, 2006.
- [103] W. Farren and G. Taylor, "The heat developed during plastic extension of metals," *Proceedings of the Royal Society of London. Series A, Containing Papers of a Mathematical and Physical Character*, vol. 107, pp. 422–451, 1925.
- [104] H. Kuhn and D. Medlin, eds., *ASM Handbook: Vol. 8*. Ohio: ASM International, 2000.
- [105] M. Meyers, *Dynamic Behavior of Materials*. New York: John Wiley and Sons, Inc., 1994.
- [106] J. Mason, A. Rosakis, and G. Ravichandran, "On the strain and strain rate dependence of the fraction of plastic work converted to heat: and experimental study using high speed infrared detectors and the Kolsky bar," *Mechanics of Materials*, vol. 17, pp. 135–145, 1994.

- [107] D. Rittel, “On the conversion of plastic work to heat during high strain rate deformation of glassy polymers,” *Mechanics of Materials*, vol. 31, pp. 131–139, 1999.
- [108] A. Trojanowski, C. Ruiz, and J. Harding, “Thermomechanical properties of polymers at high rates of strain,” *J. Phys IV France*, vol. 7, pp. C3–447 – C3–452, 1997.
- [109] G. Adams and R. Farris, “Latent energy of deformation of bishpenol A polycarbonate,” *Journal of Polymer Science: Part B: Polymer Physics*, vol. 26, pp. 433–445, 1988.
- [110] T. Xie and I. Rousseau, “Facile tailoring of thermal transition temperatures of epoxy shape memory polymers,” *Polymer*, vol. 50, pp. 1852–1856, 2009.
- [111] D. Montgomery, *Design and Analysis of Experiments*). New York: John Wiley and Sons, Inc., 1997.
- [112] D. R. Lide, ed., *CRC-Handbook of Chemistry and Physics, 83rd Edition*, ch. 12. Boca Raton, Florida: CRC Press LLC, 2002–2003.
- [113] J. Achenbach, *Wave Propagation in Elastic Solids (North-Holland Series in Applied Mathematics and Mechanics)*, ch. 2. Amsterdam, The Netherlands: Elsevier Science Publishers B.V., 1975.
- [114] G. Taylor, “The use of flat-ended projectiles for determining dynamic yield stress. I. Theoretical considerations,” *Proceedings of the Royal Society of London. Series A, Mathematical and Physical Sciences*, vol. 194, pp. 289–299, 1948.
- [115] L. Ferranti Jr. and N. N. Thadhani, “Dynamic mechanical behavior characterization of epoxy-cast Al + Fe_2O_3 thermite mixture composites,” *Metallurgical and Materials Transactions A*, vol. 38, pp. 2697–2715, 2007.
- [116] J. Spowart, B. Maruyama, and D. Miracle, “Multiscale characterization of spatially heterogeneous systems: Implications for discontinuously reinforced metal-matrix composite microstructures,” *Materials Science and Engineering*, vol. 38A, pp. 75–82, 2001.
- [117] M. Tschopp, G. Wilks, and J. Spowart, “Multi-scale characterization of orthotropic microstructures,” *Modelling and Simulation in Materials Science and Engineering*, vol. 16, p. 065009, 2008.
- [118] W. Voigt, “Lehrbuch de kristallphysik,” *Teubner, Leipzig*, 1928.
- [119] A. Reuss, “Berechnung der fliegrenze von mischkristallen auf grund der plastizitätsbedingung fr einkristalle,” *Journal of Applied Mathematics and Mechanics / Zeitschrift fur Angewandte Mathematik und Mechanik*, vol. 9, pp. 49–58, 1929.

- [120] *Metals Handbook 9th Edition, Vol 2 Properties and Selection: Nonferrous Alloys and Pure Metals*. Metals Park, Ohio, 44073: American Society for Metals, 1979.
- [121] M. Kouzeli, L. Weber, C. S. Marchi, and A. Mortensen, “Quantification of microdamage phenomena during tensile straining of high volume fraction particle reinforced aluminium,” *Acta mater.*, vol. 49, pp. 497–505, 2001.
- [122] Z. Xu, K. Chawla, A. Wolfenden, A. Neuman, G. Liggett, and N. Chawla, “Stiffness loss and density decrease due to thermal cycling in an alumina fiber/magnesium alloy composite,” *Materials Science and Engineering A*, vol. 203, pp. 75–80, 1995.
- [123] P. Chen, F. Huang, and Y. Ding, “Microstructure, deformation, and failure of polymer bonded explosives,” *Journal of Materials Science*, vol. 42, pp. 5272–5280, 2007.
- [124] B. Benedikt, M. Lewis, and P. Rangaswamy, “On elastic interaction between spherical inclusions by the equivalent inclusion method,” *Computational Materials Science*, vol. 37, pp. 380–392, 2006.
- [125] R. Li, “Time-temperature superposition method for glass transition temperature of plastic materials,” *Materials Science and Engineering A*, vol. 278, pp. 36–45, 2000.
- [126] E. Matsubara, T. Ichitsubo, K. Itoh, T. Fukunaga, J. Saida, N. Nishiyama, H. Kato, and A. Inoue, “Heating rate dependence of T_g and T_x in Zr-based bmgs with characteristic structures,” *Journal of Alloys and Compounds*, vol. 483, pp. 8–13, 2009.
- [127] S. Barrau, P. Demont, C. Maraval, A. Bernes, and C. Lacabanne, “Glass transition temperature depression at the percolation threshold in carbon nanotube-epoxy resin and polypryrrole-epoxy resin composites,” *Molecular Rapid Communications*, vol. 26, pp. 390–394, 2005.
- [128] N. Abdel-Aal, F. El-Tantawy, A. Al-Hajry, and M. Bououdina, “Epoxy resin/plasticized carbon black composites. Part II. Correlation among network structure and mechanical properties,” *Polymer Composites*, vol. 29, pp. 804–808, 2008.
- [129] A. Omrani, S. Afsar, and M. A. Safarpour, “Thermoset nanocomposites using hybrid nano $\text{TiO}_2\text{-SiO}_2$,” *Materials Chemistry and Physics*, vol. 122, pp. 343–349, 2010.
- [130] A. Nichols III, “Users manual for ALE 3D: An Arbitrary Lagrangian/Eulerian 3D Code System,” *LLNL, UCRL-MA-152204*, vol. Rev 6, 2007.
- [131] “Particle pack 2.4.” Developed by Gary Friedman at LLNL, Software embedded as a feature of ALE3D.

- [132] D. Steinberg, S. Cochran, and M. Guinan, “A constitutive model for metals applicable at high-strain rate,” *Journal of Applied Physics*, vol. 51, p. 1948, 1980.
- [133] C. Siviour, P. Laity, W. Proud, J. Field, D. Porter, P. Church, P. Gould, and W. Huntingdon-Thresher, “High strain rate properties of a polymer-bonded sugar: Their dependence on applied and internal constraints,” *Proceedings of The Royal Society A*, vol. 464, pp. 1229–1255, 2008.
- [134] N. Diah, P. Leever, and J. Williams, “Thickness effects in split Hopkinson pressure bar tests,” *Polymer*, vol. 34, pp. 4230–4234, 1993.
- [135] F. Motamedi, M. Isomaki, M. S. Trimmer, and R. Vaia, “Molecular characteristics of self-reinforced thermoplastic polyphenylenes,” *Annual Technical Conference-ANTEC, Conference Proceedings (M10) 220*, vol. 2, p. 1772, 1998.
- [136] A. L. Woodcraft, V. Martelli, and G. Ventura, “Thermal conductivity of Tecamax SRP from millikelvin temperatures to room temperature,” *Cryogenics*, vol. 50, pp. 66–70, 2010.
- [137] “Product Information: Tecamax SRP extreme strength without fibre reinforcement.”
- [138] Z. Ge, Z. Tao, G. Li, J. Ding, L. Fan, and S. Yang, “Synthesis and properties of novel fluorinated epoxy resins,” *Journal of Applied Polymer Science*, vol. 120, pp. 148–155, 2011.
- [139] M. E. Wright, K. M. Lott, M. A. McHugh, and Z. Shen, “Synthesis of fluorinated and hydrocarbon ester functionalized poly(p-phenylenes) and their solubility in supercritical fluids,” *Macromolecules*, vol. 36, pp. 2242–2247, 2003.
- [140] J. Feng, *Interaction and permeability of water with liquid crystalline thermoset*. PhD thesis, University of Florida, 2001.